

**Land Surface Temperature derived from the Along Track
Scanning Radiometer**

Andrew Shepherd

**Presented for the degree of Doctor of Philosophy at the
University of Leicester, 1999.**

Land Surface Temperature derived from the Along Track Scanning Radiometer

Andrew Shepherd

Presented for the degree of Doctor of Philosophy at the University of Leicester, 1999.

Abstract

Terrestrial radiometric surface temperatures were recorded at multiple observation angles in conjunction with satellite overpasses of the Along Track Scanning Radiometer (ATSR) over two florally distinct regions of Zimbabwe. The experimental sites were, respectively, an open grassland savannah and a medium density natural woodland, each of which extended over some 1000 square kilometers of predominantly flat terrain. The principal surface components at each location were vegetation and soil in varying proportions.

Infrared brightness temperatures were corrected for atmospheric effects using solutions to the radiative transfer equation with coefficients derived from local atmospheric radiosoundings. The empirical equations of Idso (1981) and the RADGEN radiative transfer model (Zavody *et al.*, 1995) were used to derive atmospheric emittance and transmittance for the *in-situ* and ATSR data respectively.

Both *in situ* and ATSR derived radiative temperatures exhibited a pronounced angular variation over each surface, with differences upwards of 5°C between measurements at nadir and forward (55°) zenith angles. This effect has been attributed to the temperature differentials that exist within heterogeneous canopies, which typically display variations in vegetation cover related to the observation angle.

A simple two component canopy architecture was coupled with a linear mixture model to partition the ensemble surface emission. The fractional vegetation cover was estimated using multi-angle radiative temperatures and was in excellent agreement with *in situ* estimates. Empirical equations were derived from the *in situ* data which related vegetation and soil temperatures at each location. These relationships were used to constrain the surface component temperature regime so that ATSR dual-angle radiative surface temperatures were sufficient to derive the vegetation and soil temperatures and fractional cover. The difference between canopy and soil temperatures separated using the dual-angle data was greater than 30°C at certain times of the year, and the modal standard deviation for all component temperature estimates was 3.2°C.

Contents

| | |
|---|----|
| | 1 |
| Abstract..... | 2 |
| Contents..... | 3 |
| Acknowledgements..... | 5 |
| 1 Introduction..... | 6 |
| 1.1 Background to study..... | 6 |
| 1.1.1 The role of land surface temperature within the environment..... | 6 |
| 1.1.2 Land surface temperature in Zimbabwe..... | 7 |
| 1.2 Remote sensing and land surface temperatures..... | 9 |
| 1.3 Questions addressed by this work..... | 11 |
| 1.4 Thesis structure..... | 12 |
| 2 Radiative Land Surface Temperature Retrieval at Infrared Wavelengths: Theory..... | 14 |
| 2.1 Introduction..... | 14 |
| 2.2 Land Surface Temperature Measurement..... | 15 |
| 2.3 Radiative Transfer Theory for Land Surface Temperature Retrieval..... | 16 |
| 2.4 Correcting infrared radiation for atmospheric effects..... | 20 |
| 2.4.1 Quantifying the effects of attenuation and emission within the atmosphere..... | 23 |
| 2.4.2 Empirical techniques for estimating infrared atmospheric emittance and transmittance..... | 28 |
| 2.4.3 Numerical techniques for estimating infrared atmospheric emittance and transmittance..... | 34 |
| 2.4.4 Summary..... | 37 |
| 2.5 Differential techniques for Land Surface Temperature Retrieval..... | 38 |
| 2.6 Estimating the Temperature of a Heterogeneous Surface..... | 42 |
| 2.7 Summary..... | 46 |
| 3 A Laboratory calibration of terrestrial Infrared Radiometers..... | 48 |
| 3.1 Introduction..... | 48 |
| 3.2 Angular response..... | 49 |
| 3.3 Absolute Radiometric Calibration..... | 51 |
| 3.3.1 Experiment description and method..... | 52 |
| 3.3.2 Results..... | 53 |
| 3.4 Summary..... | 55 |
| 4 Radiative Land Surface Temperature Retrieval at Infrared Wavelengths: Methodology..... | 57 |
| 4.1 Introduction..... | 57 |
| 4.2 Data Sources..... | 59 |
| 4.2.1 The Along Track Scanning Radiometer Dataset..... | 60 |
| 4.2.2 Terrestrial Infrared Radiometer Dataset..... | 63 |
| 4.2.3 Atmospheric Radiosoundings..... | 64 |
| 4.3 Experimental Method..... | 66 |
| 4.3.1 Chizengeni..... | 69 |
| 4.3.2 Tambuti..... | 75 |
| 4.3.3 Experiment Procedure..... | 79 |
| 4.4 Emissivity Prescription..... | 84 |
| 4.5 Satellite Data Processing..... | 87 |

| | | |
|-------|--|-----|
| 4.6 | Land Surface Temperature Retrieval | 90 |
| 5 | Results | 91 |
| 5.1 | Error analysis | 91 |
| 5.1.1 | Errors in the satellite data | 92 |
| 5.1.2 | Errors in the terrestrial data..... | 92 |
| 5.1.3 | Errors in the surface emissivity prescription..... | 93 |
| 5.1.4 | Errors in the atmospheric correction..... | 93 |
| 5.1.5 | Errors in the radiative transfer calculations..... | 94 |
| 5.2 | Infrared atmospheric correction parameters derived for Zimbabwe | 95 |
| 5.2.1 | The relationship between multi-spectral and monochromatic atmospheric transmittance..... | 95 |
| 5.2.2 | Diurnal variability of the atmosphere | 100 |
| 5.2.3 | Broadband infrared atmospheric correction parameters | 104 |
| 5.2.4 | A comparison between numerical and empirical atmospheric correction techniques..... | 108 |
| 5.2.5 | Summary..... | 109 |
| 5.3 | Land Surface Temperatures derived from terrestrial Infrared radiometric data..... | 110 |
| 5.3.1 | Surface Temperature Heterogeneity | 110 |
| 5.3.2 | Surface component Radiative Temperatures..... | 111 |
| 5.3.3 | Angular Variation of Radiative Temperature..... | 113 |
| 5.3.4 | Component Temperature Separation within a Mixed Canopy | 118 |
| 5.3.5 | Summary..... | 125 |
| 5.4 | Land Surface Temperatures derived from the ATSR..... | 126 |
| 5.4.1 | Temperature Heterogeneity..... | 126 |
| 5.4.2 | LST estimation..... | 131 |
| 5.4.3 | Angular Variation in LST | 139 |
| 5.4.4 | Mixed Surface LST separation | 143 |
| 5.4.5 | Summary..... | 153 |
| 5.5 | A comparison between Satellite and terrestrial radiative temperatures | 158 |
| 6 | Conclusions and suggestions for future work | 167 |
| 6.1 | Main Conclusions | 167 |
| 6.2 | Future work..... | 176 |
| 6.2.1 | (i) Fieldwork | 176 |
| 6.2.2 | (ii) Satellite data..... | 177 |
| 6.2.3 | (iii) Canopy Modeling..... | 178 |
| | Appendix A : Atmospheric heating model | 179 |
| | References | 185 |

Acknowledgements

I would like to thank my supervisors, David Llewellyn-Jones, Chris Mutlow and John Stewart for their help and guidance throughout this work. The assistance of John and Mlindelwa Lupankwa during our field campaigns was invaluable, and our experiences in Zimbabwe will remain amongst my happiest memories. I would also like to thank the staff and friends at the University of Leicester, the Institute of Hydrology and Rutherford Appleton Laboratory who have helped me complete this work. In particular I am grateful to Dave Adams, Vince Brookbank, Ray Mclearn and Alan Wright for their time and effort during the instrument calibrations and the construction of experimental apparatus. Finally, I would especially like to thank Claire, my parents and my rapidly increasing family for their constant support throughout my studies, which no doubt will continue.

Chapter 1

Introduction

1.1 Background to study

1.1.1 The role of land surface temperature within the environment

The sun provides virtually all of the energy received by the earth. Incoming solar radiation drives biophysical and geophysical processes such as photosynthesis, evaporation and heat exchanges between the earth's surface and the atmosphere. The surface temperature plays a pivotal role in each of these major energy transfers, and is a sensitive indicator to the state of the energy balance. Accurate measurements of surface temperatures are desirable for a wide range of environmental studies. Land surface temperatures (LST's) are of fundamental importance to the net radiation at the earth's surface and can be used as initialisation data in meteorological models. The LST is important for monitoring the state of crops and vegetation at a variety of spatial resolutions, from field scale studies to micrometeorological investigations of individual plant physiology.

The required accuracy for LST's depends upon the particular application. In field scale energy balance studies it has been found that the LST has to be estimated to a precision of around $\pm 2^{\circ}\text{C}$ for successful partition of the energy budget (Koshiek *et al.*, 1992). For mesoscale climate modeling, an accuracy of $\pm 1.5^{\circ}\text{C}$ is sufficient to estimate the longwave radiation flux to within 2% (Prata, 1993). For most applications, significant improvements in LST accuracies are desirable.

The LST can be estimated using a variety of techniques, from contact thermometry to remotely sensed infrared radiometry. Consequently a range of physical definitions are widely used to describe the LST. The thermodynamic temperature as measured by a contact thermometer is a macroscopic quantity shared by objects in thermodynamic equilibrium. An

individual measurement of the thermodynamic temperature is typically representative of only a small area. The temperature measured by a radiometer is dependent upon the electromagnetic emission from the surface. Radiometric temperatures are derived from a mixture of the emission from all of the objects that appear within the radiometer field of view. The radiometric and thermodynamic temperatures are equal if the object is a perfect emitter. The aerodynamic temperature of a surface is derived from the magnitude of the heat flux between the surface and the atmosphere. Aerodynamic temperatures are artificial quantities dependent upon the resistance to heat transfer of the near surface atmosphere. The relationship between aerodynamic temperatures, used in flux calculations, and the radiometric or thermodynamic temperatures, which can be measured *in situ*, is not obvious and is typically determined empirically.

The solar radiation is dissipated at the surface principally through heat transfer and evaporation into the atmosphere. Conductive, convective and radiative heat exchange between the surface and the atmosphere are conventionally defined as sensible heat. The sensible heat flux has been related to the temperature potential across the interface between the surface and the atmosphere. Transfer coefficients have been derived over a variety of natural and artificial surfaces (e.g. Stewart *et al.*, 1994). Simultaneous measurements of the LST and the air temperature can be used to investigate the nature of the energy partition at the surface. Estimations of surface fluxes using resistive parameterisations yield typically 25% errors under conditions of strong sunlight (high surface to air temperature differentials). This level of accuracy can be sufficient to successfully delimit periods of intense evaporation. The LST is an influential factor in both the surface energy and hydrological balance, so that its impact upon the environment is wide reaching.

1.1.2 Land surface temperature in Zimbabwe

Zimbabwe in southern Africa lies within the tropics, from 15.5 to 22.5° South and from 23.5 to 33° East. The country is divided topographically into high and low watershed regions. The altitude of the high land, or Highveld, is generally between 1200m and 1500m, whereas the lower lying areas, known as the Lowveld, are typically below 500m in elevation. A significant distinction exists between the climatology of these regions. Mean annual rainfall in the Highveld approaches 900 mm in the wettest areas. Rainfall levels in the Lowveld are

generally below 400 mm per year. The hydrological regimes of the two regions differ quite dramatically, and extensive waterways have been constructed to provide irrigation to commercial plantations in the Lowveld. The country as a whole receives dramatically variable rainfall. Interannual variability in precipitation levels can be greater than 300%, and severe periods of drought are not uncommon. Potential evaporation rates across the country typically exceed rainfall levels by a factor of two, so that water conservation is a principal concern.

Much of the non-commercial land in Zimbabwe is farmed rurally as smallholdings. The Highveld region is characterised by its inland valleys, or dambos. These areas are prevalent throughout southern Africa, and the dambos serve as potential reservoirs for episodic rainfall. Dambo hydrology has been studied keenly in the recent past (see Bell *et al.*, 1987, Owen *et al.* 1994), and surface evaporation rates are known to be a major factor in the hydrological balance. The natural vegetation of Zimbabwe is characteristically open forest. Much of this woodland has experienced deforestation, or significant degradation, so that the arable dambos in the Highveld are presently dominated by grassland savannah. In the arid Lowveld a substantial proportion of natural woodland is still maintained, largely as privately managed estates or wildlife reserves. The principal vegetation cover in the Highveld and Lowveld regions differs significantly.

Temperatures in the Highveld are considerably lower than in the Lowveld. The mean annual air temperature at Chiota in the Highveld is approximately 18°C. At Tambuti in the Lowveld, air temperatures average over 22°C per annum and regularly exceed 40°C in the hottest months of the year. The land surface temperature in Zimbabwe is potentially the most significant geophysical parameter because of its role in the surface energy balance. Evaporation rates are principally driven by the LST, and this impacts severely upon the hydrological balance. In turn groundwater depletion restricts vegetation growth, and the onset of seasonal periods of senescence is accelerated. Monitoring the LST in such semi-arid environments offers a valuable insight into these particularly sensitive climate systems.

1.2 Remote sensing and land surface temperatures

Land surfaces are typically composed of a heterogeneous mixture of distinct elements, such as soil, rocks, vegetation and bare trees. Accurately estimating the temperature of the land is complicated by the spatial variability that exists at different scales. For regional climate studies it is necessary to determine the LST over large areas, whereas canopy modeling requires highly localised measurements.

The only practical, consistent and scale independent method of accurately estimating the LST is to record the infrared surface emission, which is related to the thermodynamic temperature through Planck's radiation law. Infrared emission can be remotely sensed at significantly different resolutions using radiometers mounted on satellite, aircraft and terrestrial platforms. Radiometric temperatures have to be adjusted for the effects of the intervening atmosphere and the emissivity of the surface. Atmospheric corrections can be performed using empirical formulae or retrieval algorithms with coefficients derived from radiative transfer solutions (e.g. Idso, 1981; Zavody *et al.*, 1995). Infrared emissivities have been independently determined for many natural surfaces, and consistent estimates for vegetation and soils are present within the literature. The angular variation of surface emissivity has also been investigated for bare soils (Nerry *et al.*, 1988; Labed & Stoll, 1990), and it was found that even in the most irregular samples off-nadir differences are less than 1% at zenith angles below 60°. The ATSR sensor views the Earth's surface at below 56° at all times.

Satellite estimates of the LST are particularly useful as they are periodically recorded over the same surface area. In addition the earth footprints of spaceborne radiometers are generally much larger than can be achieved using terrestrial instruments. The major drawback of satellite retrieved LST's is that they are often recorded at the same time at every repeat pass. One-time-of-day measurements are often insufficient to accurately estimate daily totals or diurnal trends in geophysical parameters. The diurnal progression of the surface energy budget is a complex process involving interactions between the atmosphere, canopy and the soil. The ratio between latent heat and evaporation, the evaporative fraction, has been observed to be moderately conserved throughout most of the day (Crago, 1996). However, estimates of daytime evaporation rates over savannah from instantaneous values were fre-

quently inaccurate, and for individual days 80% of predictions were between 80 and 140% of the measured values (Stewart *et al.*, 1996).

Satellite derived LST's generally have much larger errors than *in situ* measurements, which principally arise from inaccurate surface emissivity prescriptions and atmospheric corrections. A 1% change in surface emissivity can in certain instances result in up to a 2°C change in radiometric temperature. However, the errors associated with satellite LST estimates are comparable in magnitude to the spatial variability in temperature observed over many natural surfaces.

Interpretation of the radiative emission from the earth's surface can be very difficult if the land cover is not uniform. The infrared emission recorded over a heterogeneous surface is a mixture of the radiation from each object within the field of view of the radiometer. The exact nature of thermodynamic interactions within natural surfaces are often poorly defined, and the combined radiation from a sparse canopy, with vegetation and soil components, is frequently aggregated using linear mixture models (e.g. Settle and Drake, 1995). However, due to the nonlinearities in the relationships between temperature and radiance, a simple average of temperature components is inappropriate. Reasonable consideration of each individual component's emission has to be made.

In general linear mixture models are not invertible, so that the distinct temperatures that exist within a sparse canopy cannot readily be determined from a single areally extensive radiometric measurement. However, when viewing natural surfaces the relative proportions of distinct elements varies with observation angle. The angular variation in fractional cover can be well prescribed using standard canopy architecture models. If temperature differentials exist between the vegetation and soil then the ensemble radiometric surface temperature will also exhibit angular variability. The temperature of individual surface elements can then be determined by recording the emission at multiple observation angles. For a simple two component surface, the component temperatures can be determined if the radiative temperature is recorded at two different view angles.

Satellite retrieved LST's are frequently recorded over mixed surfaces because of their large earth footprints. The Along Track Scanning Radiometer (ATSR) is flown on the European Remote Sensing satellites (ERS-1 and ERS-2). The ATSR is an imaging infrared radiome-

ter and records the earth's radiative emission across several discrete spectral bands. The instrument footprint size is approximately 1 km² and the ERS satellites operate predominantly in a 35 day repeat cycle. Extensive details of the ATSR instrument are described for example by Edwards *et al.* (1990). In particular, the ATSR has the unique ability to view the earth's surface through two independent optical paths. The dual-angle viewing geometry of the ATSR has enabled significant reductions in satellite derived Sea Surface Temperature (SST) errors (e.g. Mutlow *et al.* 1994). The ATSR offers the potential to improve LST estimates in a similar manner. Additionally, the dual-angle viewing geometry can detect angular variations in LST. Using existing radiative transfer models the difference between nadir and oblique radiative temperatures can be investigated over a variety of earth surfaces. Observed angular variations in LST can be related to the surface canopy architecture, with the potential to resolve sub-pixel heterogeneity.

1.3 Questions addressed by this work

The overall aim of this thesis is to investigate the spatial and temporal variation in land surface temperature over a sparsely vegetated region. The radiative transfer calculations required for accurate estimates of the atmospheric effects follow the work of Zavody *et al.* (1995) for satellite measurements and Idso (1981) for terrestrial measurements. Land surface temperatures are determined explicitly by direct solution of the radiative transfer equation, and these are compared to similar estimates derived using the dual-angle algorithm of Prata (1993). Prata's semi-empirical equation was developed for use over a uniform surface with no angular dependence to the emission. The surfaces studied in this work are florally distinct with inhomogeneous three dimensional vegetation canopies. The field sites deviate substantially from the uniform surfaces previously studied, and a model is developed to describe the ensemble emission from the complex surfaces. After correction for atmospheric effects, component temperatures are aggregated linearly following the work of Settle and Drake (1995), and the angular variation in fractional cover is estimated using a canopy architecture described by Normal *et al.* (1995). Using empirically relationships between the canopy and understory temperatures and air temperature as a surrogate for vegetation temperature, estimates of the component temperatures and fractional cover are made from dual-

angle ATSR satellite radiative temperatures. Empirical LST retrieval algorithms are then derived from the satellite data based upon these results.

The work will address in particular the following specific questions:

i) How is the land surface temperature related to the infrared emission from the Earth's surface ?

ii) How does the land surface temperature vary spatially and temporally over surfaces with different canopy architectures ?

iii) Is there evidence of angular variations in land surface temperature estimates ?

iv) Can dual angle satellite data be used to investigate the canopy architecture ?

v) What does this work tell us about the reliability of land surface temperatures derived from satellite data, and is the technique applicable on a global scale ?

1.4 Thesis structure

The following two chapters will outline the principals upon which the remote sensing of land surface temperatures are based. Chapter 2 details the theory of LST retrieval and discusses two methods of correcting the data for atmospheric effects. Chapter 3 describes the rigorous laboratory calibration of a series of terrestrial infrared radiometers which were used in the study to record *in situ* radiative temperatures. The LST retrieval methods, including a full description of the independent data sources, the field experiments and the satellite image processing are detailed in Chapter 4. The final results are presented in Chapter 5, including a complete analysis of the errors associated with the LST retrieval, quantifying both known and potential uncertainties. The results are discussed in detail and conclusions are drawn in Chapter 6, with reference to the surface canopy structure and temperature regime

at two study areas in Zimbabwe. Recommendations for future work are also made in Chapter 6.

Chapter 2

Radiative Land Surface Temperature Retrieval at Infrared Wavelengths: Theory

2.1 Introduction

The absolute value of land surface temperature (LST) measurements is intrinsically related to the detection system employed. Infrared emission, which can be remotely sensed at a distance from the surface, can be used to estimate the LST if the effects of the intervening atmosphere are reasonably considered. This chapter describes the concept of remotely sensed LST's and their retrieval within the framework of radiative transfer theory.

Empirical and numerical methods for determining the atmospheric correction at different infrared wavelength regions are discussed in detail. The two separate approaches were required to determine the correction for terrestrial and satellite measurements, as neither method was suitable for both. Using numerical techniques, LST's can be accurately estimated using a direct solution of the radiative transfer equation given estimates of the atmospheric correction and the surface emissivity. However, here the spectral domain of the radiative transfer model used was not sufficient to cover the region sensed by terrestrial radiometers, and so the empirical equations were also required.

Familiar techniques for simplifying the derivation of LST's using both multi-channel and multi-angle radiometric data are also outlined. The dual-angle algorithm presented (after Prata, 1993, hereafter the Prata dual-angle algorithm) is semi-empirical in nature and requires estimates of the atmospheric transmittance to determine the LST. The utility of the Prata dual-angle algorithm over a mixed component surface can be readily compared to the full radiative transfer solution.

Empirical LST retrieval coefficients can be determined using a representative dataset of dual-angle satellite brightness temperatures and coincident *in-situ* atmospheric data for LST's derived from either the complete solution of the radiative transfer equation (which requires fine spectral resolution) or the Prata dual-angle algorithm (which requires only atmospheric transmittance in each instrument channel). These coefficients, if sufficiently accurate, can be used powerfully in the absence of atmospheric data to determine the LST from dual-angle satellite radiometric temperatures.

The problems of LST estimation over heterogeneous surfaces are also considered, and a dual-angle method for resolving the distinct temperatures of a simple two component surface is presented.

2.2 Land Surface Temperature Measurement

The ability to record the LST at a variety of spatial scales is essential in climate studies. This can only be achieved consistently by monitoring the radiative surface temperature from remote platforms. Satellite retrieved LST's offer the advantage of large spatial coverage. When considering the impact of the LST on regional climate, through the surface exchanges of heat and water, coarse resolution data is required.

Radiative temperatures are a measure of the energy emitted by the surface. The radiance recorded by a distant radiometer is affected by the intervening atmosphere, the emissive properties of the surface, and the characteristics of the instrument sensor. At infrared wavelengths, the transmission of radiation through the atmosphere is relatively high. As a consequence, terrestrial and satellite radiometers measure the surface radiance within this atmospheric window to estimate the LST.

The demand for satellite retrieved LST's has led to the development of instrument specific algorithms, which couple radiance information from multiple instrument channels. The radiance measured through different spectral filters is contrasted in so-called split-window algorithms. A recent extension to this technique has been the development of dual-angle algorithms, which compare the radiance measured through different viewing geometries. Using tabulated atmospheric profiles, coefficients have been derived for radiative surface temperature algorithms which remove the requirement for *in situ* atmospheric data.

Typical sea surface temperature algorithms perform with very high accuracy, achieving errors of less than $\pm 0.5^\circ\text{C}$ (Barton *et al.*, 1993; Sobrino *et al.*, 1996). LST algorithms are far less precise, because of both heterogeneity in the surface cover and major uncertainties in the emissive properties of the surface. These factors when combined limit LST algorithms to accuracies of around ± 2 to 3°C over well defined surface cover when compared to *in situ* data (Vidal, 1991; Prata, 1994). The errors reflect the LST accuracy to be expected over a well defined field site, and uncertainties increase dramatically over unfamiliar terrain.

In principle, the errors in LST algorithms can be divided between atmospheric and surface emissivity effects. A rough guide to the relative contributions of these error sources can be gained by contrasting SST and LST accuracy. When the surface emissivity is high and well prescribed, as is the case for the sea, the algorithms perform well. Over land, each percentage error in the surface emissivity contributes around 1°C of inaccuracy in the LST estimate.

The radiative transfer theory of infrared emission from the earth's surface through the atmosphere is discussed. The techniques are applicable to both terrestrial and satellite radiometry. A selection of differential radiometric LST algorithms are also presented, which may be used to investigate the utility of such an approach. The problems of aggregating and interrogating the emission from a mixed surface with heterogeneities at sub-pixel scale are also addressed.

2.3 Radiative Transfer Theory for Land Surface Temperature Retrieval

The total upwelling radiation recorded by a radiometer viewing the earth's surface is a combination of emission from the surface, the atmosphere and the sun. At thermal infrared wavelengths (approximately 8-14 μm) reflected and scattered solar radiation is negligible relative to emission from the surface and atmosphere. Direct and reflected radiation from the earth's surface is modified in its passage through the atmosphere via absorption, scattering and emission caused by the atmospheric constituents.

The principal components of emission received by a radiometer situated above the earth's surface are the radiation emitted by the surface $I_{surf}(\nu, \theta)$ the upwelling radiation emitted by the intervening atmosphere $I_{atm}(\nu, \theta)$ and the downwelling radiation emitted by the whole

atmosphere and reflected from the surface $I_{ratm}(\nu, \theta)$. Under these assumptions, the total directional upwelling radiance $I(\nu, \theta)$ measured at an angle θ to the surface and at a frequency ν , can be written as

$$I(\nu, \theta) = I_{surf}(\nu, \theta) + I_{atm}(\nu, \theta) + I_{ratm}(\nu, \theta) \quad (2.1)$$

The directional surface radiance component $I_{surf}(\nu, \theta)$ can be expressed in terms of the surface emissivity $\epsilon(\nu, \theta)$ the transmittance of the atmosphere $\tau(\nu, \theta, z1, z2)$ where $z1$ and $z2$ are the heights of the base and top of the atmosphere, and the radiative surface temperature T_s , so that

$$I_{surf}(\nu, \theta) = \epsilon(\nu, \theta) \tau(\nu, \theta, 0, Z) B(\nu, T_s) \quad (2.2)$$

where $B(\nu, T_s)$ is the Planck function evaluated at a temperature T_s and frequency ν , and Z is the height of the radiometer above the surface. The surface temperature T_s is the aggregate radiative surface temperature recorded across the instruments instantaneous field of view.

The Planck function is given by

$$B(\nu, T) = \frac{(2h\nu^3)}{c^2 (e^{h\nu/kT} - 1)} \quad (2.3)$$

where k is Boltzmann's constant, c is the speed of light and h is Planck's constant.

In an isotropic atmosphere, the downwelling and upwelling radiance can be expressed as the integral of the radiation emitted from stratified layers, so that

$$I_{atm}(\nu, \theta) = \int_0^Z B(\nu, T(z)) \left(\frac{\delta\tau(\nu, \theta, z, Z)}{\delta z} \right) dz \quad (2.4)$$

and

$$I_{ratm}(\nu, \theta) = \rho(\nu, \theta) \tau(\nu, \theta, 0, Z) \int_0^\infty B(\nu, T(z)) \left(\frac{\delta\tau(\nu, \theta, 0, z)}{\delta z} \right) dz \quad (2.5)$$

where $\rho(\nu, \theta)$ is the surface reflectivity, $T(z)$ is the atmospheric temperature profile, and Z is the path length from the surface to the radiometer at a view zenith angle of θ . The former of these two integrals may be expanded over its finite range using the mean value theorem, so that

$$I_{atm}(\nu, \theta) = B(\nu, T_a) (1 - \tau(\nu, \theta, 0, Z)) \quad (2.6)$$

where T_a is the mean value of the atmospheric temperature. A similar partition of the multiple integral is not possible for the reflected atmospheric radiance since contributions to I_{ratm} are received from infinite distances.

In general it is difficult to establish a relationship between the surface reflectivity and emissivity. If the atmosphere and surface are in thermodynamic equilibrium, then Kirchoff's law implies that the reflectivity and emissivity are related through the conservation of the sky radiance at the interface. By assuming that there is no azimuthal variation in either emissivity or reflectivity, i.e. the surface behaves as a mirror-like reflector, then

$$\varepsilon(\nu, \theta) + \rho(\nu, \theta) = 1$$

(2.7)

Under these assumptions, the combined surface and atmospheric emission at a frequency ν and zenith angle θ can be expressed as

$$I(\nu, \theta) = \varepsilon(\nu, \theta)\tau(\nu, \theta)B(\nu, T_s) + I_{up}(\nu, \theta) + \rho(\nu, \theta)\tau(\nu, \theta)I_{down}(\nu, \theta)$$

(2.8)

where $\tau(\nu, \theta) = \tau(\nu, \theta, 0, Z)$ and $I_{up}(\nu, \theta)$ and $I_{down}(\nu, \theta)$ are respectively the upwelling and downwelling radiance of the atmosphere, given as

$$I_{up}(\nu, \theta) = B(\nu, T_a)(1 - \tau(\nu, \theta))$$

$$I_{down}(\nu, \theta) = \int_0^\infty B(\nu, T(z)) \left(\frac{\delta\tau(\nu, \theta, 0, z)}{\delta z} \right) dz$$

(2.9)

When measuring radiances with real instruments, the radiation filter will affect the colour and intensity of the incoming signal. It is useful to introduce the monochromatic quantity I_i which represents the mean spectral radiance integrated over an instrument bandpass filter. If $\Phi_i(\nu)$ is the filter response of a particular instrument channel i , then the total spectral radiance received is given by

$$I_i(\theta) = \frac{\int_{\nu_1}^{\nu_2} I(\nu, \theta) \Phi_i(\nu) d\nu}{\int_{\nu_1}^{\nu_2} \Phi_i(\nu) d\nu}$$

(2.10)

In the subsequent derivations, it is assumed that multi-spectral radiative transfer components can be represented in a similar manner when channel integrated values are required. In general this is a good approximation over a modest temperature range (0-50°C) when dealing with infrared radiation (see Prata, 1993; this work, Chapter 6). Using this representation, the total radiance recorded by an instrument channel i is then

$$I_i(\theta) = \varepsilon_i(\theta)\tau_i(\theta)B_i(T_s) + I_{iup}(\theta) + \rho_i(\theta)\tau_i(\theta)I_{idown}(\theta) \quad (2.11)$$

where

$$B_i(T) = \frac{\int_{\nu_{i1}}^{\nu_{i2}} \varepsilon(\nu)B(\nu, T)\Phi_i(\nu)d\nu}{\int_{\nu_{i1}}^{\nu_{i2}} \Phi_i(\nu)d\nu} \quad (2.12)$$

is an approximate solution to the Planck function evaluated across the spectral domain specified by $\Phi_i(\nu)$, which provides a relationship between the surface emission and radiative temperature T in channel i .

2.4 Correcting infrared radiation for atmospheric effects

Radiation emitted from the earth's surface is affected by the presence of the atmosphere. When detecting infrared emission from above the surface the atmospheric effects have to be considered. In this study, radiometric surface temperatures derived from both satellite and terrestrial measurements were used. The radiances were recorded in separate wavelength regions, and it was necessary to use different techniques for generating estimates of the atmospheric emittance and transmittance. A numerical radiative transfer model was used correct ATSR derived brightness temperatures for atmospheric effects. The empirical

equations of Idso (1981) were used to correct *in situ* radiometric temperatures for atmospheric effects.

The earth's atmosphere is composed of a variety of radiatively active substances, ranging from simple gases to complex aerosols and dust particles. Radiatively active substances are capable of affecting radiation emitted from the earth's surface through the processes of absorption, emission or scattering. Absorption by the atmosphere attenuates radiation emitted from the surface, and atmospheric emission contributes to the total radiation measured. Scattering processes within the atmosphere are either net attenuators or contributors to upwelling radiation from the earth's surface. Figure 2-1 indicates the relative abundances of the major trace species according to their specific volume mixing ratios throughout the atmosphere. Each of these species are radiatively active within particular regions of the electromagnetic spectrum.

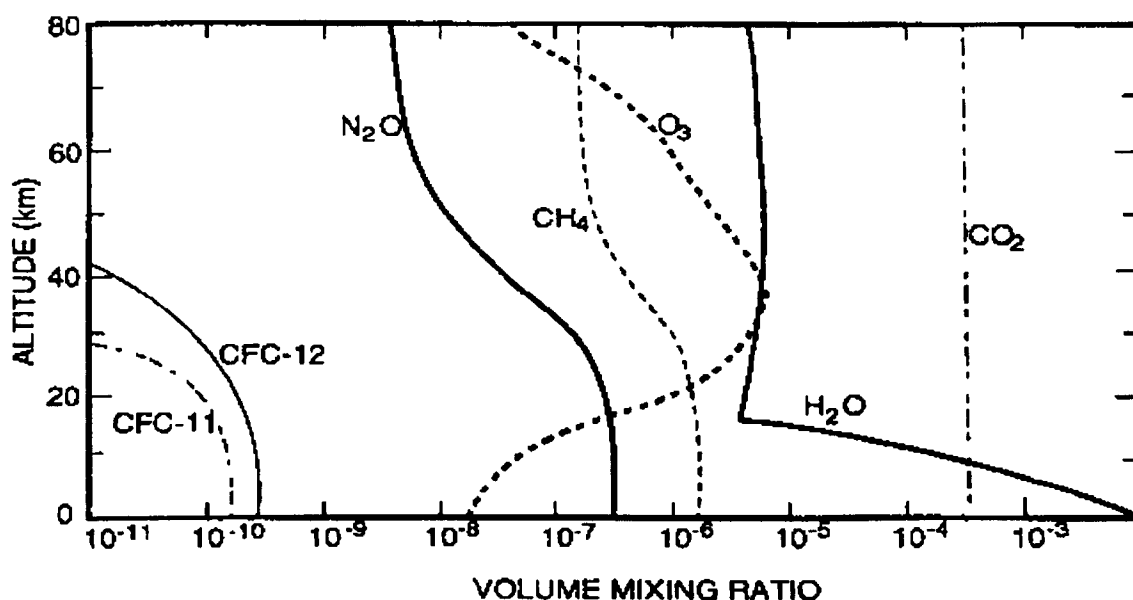


Figure 2-1 Mixing ratios of radiatively active trace species in the atmosphere. (after Goody and Yung, 1989).

At infrared wavelengths, the most important absorber is water vapour (H_2O), followed by carbon dioxide (CO_2) and ozone (O_3), with minor contributions from methane (CH_4), nitrous oxide (N_2O), ammonia (NH_3) and other trace gases. Whilst CO_2 is a major atmospheric constituent, its absorptive properties are relatively weak and its effect upon surface

emission is practically constant because of the constant mixing ratio. The absorption bands of O₃ (9.6 μm), H₂O (6.3 μm) and CO₂ (4.3 and 15 μm) are impressive upon theoretical atmospheric transmission spectra (Figure 2-2), and standard atmospheric windows of high transmission can be readily identified (typically 3.4-4 μm, 8-9.5 μm and 10.5-13 μm).

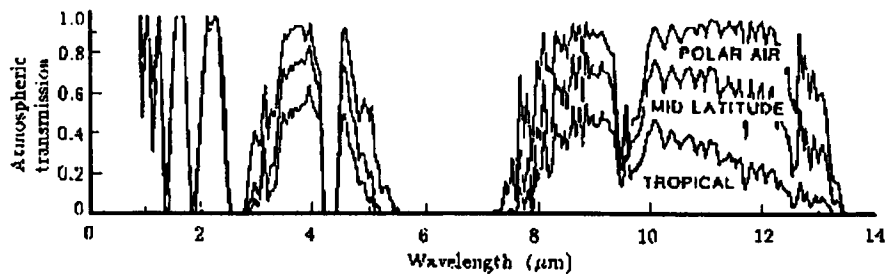


Figure 2-2 Theoretical spectra of atmospheric transmission in the nadir view for three standard atmospheres. The total precipitable water amounts were 7 mm for polar, 29 mm for mid-latitude and 54 mm for tropical. (after Zavody *et al.*, 1995)

Standard thermal infrared channels, or regions of the electromagnetic spectrum within which radiation is measured, lie inside these atmospheric windows where absorption is low. However, the absorption, even in these windows, is not negligible, and where it exists it is largely due to water vapour. Water vapour is the principal absorber and emitter within the atmosphere and is also the most variable constituent within the troposphere (see Figure 2-1), where the majority of absorption occurs. To illustrate the overwhelming effects of H₂O upon atmospheric attenuation, Guillory *et al.* (1993) computed spectral transmittance for a standard atmosphere initially accounting for, and then in the absence of, water vapour (Figure 2-3). H₂O is responsible for the majority of absorption at these wavelengths and an accurate description of the water vapour profile should lead to a good estimate of the atmospheric correction at any given time.

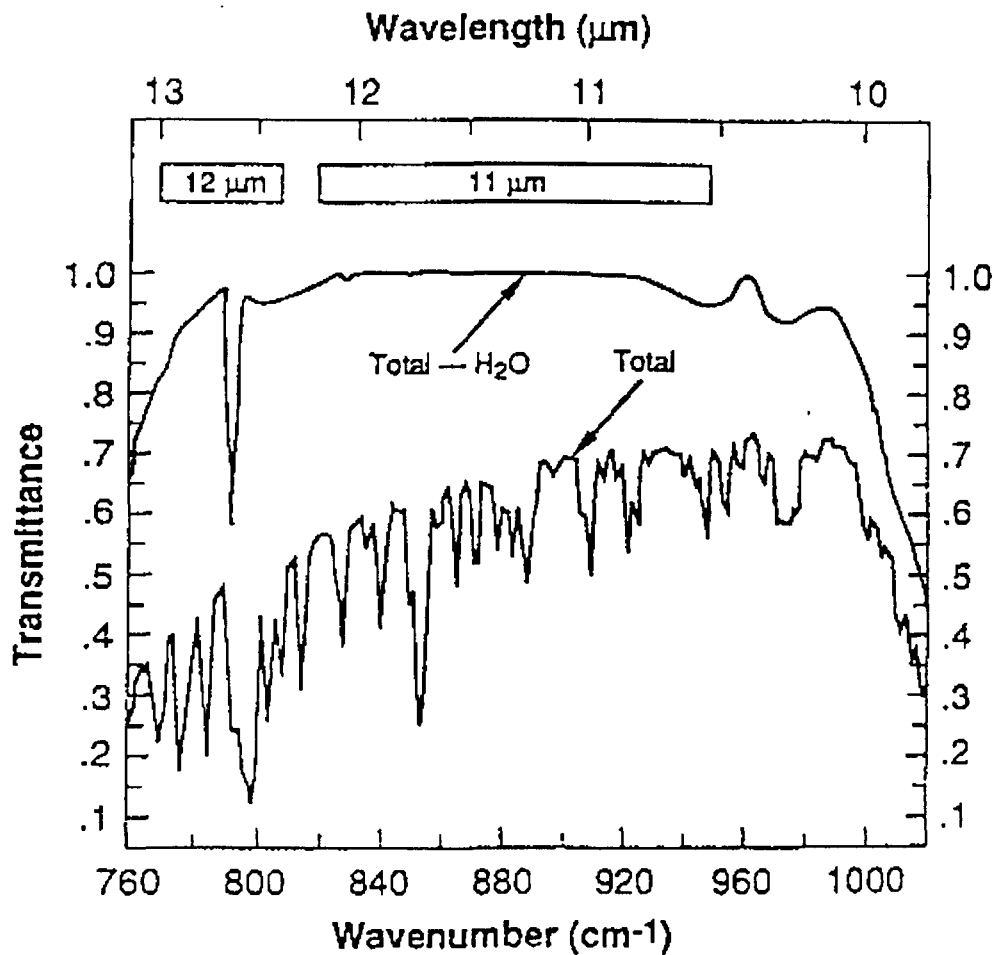


Figure 2-3 Spectral transmittance in the 10-13 μm region with and without H_2O (after Guillory *et al.*, 1993)

2.4.1 Quantifying the effects of attenuation and emission within the atmosphere

The thermal radiance of a uniform flat surface, characterised by a directional emissivity and reflectivity, measured through the earth's atmosphere can be written using the radiative transfer equation (Equation 2.8). The three terms of the radiative transfer equation represent the surface, atmospheric and reflected atmospheric radiances respectively.

The equivalent blackbody temperature, or brightness temperature T_b that would emit the same radiance $I_i(\theta)$ through the instrument filter $\Phi_i(\nu)$ can be determined by evaluating the integral

$$I_i(\theta) = \frac{\int_{\nu_{i1}}^{\nu_{i2}} B(\nu, T_b) \Phi_i(\nu) d\nu}{\int_{\nu_{i1}}^{\nu_{i2}} \Phi_i(\nu) d\nu} \quad (2.13)$$

Brightness temperatures do not consider the effects of the intervening atmosphere and are inaccurate estimates of the true surface radiative temperature. The difference between T_b and T_s is an indication of the magnitude of the required atmospheric correction. Deschamps and Phulpin (1980) generated estimates of T_s from satellite brightness temperatures using several standard atmospheric profiles (Figure 2-4).

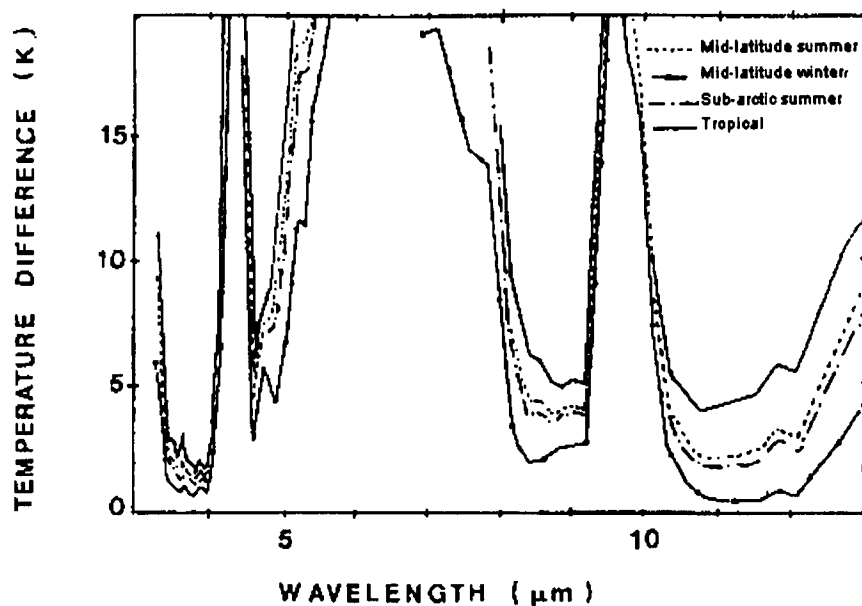


Figure 2-4 Spectral variations of the atmospheric correction as computed for several model atmospheres (after Deschamps and Phulpin, 1980).

The corrections, calculated for a perfectly emitting surface, were observed to vary strongly across the thermal infrared region. The emissivity of natural surfaces is typically less than unity and the power emitted is correspondingly less than from a blackbody. Increased reflection of atmospheric radiation partially compensates for this loss. The smallest corrections occur in the atmospheric windows, with typically low values for arctic atmospheres and high values of up to 10°C in tropical regions.

To accurately estimate the temperature of the earth's surface from remotely sensed radiances, the data has to be corrected for atmospheric effects. The solution of the radiative transfer equation relies upon determining the atmospheric transmittance and the upwelling and downwelling emittance, $\tau_i(\theta)$, $I_{iup}(\theta)$ and $I_{idown}(\theta)$. Using detailed atmospheric profiles, such as the data collected by radiosoundings released from meteorological stations, it is possible to estimate values for these quantities with the aid of numerical radiative transfer models. Empirical expressions for $\tau_i(\theta)$, $I_{iup}(\theta)$ and $I_{idown}(\theta)$ can also be generated from large atmospheric datasets.

Knowledge of the surface emissivity and reflectivity, $\epsilon_i(\theta)$ and $\rho_i(\theta)$, and the filter response function of the radiometer, $\Phi_i(\nu)$ are also essential. For a given atmospheric state, the upwelling and downwelling radiation integrated across an instrument channel i can be expressed as

$$I_{iup}(\theta) = \frac{\int_{\nu_{i1}}^{\nu_{i2}} I_{up}(\nu, \theta) \Phi_i(\nu) d\nu}{\int_{\nu_{i1}}^{\nu_{i2}} \Phi_i(\nu) d\nu}$$

$$I_{idown}(\theta) = \frac{\int_{\nu_{i1}}^{\nu_{i2}} I_{down}(\nu, \theta) \Phi_i(\nu) d\nu}{\int_{\nu_{i1}}^{\nu_{i2}} \Phi_i(\nu) d\nu}$$
(2.14)

and the downwelling atmospheric radiance transmitted back through the atmosphere to the satellite is

$$\tau_{i_{down}}(\theta) = \frac{\int \tau(\nu, \theta) I_{down}(\nu, \theta) \Phi_i(\nu) d\nu}{\int_{\nu_{i1}-\nu_{i2}} \Phi_i(\nu) d\nu} \quad (2.15)$$

In the thermal-infrared region of the electromagnetic spectrum the atmospheric attenuation can generally be considered to have a weak, roughly linear spectral dependence. Under such an approximation, the bulk atmospheric attenuation in channel i , $\tau_i(\theta)$, can be substituted for the spectral attenuation. In principle $\tau_i(\theta)$ will be a function of temperature, but in practice at thermal-infrared wavelengths this is slowly varying between -20 and 80°C , typically less than 1%. The bulk atmospheric attenuation $\tau_i(\theta)$ is defined as

$$\tau_i(\theta) = \frac{\int_{\nu_{i1}}^{\nu_{i2}} \varepsilon(\nu, \theta) B(\nu, T) \tau(\nu, \theta) \Phi_i(\nu) d\nu}{\int_{\nu_{i1}}^{\nu_{i2}} \varepsilon(\nu, \theta) B(\nu, T) \Phi_i(\nu) d\nu} \quad (2.16)$$

Note that $\tau_i(\theta)$ is weighted by the surface radiance, and is not equal to the expectation value of the attenuation, $\langle \tau_i(\theta) \rangle$. Under these assumptions,

$$\tau_i(\theta) I_{i_{down}}(\theta) \approx \tau_{i_{down}}(\theta) \quad (2.17)$$

The magnitude of the atmospheric effect is dependent upon the depth of atmosphere through which the measurement is taken. For terrestrial radiometry, the effects of atmospheric attenuation upon the signal are negligible, as is the contribution due to upwelling radiation from the intervening atmosphere. In this instance, the total power received by the radiometer in channel i can be approximated to

$$I_i(\theta) = \varepsilon_i(\theta) B_i(T_s) + \rho_i(\theta) I_{i_{down}}(\theta)$$

The Along Track Scanning Radiometer (ATSR) satellite instrument has two thermal-infrared radiometric channels, centred at approximately 11 μm and 12 μm (Figure 2-5).

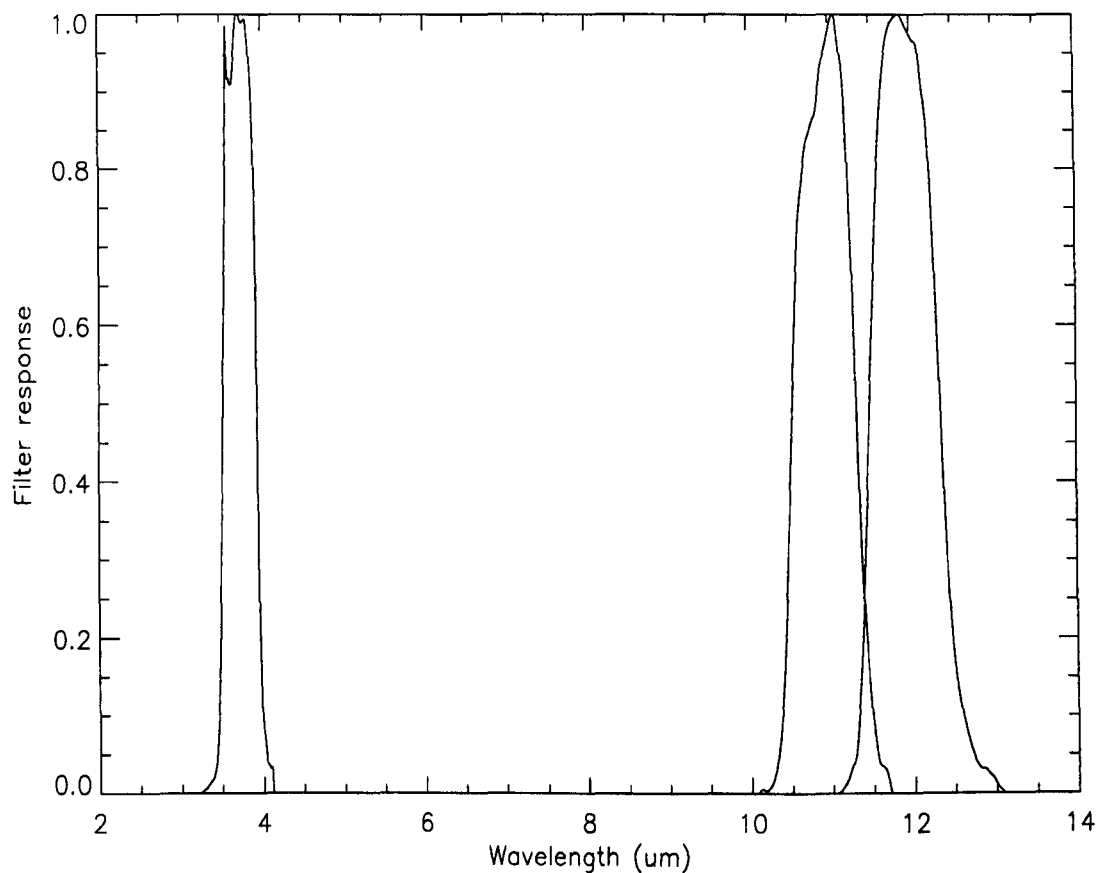


Figure 2-5 Filter response function for the ATSR thermal-infrared channels.

Everest Interscience terrestrial infrared radiometers have a broadband filter with nominally 100 % transmission in the 8-14 μm wavelength region (Everest Interscience, personal communication). The bulk atmospheric parameters that are required to correct radiometric surface temperatures measured by both the ATSR satellite and Everest terrestrial radiometers are summarised in Table 2-1.

| Platform | $I_{up}(\theta)$ | $I_{down}(\theta)$ | $t_i(\theta)$ |
|-------------|------------------|--------------------|---------------|
| Terrestrial | no | Yes | no |
| Satellite | yes | Yes | yes |

Table 2-1 Parameters required for atmospheric correction of satellite (ATSR) and terrestrial (Everest) radiometric data. For parameter definitions see text.

2.4.2 Empirical techniques for estimating infrared atmospheric emittance and transmittance

The principal source of attenuation and emission within the atmosphere is water vapour. Historically, empirical parameterisations for atmospheric correction factors have been based upon the water vapour profile. Various benchmarks have been suggested for modeling the atmospheric water vapour profile, which in many regions is frequently unobtainable. Choudhury (1996) related the precipitable water, or column integrated water vapour content, to the surface level vapour pressure, which can be monitored from terrestrial meteorological stations (Figure 2-6), and semi-empirical models gave highly significant correlations between the two.

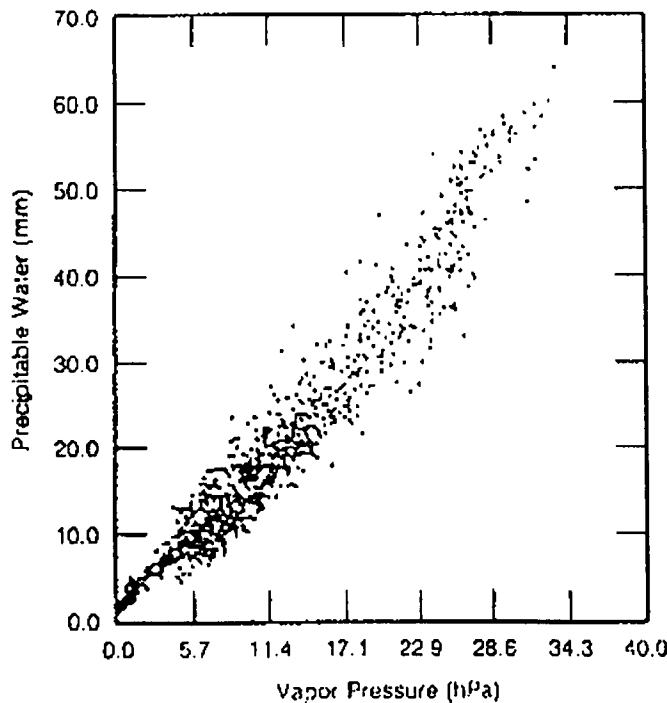


Figure 2-6 Scatter plot of precipitable water and surface level vapour pressure using mean monthly radiosonde ascents from a globally distributed dataset (after Choudhury, 1996).

A quantitative knowledge of the atmospheric water content is required to formulate empirical correction parameters for satellite observations (e.g. Soufflet *et al.*, 1991; Choudhury, 1993). Sobrino *et al.* (1996) evaluated the expectation value of the spectral atmospheric transmission, $\langle \tau_{Hi}(\nu) \rangle$, for the ATSR thermal infrared channels using the LOWTRAN radiative transfer code and radiosoundings extracted from the TIGR database. Strong correlation was observed between the transmissivity and the column integrated precipitable water (Figure 2-7), highlighting water vapour as the principle source of attenuation.

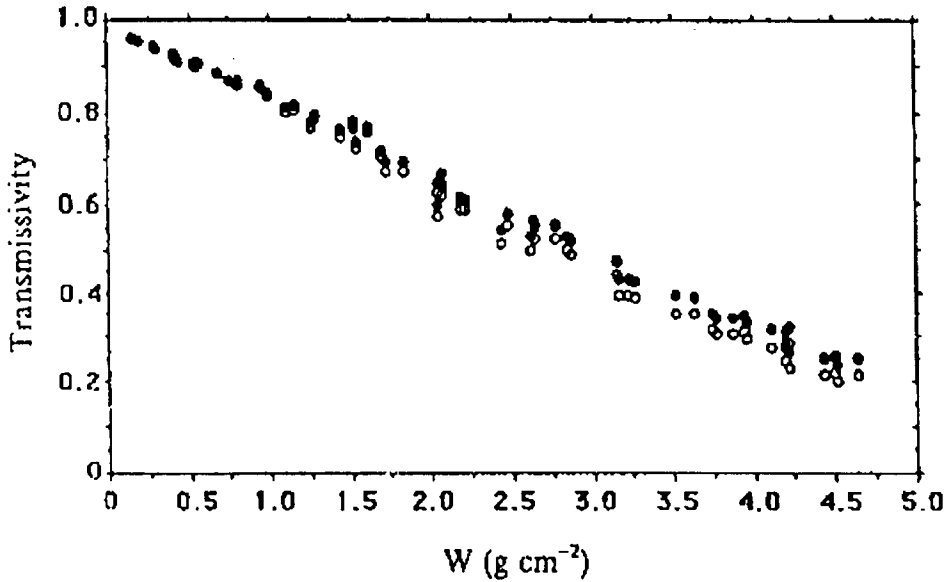


Figure 2-7 Atmospheric transmissivity for ATSR channel 3 forward view and channel 4 nadir view as a function of the atmospheric water vapour content at nadir (after Sobrino *et al.*, 1996).

Empirical expressions which relate the atmospheric emission and transmittance to surface level observations are outlined below.

Atmospheric emittance

The thermal radiative characteristics of water vapour within cloudless atmospheres are generally expressed in terms of an effective emissivity ϵ_a defined as the ratio of the observed atmospheric emission to that of a blackbody, so that

$$I_{down} = \epsilon_a \sigma T_0^4 \quad (2.19)$$

where I_{down} is the nadir full spectrum atmospheric emission, σ is the Stefan-Boltzmann constant and T_0 is the surface or screen-level air temperature. In such parameterisations the emissivity is independent of frequency and therefore the atmosphere is assumed to radiate as

a grey body. When considering emission in a particular wavelength region, or that recorded in an instrument channel, the atmospheric emissivity is then modified to the simple ratio

$$\epsilon_{a_i} = \frac{\int_{\nu_{i1}-\nu_{i2}} B(\nu, T_i) d\nu}{\int_{\nu_{i1}-\nu_{i2}} B(\nu, T_0) d\nu} \tag{2.20}$$

where B is the Planck function and T_i is the brightness temperature of the atmosphere in channel i , so that

$$I_{idown} = \epsilon_{a_i} \int_{\nu_{i1}-\nu_{i2}} B(\nu, T_0) d\nu \tag{2.21}$$

is the total nadir power emitted by the atmosphere in channel i . Such empirical relationships in general do not differentiate between upwelling and downwelling atmospheric radiation, which in practice are approximately equal when considering the whole atmosphere. Several empirical long wave radiation models have been proposed which provide different methods of evaluating the atmospheric emittance. Hatfield *et al.* (1983) tested a variety of empirical formulae for atmospheric emittance on a comprehensive radiosonde dataset covering a range in latitude from approximately 26 to 48° North and an elevation range from -30m to 3342m. Results show that parameterisations based upon both the surface level water vapour pressure (e_0) and temperature (T_0) provide the best estimates of long-wave radiation (Table 2-2).

| Formula | f(e_0) | f(T_0) | r ² | S _v /K/m ² /h | Formulation | reference |
|--------------|------------|------------|----------------|-------------------------------------|--|-----------------------|
| Idso-Jackson | No | yes | 0.759 | 70.053 | 1-0.261*(-7.704*(273-T ₀) ²) | Idso & Jackson (1969) |
| Swinbank | No | yes | 0.762 | 66.967 | 0.92*10 ⁻³ *T ₀ ² | Swinbank (1963) |
| Brunt | Yes | no | 0.881 | 49.055 | 0.51+0.66*e ₀ ^{0.5} | Brunt (1932) |
| Brutsaert 2 | Yes | no | 0.883 | 50.734 | 0.575*e ₀ ^{1/7} | Idso (1981) |

| | | | | | | |
|-------------|-----|-----|-------|--------|---|------------------|
| Brutsaert 1 | Yes | no | 0.883 | 48.738 | $0.533 \cdot e_0^{1/7}$ | Brutsaert (1975) |
| Idso2 | Yes | yes | 0.883 | 47.846 | $0.7 + 5.95 \cdot 10^{-5} \cdot e_0^2 \cdot e^{(1500/T_0)}$ | Idso (1981) |
| Idsol | Yes | yes | 0.893 | 40.586 | $0.179 \cdot e_0^{1/7} \cdot e^{(350/T_0)}$ | Idso (1981) |

Table 2-2 Long wave radiation formulas compared by Hatfield *et al.* (1983) and their relative performances when using the same data set. The range of longwave radiation measurements was 947 to 1530 KJ m⁻² hr⁻¹.

The formulae of Idso are semi-empirical and are based upon results from an experiment conducted at Phoenix, Arizona, monitoring in addition to the full spectrum thermal radiation those fractions of the flux that are contained in the 8-14 μm and 10.5-12.5 μm sub-regions. The source of water vapour associated thermal emittance variations of the cloudless sky was attributed to the variable atmospheric concentration of water dimers, pairs of water molecules linked together by weak hydrogen bonds. Idso's second full-spectrum formula incorporates the water dimer theory which accommodates the binding energy of the water dimer's hydrogen bond within the exponent. By incorporating some physical basis into his formula, Idso reduced the accuracy according to Hatfields linear regression analysis, which tested all formulae upon a wider distribution of atmospheric profiles. However, correlations for the water dimer equation are still very high and since the hypothesis is more compatible with Idso's training data it seems reasonable to adopt the semi-empirical approach towards estimating atmospheric emittance. The standard predicting error for full spectrum radiation using this formulation lies between 3 and 5%.

Idso's final set of semi-empirical equations for full spectrum, 10.5-12.5 μm and 8-14 μm atmospheric emissivity are

$$\epsilon_{a_{full}} = 0.7 + 5.95 \times 10^{-5} \epsilon_0^2 e^{\left(\frac{1500}{T_0}\right)}$$

$$\epsilon_{a_{10.5-12.5}} = 0.1 + 3.53 \times 10^{-8} \epsilon_0^2 e^{\left(\frac{3000}{T_0}\right)}$$

$$\epsilon_{a_{8-14}} = 0.24 + 2.98 \times 10^{-8} \epsilon_0^2 e^{\left(\frac{3000}{T_0}\right)}$$

(2.22)

and can be used to determine the atmospheric radiances in the 8-14 μm and 10.5-12.5 μm sub-regions as a function of surface level vapour pressure and temperature.

Models for predicting thermal radiation from partly cloudy and overcast skies use clear sky equations for predicting sky emittance and transmittance and then assume that the cloud contribution to sky thermal radiation must be transmitted to the earth's surface through the atmospheric window. Kimball *et al.* (1982) predicted an increase in sky emittance due to 100% cloud cover of around 18%, with excellent agreement (r^2 greater than 90%) between predicted and measured radiances.

Atmospheric transmittance

Quantitative empirical formulae for atmospheric transmittances at infrared wavelengths are difficult to find in the literature. Kimball *et al.* (1982) developed an expression for the transmittance of the atmosphere in the 8-14 μm window, t_{8-14} , assuming that the hemispherical transmittance was the complement of the hemispherical emissivity. The hemispherical emissivity can be related to the zenithal sky emissivity ϵ_{a8-14} of Idso (1981b) through Idso's (1981a) correction

$$\epsilon_{8-14} = \epsilon_{a8-14} (1.4 - 0.4\epsilon_{a8-14}) \quad (2.23)$$

and the hemispherical, or nadir atmospheric transmittance is then

$$\tau_{8-14} = 1 - \epsilon_{8-14} \quad (2.24)$$

The broadband atmospheric transmittance was generated under the assumption of a grey atmosphere. Idso's formula for ϵ_{8-14} is wholly empirical with no such physical basis as the water dimer theory for atmospheric emissivity, and should be used with care. There is no

easy method of parameterising the transmission within discrete wavelength ranges, and in practice for satellite observations the atmospheric transmittance should be generated using radiative transfer code. Moreover, for terrestrial radiometry it is not necessary to establish the atmospheric transmittance since attenuation is negligible over such short atmospheric path-lengths.

2.4.3 Numerical techniques for estimating infrared atmospheric emittance and transmittance

Atmospheric attenuation and emission can be theoretically calculated using radiative transfer models if the vertical temperature and humidity profiles are known. Temperature and humidity profiles can be obtained using radiosonde ascents. Barnes & Lilly (1975) determined that tropospheric mixing ratios for water vapour vary by typically less than 20% horizontally at scales below 100 km within non-stormy environments. The accuracy of data retrieved from an individual radiosounding is of the order 10-15 %, and it is reasonable to assume that a single sounding would yield representative atmospheric data over similar spatial scales. Maul & Sidran, (1973) estimated that the atmospheric data retrieved from a single sounding lead to an instantaneous accuracy of around 1°C when estimating the surface temperature from spaceborne radiometers. Smith *et al.* (1994) tested the retrieval accuracy of the RAL radiative transfer model and found biases of approximately 0.7°C when comparing airborne and ATSR sea surface temperature measurements. These accuracies are around the same level achieved using a statistical estimate of the bulk atmospheric attenuation and emission accounting for geographical location and seasonal variability.

The RAL atmospheric radiative transfer model

The RAL (Rutherford Appleton Laboratory) radiative transfer model (RADGEN), developed by Zavody *et al.* (1995), was designed to produce sea surface temperature retrieval coefficients for the ATSR instrument. A comprehensive description of the model can be found in Zavody *et al.* (1995). Comparison with other atmospheric models (Barton *et al.*, 1989) has shown good overall agreement and the RAL model has been validated with ATSR data on numerous occasions (e.g. Mutlow *et al.*, 1994; Smith *et al.*, 1994).

RADGEN is a parametric line-by-line model and generates fine spectra of atmospheric transmission, upwelling and downwelling radiation in the thermal infrared region (approximately 10-13 μm). These spectra can be used to accurately correct real time satellite retrieved brightness temperatures for atmospheric effects. Parameters required by the model are standard atmospheric temperature, pressure and water vapour profiles commonly obtained using radiosonde ascents. The model calculates attenuation and emission for stratified layers within the atmosphere.

In the absence of scattering by particles, the atmospheric radiance from a thin layer of thickness δz at a height h is given as

$$I(\nu, h)\delta z = B(\nu, T(h))\alpha(\nu, h)\delta z \tag{2.25}$$

where $\alpha(\nu, h)$ is the atmospheric absorption, which is related to the transmittance by

$$\tau(\nu, \theta, z1, z2) = e^{\left(-\int_{z1-z2} \alpha(\nu, z) dz\right)} \tag{2.26}$$

so that

$$\frac{\delta \tau(\nu, \theta, z1, z2)}{\delta z} = -\tau(\nu, \theta, z1, z1)\alpha(\nu, z) \tag{2.27}$$

and, for instance, the upwelling atmospheric radiance is then written as

$$I_{up}(\nu, \theta) = \int_{0-Z} I(\nu, h) \tau(\nu, \theta, z, Z) dz \quad (2.28)$$

The final integration of elemental layers is performed with respect to pressure (p) using the (viewing angle independent) reciprocal scale height H_{rsc} where

$$H_{rsc} = \frac{\delta z}{\delta p} \quad (2.29)$$

so that

$$\int_{0-Z} I(\nu, h) \tau(\nu, \theta, z, Z) dz = \int_{p0-pH} H_{rsc} B(\nu, T(p)) \alpha(\nu, p) \tau(\nu, \theta, p0, pH) dp \quad (2.30)$$

This simplifies the atmospheric calculations with respect to the viewing angle θ which is required for the ATSR instrument. The model assumes that absorption can be fully specified by a combination of the atmospheric sounding data coupled with estimates for the absorption caused by molecular H₂O, the water vapour continuum, uniformly mixed gases and aerosols. Line-by-line absorption is performed for the most significant absorbers, using pre-calculated data at various pressure levels cross referenced to the individual sounding data. These absorption contributions are then modified according to the temperature difference of the sounding pressure level from the tabulated data. For discrete absorption lines the code sources the HITRAN database (Rothman *et al.*, 1987) and uses the line shape profiles of Gross (1995). Details of the aerosol contributions are outlined by Dundas (1997). The spectral resolution of the model is 0.04 cm⁻¹ wavenumbers, and the bandwidth of the output spectra in the thermal-infrared is 760 to 1000 cm⁻¹ wavenumbers, which is equivalent to a wavelength range of approximately 10 to 13 μm. The spectral range of the RAL atmos-

pheric model encompasses the thermal infrared channels of both the ATSR and AVHRR satellite instruments, but does not extend to the broadband 8-14 μm filters of many terrestrial infrared radiometers.

2.4.4 Summary

Radiatively active substances present within the atmosphere, principally water vapour and trace gases, affect infrared radiometric measurements of the earth's surface primarily through the processes of emission and absorption. The magnitude of these effects can be quantified using numerical and empirical techniques, which relate the atmospheric emission and transmission to meteorological parameters.

The numerical techniques outlined generate high resolution spectra of atmospheric emission and transmission, whereas the empirical formulae predict the emission and transmission in particular wavelength regions of interest.

The empirical equations of Idso (1981) relate atmospheric transmission and emission to surface level air temperature and vapour pressure across discrete wavelength regions (full-spectrum, 10.5-12.5 μm and 8-14 μm). Idso's semi-empirical expressions for the effective atmospheric emissivity and transmission were found to have a prediction accuracy of around 3 - 5% (Hatfield *et al.*, 1982). The parameters can be used to correct terrestrial infrared radiometric measurements for the effects of atmospheric transmission and emission.

The RAL atmospheric radiative transfer model calculates multi-spectral atmospheric attenuation, downwelling and upwelling radiation across the thermal-infrared wavelength region (approximately 10-13 μm) using radiosonde ascents as the principle source of atmospheric data. From these spectra, bulk atmospheric correction parameters, akin to the empirical parameters, can be determined by integrating over discrete wavelength sub-regions or particular instrument channels using the appropriate filter response function. The parameters can be calculated for any viewing angle through the atmosphere, and can be used to correct ATSR satellite brightness temperatures for atmospheric effects.

The atmospheric parameters generated using the empirical equations of Idso and the RAL radiative transfer code are summarised in Table 2-3. In particular, the 10.5-12.5 μm wavelength region is common to both techniques.

| Wavelength region | emittance | transmittance |
|-------------------------|-----------|---------------|
| 0-infinity | IDSO | - |
| 8-14 μm | IDSO | IDSO |
| 10.5-12.5 μm | RAL/ IDSO | RAL |
| ATSR 11 μm | RAL | RAL |
| ATSR 12 μm | RAL | RAL |

Table 2-3 Bulk atmospheric parameters generated using the empirical relationships of Idso (1981) and the RAL radiative transfer code.

2.5 Differential techniques for Land Surface Temperature Retrieval

The transfer of infrared radiation through the earth's atmosphere within spectrally or geometrically different optical paths can be closely related to one another. This is because of the well documented behaviour of the atmosphere through the infrared transmission window. These so called split-window and dual-angle techniques can be used to improve the radiometric accuracy for LST estimation in the absence of *in situ* atmospheric data. Satellite instruments such as the AVHRR and the ATSR use multiple infrared channels, closely separated in wavelength, to exploit the spectral variation in atmospheric transmission. The ATSR instrument also records surface radiance through two viewing geometries to obtain additional information on the atmospheric optical depth.

The theoretical basis of both dual-angle and dual-channel differential techniques is a first order expansion of the Planck function, $B(\nu, T)$, which enables linearisation of the radiative transfer equation. Non-linear terms are typically discarded or parameterised in most differential retrieval algorithms, so that many are essential semi-empirical in nature. In general, algorithms are tested for authenticity using archived atmospheric radio-sounding data to synthesise parameters such as, for instance, the latitudinal variation in atmospheric transmission. Coefficients are then generated for various geographical and temporal scenario,

which can be applied autonomously to satellite data to generate surface temperature products.

An example of a split-window LST algorithm, which is extended to accommodate dual-angle data, is presented below. The theory follows the work of Prata (1993) which describes both a dual-channel and a dual-angle LST retrieval algorithm, and highlights the various assumptions the author makes.

For small deviations about a central wavenumber, a first order Taylor series expansion of the Planck function is a reliable approximation over a reasonable temperature range. The radiance at temperature T in channel i can then be expressed in terms of the radiance in a different, spectrally close, channel j , so that

$$B_i(T) = B_j(T) + (\nu_i - \nu_j) \left(\frac{\delta B_j(T)}{\delta \nu} \right) \quad (2.31)$$

By expressing the individual components of the radiative transfer equation in this manner and differencing the emission from two channels, a split-window expression for the upwelling surface radiance is

$$B_j(T_s) = aB_j(T_j) + bB_j(T_i) + c \quad (2.32)$$

where derivatives of the Planck function are neglected, and the coefficients are related to the atmospheric transmittance and emittance and the surface emissivity through Equations 2.33.

$$a = \frac{(1 + g_\nu)}{(\epsilon_i + g_\nu \tau_j \delta \epsilon_\nu)}$$

$$b = \frac{-g_v}{(\varepsilon_j + (1 + g_v)\tau_i\delta\varepsilon_v)}$$

$$c = \frac{(1 - \varepsilon_j - g_v\tau_i\delta\varepsilon_v)}{(\varepsilon_j + g_v\tau_i\delta\varepsilon_v)}\delta I_{down}$$

$$g_v = \frac{(1 - \tau_i)}{(\tau_i - \tau_j)}$$

$$\delta\varepsilon_v = \varepsilon_i - \varepsilon_j$$

$$\delta I_{down} = g_v\tau_i I_{idown} - (1 + g_v)\tau_j I_{jdown}$$

(2.33)

Provided that all temperatures are close in magnitude, a radiance error of typically less than 2% is introduced by neglecting the differential terms (Prata, 1993). The offset term in the radiance algorithm δI_{down} is due to the difference in downwelling sky radiance in individual channels. Prata investigated the variability of this term using radiosounding data collected over an 18 year period from stations distributed around the Australian continent. It was noted that values for δI_{down} calculated for two AVHRR infrared channels varied between -18 to 7 $\text{mW m}^{-2}\text{sr}^{-1}\text{cm}^{-1}$, with a mean value of 3.6 $\text{mW m}^{-2}\text{sr}^{-1}\text{cm}^{-1}$. The total variation (in δI_{down}) constitutes only a small effect on the final LST determined by the algorithm (Prata, 1993). If a constant value for δI_{down} is assumed, then the LST algorithm is reduced to a function of the two channel radiances, surface emissivities and atmospheric transmittances. In this sense, the LST algorithm becomes somewhat localised in nature, valid effectively only in the appropriate regions of the southern hemisphere. However, the method is evidently portable given a reasonable atmospheric sounding dataset from which to estimate a value of δI_{down} .

The analogous Prata dual-angle algorithm takes the same form as the split-window algorithm (2.31). The surface emittance is then related to the radiance recorded at two incidence angles, I_{θ_1} and I_{θ_2} , such that

$$B_i(T_s) = aI_{\theta_1} + bI_{\theta_2} \quad (2.34)$$

where

$$a = \frac{(1 + g_\theta)}{(\epsilon_{\theta_1} + g_\theta \tau_{\theta_2} \delta\epsilon_\theta)}$$

$$b = \frac{-g_\theta}{(\epsilon_{\theta_2} + (1 + g_\theta) \tau_{\theta_1} \delta\epsilon_\theta)}$$

$$g_\theta = \frac{(1 - \tau_{\theta_1})}{(\tau_{\theta_1} - \tau_{\theta_2})}$$

$$\delta\epsilon_\theta = \epsilon_{\theta_1} - \epsilon_{\theta_2} \quad (2.35)$$

and i is the common spectral channel, and θ_1 and θ_2 are the different radiometric observation angles. In Equation 2.34, the dual-angle radiances I_{θ_1} and I_{θ_2} can equally be expressed in terms of the equivalent satellite brightness temperatures, T_{θ_1} and T_{θ_2} , using the Planck function $B_v(T)$.

According to Prata, there is no offset term in the dual-angle algorithm because the differential downwelling radiance, δI_{down} , reduces to zero when comparing radiances under isotropic skies.

The atmospheric transmittance is a function of zenith angle and, for weak absorption, the angular variation can be expressed in terms of the integrated water vapour content w and an absorption coefficient k_v which includes the effects of all gaseous absorbers, so that $\tau_v(\theta) \approx 1 - k_v w \sec \theta$ and then $g_\theta = (\cos \theta_1 / \cos \theta_2 - 1)^{-1}$. For the ATSR, the parameter g_θ varies between 1.345 along the ground track to 2.565 at the edge of the instrument swath.

To obtain an LST retrieval algorithm that is linearly related to brightness temperatures, the Planck function can be expanded as a first order Taylor series with respect to temperature, so that

$$B_i(T) = B_i(\langle T \rangle) + (T - \langle T \rangle) \frac{\delta B_i}{\delta T_{\langle T \rangle}} \quad (2.36)$$

where $\langle T \rangle$ is a mean temperature close to T . For moderate temperature departures the expansion is accurate to within 1% at infrared wavelengths.

The final dual-angle algorithm relating the LST to radiometric temperature measurement at two observation angles in the same waveband is then

$$T_s = T_{\theta_1} + b(T_{\theta_2} - T_{\theta_1}) + (a + b - 1)B_i(T_{\theta_1}) \left(\frac{\delta B}{\delta T_{\langle T_{\theta_1} \rangle}} \right)^{-1} \quad (2.37)$$

The emissivity of bare soils has been observed to exhibit angular behaviour, with typically a pronounced decrease at incidence angles of greater than 60° (Nerry *et al.*, 1988; Labed & Stoll, 1990). The ATSR instrument has nadir and forward viewing radiometers, and along the satellite ground track the view zenith angles are approximately 0 and 55° respectively. If negligible angular variation in surface emissivity is assumed, then the coefficients for the dual angle LST algorithm reduce to $a = (1 + g_\theta)/\epsilon_\theta$ and $b = -g_\theta/\epsilon_\theta$, where ϵ_θ is a mean surface emissivity.

2.6 Estimating the Temperature of a Heterogeneous Surface

Over a three dimensional mixed cover surface it is not possible to solve for the radiative surface temperature using the simple dual-angle algorithms described previously. This is because the mean surface temperature will often exhibit some angular dependence because of

the canopy architecture. Satellite derived LST's are typically estimated at spatial resolutions far greater than the roughness size of the distinct surface elements present within the imaged pixel. The mean temperature of a heterogeneous land surface is then a mixture of the individual component temperatures, which can generally be grouped into discrete field classifications such as vegetation and soils. The nature of thermal interactions between surface emitters is related to the instantaneous partition of the surface energy budget. Effective parameters for averaging energy fluxes over heterogeneous terrain have been derived, based upon scaling up the small scale physical interactions and the conservation of radiation at the surface (Chehbouni *et al.*, 1995; Lhomme *et al.*, 1994). The usual model for conserving the surface radiance is a simple linear mixture of the component signals (Settle and Drake, 1995). The basic physical assumption underlying linear mixture models is that there is no significant amount of multiple scattering between the different cover types. The energy received by a radiometer viewing a heterogeneous surface can then be considered a simple sum of the energies received from each cover component. Each surface cover type will contribute an amount of energy proportional to the area covered by that field within the radiometric field of view. The combined surface radiance from a mixed pixel, using a linear mixing assumption, is simply

$$I_{surf}(v, \theta) = \sum_j f_j(\theta) I_j(v, \theta) \quad (2.38)$$

where $f_j(\theta)$ is the fractional occupancy of surface field j , $I_j(v, \theta)$ is the radiance of field j , and $\sum_j f_j(\theta) = 1$. Note that the fractional occupancy of individual classes may exhibit a characteristic angular dependence, because of the three dimensional nature of natural surfaces. The fractional occupancy of vegetation is frequently dependent upon the angle at which the surface is observed (Lagouarde *et al.*, 1995, Kimes *et al.*, 1980), and for mixed soil and vegetation pixels, $f_j(\theta)$ can be related to the particular canopy architecture.

The linear conservation of emitted energy implies that surface parameters such as temperature will not aggregate linearly. The functional form of sub-pixel temperature aggregation will depend upon the spectral domain of the instrument channel. For infrared radiation, the

aggregation scheme is often approximated using a power law relationship between emittance and radiative temperature (e.g. Norman *et al.*, 1995). Here, a suitable linearisation is obtained using expansions of the Planck function with respect to temperature and wavelength.

For a simple two component surface, such as one with a sparsely vegetated canopy, the combined radiance measured at instrument channel i may be written

$$I_{surfi}(\theta) = f_{veg}(\theta)I_{iveg}(\theta) + (1 - f_{veg}(\theta))I_{isoil}(\theta) \quad (2.39)$$

where $f_{veg}(\theta)$ is the fractional occupancy of vegetation and $I_{iveg}(\theta)$ and $I_{isoil}(\theta)$ are the vegetation and soil emittance in channel i . The directional heterogeneous surface emittance $B_i(T_s(\theta))$, can then be expressed in terms of the component temperatures and emissivities, so that

$$B_i(T_s(\theta)) = \frac{1}{\epsilon_i(\theta)} (f_{veg}(\theta)\epsilon_{iveg}B_i(T_{veg}) + (1 - f_{veg}(\theta))\epsilon_{isoil}B_i(T_{soil})) \quad (2.40)$$

where $T_s(\theta)$ is the (angular dependent) mean surface radiative temperature, T_{veg} and T_{soil} are the vegetation and soil radiative temperatures and ϵ_{iveg} and ϵ_{isoil} are the component emissivities which are assumed to exhibit negligible angular variation. The mean surface emissivity $\epsilon_i(\theta)$ can be expressed in terms of the component emissivities (Lhomme *et al.*, 1994) so that

$$\epsilon_i(\theta) = f_{veg}(\theta)\epsilon_{iveg} + (1 - f_{veg}(\theta))\epsilon_{isoil} \quad (2.41)$$

In this way, the remotely sensed surface radiance is partitioned into three unknown parameters, T_{veg} , T_{soil} and $f_{veg}(\theta)$. The proportion of the scene occupied by vegetation $f_{veg}(\theta)$ will typically increase from a minimum in the nadir view to a maximum when viewing par-

allel to the surface, assuming the vegetation is infinite in extent. In a simple canopy of randomly oriented and spherically distributed leaf elements, the fractional vegetation cover can be expressed in terms of the nadir fractional vegetation cover F and the observation angle (e.g. Norman *et al.*, 1995), such that

$$f_{veg}(\theta) = 1 - e^{\left(\frac{\ln(1-F)}{\cos\theta}\right)} \quad (2.42)$$

The architecture of other, more complex, canopies can be represented using similar parameterisations. To completely delineate T_{veg} , T_{soil} and F would require surface radiances measured at three observation angles. Using radiative surface temperatures retrieved at only two view zenith angles (θ_1 and θ_2), T_{soil} can be eliminated from the two radiative transfer equations and the fractional vegetation cover can then be related to the canopy temperature T_{veg} so that

$$af_{veg}(\theta_1) + bf_{veg}(\theta_2) + cf_{veg}(\theta_1)f_{veg}(\theta_2) + d = 0 \quad (2.43)$$

where

$$\begin{aligned} a &= \epsilon_{soil} (B_i(T_s(\theta_2)) - B_i(T_s(\theta_1))) + \epsilon_{iveg} (B_i(T_s(\theta_1)) - B_i(T_{veg})) \\ b &= \epsilon_{soil} (B_i(T_s(\theta_2)) - B_i(T_s(\theta_1))) + \epsilon_{iveg} (B_i(T_{veg}) - B_i(T_s(\theta_2))) \\ c &= (\epsilon_{iveg} - \epsilon_{soil}) (B_i(T_s(\theta_2)) - B_i(T_s(\theta_1))) \end{aligned}$$

$$d = \varepsilon_{soil} (B_i(T_s(\theta_1)) - B_i(T_s(\theta_2))) \quad (2.44)$$

The nadir fractional vegetation cover F can then be determined numerically using the canopy architecture relationship described by Equation 2.42 given the coefficients a , b , c and d in Equation 2.44. The values of a , b , c and d are calculated as a function of the vegetation temperature T_{veg} , dual-angle radiative surface temperatures $T_s(\theta_1)$ and $T_s(\theta_2)$ derived from radiometric brightness temperatures (corrected for atmospheric effects) and estimates of the soil and vegetation emissivities ε_{soil} and ε_{veg} . The resulting relationship can be used to express T_{soil} and T_{veg} in terms of a known fractional vegetation cover.

Similar expressions for the coefficients of Equation 2.43 can be derived to resolve either T_{soil} and f_{veg} in using an estimate of T_{veg} or alternatively T_{soil} and T_{veg} using an estimate of f_{veg} . Therefore, for a two component surface, two out of three unknown parameters are readily resolved using radiometric temperatures from independent viewing angles. Typically, T_{veg} or F can be confidently estimated or measured *in situ*.

2.7 Summary

The land surface temperature is an important geophysical parameter used in a variety of environmental applications. The necessity to reproduce LST's consistently at a variety of spatial scales has led to the use of radiative surface temperatures in many dynamic models. To accurately determine the LST from remotely sensed surface radiances a thorough consideration of the radiative transfer through the earth's atmosphere is required. The magnitude of atmospheric effects can be estimated using both numerical and empirical techniques. Examples of each approach have been discussed. Estimates of the atmospheric emission and transmittance can be made using the RAL radiative transfer model in the wavelength regions sensed by the ATSR instrument. Similar estimates can be made across broadband infrared channels sensed by ground based radiometers using the empirical equations of Idso (1981). A direct comparison between the two methods can be made in an overlapping spectral region.

Using reasonable approximations, it is possible to parameterise the LST using differential radiometric measurements of the same scene. This has led to the development of both split-window (and multi-channel) and dual-angle LST algorithms, which utilise the predictable differential atmospheric absorption between spectrally or geometrically independent atmospheric paths. Using LST algorithms, accuracies of between 3 - 5°C have been obtained over well classified surfaces (Prata, 1994). The error associated with LST algorithms is shown to be dependent upon both the atmospheric water vapour content, which can often be parameterised, and the surface emissivity prescription. Emissivity values of natural surfaces are known to vary greatly both spatially and temporally, and this can lead to large uncertainties in the resultant LST if its value is poorly prescribed. Using a linear mixture model it is possible to determine the emission from a heterogeneous surface as a function of the radiance of individual components. Dual-angle radiometric surface temperatures can be used to delineate the temperatures of a two component mixed surface. This principle can be used to compare satellite retrieved surface temperatures to *in situ* component temperatures over a mixed element surface.

Chapter 3

A Laboratory calibration of terrestrial Infrared Radiometers

The calibration of a series of aged commercially available infrared radiometers, provided by the Institute of Hydrology, is described. Each instrument consists of a thermopile radiation sensor and a thermistor which monitors the internal detector temperature. The radiometric field of view was estimated and was found to be in agreement with the manufacturers specifications. Each instrument was independently calibrated against a high precision, broad aperture, blackbody reference source. The calibration experiments were repeated on a number of occasions using a comprehensive range of target temperatures. Linear correction algorithms were derived for each instrument which compensated for the observed differences between the sensor and calibration source temperatures.

3.1 Introduction

The radiative temperature of a body can be determined from its infrared emission using Planck's radiation law. Commercially available infrared radiometers are frequently used in field applications for the remote detection of crop and soil radiative temperatures.

An array of terrestrial infrared radiometers was available to study vegetation canopy temperatures in a semi-arid environment. In perfect condition the instruments were known to be sufficiently accurate for most environmental applications. However, the instrument performance was observed to deteriorate significantly with age, and re-calibration of each sensor was required prior to the study. The performance of each radiometer was rigorously investigated before, during and after the field experiments using a controlled laboratory calibration procedure.

Ten Everest Interscience model 4000 infrared radiometers were used in the study. The sensors included a chopped aperture, which periodically exposes an internal target of known temperature for self-calibration purposes. Similar instruments have been independently calibrated in both laboratory and simulated field conditions. An empirical relationship between the thermopile output voltage, the internal reference temperature and the target radia-

tive temperature was derived by Kalma *et al.* (1988). The relationship was shown to be reliable across a broad range of internal detector temperatures. Wright (1990) studied the effects of external temperature fluctuations upon the sensor response. Earlier model instruments which did not incorporate the mechanically chopped aperture were found to respond poorly to environmental temperature changes. Empirical corrections were derived which compensated for the slow response of the body temperature to changing ambient conditions. The introduction of the internal reference target was shown to significantly improve the thermal stability of the instruments. No advantage was gained by applying empirical corrections for external temperature fluctuations to the chopped radiometer output. It was concluded that the chopped radiometers performed adequately, even when exposed to unrealistically large external temperature gradients.

The radiometers are small, self contained non-contact temperature transducers. The instruments use 35 mm precision corrected refractive optics and a Fresnel objective lens to focus incoming radiation. An interference filter with a spectral bandpass of 8-14 μm restricts the measured radiation to the infrared wavelength region, where atmospheric transmission is relatively high and should not affect the detected signal at reasonable separations. The radiometric field of view is 15° with an operating distance between 2 cm and 1000 feet. The thermal response time is less than 1 second and temperatures are recorded to 0.5°C accuracy at 0.1°C resolution. The temperature sensing range of the instrument was -30 to 100°C . The noise effective temperature (NEdT) was less than 0.05°C , and the recommended operating environmental temperature was between -10 and 65°C .

3.2 Angular response

The limiting aperture of the Everest infrared radiometer was 20 mm in diameter. Accounting for the recommended operating distance and the instrument field of view, the minimum target diameter required was approximately 23 mm. The maximum aperture of the black-body reference source was approximately 25 mm, and the calibration experiment was close to the limiting performance of the apparatus.

An investigation of the radiometer angular response was undertaken to independently determine the instrument field of view. The radiometric temperature of a point source was

measured from a variety of incidence angles. The target was placed at a distance of approximately 250 mm from the infrared sensor and subtended an angle of less than 1.5° to the radiometer aperture. Temperatures were recorded as the source was passed across the radiometer aperture perpendicular to the line of sight of the instrument. Measurement errors were introduced primarily through inaccuracies in the location of the thermopile detector within the radiometer.

The normalised angular response of the Everest infrared radiometer was determined as a function of the minimum and maximum source temperature observed during the experiment (see Figure 3-1).

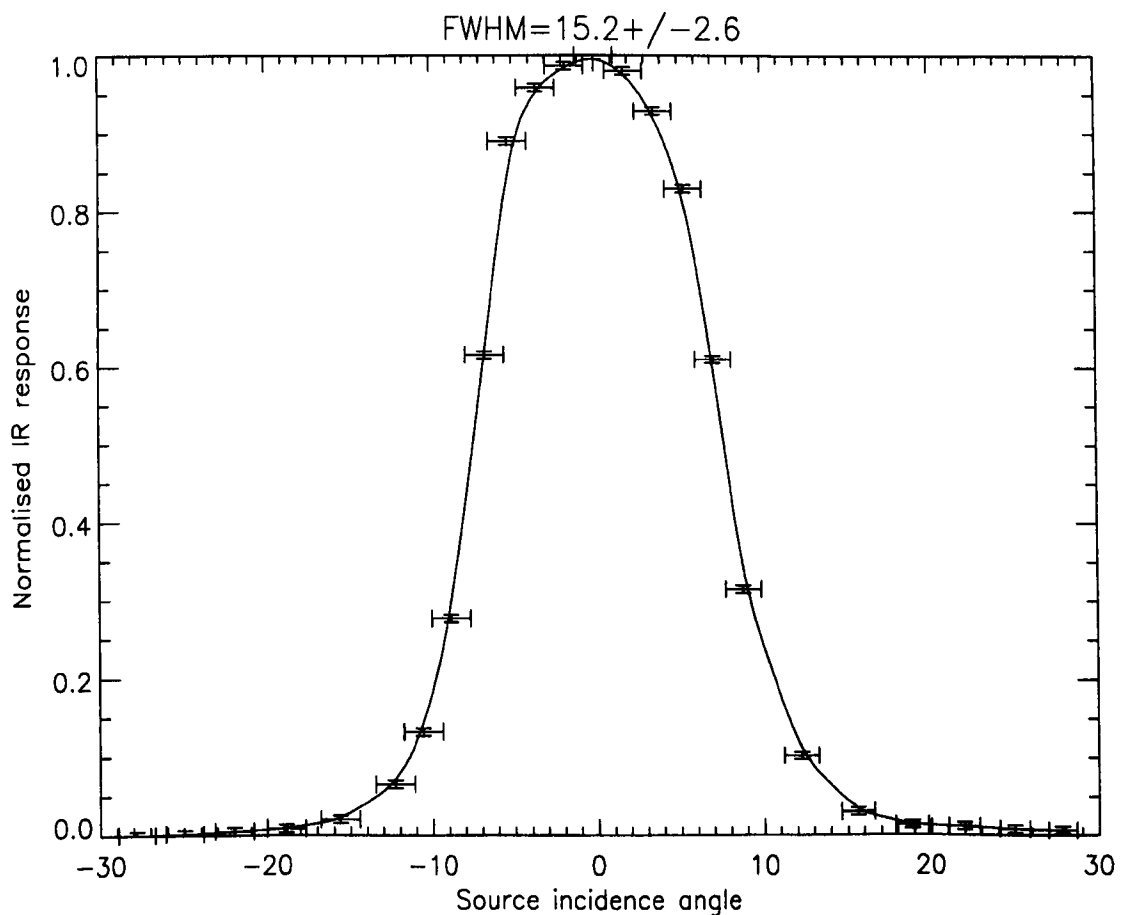


Figure 3-1 Normalised angular response of Everest Interscience model 4000 infrared radiometer.

The peak source temperature recorded was 84.8°C. The full-width at half maximum (*FWHM*) of the radiometric response curve was estimated to be $15.2 \pm 2.6^\circ$. This result is in excellent agreement with the manufacturers quoted instrument field of view (15°). Assuming the thermopile detector has a lambertian response function, approximately 94 % of incoming radiation is collected from within the 15 ° field of view.

3.3 Absolute Radiometric Calibration

The radiometric calibration of Kalma *et al.* (1988) was performed on perfectly conditioned instrumentation. Wright (1990) determined empirical corrections for unchopped radiometers which were based upon the sensor body temperature. No explicit inter-comparison between individual radiometer performance was presented in either study. Significant differences in radiometric temperatures (upwards of 3°C) of the same target were recorded by separate instruments under laboratory conditions. It was concluded that the aged radiometers required re-calibration prior to use.

The calibration target used was a commercially available Working Standards WS153 blackbody reference source. The blackbody consisted of an air cooled recessed conical cavity with a linearly proportional temperature control. The apparent emissivity of the source was determined analytically by Chandos & Chandos (1974) to be 0.99 ± 0.01 . The source could generate blackbody radiation between room temperature and 1000°C and thermal stability was reached in approximately 90 minutes. The cavity temperature was stable to within 0.1°C and the core temperature was continuously monitored using a platinum resistance thermometer with a precision of 0.01°C. The linear temperature control was periodically calibrated and the blackbody cavity temperature was typically accurate to within 0.2°C (see Figure 3-2).

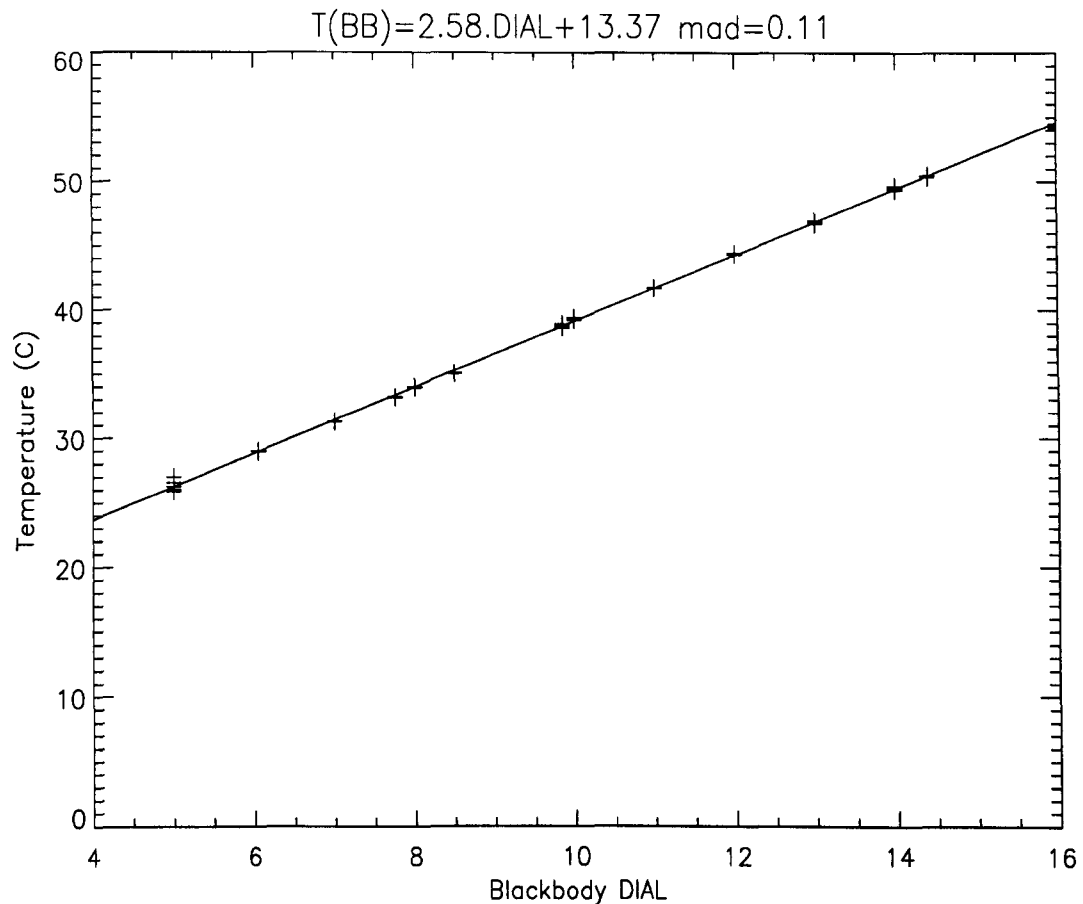


Figure 3-2 Temperature calibration curve derived for WS153 blackbody reference source.

3.3.1 Experiment description and method

Radiometers were mounted upon a moveable track specifically designed to interface with the blackbody calibration source (see Figure 3-3). To reduce potential loss mechanisms from the experimental apparatus a thermally insulated infrared light-pipe aperture was constructed between the radiometer and the blackbody. Cylindrical tubes of aluminised Mylar, approximately 30 mm in length, were positioned between the sensor and source. Clean aluminised Mylar sheeting of this form has been shown to have a thermal emissivity near to $0.044 \pm 1.3 \%$ (Domen 1991). This interface was incorporated to overcome physical restrictions presented by both the radiometer sunken aperture and the blackbody source aperture baffle. The nominal 15 degree radiometric field of view suggested that the light-pipe was not necessary, but independent verification of the sensor optics indicated that approximately 6 % of incoming radiation could be collected from beyond this range. Remillard *et*

al. (1992) have shown that attenuation in optical light pipes is typically less than 0.5 % cm⁻¹ for incidence angles of below 20°.

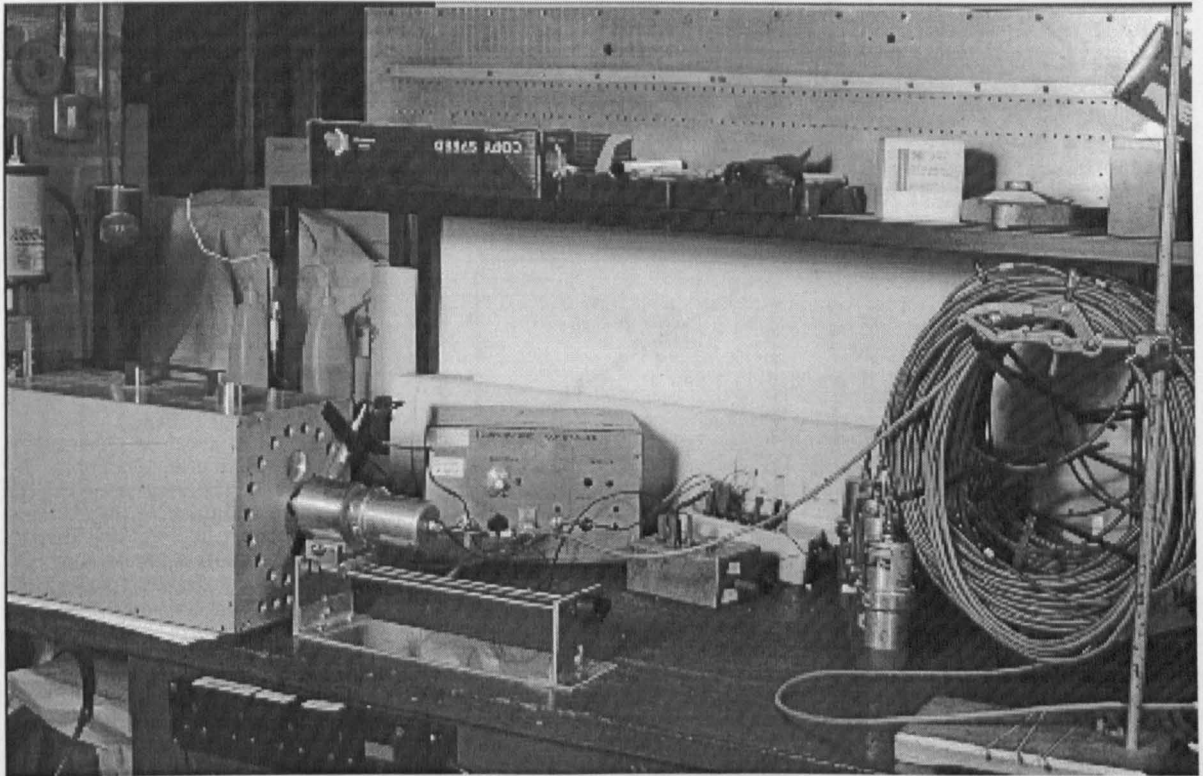


Figure 3-3 Calibration of infrared radiometers using a precision blackbody reference source.

Each of the ten infrared radiometers was presented in turn at the aperture of the blackbody. The calibration source was varied between room temperature and 65°C at discrete temperature intervals. The reference source was left to stabilise for approximately 120 minutes between each temperature level. Radiometer and blackbody temperatures were continuously recorded by a Campbell Scientific CR10 datalogger for 10 minute periods using a 1 second sampling interval. The mean and standard deviations of all temperatures were calculated at each temperature level.

3.3.2 Results

Calibration experiments were performed on three separate occasions over a 2 year time interval. Figure 3-4 shows scatter plots of the temperature differential between the calibration

source and each infrared radiometer against the blackbody cavity temperature. Data are presented from different calibration periods on each chart.

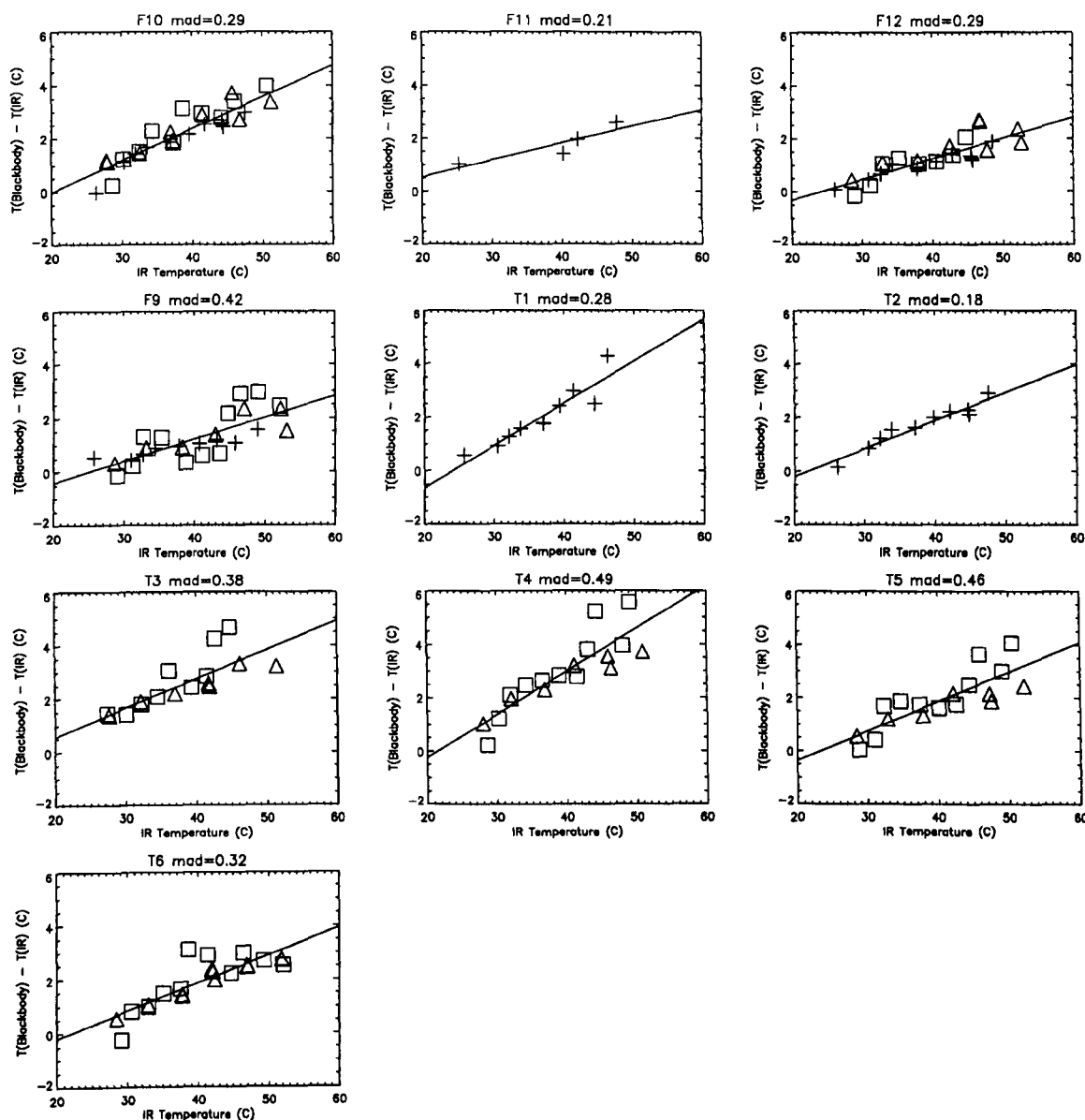


Figure 3-4 Scatter plots of the difference between blackbody reference temperature T_{BB} and infrared radiometer temperature T_{IRR} against T_{BB} for ten infrared radiometers. Data are presented from 3 different calibrations.

Temperature data were combined to derive empirical correction algorithms for each radiometer. Linear regression was performed between the radiometer and blackbody temperatures, T_{IRR} and T_{BB} respectively. A temperature correction equation of the form

$$T_{BB} = a_0 T_{IR} + a_1 \tag{3.1}$$

was derived for each instrument. The coefficients, mean absolute deviation *mad* and correlation coefficient obtained for each radiometer are presented in Table 3-1. The correlation coefficient was calculated for the temperature difference between the sensor and the source.

| Radiometer | a0 | a1 | r | mad |
|------------|-------|--------|-------|-------|
| F10 | 1.119 | -2.421 | 0.920 | 0.289 |
| F11 | 1.064 | -0.740 | 0.895 | 0.215 |
| F12 | 1.078 | -1.889 | 0.838 | 0.290 |
| F9 | 1.081 | -2.020 | 0.770 | 0.420 |
| T1 | 1.157 | -3.795 | 0.929 | 0.276 |
| T2 | 1.105 | -2.303 | 0.961 | 0.176 |
| T3 | 1.109 | -1.603 | 0.787 | 0.377 |
| T4 | 1.160 | -3.433 | 0.872 | 0.487 |
| T5 | 1.111 | -2.591 | 0.829 | 0.455 |
| T6 | 1.103 | -2.266 | 0.845 | 0.317 |

Table 3-1 Empirically derived temperature correction coefficients for ten infrared radiometers.

3.4 Summary

Ten aged infrared radiometers were calibrated against a high precision blackbody reference source. Temperature differences of greater than 3°C were recorded between individual instruments viewing the same target. The cavity temperature was calibrated to within 0.2°C and the effective aperture emissivity was approximately 0.99 ± 0.01 .

The angular response of a sample radiometer was found to be $15.2 \pm 2.6^\circ$, which is in excellent agreement with the manufacturers specifications. The temperature calibration apparatus was designed to accommodate the broad nature of the radiometric field of view.

Each infrared radiometer was pointed in turn directly at the blackbody aperture and the reference source was cycled through a comprehensive range of temperatures. The calibration experiments were repeated on a number of occasions. No significant difference was observed between calibration periods. Temperature correction algorithms were derived for each sensor using linear regression of the radiometric temperature against the blackbody cavity temperature. The mean absolute deviation of temperatures from these relationships ranged from 0.17 to 0.49°C. The manufacturers calibration accuracy was 0.5°C.

Chapter 4

Radiative Land Surface Temperature Retrieval at Infrared Wavelengths: Methodology

This chapter outlines the methodology employed to estimate land surface temperatures (LST's) using both satellite and terrestrial infrared radiances. The satellite data was retrieved by the Along Track Scanning Radiometer at approximately 1 km² resolution. Ground data were collected at and around the time of satellite overpass during two field campaigns at approximately 1 m² resolution. The data were corrected for the effects of the earth's atmosphere using a numerical radiative transfer model, empirical equations and a dual-angle LST retrieval algorithm. The surfaces studied exhibited heterogeneities in composition at sub-pixel scales, and a linear mixture model was used to aggregate the *in situ* surface emission from individual components to scale the LST up to the satellite resolution.

4.1 Introduction

The land surface temperature can be estimated from remotely sensed infrared radiances if the effects of the intervening atmosphere are considered. In the absence of complementary atmospheric data, it is necessary to simplify the radiative transfer equation to obtain the LST. Numerous semi-empirical algorithms have been proposed, which relate the LST to the infrared brightness temperatures in different satellite instrument channels. Differential radiometry can be performed using multiple spectral windows or with radiometric measurements through independent atmospheric paths. Most surface temperature algorithms are derived using numerical simulations of atmospheric sounding data (e.g. Becker and Li, 1990; Sobrino *et al.*, 1996). These methods are extensions of the well documented techniques for deriving sea surface temperature (SST), which can be validated on a global scale relatively easily using networks of *in situ* measurements (e.g. Llewellyn-Jones *et al.*, 1984). The LST is far more heterogeneous in nature, and in practice it is extremely difficult to compare satellite estimates with ground based measurements because of the differences in scale.

Few studies have presented direct comparisons between satellite and *in situ* estimates of the LST. Over a well calibrated site in southern Australia, Prata (1994) obtained *in situ* contact LST's that compared favourably with satellite radiometric LST's from the AVHRR sensor. Based upon a theoretical split-window algorithm, coefficients were derived using multiple regression to obtain the least-error solution. These local split window coefficients were shown to provide LST estimates with an accuracy of approximately $\pm 1.5^{\circ}\text{C}$ over soils and crops. Comparison between the regressed coefficient algorithms and algorithms based upon atmospheric modeling were also made. These showed little variation between the various algorithm estimates of LST for a limited set of night time data, covering a temperature range of around 0 - 5°C . However, when using a non-coincident dataset of atmospheric radio-soundings collected across the Australian sub-continent, strong dependence upon the prescription of the surface emissivity and atmospheric type was noted, with errors increasing to around $\pm 5^{\circ}\text{C}$ in some instances. The spatial variability in the LST was estimated to be greater than 3°C at the sub-pixel scale (approximately 1 km^2). As a consequence of the lack of experimental studies, the aggregation processes when scaling up the LST and temperature driven surface fluxes are not well understood (Chehbouni *et al.*, 1994; Stewart *et al.*, 1996).

A comprehensive field campaign was undertaken to address the principal problem of relating satellite derived LST's to *in situ* component radiometric temperatures. Ground based measurements were collected in conjunction with the satellite overpasses of the Along Track Scanning Radiometer (ATSR) during October 1995 and May 1996 in Zimbabwe, southern Africa. The ATSR has an impressive record for retrieving SST's, due to the instrument's high radiometric accuracy and dual-viewing geometry. Over heterogeneous terrain, the three dimensional nature of vegetation canopies may introduce a significant angular variation in the effective radiative surface temperature. The dual-viewing ATSR can contribute to our understanding this phenomenon.

Estimates of LST are largely determined by the surface emissivity prescription. Separating the effects of temperature and emissivity is of paramount importance when generating estimates of the LST (Becker, 1987). Using tabulated data, infrared emissivities were estimated for the surfaces considered.

All radiometric data were corrected for atmospheric effects using the numerical and empirical methods described in Chapter 3. Land surface temperatures were estimated from the terrestrial and satellite radiometric measurements using the techniques described in Chapter 2.

4.2 Data Sources

Radiometric surface temperatures were available from the ATSR satellite and complementary ground based measurements were collected using an array of infrared radiometers at two different locations. Atmospheric correction data were obtained from radiosoundings recorded at the nearby meteorological station at Belvedere, Harare. Ancillary climatology was also available from the 28 year record at Harare meteorological station. Hourly automatic weather station data, including air temperature and humidity, were recorded close to one of the field sites during 1995 and 1996. The temporal distribution of the major radiometric and atmospheric datasets is shown in Figure 4-1.

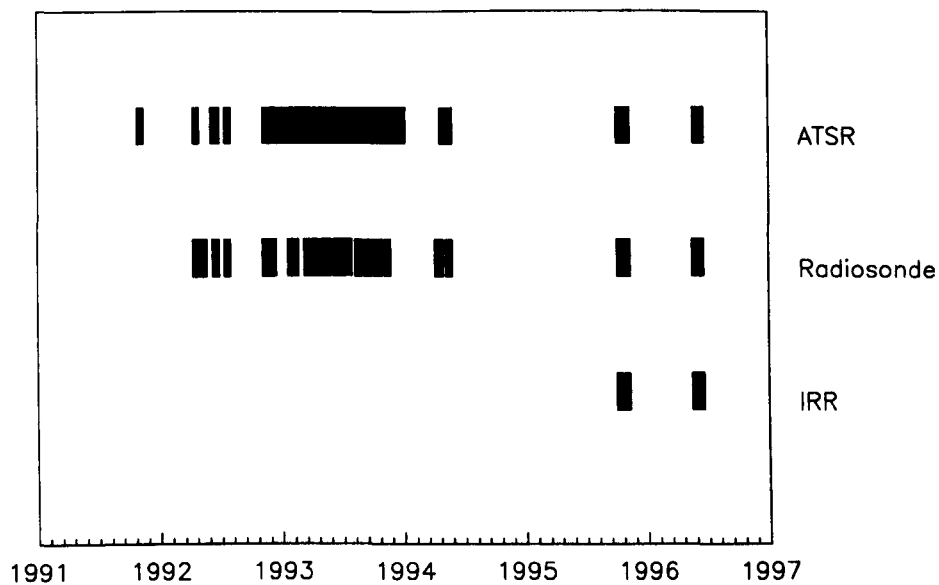


Figure 4-1 Temporal distribution of the radiometric and atmospheric datasets.

Surface and atmospheric measurements were timed to coincide with the satellite data.

Problems due to cloud contamination and the unavailability of the ATSR2 instrument af-

affected the continuity of the satellite dataset. From an initial dataset of over 100 ATSR BT images distributed over a five year period, the final training set of satellite data contained approximately 30 overpasses.

4.2.1 The Along Track Scanning Radiometer Dataset

The ATSR is an imaging radiometer carried onboard the earth orbiting European Remote Sensing satellites (ERS1 and ERS2). The radiometer has infrared channels centred in wavelength at 1.6, 3.7, 11 and 12 μm (see Figure 3-5), similar to the Advanced Very High Resolution Radiometer (AVHRR). The 1.6 μm and 3.7 μm channels are interchanged, so that the 1.6 μm is used during the day-time for improved cloud detection and the 3.7 μm is used at night under conditions of low reflected radiation from the surface. The ATSR instrument design incorporates improved technology over the AVHRR and as a result has a higher degree of radiometric accuracy. The onboard blackbody sources, for automatic calibration of the thermal-infrared sensor channels improved the absolute radiometric accuracy of the sensor. This ensured that the pre-launch radiometric resolution of the instrument would help meet the requirements of the World Climate Research Program (WCRP, 1985). In addition, the ATSR instrument uses a conical scan mirror (see Figure 4-2) to provide two independent views of the earth's surface, separated in time by approximately 2.5 minutes.

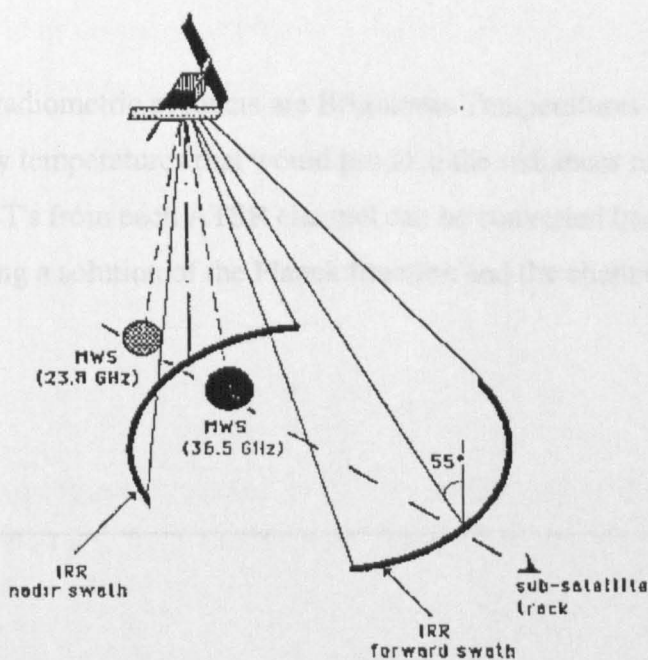


Figure 4-2 Schematic diagram of the ATSR viewing geometry

The dual-viewing geometry produces measurements of the upwelling radiance from the same spot on the surface through two different atmospheric paths, the lengths being proportional to the secant of the view-zenith angle. The atmospheric correction is related to the amount of emission and absorption that occurs through the atmospheric path, and the dual-view can exploit this difference to improve the correction. The principal radiometric measurement is made at nadir along the sub-satellite track, with a forward view at a zenith angle of approximately 55° . The conical scan of the ATSR traces curved swaths across the surface extending to 512 km in width. The nadir swath zenith angle varies from 0° to 21.6° , and the forward swath varies from 52.4° to 55° . The instantaneous field of view of the ATSR along the sub-satellite track is 1 km x 1 km for the nadir view and 1.5 km x 2 km for the forward view.

The ERS-1 satellite is in a near polar sun-synchronous orbit of inclination 98.5° at a mean altitude of 785 km above the surface. The orbital period is approximately 100 minutes and the satellite is operationally in a 35 day repeat cycle. This produces global coverage below around $\pm 80^\circ$ latitude and an image of the same location roughly every 3 days.

The ATSR infrared radiometric products are Brightness Temperatures (BT's), which are the equivalent blackbody temperatures that would produce the radiances measured in each instrument channel. BT's from each ATSR channel can be converted back to the original upwelling radiance using a solution of the Planck function and the channel filter profile (Figure 4-3).

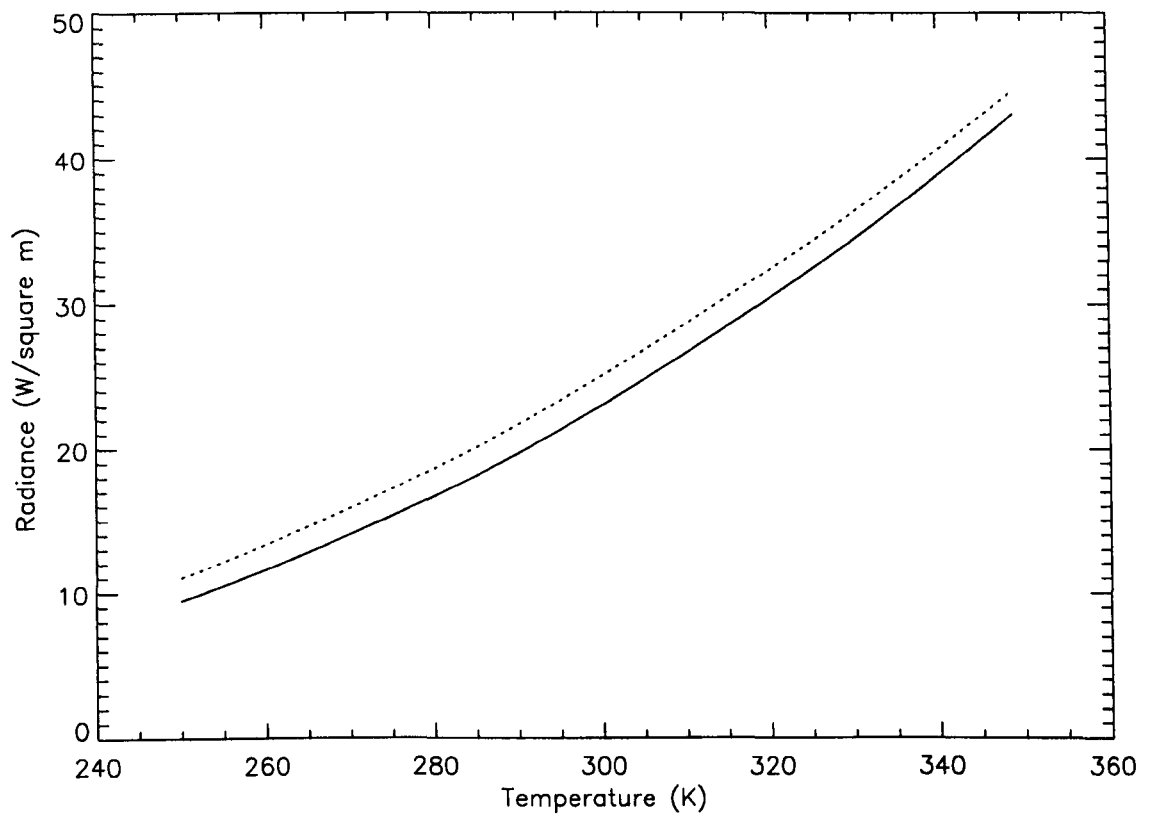


Figure 4-3 Radiance - BT relationship for ATSR1 11 μm (solid line) and 12 μm (dotted line) channels.

The radiance threshold of the thermal-infrared channels restricts the maximum BT retrieved (Table 4-1). These limits were designed for SST retrieval. LST's in hot climates frequently exceed the thresholds and saturate the instrument channels. The ATSR2 thresholds are significantly higher than ATSR1.

| | 11 μm | 12 μm |
|-------|------------------|------------------|
| ATSR1 | 312 | 314 |
| ATSR2 | 322 | 324 |

Table 4-1 Brightness temperature thresholds (K) for ATSR1 and ATSR2 infrared channels.

4.2.2 Terrestrial Infrared Radiometer Dataset

An array of Everest Interscience* infrared radiometers (IRR's) was used to record the radiometric temperature of surface elements during the field campaigns. Measurements were timed to coincide with the overpasses of the ATSR satellite radiometer. Surface radiometric data were collected during field campaigns in October 1995 and May 1996 (see Figure 4-1). Approximately 220 hours of data were recorded on a total of 27 days. These included 2 separate occasions which were coincidental with ATSR satellite overpasses.

The IRR's had a spectral bandpass filter with 100% transmission in the 8-14 μm wavelength region (Everest Interscience*, personal communication). The radiometers had a conical field of view with an apex angle of approximately 15°. Radiometric temperatures recorded using a finite field of view are a combination of emission from a range of angles around the central orientation. However, vertical temperature gradients are often weak in uniform or low canopies and the dominant factor affecting ensemble emission is heterogeneity in surface cover. For typical canopy architectures the leaf area index averages linearly with observation angle, so that the fractional vegetation cover viewed by an optical instrument with a finite field of view is equal to the theoretical value at the central observation angle. Under

* Trade name implies no recommendation or endorsement by the author and is for the benefit of the reader only.

these circumstances, the angular brightness temperature recorded with a broad field of view instrument is approximately equal to that from the central angle alone.

The radiometers contained chopped apertures which allowed the devices to periodically self-calibrate against an internal reference. All IRR's were independently calibrated against a Working Standards WS153 blackbody reference source before and after the field campaigns (see Chapter 4). The radiometric resolution of the IRR's was 0.1°C with a temporal resolution of less than 1 second. The calibrations were performed across a comprehensive range of temperatures and each sensor was accurate to within 0.5°C at room temperature.

4.2.3 Atmospheric Radiosoundings

The principal source of atmospheric data was a set of 60 clear sky radio-soundings recorded at Harare meteorological station (17.9° East, 31.1° South) between 1992 and 1996 (see Figure 4-4). The data represent an even distribution throughout the year over a 4 year period, plus extra dates coincidental with the field campaign. The station was approximately 50 km from the field site, at an altitude of 1453 m, a difference of around 30 m in elevation to the site. The data were supplied by the UK meteorological office. The ascents were performed at approximately 0000 hours UT, 0220 local time.

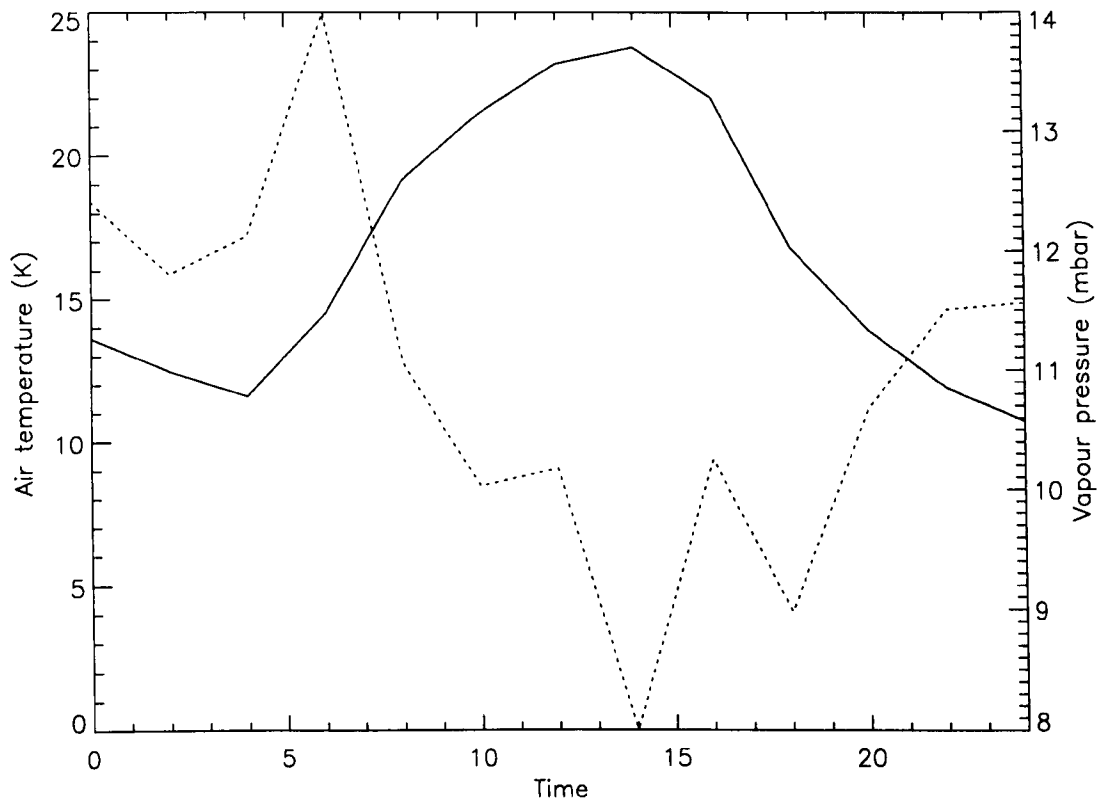


Figure 4-4 Annual variation in surface-level air temperature, vapour pressure and column integrated water content derived from atmospheric radiosoundings.

The annual trend in the atmospheric data was particularly pronounced. Whilst surface level temperature exhibited a relatively smooth annual variation, the atmospheric water vapour resembled a tophat profile throughout the year. At the cusps of the wet and dry seasons there was a substantial transition in the airmass over the region. However, the annual rainfall is extremely erratic, and accurately predicting the transition period is inherently difficult. The surface level air temperature and relative humidity exhibited considerable diurnal variation due to the solar heating (see Figure 4-5).

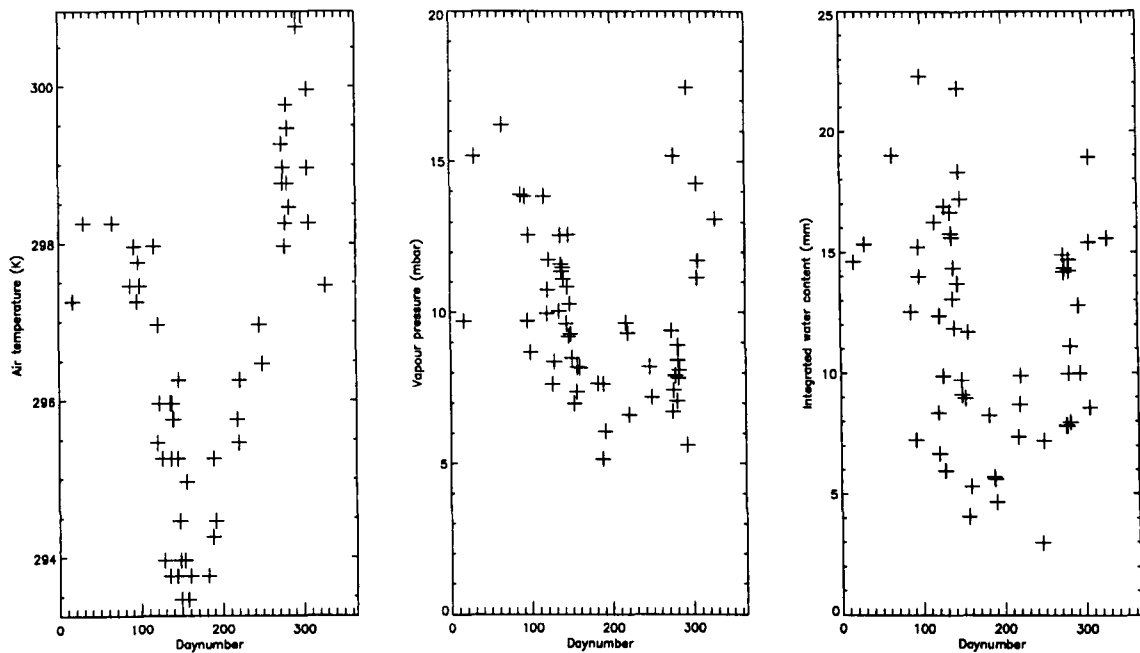


Figure 4-5 Diurnal variation in surface level air temperature (solid line) and relative humidity (dotted line) (after Bell *et al.*, 1987)

Using the equations of Idso (see Chapter 3), the associated variability in atmospheric emission and transmission were estimated from these data. The ATSR satellite overpass time was approximately 1030 local time. To simulate the effects of the diurnal solar heating cycle the temperature and water vapour profiles derived from the midnight GMT radiosoundings were adjusted using a simple one dimensional atmospheric model. Details of the atmospheric heating model can be found in Appendix A.

4.3 Experimental Method

The combined radiative emission from a heterogeneous land surface is related to the architecture of the different surface components. To accurately retrieve LST's over a mixed surface using satellite data it is necessary to delimit the various radiative contributors present at sub-pixel resolution. LST algorithms do not in general accommodate the frequent spatial variability encountered over heterogeneous surfaces. Moreover, when using dual-angle satellite data the effects of viewing geometry are also important when recording emission over certain canopy architectures.

A field experiment was undertaken to determine the effects of surface heterogeneity and canopy architecture at ground level. Directional radiometric surface temperatures were recorded over a variety of natural canopy architectures at roughly opposite ends of the vegetation growth cycle. Approximately two months of data were recorded over the dominant surface cover classifications at two field sites in Zimbabwe. Data were recorded at Chizengenji in the northeast and at Tambuti in the southwest. Figure 4-6 is an ATSR 1.6 μm reflectance image of Zimbabwe and indicates the relative location of the two field sites within the country.

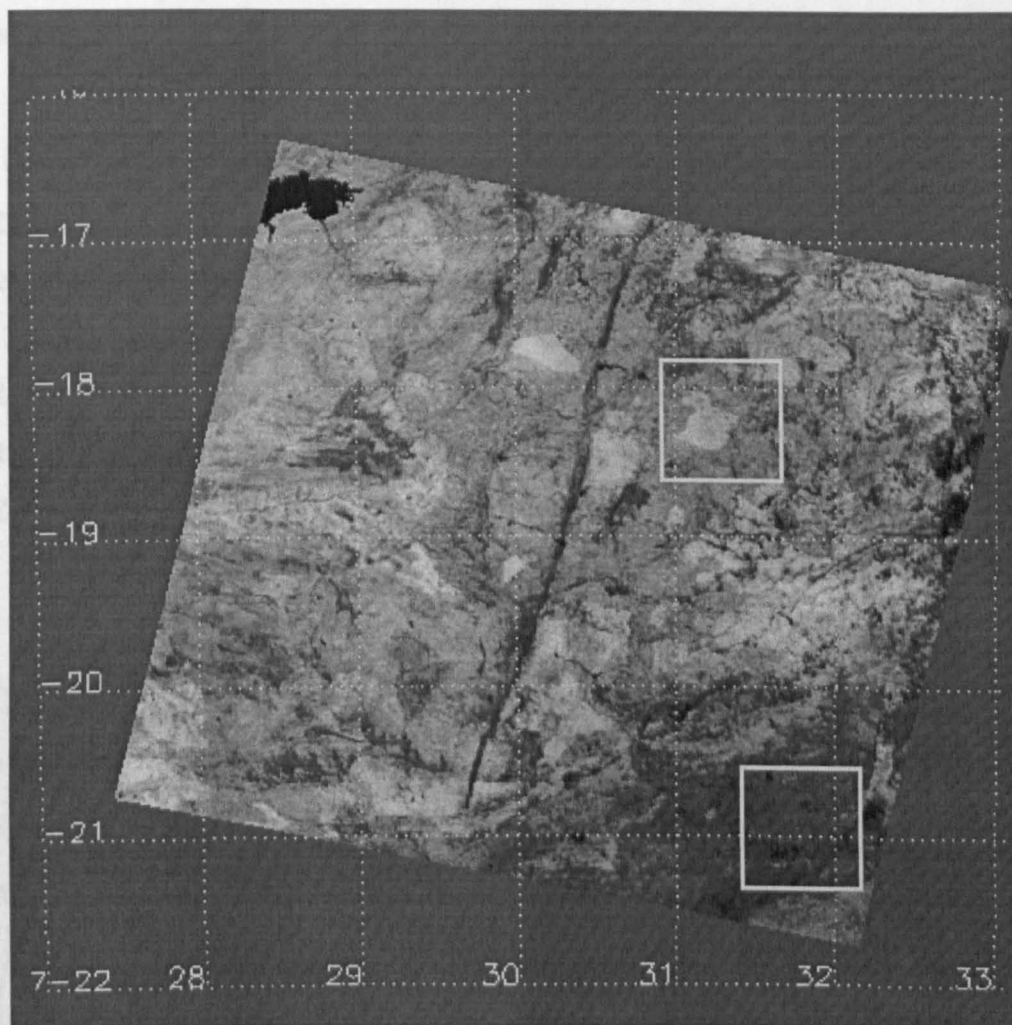


Figure 4-6 Along Track Scanning Radiometer (ATSR) 1.6 μm image of Zimbabwe showing location of the field sites at Chizengeni (north) and Tambuti (south).

Numerous coincidences with ATSR satellite overpasses were obtained. The data were compared with satellite LST estimates, under different parameterisations, to identify the most appropriate LST retrieval method. The two field sites were chosen for their distinctly different canopy architectures and their suitability for surface and satellite radiometry. Both regions were flat and reasonably uniform over substantially large areas, and they were visually identifiable at the 1 km resolution of the ATSR imagery. The two sites are discussed in

more detail in the following sections. The methods employed during the field experiments are also outlined.

4.3.1 Chizengeni

The Chizengeni site lies within the Chiota and Seke rural farmlands in north-eastern Zimbabwe and was characteristically a degraded grassland savannah. The region extended over some 1000 square kilometers (31.4 - 31.6° East, 18.0 - 18.3° South). Figure 4-7 shows an ATSR 1.6 μm image of the region, with the location of the test site indicated. Alongside the ATSR scene is an excerpt from the Zimbabwe land use classification map (Surveyor General, Zimbabwe).

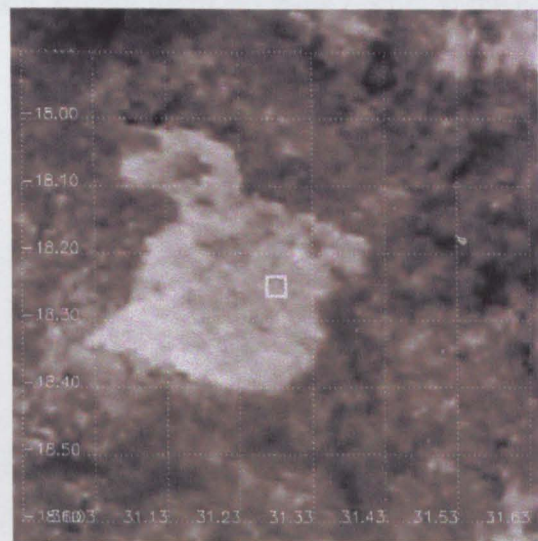
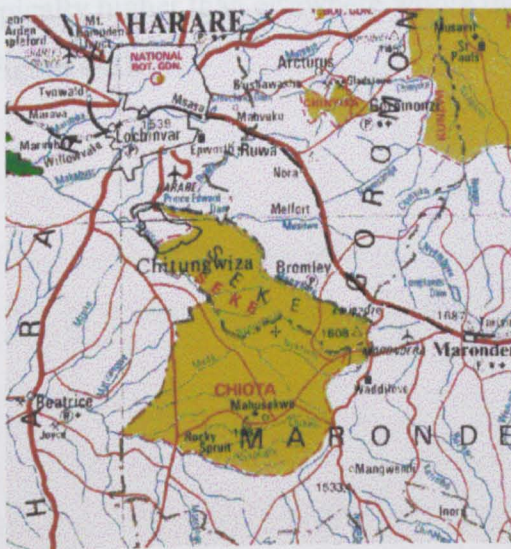


Figure 4-7 Images of the Chiota and Seke communal farmlands from a) Zimbabwe land use classification map and b) ATSR 1.6 μm channel. Highlighted is the location of the test site within the region.

The region is strikingly evident within the ATSR image because of the pronounced difference in surface reflectance, which is largely related to the vegetation cover. The surround-

ing area was commercially owned, and was a mixture of irrigated farmland and indigenous bush, both of which have relatively dense, unstressed canopies.

The region is situated upon a plateau at an altitude of approximately 1500 m and receives annually around 1000 mm of rainfall, which is higher than the national average. The terrain is typically rolling hillsides and the intervening basins are known as dambos. Dambo hydrology is of particular interest because of their apparently increased water capacity. Dambos are nationally protected wetlands in Zimbabwe but their cultivation is widespread through economic necessity. Particular concern has been paid to investigating the hydrology of dambos in recent years (Bullock, 1988 ; Owen *et al.*, 1994). The Chizengeni field site is an example of a dambo, covering an area of approximately 2 - 3 km². A significant feature of dambos is the seepage zone, a narrow band of fertile soil which encircles the basin at an intermediate elevation above its base. The moisture content of seepage zones is typically higher than elsewhere within the basin, except when flooding occurs at the centre (Figure 4-8).

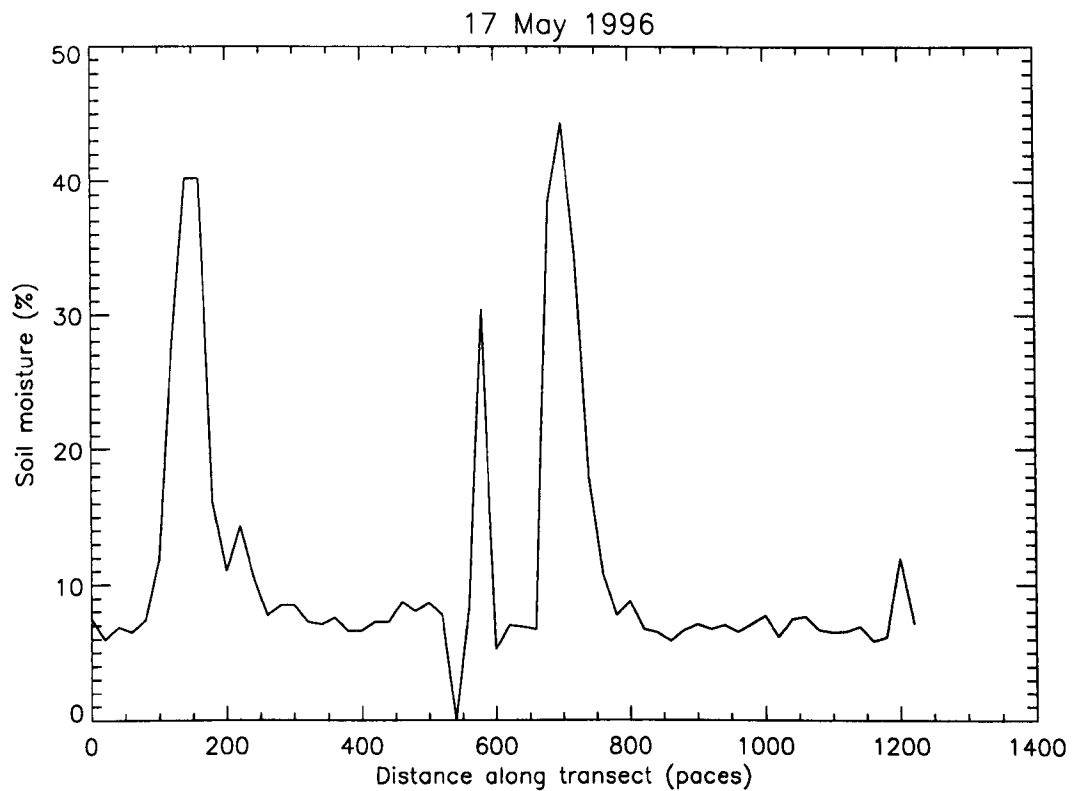


Figure 4-8 Soil moisture transect across Chizengeni dambo on 17/05/1996. (courtesy of K. Blyth, personal communication)

Vegetation growth is promoted within seepage zones as a result of the enhanced soil moisture, and this is clearly visible in aerial photography of the region (Figure 4-9). Whilst the seepage zones are frequently cultivated they represent a minor fraction of the area of the dambo as a whole. The dominant vegetation class in the farmlands is overwhelmingly grazed savannah with a characteristically short and sparse canopy. Approximately 6% of the region is devoted to agriculture, with the remainder used for grazing (Owen *et al.*, 1994).



Figure 4-9 Aerial view of Chizengeni dambo in north-eastern Zimbabwe. The seepage zone can be distinguished as a dark band encircling the basin.

Normal fractional grass cover was estimated to vary from 50% to 66% between the two field campaigns, with an associated increase in the mean canopy height from 0.01 to 0.04 cm (Figure 4-10). The vegetation was suppressed through overgrazing and bears little resemblance to the unrestricted fallow pastures bordering the region, where the canopy was over 2 m in height. The mean length of roughness elements within the canopy was estimated to be 0.02 m.

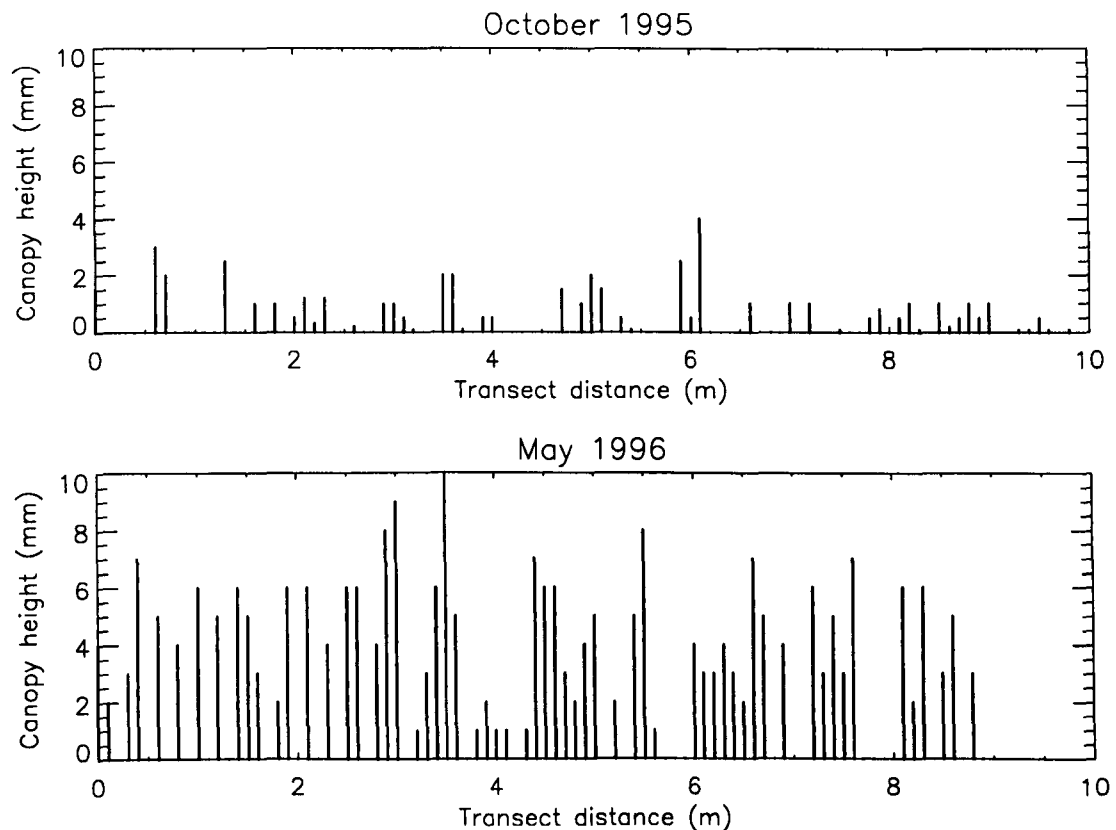


Figure 4-10 Sample transects of canopy architecture on a) 21/10/95 and b) 14/5/96.

The geology within the Chiota and Seke farmlands is predominantly metamorphosed granite rocks with the exception of occasional dykes and a small region of fine grained metavolcanic deposits (andecite and dacite). The presence of quartz within the granite bedrock, typically above 20% by volume (Whitten and Brooks, 1972), will result in highly siliceous soils in the area (M. Lupankwa, personal communication). The soil type is characteristically sandy with a low loam content. Small areas of clay deposits are exposed around the edges of the dambos and, whilst being relatively small in areal extent, have a pronounced effect upon the infiltration rates across the basin.

A digital elevation map of the region illustrates the relatively low variability in altitude across the landscape (Figure 4-11). The mean elevation of the Chiota region was $1470 \text{ m} \pm$

68 m. The terrain slopes gradually North-South with a mean aspect of 30° to North. The mean terrain slope was less than 2 %.

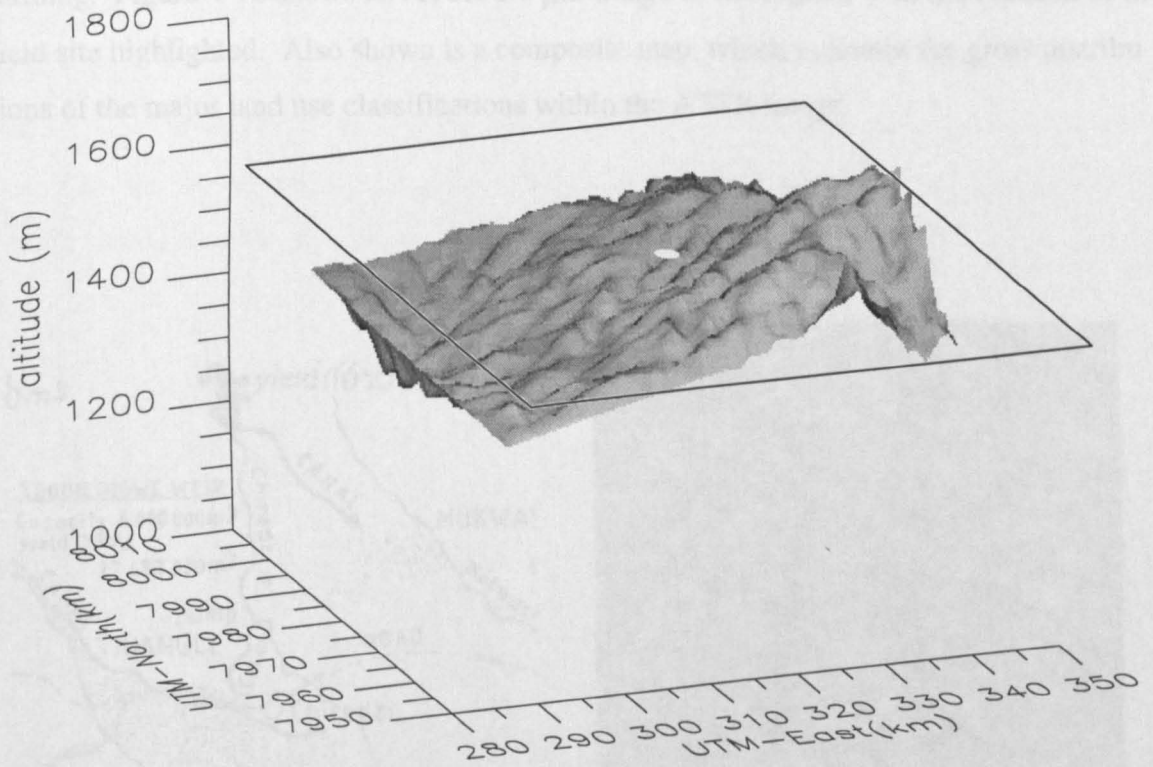


Figure 4-11 Digital elevation map of the Chiota and Seke farmlands in north-eastern Zimbabwe (courtesy M. Lupankwa, personal communication).

4.3.2 Tambuti

The second site was at Tambuti in the south-eastern lowveld of Zimbabwe and was characteristically undisturbed indigenous bush. The wider region is divided in land usage between industrial agriculture, natural woodland and communal areas which support small scale farming. Figure 4-12 shows an ATSR 1.6 μm image of the region, with the location of the field site highlighted. Also shown is a composite map, which indicates the gross distributions of the major land use classifications within the ATSR image.

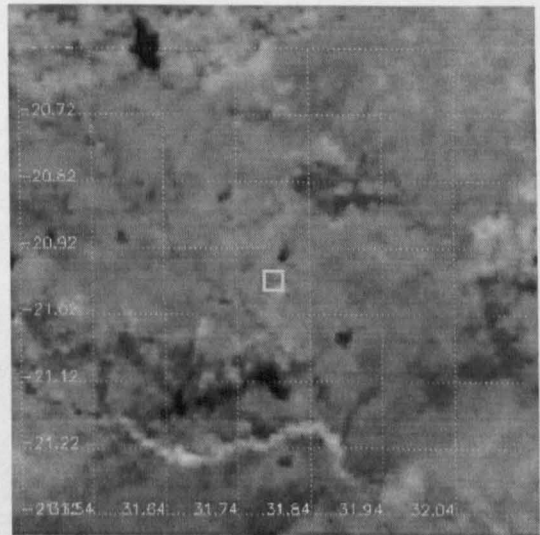
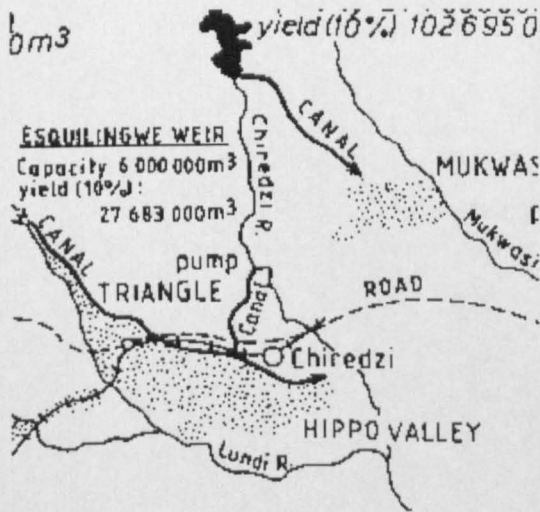


Figure 4-12 Images of the Chiredzi region within the Zimbabwean lowveld showing a) land use classification and b) ATSR 1.6 μm channel. Highlighted are the principal land uses and the location of the Tambuti test site.

The dominant feature within the imagery is the intensively irrigated sugar plantations. Around 300 km^2 of land are cultivated with sugar cane annually, and this dense vegetation has a visibly low reflectance. To the south east of the image, below the Lundi river, are the Matibi communal lands. Similar to Chiota and Seke, the Matibi area is evident as a bright region in the 1.6 μm channel because of the high reflectance. These areas are typically de-

graded woodland and open savannah, but in the south there are no dambo wetlands. The surrounding area is generally open natural forest of variable density. The canopy is predominantly mopane savannah woodland, which is found in hot, dry, lowland areas and frequently grows on cracking clay soils (ODA, 1992). The mopane trees were typically 3 - 5 m in height with a medium density grassy understory. The woodland is preserved principally through private ranches, and in neighbouring inhabited regions it has been substantially depleted. The Tambuti field site is at an altitude of approximately 333 m. Conditions were hot and mean temperatures range between 22 and 30°C, with annual rainfall of less than 500 mm. An aerial photograph showing approximately 25 km² of the ranch (Figure 4-13) illustrates the uniform nature of the woodland canopy.



Figure 4-13 Aerial photograph showing a portion of rangeland adjacent to the Tambuti site. The feature is a canal for irrigation of nearby sugar plantations.

The canal passing through the image is used to divert water to the nearby sugar plantations. It was difficult to assess the density of the canopy at low resolution. A closer view of the region (Figure 4-14) was used to estimate the fractional canopy cover, at the expense of areal representation. From this photograph, taken at approximately the period of maximum

density, the fractional tree cover was estimated to be $17.5 \pm 3.5 \%$. Additionally, there was also the annual variation in foliage density to consider. The understory was predominantly tall grass and was present throughout the year. Very little bare soil was visible above the surface. During the dry season, the canopy was leafless and the understory senesced.



Figure 4-14 High resolution aerial photograph of the Tambuti field site.

The atmospheric radiosoundings were recorded approximately 300 km from the site. Automatic weather station data, including surface level air temperature, dew point temperature and vapour pressure, were recorded approximately 5 km from the site. These data were used in conjunction with an atmospheric heating model to adjust the atmospheric profiles.

4.3.3 Experiment Procedure

Radiometric surface temperatures were recorded over the major canopy and soil components at two field sites during two one month periods. Table 4-2 indicates the locations and dates of field measurements collected during the two campaigns. Also highlighted are coincidences with the ATSR satellite overpasses.

| Date | Location | Satellite |
|------------|------------|-----------|
| 01/10/1995 | Chizengeni | ATSR1 |
| 02/10/1995 | Chizengeni | ATSR2 |
| 03/10/1995 | Chizengeni | |
| 07/10/1995 | Tambuti | |
| 08/10/1995 | Tambuti | |
| 09/10/1995 | Tambuti | |
| 10/10/1995 | Tambuti | |
| 11/10/1995 | Tambuti | ATSR1 |
| 12/10/1995 | Tambuti | ATSR2 |
| 13/10/1995 | Tambuti | |
| 14/10/1995 | Tambuti | |
| 19/10/1995 | Chizengeni | |
| 20/10/1995 | Chizengeni | ATSR1 |
| 21/10/1995 | Chizengeni | ATSR2 |
| 14/05/1996 | Chizengeni | ATSR1 |
| 15/05/1996 | Chizengeni | ATSR2 |
| 16/05/1996 | Chizengeni | |
| 17/05/1996 | Chizengeni | ATSR1 |
| 18/05/1996 | Chizengeni | ATSR2 |
| 19/05/1996 | Chizengeni | |
| 20/05/1996 | Chizengeni | |
| 24/05/1996 | Tambuti | ATSR1 |
| 25/05/1996 | Tambuti | ATSR2 |
| 26/05/1996 | Tambuti | |
| 27/05/1996 | Tambuti | ATSR1 |
| 28/05/1996 | Tambuti | ATSR2 |
| 29/05/1996 | Tambuti | |
| 30/05/1996 | Tambuti | ATSR1 |

Table 4-2 Temporal distribution of *in situ* measurements between the field sites at Chizengeni and Tambuti.

Air temperature was continuously monitored at approximately 1 m above the surface during the experiments on all but two occasions. On exceptional dates the air temperature at the time of satellite overpass was estimated using the local maximum and minimum temperatures and hourly data recorded at a nearby automatic weather station. Surface level vapour pressures were recorded at 0220 am only. These values were extrapolated throughout the day using an atmosphere heating model (see Appendix A).

A Campbell Scientific CR10 datalogger was used to record all field data. Temperatures were sampled at 1 second intervals and recorded as 10 minute averages with their temporal standard deviation. Radiometric temperatures were collected using an array of infrared radiometers suspended from tripods of variable height. The elevation of the radiometers was adjusted to ensure that the footprint of the instrument field of view upon each target was approximately equal in all experiments. Zenithally inclined radiometers were azimuthally aligned with the ERS sub-satellite track to simulate the viewing geometry of the ATSR. Field experiments were particular to each site because of the differences in canopy architecture. The details of field experiments at Chizengeni and Tambuti are discussed below.

Chizengeni

The site was dominated by a uniform surface cover of open deforested savannah, with sporadic clusters of 1-2m high shrubs. Radiometers were configured on all occasions to record both the nadir (zenithal) and the forward (55° to zenith) temperature of the sparse grass and shrubs (subject to instrument availability) simultaneously (Figure 4-15).

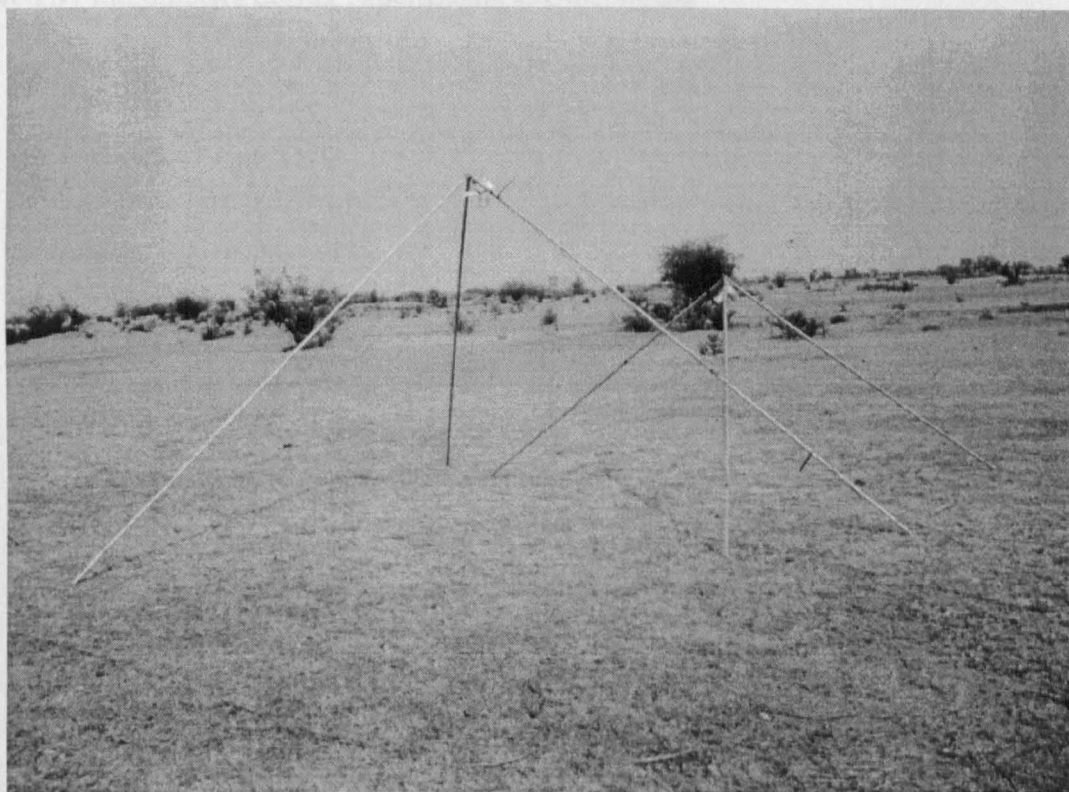


Figure 4-15 Typical assembly of infra-red radiometers viewing the same area at multiple zenith angles during the field experiments at Chizengeni.

Targeting errors were minimised by using a number of radiometers at the principle nadir and forward viewing angles. This duplicity of instrumentation increased the effective target area and indicated the spatial variability in LST. On numerous occasions the range of viewing angles was increased to investigate the angular variation in radiometric surface

temperature of the sparse grass. Measurements were made at 0, 30, 55 and 70 degree zenith angles when instruments were available. The target area was large relative to the mean area of surface roughness elements and roughly equal at all viewing angles (Table 4-3).

| Observation angle (°) | Height (m) | Target area (m ²) |
|-----------------------|------------|-------------------------------|
| 0 | 2.5 | 0.34 |
| 30 | 2.5 | 0.46 |
| 55 | 1.75 | 0.53 |
| 70 | 1 | 0.54 |

Table 4-3 Relationship between observation angles, instrument height and target areas viewed by radiometers during experiments at Chizengeni.

4.4 Emissivity Prescription

Tambuti

The site was an irregular mixture of 3 – 5 m high trees and tall grass understory (Figure 4-16). Attempts were made to investigate the spatial, temporal and angular variation in radiometric temperature of each surface component.



Figure 4-16 Typical assembly of infra-red radiometers viewing the major surface components during the field experiments at Tambuti.

The principal components of the woodland surface were grass and trees, although measurements were made over shrubs and bare soil also. Due to instrumental limitations it was not possible to perform all angular measurements on each occasion. The tree canopy at Tambuti was of variable density, and the understory was often partially visible within the radiometric field of view. Radiometric measurements over the trees were frequently a mixture of contributions from both the foliage and understory.

4.4 Emissivity Prescription

The radiative land surface temperature can be calculated using the brightness temperature and the atmospheric emittance and transmittance if the surface emissivity and reflectivity are known. Salisbury *et al.* (1994) compared directional hemispherical reflectance and emittance measurements of rock and soil samples with induced thermal gradients to determine the extent to which directional emissivity was the complement of directional reflectivity. No detectable deviation was observed on the natural samples, and it was concluded that both emissivity and reflectivity measurements can be used to calculate sample emissivity for most terrestrial surface materials.

In the absence of *in situ* measurements, emissivity values were estimated from the literature, where data exists for a variety of natural surfaces. Table 4-4 shows a selection of the broadband infrared (8-14 μm) emissivities determined by various authors.

| Surface Type | Emissivity | s | Author |
|----------------------------|------------|-------|------------------------------|
| Grasses | | | |
| Very short grass | 0.979 | - | Labeled & Stoll |
| Tufts of grass (~cm) | 0.981 | - | Labeled & Stoll |
| Grassland (~15cm) | 0.983 | - | Labeled & Stoll |
| Tall sudan grass | 0.976 | - | Fuchs & Tanner |
| Open grass(complete) | 0.958 | 0.006 | Van der Griend <i>et al.</i> |
| Tall grass(complete) | 0.958 | 0.003 | Van der Griend <i>et al.</i> |
| Mixed canopies | | | |
| Partly closed canopy | 0.976 | 0.015 | Fuchs & Tanner |
| Soil / vegetation mixture | 0.981 | 0.004 | Humes <i>et al.</i> |
| Open grass (partial) | 0.949 | 0.008 | Van der Griend <i>et al.</i> |
| Grass (partial) | 0.956 | 0.013 | Van der Griend <i>et al.</i> |
| Shrub (partial) | 0.976 | 0.008 | Van der Griend <i>et al.</i> |
| Tall vegetation | | | |
| Closed canopy | 0.980 | 0.007 | Fuchs & Tanner |
| Green foliage | 0.97* | - | Salisbury & d'Aria |
| Rushes (~100cm) | 0.994 | - | Labeled & Stoll |
| Shrubs | 0.97 | 0.005 | Hipps |
| Shrub (complete) | 0.986 | 0.006 | Van der Griend <i>et al.</i> |
| Shrubs & clumpy vegetation | 0.994 | 0.007 | Humes <i>et al.</i> |
| Soils | | | |
| Soil / rocks | 0.959 | 0.010 | Humes <i>et al.</i> |
| Lehm (fine/loamy) | 0.973* | 0.019 | Labeled & Stoll |
| Loess (coarse/loamy) | 0.961* | 0.030 | Labeled & Stoll |
| Sio2 | 0.915* | 0.073 | Labeled & Stoll |
| Soil (sandy) | 0.93 | 0.002 | Hipps |
| Soil (loamy sand) | 0.914 | 0.011 | Van der Griend <i>et al.</i> |
| Soil (sandy) | 0.93* | - | Salisbury & d'Aria |
| Soil (clay) | 0.96* | - | Salisbury & d'Aria |
| Crops | | | |
| Alfalfa | 0.977 | - | Fuchs & Tanner |
| Wheat | 0.959 | 0.005 | Huband & Monteith |
| Other surfaces | | | |
| Bark | 0.96* | - | Salisbury & d'Aria |
| Soil litter | 0.98* | - | Salisbury & d'Aria |
| Leaves (min) | 0.938 | - | Idso <i>et al.</i> |
| Leaves (max) | 0.995 | - | Idso <i>et al.</i> |
| Senescent foliage | 0.95* | - | Salisbury & d'Aria |
| Senesced crop | 0.983 | 0.012 | Fuchs & Tanner |

Table 4-4 Broadband infrared emissivity of natural surfaces in the 8-14 μm wavelength region. Values denoted with an asterisk are estimated from authors data.

The collected emissivity data has been grouped categorically. Whilst there is considerable variability within certain groups, such as soils and mixed canopies, similarities are apparent for grasses and tall vegetation. The mean value for short grasses and tall vegetation are

0.9725 ± 0.011 and 0.982 ± 0.011 respectively. Emissivities of dissimilar soils are particularly variable, in line with expectations. Sandy soils have typically low emissivities, as does SiO₂, and loamy soils have substantially higher emissivities, closer to vegetation. The mean emissivity of a sandy soil is 0.922 ± 0.009. The clay rich soil of Salisbury and D'Aria is an example of a vertisol. Vertisols contain typically 30-80% clay which dominates their reflectance spectra. The sample is significantly more reflective at lower wavelengths, with a mean emissivity of approximately 0.93 between 8-10 µm and a substantially higher emissivity of around 0.97 at 10-14 µm. This is a result of the high quartz content of such soils. Table 4-5 summarises the surface emissivity estimates used in this study. Fuchs and Tanner determined a closed crop canopy to have an emissivity of 0.98, and when senescent it was 0.983. Salisbury and D'Aria, however, measured live vegetation to have emissivities that were regularly higher than the senesced plant. According their analysis, during senescence the reflectance of vegetation (broadleaved and grasses) decreases because of the loss of the waxy cuticle from the surface. Ultimately, the spectra of senescent vegetation will converge on that of cellulose. It is possible that a small (less than 2%) reduction in emissivity occurs during senescence.

| Surface type | Emissivity | s |
|----------------------|------------|------|
| Short grass | 0.97 | 0.01 |
| Tall vegetation | 0.98 | 0.01 |
| Senescent vegetation | 0.95 | 0.01 |
| Sandy soil | 0.92 | 0.01 |
| Clay soil | 0.96 | 0.01 |

Table 4-5 Summary of broadband infrared emissivity estimates for the major surfaces present within the Chizengeni and Tambuti field sites.

The ensemble emissivity of a heterogeneous land surface is dependent upon the spatial distribution of the individual components. Infrared emissivities aggregate linearly (Lhomme *et al.*, 1994, Chebhouni *et al.*, 1995) so that the mean emissivity of a mixed surface is a simple average of the component values, weighted by their respective fractional cover. Assuming the mean values for vegetation and soil emissivities in Table 4-5, the ensemble emissivity of

the sparse grass at Chizengeni can be estimated using the *in situ* measurements of fractional grass cover. The ensemble emissivity may exhibit angular variability because of any intrinsic directional emissivity of the vegetation or soil. The angular variation of infrared emissivity has been investigated for a number of soil types (Labed and Stoll, 1991, Nerry *et al.*, 1988) characterised by composition and granularity. Emissivities were found to decrease with increasing zenith angle, and the largest effects were apparent for agricultural soils, with high biomass contents. However, it was found that fine soils exhibit less than a 1% reduction in emissivity below 60°.

The fractional occupancy of surface components over a three dimensional heterogeneous canopy will be dependent upon the viewing angle, which may also contribute to any angular behaviour in the compound emissivity. By assuming some parameterisation for the canopy architecture, the ensemble emissivity can be estimated as a function of zenithal angle and nadir fractional vegetation cover.

4.5 Satellite Data Processing

The satellite data used in this study were derived from the ATSR instruments on the ERS satellites. The data were provided by the Rutherford Appleton Laboratory. A sequence of approximately 100 daytime ATSR images were available for the study. The data were processed to eliminate cloud contamination and to correct for geometric mal-registration.

Cloud detection algorithms were used to reject contaminated data. Threshold levels were set for the maximum surface reflectance, minimum expected surface temperatures and the range of temperature differences between the thermal infrared channels (see Saunders and Kriebel, 1987). Gross cloud detection was performed manually for sequences of 50 km² images around the test sites to establish a training dataset from which local threshold levels for the ATSR infrared and reflectance channels could be obtained. Thermodynamic thresholds were propagated through the RAL radiative transfer model, using the *in situ* atmospheric radiosounding dataset to obtain brightness temperature thresholds. The surface temperature thresholds were set conservatively using climatological air temperature data as a minimum value. Local air temperature was found to be higher than the minimum LST within the cloud free training imagery on all occasions. Maximum and minimum brightness

temperature differences between the ATSR 11 μm and 12 μm channels (thin cirrus test) were calculated using the atmospheric dataset for a comprehensive range of possible surface compositions.

Co-registration of the ATSR nadir and forward views was of particular importance over the elevated terrain at the Chizengeni site. The region lies on a plateau at an altitude of approximately 1500 m. The ATSR imagery was co-registered relative to the geoid. Figure 4-17 is a schematic diagram of the potential mis-registration that can occur under such circumstances.

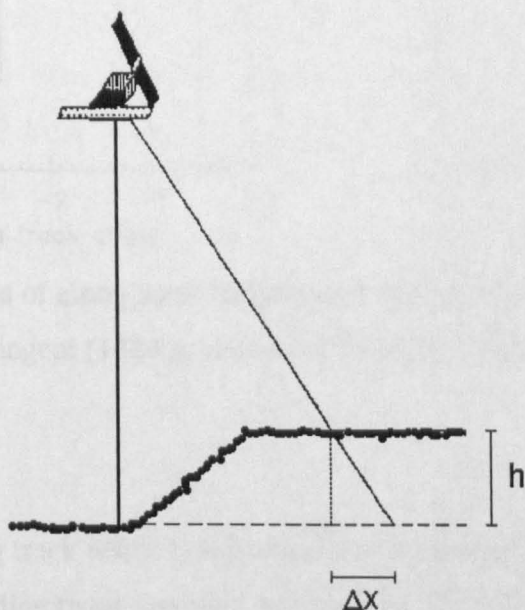


Figure 4-17 Schematic diagram of ATSR nadir and forward viewing geometry over elevated terrain. The mal-registration in the forward view (dx) is a function of elevation (h) and observation angle.

Analysis of the ATSR imagery revealed that the effects of high altitude do impact upon the registration between the nadir and forward views. A cross correlation is performed between the two images and the offsets are calculated to typically less than 1 pixel in precision. Histograms of the along track offsets (Figure 4-18) shows that the mis-registration between nadir and forward views is related to altitude.

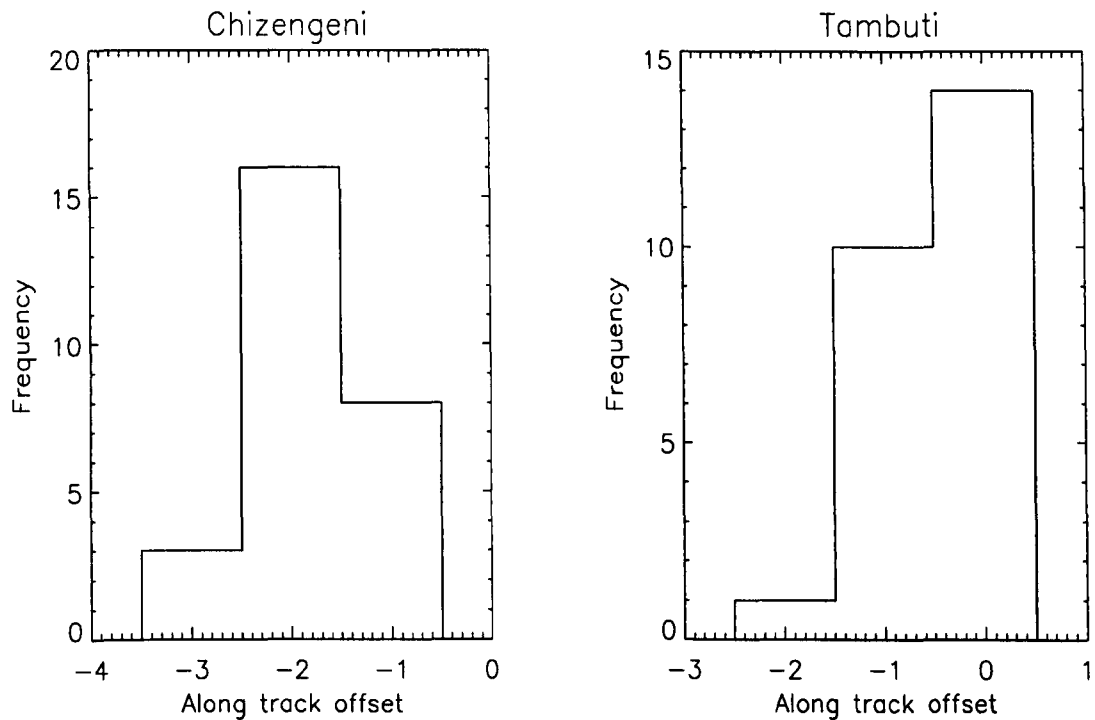


Figure 4-18 Histograms of along track and across track offsets between the ATSR nadir and forward views at Chizengeni (1484 m above sea level) and Tambuti (333 m above sea level).

The mean ATSR along track offset between nadir and forward views at Chizengeni was 1.87 pixels, corresponding to an elevation of approximately $1309 \text{ m} \pm 407 \text{ m}$. The predicted elevation at Tambuti was $320 \text{ m} \pm 392 \text{ m}$. The Chizengeni and Tambuti sites were 1484 m and 333 m above sea level respectively. Co-registering nadir and forward views using a simple correlation intensity is a crude method of estimating the surface elevation from dual angle satellite imagery. No systematic relationship was found between the across track view offsets. This was in line with expectations since the maximum zenith angle across track is approximately 21° , which would be less than 10 % sensitive to elevations above the geoid.

Co-location, or navigation of sequential images was performed in a similar manner. The cross correlation between sequential images was systematically high (typically greater than 85 %). The mean signal to noise ratio for sequential and dual angle ATSR image intensity

correlations corresponded to a registration accuracy of better than 1.25 pixels. The mean along track and across track sequential offsets in all instances was close to zero. Offsets were typically in the range ± 0 to 3 pixels over a 50 km² region.

No relationship was found between across track position and across track sequential offsets during co-registration and co-location. Similarly, there was no consistent relationship between any of the offset parameters.

4.6 Land Surface Temperature Retrieval

The ATSR data were corrected for atmospheric effects using *in situ* radiosoundings and a numerical atmospheric model (see Chapter 3). Estimates of the compound surface emissivity were made using tabulated data and rough canopy architectures. Land surface temperatures were then derived using the radiative transfer equation (see Chapter 2). A dual-angle LST algorithm was also applied to the raw satellite data. The coefficients of the algorithm were largely independent of the atmospheric state, and could be used in the absence of *in situ* atmospheric sounding data. Using the two methods, LST's were derived at the ATSR satellite resolution (1 km²) over the uniform open grassland of the Chizengeni region and the mixed canopy mopane woodland at Tambuti.

The terrestrial radiometric data were corrected for the effects of atmospheric emission using the empirical equations of Idso (see chapter 3). These equations were derived for the spectral domain of the radiometers. Using the appropriate emissivity from tabulated data, the radiative temperature of individual surface components was determined at the time of satellite overpass. The angular variation of the surface emission over the Chizengeni sparse grassland was also investigated. A linear mixture model was used to aggregate the surface emission from the heterogeneous woodland canopy at Tambuti.

Chapter 5

Results

This chapter describes the principal results obtained from the study. It will begin by discussing the potential sources of error in the radiative transfer calculations, and their impact upon land surface temperature (LST) estimates. The final results are then outlined in detail. The diurnal and annual behaviour of the atmosphere was analysed using *in situ* meteorological data. Infrared atmospheric transmittance and emittance were estimated using both empirical and numerical techniques. LST's were then derived from both *in situ* and satellite radiative temperatures using the atmospheric correction parameters.

5.1 Error analysis

The LST was derived using both satellite and terrestrial radiometric measurements, and the principal sources of uncertainty are similar for each technique. Satellite derived LST's generally have much larger errors than *in situ* measurements, but the satellite errors are comparable in magnitude to the spatial variability in temperature observed over many natural surfaces. In the first instance it is important to consider the sensor measurement errors, which include both the instrument radiometric accuracy and the surface targeting error. The uncertainty of LST's derived from radiative transfer models can then, in principle, be divided between atmospheric and surface effects. When the surface emissivity is high and well prescribed, as is the case for the sea, temperature retrieval algorithms perform well. LST algorithms are far less precise, because of the heterogeneity in surface cover and the major uncertainties in the emissive properties.

The cumulative effects of the LST measurement and derivation errors were calculated using a mutually exclusive error model. Uncertainties in all parameters were propagated through the radiative transfer calculations and the standard deviation of derived parameters was determined. Errors in parallel variables were assumed to be independent of one another, so that the predicted errors represent the maximum likelihood error, not the absolute maxi-

num. The sources of error in each stage of the LST calculations are discussed in detail below.

5.1.1 Errors in the satellite data

The ATSR satellite radiometer has been demonstrated to meet the pre-launch accuracy goal which required a 3σ uncertainty in brightness temperature less than 0.1°C (Mason *et al.*, 1996). The geolocation accuracy of individual ATSR image pixels was investigated using the clear-sky dataset, which was delimited from the complete image sequence with the aid of semi-empirical cloud detection algorithms. Both dual-angle and multi-temporal ATSR scenes were co-registered to better than 1.25 pixel accuracy. The mean geolocation error for individual locations was 0.33 pixels, and the radiometric error was calculated from the standard deviation of brightness temperatures recorded within the geolocation limits.

5.1.2 Errors in the terrestrial data

The ground-based infrared radiometers were calibrated under controlled laboratory conditions before and after each field campaign. Investigations have shown that the internal chopped reference source improves radiometric stability ($\text{NE}\delta\text{T} = 0.05^{\circ}\text{C}$), and when exposed to unrealistically large external temperature gradients the instruments performance was not significantly altered. Absolute radiometric accuracy was observed to deteriorate with age, and laboratory calibrations were required to ensure the radiometric temperature error of each device was less than 0.5°C , the manufacturers specifications. The instrument field of view (i.e. the full width at half-maximum intensity) was measured to be $15.2^{\circ} \pm 0.1^{\circ}$, and nearly 95 % of incoming radiation was recorded within this range. Surface temperatures were sampled at 1 second intervals and recorded as 10 minute averages. The radiometric temperature error was determined as a linear combination of the instrument calibration accuracy and the standard deviation of temperatures recorded across the 10 minute interval. The experimental configuration was designed in all instances to ensure that the observed target was adequately sampled, and the roughness lengths of surface elements was either larger than or significantly smaller than the radiometer footprint. On occasions where

multiple instruments recorded the same target the algebraic average of temperatures and standard deviations was used.

5.1.3 Errors in the surface emissivity prescription

Surface emissivity data was collated from the literature, and mean values were estimated for the vegetation and soil classifications present within the field study area. The dominant vegetation class in the Chizengeni region was overwhelmingly grazed savannah, with close to 95 % of the surface covered by a short, sparse grass canopy. The nadir fractional cover of the grass was observed to vary between 50 % and 66 % between the field campaigns, and the soil type was classified as silica rich. At the Tambuti site the vegetation classification was open forest, with a rough grass understory and a clay rich soil. The fractional woodland canopy cover was estimated to be 17.5 % at maximum density, and during periods of senescence the tree canopy was leafless. The standard deviation of component emissivity estimates was less than 1 % in all instances, and the surface reflectivity was assumed to be the complement of the emissivity value. The angular variation of emissivity has been observed to vary by typically less than 1 % below 60° for soil samples, and this effect was neglected for single component surfaces. The Chizengeni and Tambuti field sites were homogeneous at the satellite resolution but significantly heterogeneous at sub-pixel scales, and the ensemble emissivities were calculated as linear mixtures of the individual component values. For this purpose the fractional component cover was estimated using the ATSR 1.6 μm near infrared channel variation throughout the year as a baseline for component trends. The mean error of the ensemble surface emissivity was 1.34 %.

5.1.4 Errors in the atmospheric correction

Terrestrial and satellite retrieved radiometric surface temperatures were corrected for the effects of the earth's atmosphere by solving the radiative transfer equation in the infrared wavelength region. Estimates of the atmospheric transmittance and emittance were obtained using (broadband) empirical equations and a (multi-spectral) numerical radiative transfer model. Both methods related the emittance and transmittance to tropospheric temperature and humidity, which were derived from synoptic atmospheric radiosoundings. For

non-stormy atmospheres, radiosonde ascents are spatially representative at scales of up to 100 km, and the instantaneous accuracy of the satellite atmospheric correction derived from an individual profile is around 1°C. The temperature and humidity profiles were interpolated to sub-synoptic timescales using a one-dimensional atmospheric heating model based upon the diurnal variation in surface level air temperature. The errors in the atmospheric profile data recorded by radiosonde ascents did not significantly affect the transmittance and emittance spectra derived from the radiative transfer model. The standard error of predictions using the empirical formulations was between 3 and 5%. At infrared wavelengths the atmospheric transmittance and emittance exhibit roughly linear spectral variation, and the broadband average can be substituted for the multi-spectral values in the radiative transfer equation. Neglecting the dependence of the broadband atmospheric transmittance upon the surface temperature introduces an error of less than 1% between -20 and 80°C. The broadband transmittance can be related to the surface temperature using a simple linear correction derived from multi-spectral values. The atmospheric emittance and transmittance were calculated using a temporally extensive radiosounding dataset of over 60 profiles, and the data were interpolated to derive estimates at intermediate timescales. The mean prediction error associated with the temporal interpolation of the atmospheric data was 13.6 %.

5.1.5 Errors in the radiative transfer calculations

The radiative transfer equation was solved numerically at a spectral resolution of approximately 0.5 nm for the ATSR 11 μm and 12 μm channels and across the 8-14 μm wavelength region sensed by the terrestrial infrared radiometers. The multi-spectral nature of the individual radiative transfer components were represented by monochromatic values for each spectral channel which were integrated across the relevant wavelength region. In general this is a good approximation over a modest temperature range (0-50°C) at infrared wavelengths. Empirically derived corrections were applied to individual solutions to account for second order departures from this approximation. Differential radiometry was used to derive land surface temperature retrieval algorithms using the ATSR nadir and forward infrared channels. The individual coefficients in each retrieval algorithm were related to the principal terms of the radiative transfer equation. In the difference equations the Planck function was represented as a first order Taylor series expansion with respect to, separately,

temperature and wavelength. For small deviations about the central temperature or wavelength this is a reliable approximation, which typically introduces errors of less than 2 % into the retrieval coefficients. The radiative transfer solution is also affected by the conditions at the surface, and the magnitude of the reflected atmospheric emittance is dependent upon the surface reflectivity. Uncertainties in the surface emissivity prescription, which was approximated to be the complement of the reflectivity, were also included in the radiative transfer calculations.

5.2 Infrared atmospheric correction parameters derived for Zimbabwe

The atmospheric transmittance and emittance were required to correct remotely sensed infrared surface radiances for atmospheric effects. They can be estimated using either empirical or numerical techniques. Both methods relate the emission and transmission to atmospheric temperature and water vapour content, and the details of each approach have been discussed (see Chapter 3).

Infrared atmospheric correction parameters were derived using meteorological data and clear sky radiosoundings collected at Harare, Zimbabwe. An adiabatic heating model was used to temporally extrapolate the atmospheric sounding data. The parameters derived are location specific and can be used to correct infrared surface radiances recorded within the same region.

Results are presented for the 10.5-12.5 μm wavelength region. Estimates of the atmospheric emittance and transmittance were generated for other portions of the electromagnetic spectrum, including the ATSR 11 μm and 12 μm channels and the 8-14 μm region sensed by Everest infrared radiometers. A direct comparison between the numerical and empirical techniques is also presented.

5.2.1 The relationship between multi-spectral and monochromatic atmospheric transmittance

Empirical estimates of atmospheric transmittance, such as the values predicted by the equations of Idso (see Chapter 3), are spectrally averaged over particular wavelength bands.

These monochromatic parameters can be misleading, since the degree of attenuation through the atmosphere is also dependent upon the spectra of the surface emission. Energy from a source radiating at a single wavelength could be completely absorbed whilst the broadband transmission remains non-zero. At infrared wavelengths however, atmospheric absorption is reasonably uniform and mean values for transmission are frequently used.

To illustrate the sensitivity of monochromatic parameterisations, a comparison can be made between the expected $\langle \tau \rangle_i$ and mean $\tau(T)_i$ values of atmospheric transmittance, where

$$\langle \tau \rangle_i = \frac{\int_i \tau(\nu) \Phi_i(\nu) d\nu}{\int_i \Phi_i(\nu) d\nu} \quad (5.1)$$

$$\tau(T)_i = \frac{\int_i \tau(\nu) B(\nu, T) \Phi_i(\nu) d\nu}{\int_i B(\nu, T) \Phi_i(\nu) d\nu}$$

and

$$\tau(T)_i = a(T) \langle \tau \rangle_i + b(T) \quad (5.2)$$

The mean value of atmospheric transmittance is a function of the surface emission $B(\nu, T)$ and the instrument filter response $\Phi_i(\nu)$. Both transmission parameterisations were generated from spectra calculated with the RAL radiative transfer model using atmospheric soundings recorded at Harare. The mean value was estimated for a range of surface radiative temperatures, and was strongly correlated with the expected value (Figure 5-1).

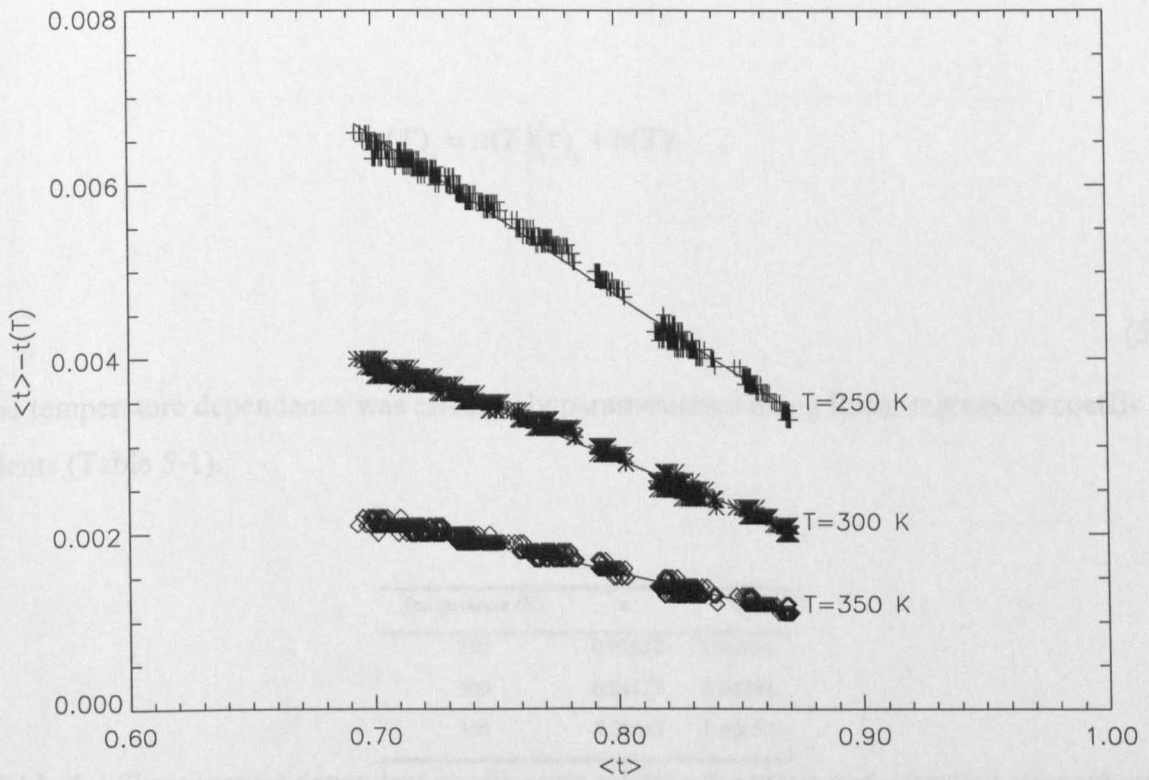


Table 5-1: Temperature dependent atmospheric transmittance and expected atmospheric transmittance in the 10.5-12.5 μm wavelength region.

The monochromatic atmospheric transmittance in an 8-12 μm wavelength region was related to the surface radiative temperature and was

Figure 5-1 Scatter plot of the difference between mean and expected atmospheric transmittance against the expected atmospheric transmittance for surfaces radiating in the 10.5-12.5 μm wavelength region.

(see Figure 5-2). The transmittance was found to be weakly dependent on temperature with a weak dependence upon air pressure.

The monochromatic atmospheric transmittance was related to the radiative temperature of the surface, but on all occasions the difference $\langle \tau \rangle_i - \tau(T)_i$ was less than 0.5 %. The temperature dependence of the monochromatic transmittance was weak, and there was good overall agreement between the two parameterisations. For high values of transmission, the agreement was more pronounced.

Using a linear parameterisation of the form

$$\tau(T)_i = a(T)\langle\tau\rangle_i + b(T)$$

(5.3)

the temperature dependence was effectively parameterised using linear regression coefficients (Table 5-1).

| Temperature (K) | a | B |
|-----------------|----------|---------|
| 250 | -0.01852 | 0.01954 |
| 300 | -0.01127 | 0.01187 |
| 350 | -0.00623 | 0.00654 |

Table 5-1 Temperature dependent coefficients relating the mean and expected atmospheric transmittance in the 10.5-12.5 μm wavelength region.

The monochromatic atmospheric transmittance in the 8-14 μm wavelength region has been related to the surface level temperature and water vapour pressure by Idso. No similar relationship was presented for the 10.5-12.5 μm wavelength region. The atmospheric transmittance in the 10.5-12.5 μm region calculated using the RAL radiative transfer model was correlated with linear combinations of the surface level vapour pressure and air temperature (see Figure 5-2). The transmittance was found to be strongly related to vapour pressure with a weak dependence upon air temperature.

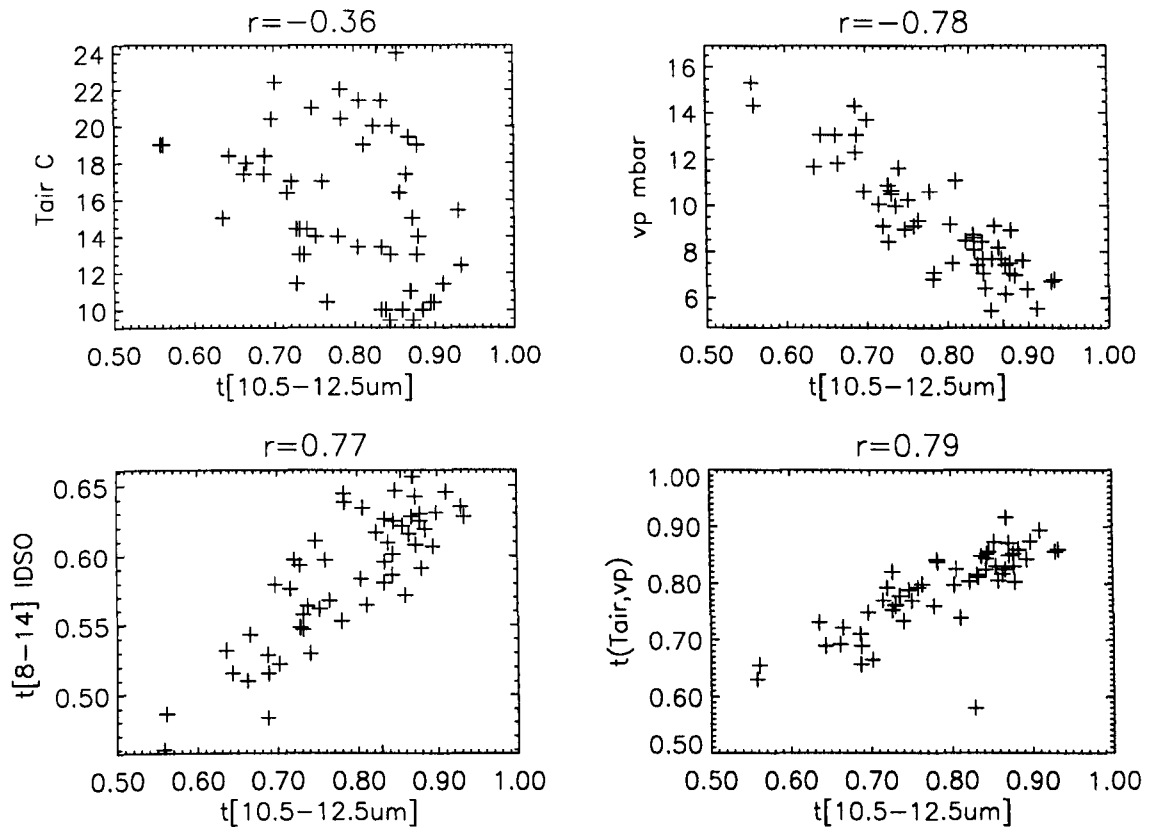


Figure 5-2 Scatter plots of atmospheric transmittance within the 10.5-12.5 μm wavelength region against (a) surface level air temperature (b) surface level vapour pressure (c) the empirical parameterisation of Idso for the transmittance within the 8-14 μm wavelength region and (d) a linear combination of surface air temperature and vapour pressure.

There was no significant difference between the correlation coefficients obtained using multiple regression and linear regression against either temperature or the 8-14 μm transmittance relationship of Idso. An empirical parameterisation of the form

$$\tau_{10.5-12.5} = aT_0 + be_0 + c \tag{5.4}$$

was used to describe the relationship between atmospheric transmittance in the 10.5-12.5 μm wavelength region and the surface level air temperature and vapour pressure. The coefficients a,b and c were determined using linear multiple regression of monochromatic transmittances from the RAL radiative transfer model against the surface level data from the atmospheric radiosoundings. Similar coefficients were determined for the ATSR 11 μm and 12 μm channels (Table 5-2).

| Wavelength | a | b | c | r | Mad |
|-------------------------|-----------|----------|--------|------|------|
| 10.5-12.5 μm | -0.001832 | -0.02549 | 1.5564 | 0.79 | 0.03 |
| ATSR 11 μm | -0.002156 | -0.02904 | 1.6454 | 0.79 | 0.03 |
| ATSR 12 μm | -0.001456 | -0.02157 | 1.4540 | 0.79 | 0.02 |

Table 5-2 Coefficients relating infrared atmospheric transmittance to surface level air temperature and vapour pressure determined using multiple regression.

5.2.2 Diurnal variability of the atmosphere

The diurnal behaviour of the atmosphere was difficult to parameterise because of the strong variability at sub-synoptic time-scales. Surface level air temperature and relative humidity were recorded at Chizengeni on 13/09/1986 (see Figure 5-5). Empirical parameterisations relate the total atmospheric emittance and transmittance to surface level values (see Chapter 3). The diurnal variability of temperature and humidity were related to the degree of solar heating. Using the equations of Idso, the associated variability in atmospheric emittance and transmittance was estimated (Figure 5-3).

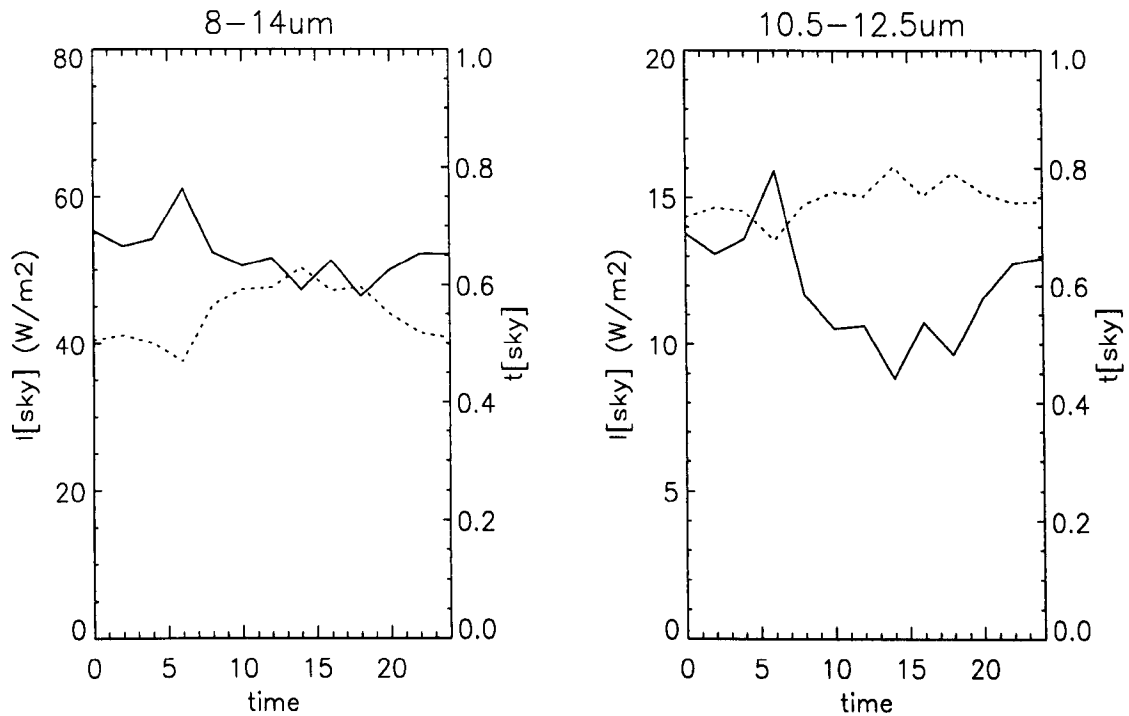


Figure 5-3 Diurnal variation in atmospheric emittance (solid line) and transmittance (dotted line) within the (a) 8-14 μm and (b) 10.5-12.5 μm wavelength regions on 13/09/1986.

The trends in relative humidity and air temperature opposed one another, and as a result there was little diurnal variation in infrared atmospheric emittance or transmittance. Absorption at infrared wavelengths was insensitive to the solar heating. Empirical models typically relate the atmospheric transmission to the total column water vapour content, which is approximately conserved over short time-scales.

The difference between satellite retrieved and surface level radiative temperatures (the so-called atmospheric correction) illustrates the effects of the diurnal variation of the atmosphere (Figure 5-4). On 13/09/1986, the diurnal variation in the atmospheric correction ranged from 6.75 to 7.25°C at 8-14 μm and 1.0 to 8.0°C within the 10.5-12.5 μm wavelength region. The surface was assumed to be radiating at air temperature.

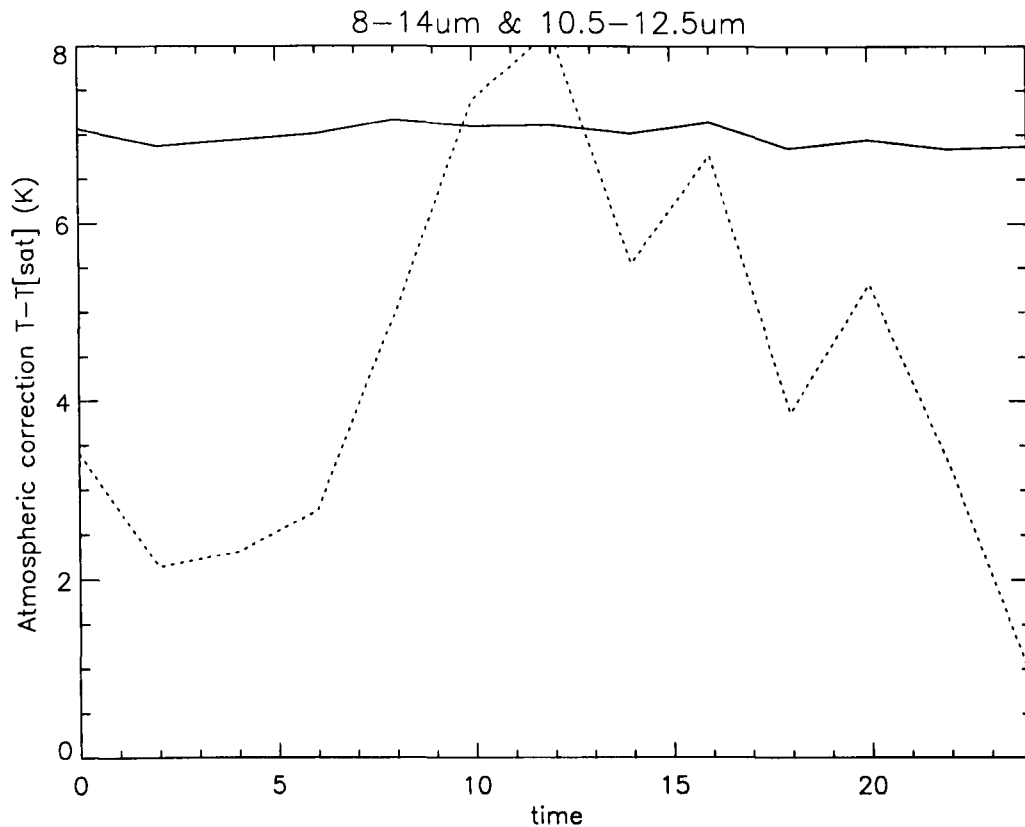


Figure 5-4 Diurnal variation in the atmospheric correction on 13/09/1986 for a surface radiating at air temperature in the 8-14 μm (solid line) and 10.5-12.5 μm (dotted line) wavelength regions.

The correction at 0220 local time was 6.9°C, and at 1030 (the approximate local overpass time of the ATSR satellite) the correction was 7.1°C. Much higher variability was apparent in the 10.5-12.5 μm region. This was largely due to the atmospheric transmission at 8-14 μm being significantly lower than at 10.5-12.5 μm (see Figure 3-2).

Atmospheric profile data, recorded at one time of day only, were interpolated throughout the day using diurnal air temperatures as the primary input to a solar heating model (see Appendix A). The surface level relative humidity calculated on 13/09/1986 using the adiabatic heating model is illustrated in Figure 5-5. There was moderate departure between the observed and predicted relative humidity for low values.

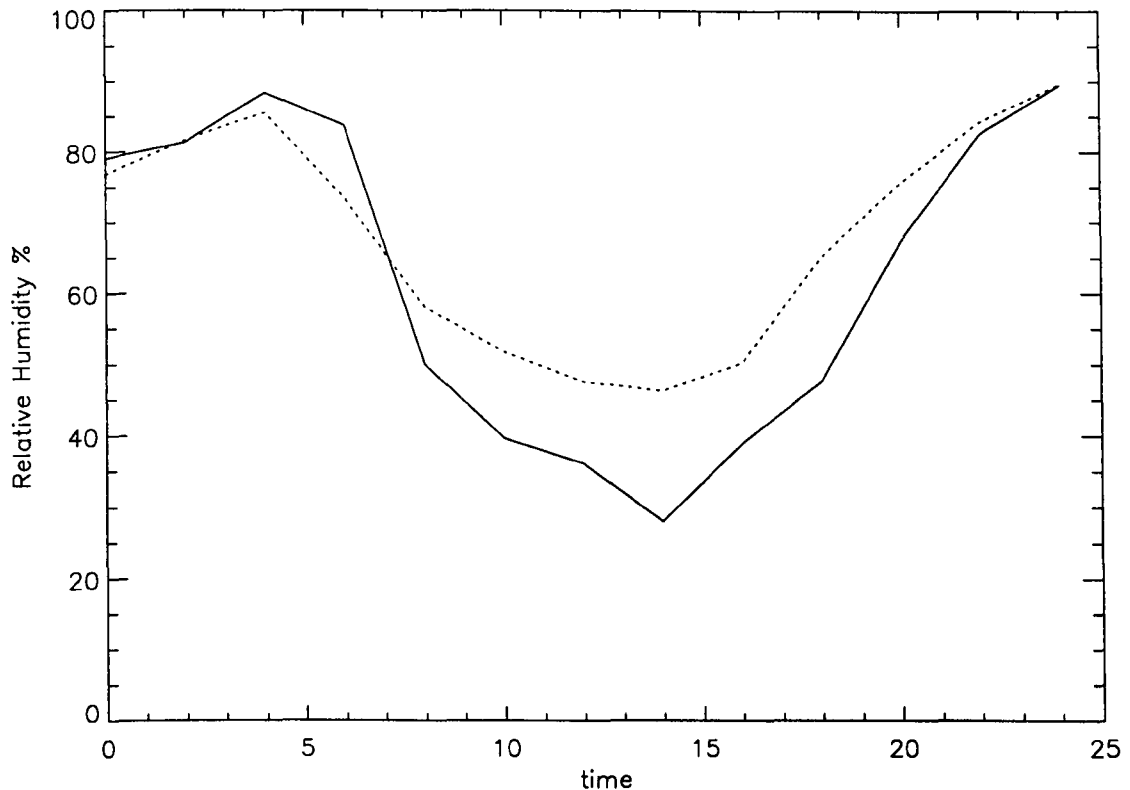


Figure 5-5 Diurnal variation in surface level relative humidity on 13/09/1986 derived from *in situ* data (solid line) and using an adiabatic atmospheric heating model (dotted line).

Continuous surface level air temperatures were recorded at 10 minute intervals at both field sites on each day during the *in situ* data collection period (see Table 4-2). The diurnal variation in atmospheric emittance and transmittance was estimated using adiabatically heated atmospheric profiles and the RAL radiative transfer model. The atmospheric heating model accommodates the diurnal trends in temperature and humidity profiles that are observed in *in situ* data (see Figure 5-5). The heating model is one-dimensional and underestimates the atmospheric water vapour content for low values only. The errors in humidity estimation are therefore greatest when the atmospheric correction is smallest in magnitude.

5.2.3 Broadband infrared atmospheric correction parameters

The downwelling atmospheric emittance, I_{atm} , was calculated using both the empirical formulae of Idso and the RAL radiative transfer model in the 10.5-12.5 μm wavelength region, which was common to both techniques (Figure 5-6). There was good agreement between the two estimates and a pronounced annual trend in atmospheric emittance was apparent.

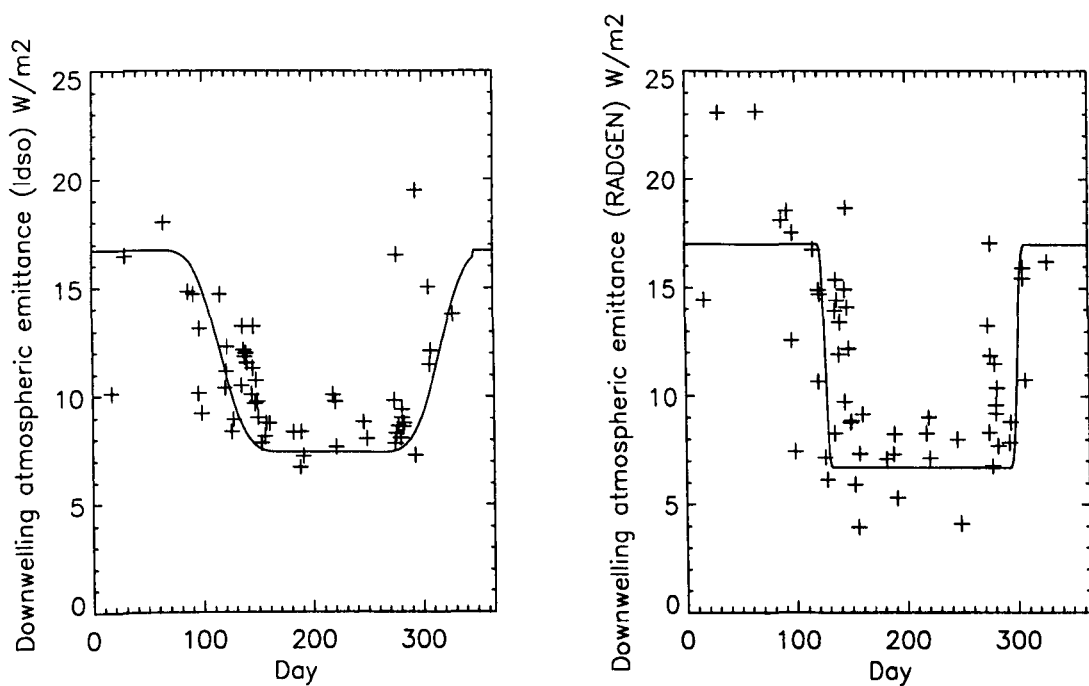


Figure 5-6 Annual variation of the nadir downwelling atmospheric emittance calculated in the 10.5-12.5 μm wavelength region using (a) the formula of Idso and (b) the RAL radiative transfer model.

High values of emittance were observed during the summer months, between September and March, and distinctly lower values of emittance occur in the winter. This was in qualitative agreement with the regional climatology, as the winter months were significantly dryer and cooler than the summer (Figure 5-7).

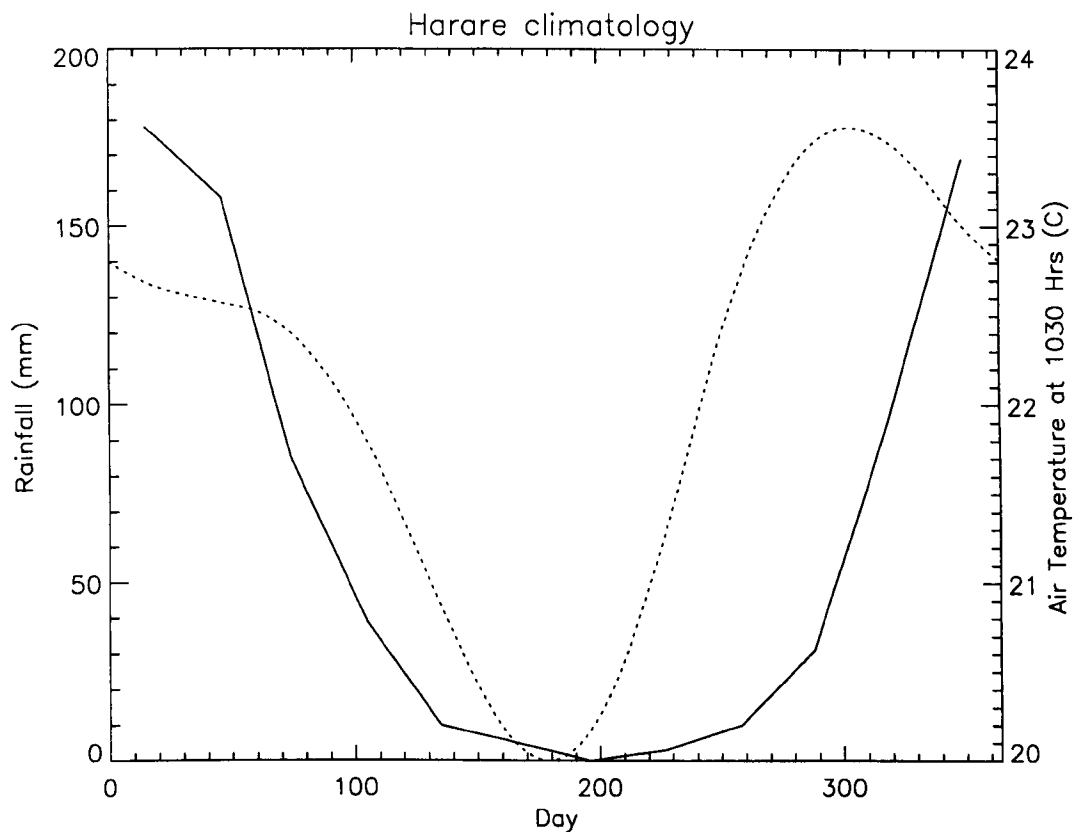


Figure 5-7 Mean annual variation of surface level air temperature and daily rainfall at Harare.

Similar annual variation was apparent in numerical estimates of the atmospheric transmittance (Figure 5-8). The maximum and minimum values of transmittance in the 10.5-12.5 μm region were approximately 60 % and 90 % respectively, with low transmission occurring during periods of high humidity. There was considerable difference between the maximum and minimum atmospheric transmittance, and the total atmospheric correction for satellite retrieved radiances varied significantly throughout the year.

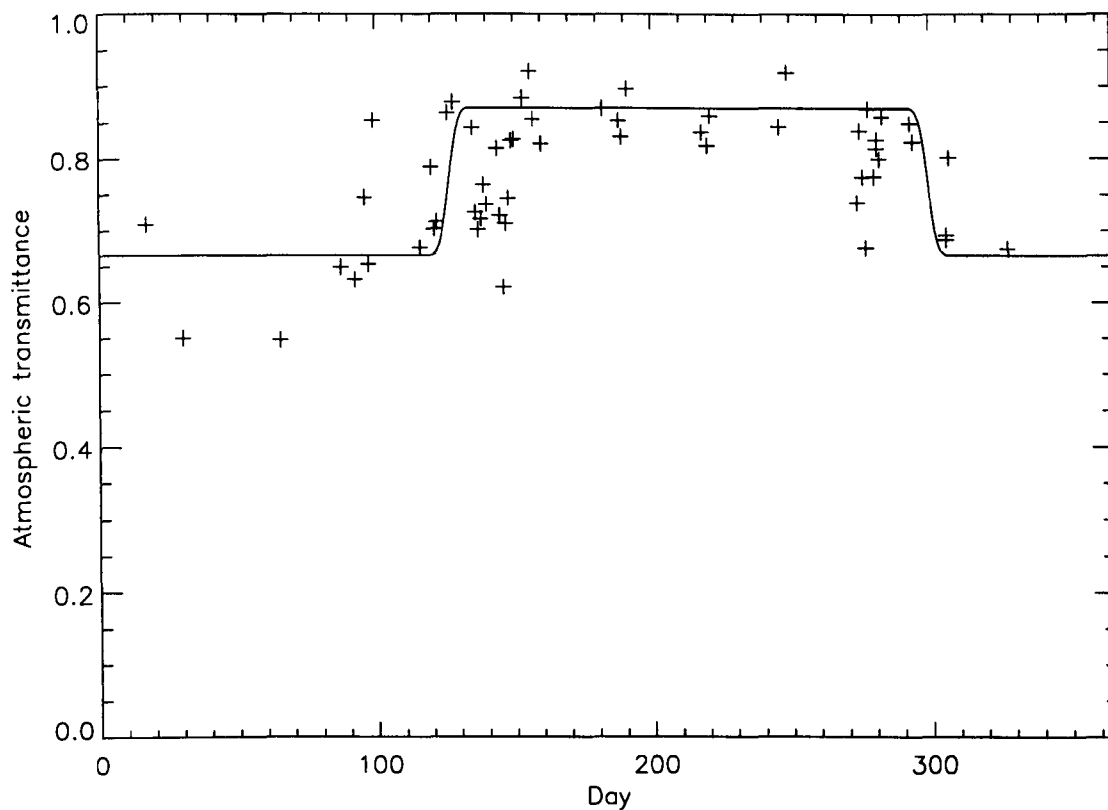


Figure 5-8 Annual variation of the nadir atmospheric transmittance in the 10.5-12.5 μm wavelength region calculated using the RAL radiative transfer model. Also indicated is an approximate parameterisation of the annual trend.

The atmospheric data covered a period of approximately 4.5 years, and whilst the transition between high and low emittance or transmittance was quite distinct, the actual timing of the change was relatively unclear. In particular, it was difficult to predict the onset of high atmospheric transmission, which in practice coincided with the arrival of the annual rainfall season. The annual trend in atmospheric emission and transmission could be described using a variety of parameterisations. Qualitatively, the transmittance and emittance assumed maximum or minimum values during summer and winter, with a temporally finite transition

period at the seasonal cusps. A free trapezium shaped tophat style function was used to represent the discrete zonal behaviour of the atmosphere (see Figure 5-8). The individual parameters which describe the trapezium function were obtained by minimising the absolute deviation from the curve.

Table 5-3 shows values of the nadir atmospheric emittance and transmittance calculated on individual days during the field campaigns. The atmospheric transmittance was not calculated in the 8-14 μm window because the attenuation at surface level was assumed to be negligible.

| Date | $I_{(8-14\mu\text{m})}$ (Wm^{-2}) | $I_{(11\mu\text{m})}$ (Wm^{-2}) | $\tau_{(11\mu\text{m})}$ | $I_{(12\mu\text{m})}$ (Wm^{-2}) | $\tau_{(11\mu\text{m})}$ |
|----------|--|--|--------------------------|--|--------------------------|
| 135/1996 | 50.11 | 2.53 | 0.88 | 4.36 | 0.81 |
| 136/1996 | 57.79 | 4.44 | 0.78 | 7.22 | 0.68 |
| 137/1996 | 54.76 | 4.90 | 0.76 | 7.87 | 0.65 |
| 138/1996 | 54.29 | 4.58 | 0.77 | 7.41 | 0.67 |
| 139/1996 | 54.61 | 3.75 | 0.81 | 6.21 | 0.72 |
| 140/1996 | 53.53 | 4.25 | 0.79 | 6.95 | 0.69 |
| 144/1996 | 49.08 | 3.01 | 0.85 | 5.08 | 0.78 |
| 145/1996 | 52.71 | 4.73 | 0.77 | 7.60 | 0.67 |
| 146/1996 | 57.91 | 6.20 | 0.69 | 9.70 | 0.56 |
| 147/1996 | 48.36 | 4.50 | 0.77 | 7.31 | 0.66 |
| 148/1996 | 50.79 | 3.87 | 0.80 | 6.41 | 0.70 |
| 149/1996 | 48.16 | 2.67 | 0.86 | 4.54 | 0.79 |
| 150/1996 | 46.26 | 2.70 | 0.86 | 4.56 | 0.79 |

Table 5-3 Nadir atmospheric emittance and transmittance in the 8-14 μm and the ATSR 11 μm and 12 μm channel wavelength regions estimated on individual days during the field campaign.

5.2.4 A comparison between numerical and empirical atmospheric correction techniques

The formula of Idso and the RAL radiative transfer model were compared using the monochromatic atmospheric emittance calculated in the 10.5-12.5 μm wavelength region. The raw atmospheric sounding dataset was used for the comparison.

There was good qualitative agreement between the Idso formula and the RAL model (Figure 5-9).

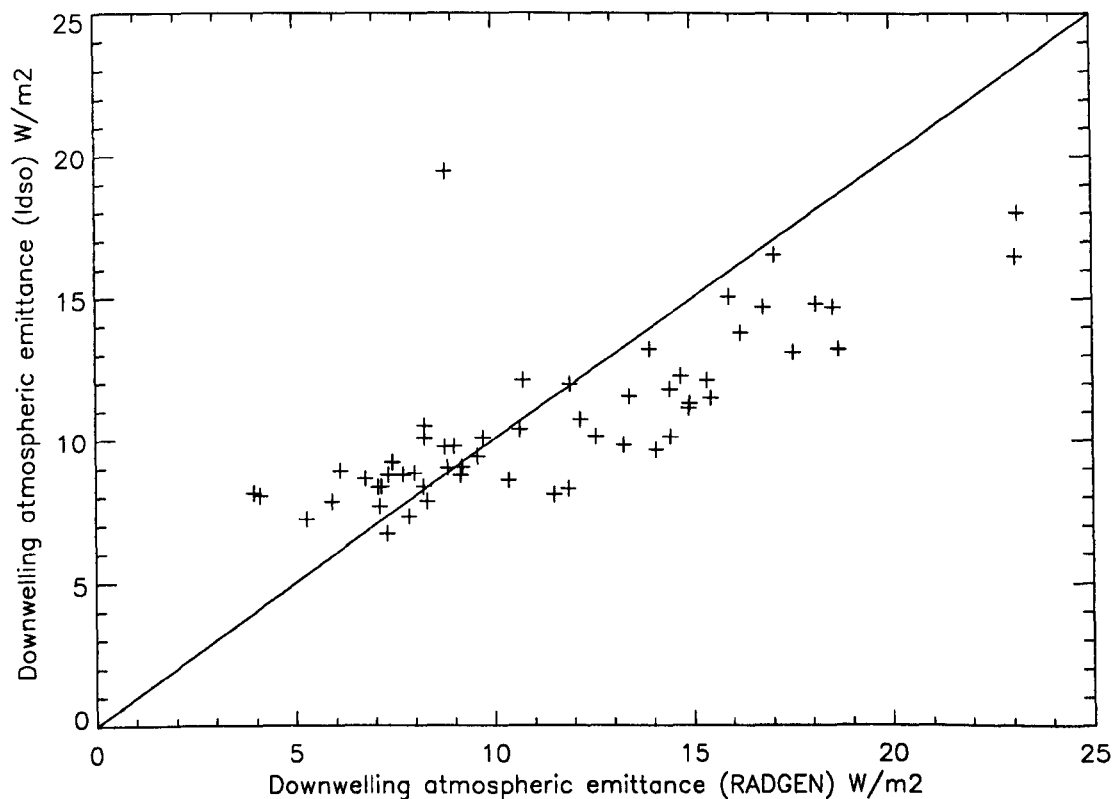


Figure 5-9 Scatter plot of downwelling atmospheric emittance calculated with the formula of Idso and the RAL radiative transfer model in the 10.5-12.5 μm wavelength region.

The mean absolute difference between numerical and empirical estimates of the atmospheric emittance was 1.1 W m^{-2} . The Idso formula undercuts the RAL model for high values of

atmospheric emittance, and the RAL model generates the lowest values at low emittances. The closure between the two approaches was excellent, and there was no evidence to choose either method preferentially. The choice of numerical or empirical technique was in practice dependent upon the wavelength region of interest.

5.2.5 Summary

Atmospheric correction parameters were estimated using a set of clear sky radiosonde ascents recorded at Harare, Zimbabwe. Using the fine spectra produced by the RAL radiative transfer model, the expected atmospheric transmittance in the 10.5-12.5 μm wavelength region was shown to be closely related to the mean value with a weak temperature dependence. A linear relationship was established between the mean and expected transmittance with temperature dependent coefficients.

An empirical formula relating the monochromatic atmospheric transmittance within the 10.5-12.5 μm wavelength region to the surface level air temperature and vapour pressure was proposed. The coefficients for this linear relationship were obtained through multiple regression.

The diurnal variability of the atmosphere was investigated using *in situ* data recorded at the field site. The magnitude of the atmospheric correction was found to vary between 0 and 10°C throughout the day. The largest variation was observed at 10.5-12.5 μm . Using an adiabatic atmospheric heating model, the one-time-of-day radiosounding data was extrapolated diurnally using *in situ* air temperatures. The diurnal variation in the atmospheric correction determined on a number of occasions using this method was consistent with that observed on 13/09/1986.

The annual variation of the atmospheric emittance and transmittance were calculated using the adiabatically heated atmospheric profiles within the RAL radiative transfer model. Monochromatic values were estimated in the 10.5-12.5 μm and ATSR 11 μm and 12 μm wavelength regions.

A direct comparison was made between the formula of Idso and the RAL radiative transfer model in the 10.5-12.5 μm wavelength region. Excellent qualitative agreement was ob-

served between empirical and numerical estimates of the atmospheric emittance, and the mean absolute deviation between the two was 1.1 W m^{-2} .

5.3 Land Surface Temperatures derived from terrestrial Infrared radiometric data

The radiometric surface temperatures of principal surface elements were recorded over an open grassland (Chizengeni) and a medium density natural woodland (Tambuti) on 28 separate occasions during 1995 and 1996. Empirical equations were used to estimate the atmospheric emittance from *in situ* meteorological data. Land surface temperatures were calculated using the radiative transfer equation.

Field measurements were timed to coincide with daytime overpasses of the ATSR instrument on the ERS satellites. The time of satellite overpass (TSOP) was approximately 1020 am local solar time.

Meteorological conditions varied significantly during the field campaigns and cloud cover ranged from clear to completely overcast skies. At the time of satellite overpass, clear sky conditions were present on 18 occasions. All data are included in the analysis.

5.3.1 Surface Temperature Heterogeneity

Radiometric surface temperatures were recorded at a variety of observation angles, with multiple instruments when available. At least 2 radiometers recorded nadir and 55 degree surface temperatures on all occasions. The mean standard deviation of radiometric temperatures at similar observation angles, $s_{\text{instrument}}$, was in all instances smaller than the mean standard deviation of temperatures across the sampling interval, s_{TIME} (Table 5-4). The sampling interval was chosen after investigating the temporal stability of surface temperature during controlled experiments. There was no significant difference in sampling interval standard deviations across all viewing angles. The majority of duplicate measurements were recorded at 0 and 55°, and the low values of $s_{\text{instrument}}$ at 30 and 70° was a result of under sampling.

| Target | View Angle | S _{INSTRUMENT} | S _{TIME} |
|------------|------------|-------------------------|-------------------|
| Tambuti | | | |
| GRASS | 00 | 1.61 | 1.14 |
| SHRUB | 00 | - | 1.13 |
| SOIL | 00 | - | 0.99 |
| TREE | 00 | 0.76 | 0.73 |
| GRASS | 55 | 0.86 | 1.16 |
| SHRUB | 55 | - | 1.21 |
| TREE | 55 | 0.81 | 0.67 |
| Chizengeni | | | |
| GRASS | 00 | 0.68 | 1.41 |
| SHRUB | 00 | - | 0.65 |
| SOIL | 00 | - | 1.35 |
| GRASS | 30 | 0.83 | 1.58 |
| GRASS | 55 | 0.32 | 1.58 |
| SHRUB | 55 | - | 0.65 |
| SOIL | 55 | - | 1.42 |
| GRASS | 70 | 0.14 | 1.61 |

Table 5-4 Standard deviations of radiometric temperatures across the sampling interval (S_{time}) and between individual instruments with similar view-angles ($S_{instrument}$) over various surface elements.

In general the differences between individual instruments viewing the same surface elements were similar or lower than the standard deviation of the readings across the sampling interval. The exception was the nadir measurements over long grass at Tambuti. At Chizengeni the instrument differences were much lower than the temporal deviation. This indicates that surface temperature heterogeneities were present at scales smaller than could be resolved by the experiment. The Chizengeni short grass canopy had mean roughness elements an order of magnitude smaller than the sampling area of radiometric measurements.

5.3.2 Surface component Radiative Temperatures

The principal surface elements at the Chizengeni and Tambuti field sites are listed in Table 5-4. Radiometric temperatures were recorded over these surfaces under a variety of experimental configurations. The downwelling atmospheric radiation was estimated using the

equations of Idso, which relate atmospheric emittance to the surface level air temperature and vapour pressure. Atmospheric transmission was assumed to be total for all terrestrial measurements. Emissivity data was obtained from the literature.

Surface temperatures were determined by solving the radiative transfer equation using the nadir radiometric temperatures. Where multiple instruments were available the mean radiative temperature was calculated. Radiometric temperatures were recorded for extended periods on each day of the experiment. Figure 5-10 shows a typical diurnal trend of the temperatures recorded at Chizengeni and Tambuti on a clear day during the experiment. The time of satellite overpass is also indicated.

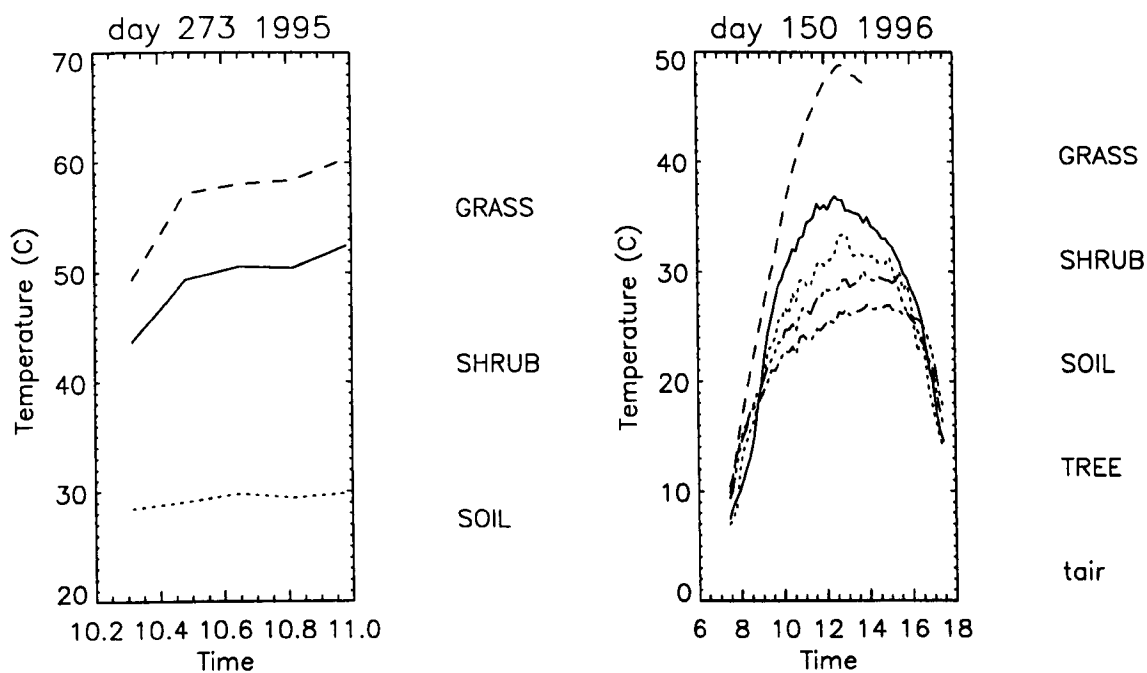


Figure 5-10 Radiative surface temperature of the principal surface elements at (a) Chizengeni on 273/1995 and (b) Tambuti on 150/1996.

Table 5-5 shows the nadir radiative surface temperature of each surface element at the time of satellite overpass at Chizengeni and Tambuti. Also indicated are the air temperature measured at 1m.

| Year | Date | T _{GRASS} | S _{GRASS} | T _{BUSH} | S _{BUSH} | T _{TREE} | S _{TREE} | T _{SOIL} | S _{SOIL} | T _{AIR} | S _{AIR} |
|------------|------|--------------------|--------------------|-------------------|-------------------|-------------------|-------------------|-------------------|-------------------|------------------|------------------|
| Chizengeni | | | | | | | | | | | |
| 1995 | 273 | 48.72 | 1.28 | 28.38 | 0.97 | - | - | 55.87 | 1.41 | - | - |
| 1995 | 274 | 52.47 | 1.66 | 28.46 | 0.72 | - | - | 49.92 | 1.18 | - | - |
| 1995 | 293 | 50.90 | 1.45 | 30.16 | 0.75 | - | - | - | - | 22.65 | 0.64 |
| 1996 | 134 | 27.15 | 0.64 | 22.16 | 0.42 | - | - | - | - | 22.23 | 0.62 |
| 1996 | 135 | 21.84 | 0.62 | - | - | - | - | - | - | 18.89 | 0.44 |
| 1996 | 136 | 25.23 | 0.68 | - | - | - | - | - | - | 20.93 | 0.54 |
| 1996 | 137 | 28.66 | 1.16 | - | - | - | - | - | - | 21.28 | 0.84 |
| 1996 | 138 | 36.56 | 1.50 | - | - | - | - | - | - | 22.10 | 1.07 |
| 1996 | 139 | 33.05 | 3.54 | - | - | - | - | - | - | 21.28 | 1.40 |
| 1996 | 140 | 24.04 | 0.81 | - | - | - | - | - | - | 18.51 | 0.47 |
| Tambuti | | | | | | | | | | | |
| 1995 | 279 | 48.93 | 1.30 | - | - | 40.35 | 1.13 | - | - | 25.67 | 0.96 |
| 1995 | 280 | 43.06 | 1.69 | - | - | 39.83 | 0.94 | - | - | 26.84 | 0.76 |
| 1995 | 281 | 46.98 | 1.47 | - | - | - | - | - | - | 27.20 | 0.76 |
| 1995 | 283 | 44.46 | 1.98 | - | - | 43.42 | 1.01 | - | - | 26.17 | 0.90 |
| 1995 | 284 | 53.52 | 1.55 | - | - | 50.72 | 1.00 | - | - | 29.75 | 1.70 |
| 1995 | 285 | 48.98 | 1.82 | - | - | - | - | - | - | 27.86 | 0.92 |
| 1995 | 286 | 37.11 | 3.28 | - | - | - | - | - | - | 22.45 | 1.06 |
| 1996 | 144 | 29.07 | 0.77 | - | - | - | - | 39.45 | 0.82 | 27.89 | 1.21 |
| 1996 | 145 | - | - | - | - | 23.82 | 0.55 | 38.47 | 0.96 | - | - |
| 1996 | 146 | 18.39 | 0.63 | - | - | 16.34 | 0.38 | 21.27 | 0.66 | 17.74 | 0.32 |
| 1996 | 147 | 22.98 | 1.78 | - | - | 19.73 | 1.41 | 29.88 | 1.76 | 20.66 | 1.02 |
| 1996 | 148 | 22.77 | 0.88 | 19.26 | 0.85 | - | - | 27.94 | 1.47 | 19.06 | 0.52 |
| 1996 | 149 | 27.72 | 4.97 | 22.35 | 3.62 | 19.96 | 2.40 | 34.17 | 3.96 | 21.48 | 2.41 |
| 1996 | 150 | 31.23 | 1.21 | 28.09 | 1.24 | 22.86 | 0.75 | 38.55 | 1.02 | 25.07 | 1.21 |

Table 5-5 Radiative surface temperatures recorded at the time of satellite overpass.

5.3.3 Angular Variation of Radiative Temperature

Angular variations in apparent radiative surface temperature can arise within heterogeneous canopies because of temperature differentials between distinct elements within the radiometric field of view. The effects of angular variations in surface emissivity were not directly investigated, although the variation in similar soil samples has been recorded as less

than 1% for view angles below 60 degrees, which is smaller than the error associated with emissivity estimates (see Section 4.4)

Radiative temperatures of components at Chizengeni and Tambuti were measured at a variety of zenith observation angles (see Table 5-4). Radiative temperatures of the short grass canopy at Chizengeni were monitored at 0, 30, 55 and 70 degree zenith angles. Measurements over long grass and trees at Tambuti were restricted to 0 and 55 degree zenith angles. No off-nadir measurements were made over dense shrubs as preliminary experiments indicated little or no angular variation. Instruments were orientated parallel to the ERS satellite track to simulate the ATSR viewing geometry. The effects of azimuth angle were not investigated. Simultaneous measurements were recorded at different view angles during daylight hours and the experiments were repeated on a number of occasions.

Figure 5-11 indicates the daily trend in the difference between nadir and forward (55° to zenith) radiative temperatures over various surface elements.

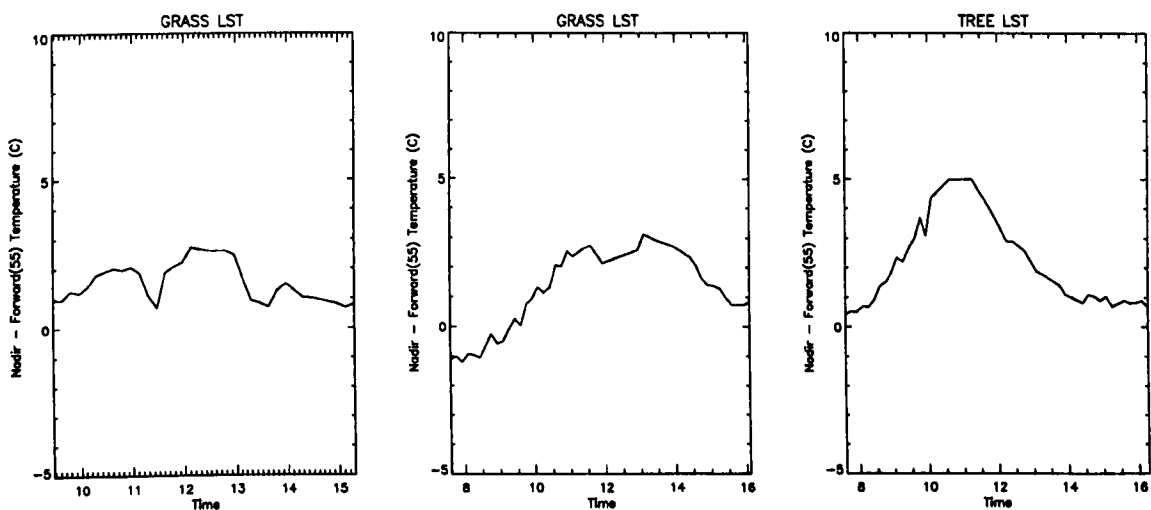


Figure 5-11 Difference between nadir and forward (55° to zenith) radiative temperatures of a) Short grass at Chizengeni, b) Long grass at Tambuti and c) Tree canopy at Tambuti.

The nadir radiative temperatures were in general greater than the oblique temperatures, and the magnitude of the difference changed throughout the day. Maximum temperature differ-

ences of up to 6.5°C over tree canopies, 4°C over long grass and 3.5°C over short grass were observed. The greatest differences tended to occur at positions of maximum solar elevation. At the time of satellite overpass, differences between nadir and forward radiative temperatures were generally much smaller, and varied substantially between individual days. Scatter plots of the nadir-forward difference against the nadir radiative temperature indicate varying degrees of correlation.

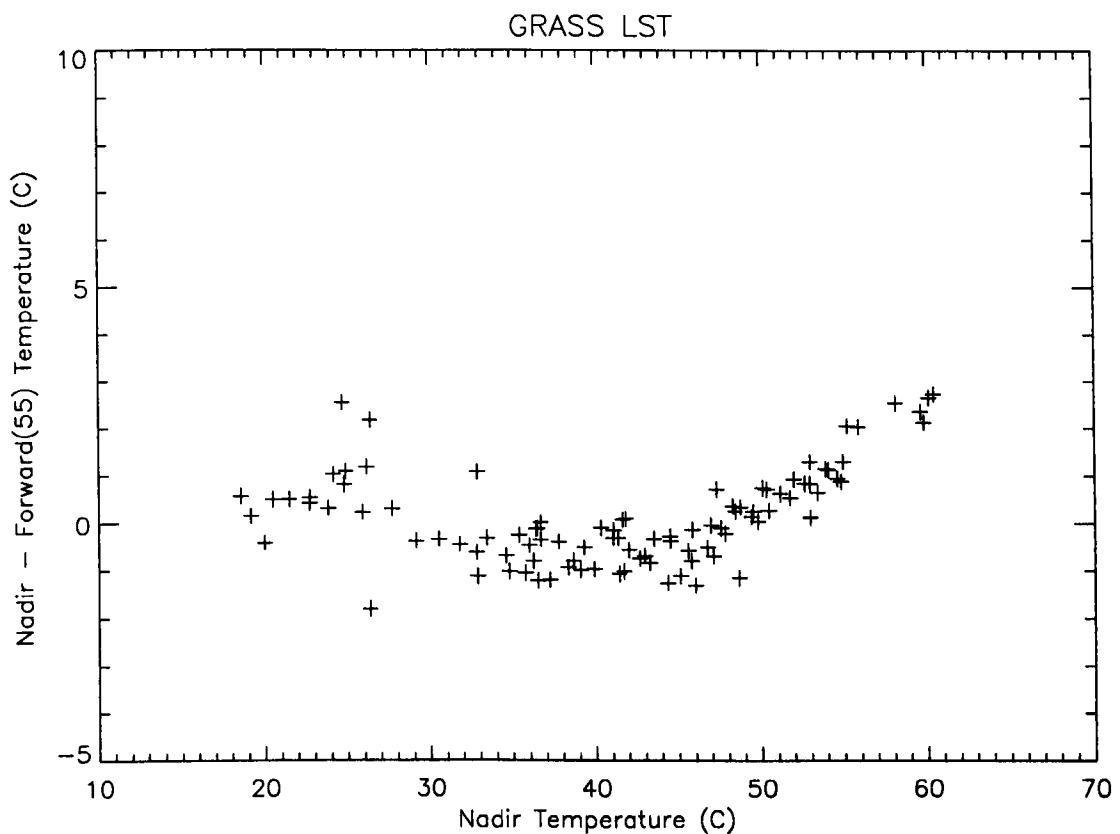


Figure 5-12 Scatter plot of nadir-forward temperature differences against the nadir radiative temperature over long grass at Tambuti.

Over the long grass at Tambuti, no significant angular variation in radiative temperature was observed below temperatures of around 50°C (Figure 5-12). Above this threshold the difference increased linearly with temperature to a maximum of approximately 4°C.

The tree canopy at Tambuti exhibited a complex angular variation in radiative temperature, and the temperature difference between nadir and forward views was most strongly related to solar elevation (see Figure 5-13). Differences increased approximately linearly with nadir temperature to a maximum of around 5°C.

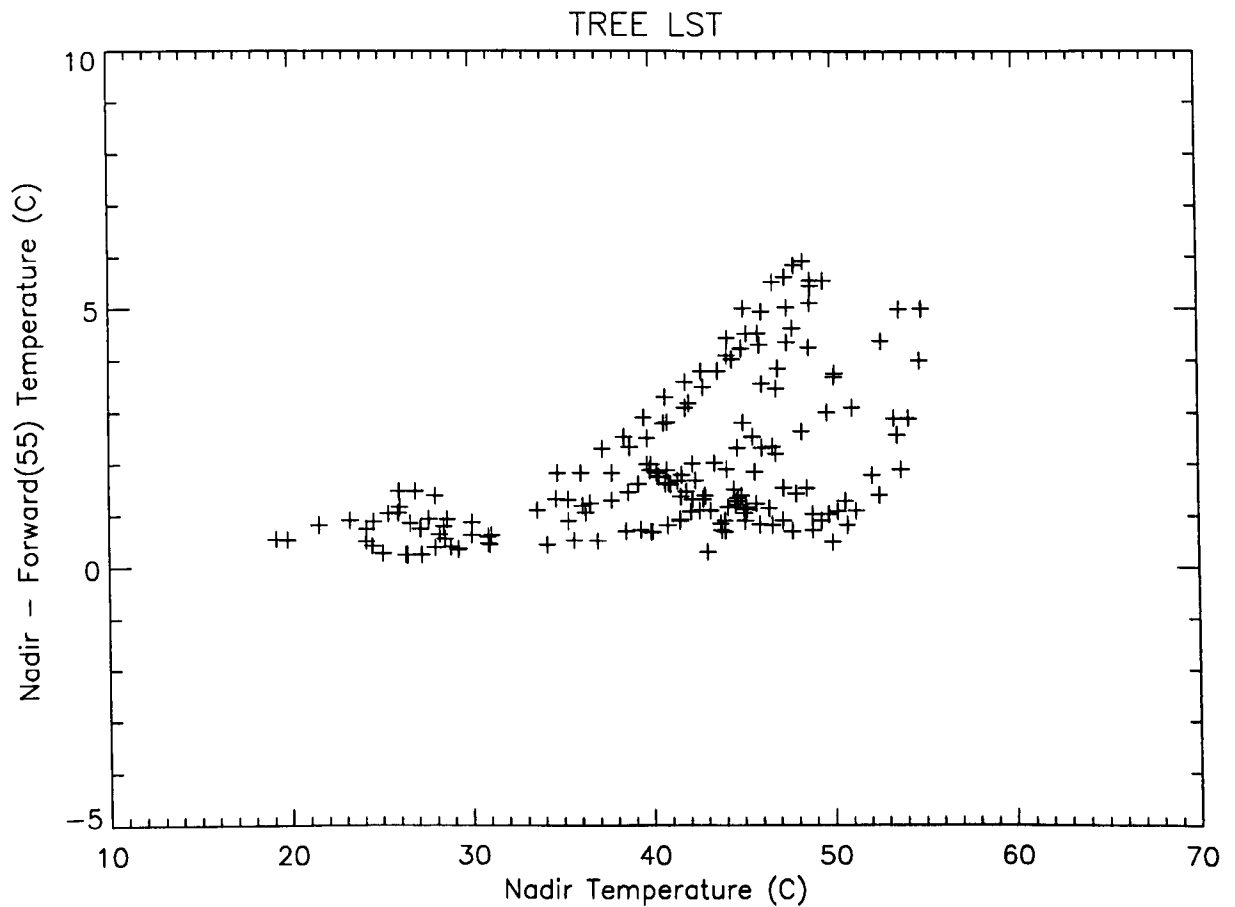


Figure 5-13 Scatter plot of nadir-forward temperature differences against the nadir radiative temperature of the tree canopy at Tambuti.

The gradient and onset temperature for this portion of the trend were temporally inconsistent. The maximum difference was roughly coincidental with the peak in solar elevation. Subsequently the nadir and forward temperatures quickly equalised and decreased in tandem with time through the afternoon. This behaviour was consistent with the effects of shadow presence within the radiometric field of view. When the understory was unshaded in both

views, the nadir and forward tree canopy temperatures were approximately equal. The typical diurnal behaviour of nadir and forward tree canopy temperatures can be seen more clearly in Figure 5-14.

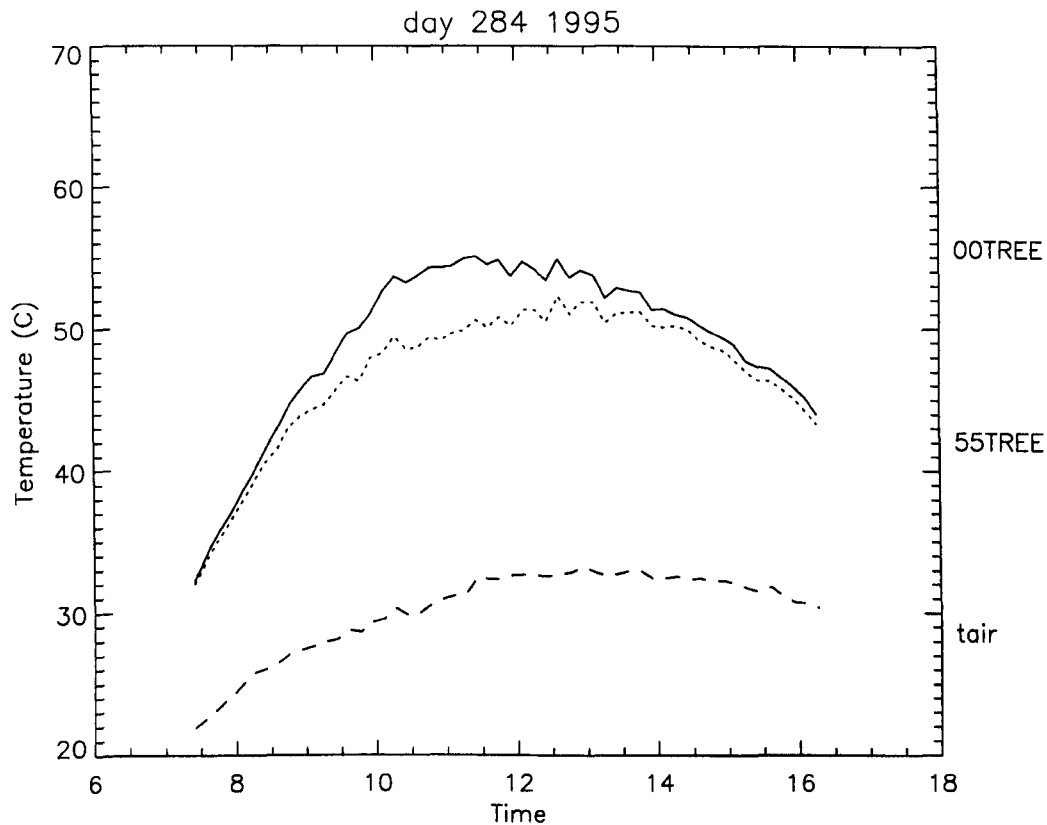


Figure 5-14 Diurnal variation in nadir and forward (55° to zenith) radiative temperatures over a tree canopy at Tambuti on 284/1995. The presence of shadow within the forward view alone reduces the forward temperature for a period of time.

The angular behaviour of the radiative temperature over the short grass at Chizengeni was studied in more detail. Temperatures were recorded at 0, 30, 55 and 70 degree zenith angles. The data were collected during both clear and intermittently cloudy conditions. A pronounced angular variation in the radiative temperature was evident on all occasions (Figure 5-15).

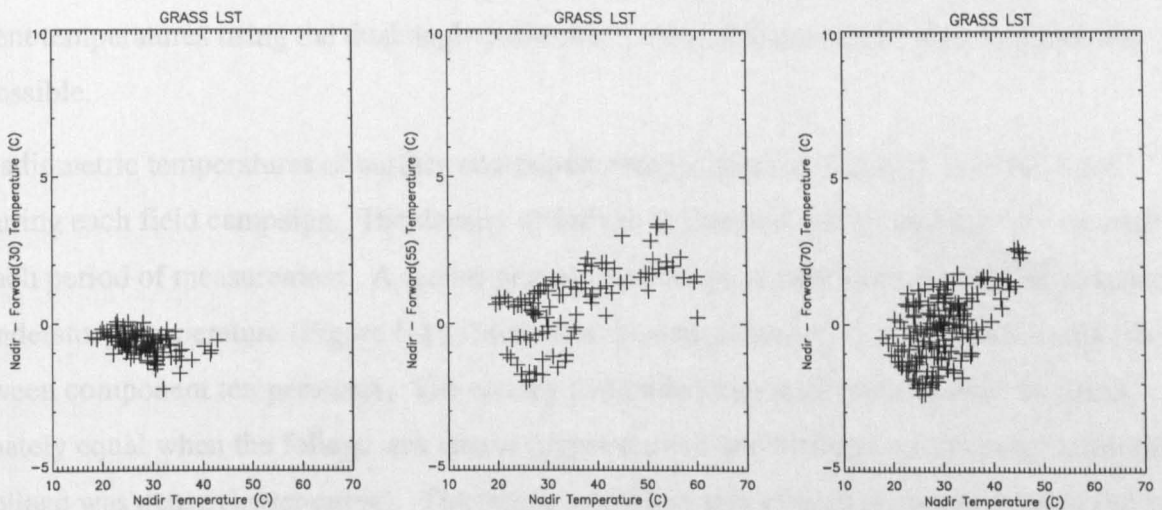


Figure 5-15 Scatter plot of nadir-forward temperature differences against the nadir radiative temperatures of the short grass at Chizengeni for forward views at a) 30°, b) 55° and c) 70°.

The radiative temperature of the sparse canopy in general decreased with increasing view zenith angle. The magnitude of the effect was related to the absolute temperature of the surface. Differences between oblique and nadir radiative temperatures were close to zero at approximately the same temperature on all occasions. No significant difference was observed between measurements at nadir and 30°. Differences of up to 3.5°C were observed between the nadir and 55 degree radiative temperature, with typically a 0.5 - 1.5°C difference at the time of satellite overpass. A similar effect was apparent at the 70 degree observation angle, where temperature differences upwards of 4°C were recorded.

5.3.4 Component Temperature Separation within a Mixed Canopy

Tambuti

Radiative temperatures obtained over partially closed tree canopies are in general a mixture of foliage and understory temperatures. The angular variation in radiative temperature of the long grass and tree canopy at Tambuti was either negligible or correlated to solar elevation. Dual-angle radiative temperatures recorded above the tree canopy were contaminated by differential shading between the nadir and forward views. The experiments were insuffi-

ciently constrained to determine the degree of shading present. Separation of the component temperatures using the dual angle radiometric measurements alone was therefore not possible.

Radiometric temperatures of surface component temperatures at Tambuti were recorded during each field campaign. The density of foliage at Tambuti varied substantially between each period of measurement. A scatter plot of tree canopy temperature against the vegetated understory temperature (Figure 5-16) illustrates the annual variation in the relationship between component temperatures. The canopy and understory temperatures were approximately equal when the foliage was sparse (upper curve), and differed significantly when the foliage was dense (lower curve). The sparse woodland was effectively transparent to infrared radiation.

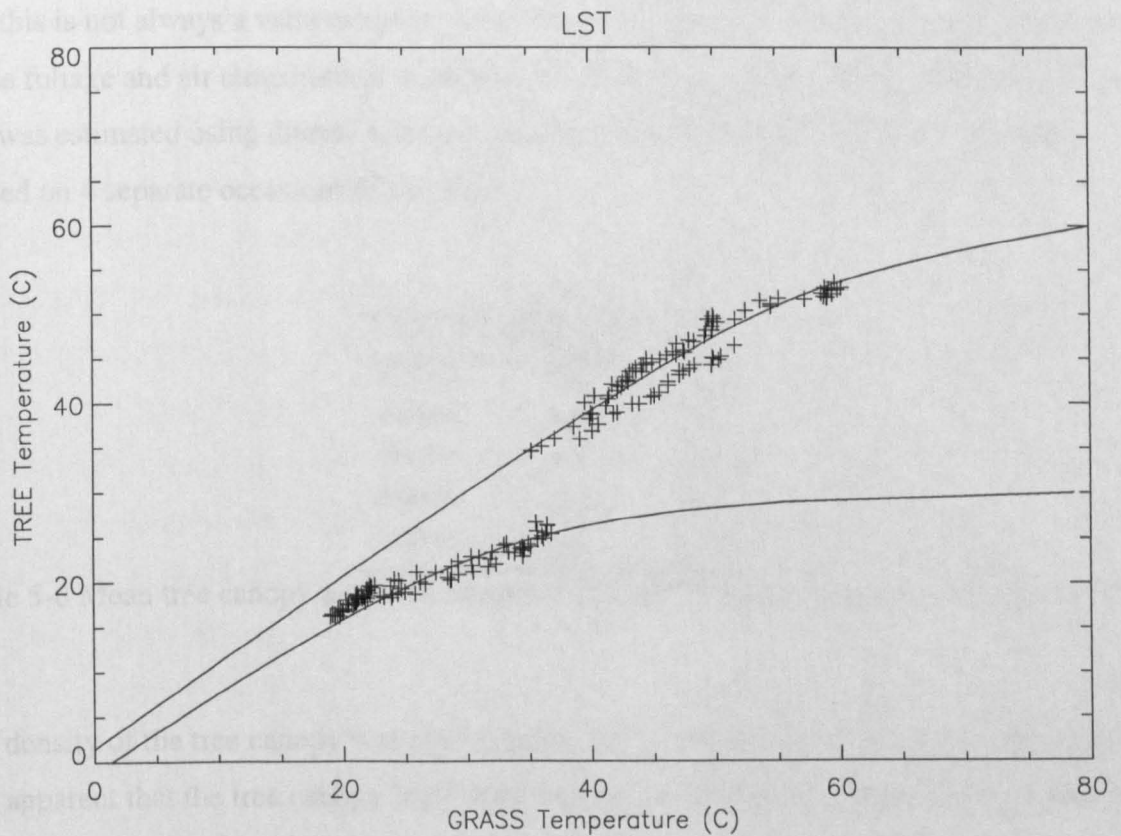


Figure 5-16 Scatter plot of vegetated understory and tree canopy component temperatures recorded during two field campaigns at Tambuti. The tree canopy density varied significantly between the each period of measurement. The lower curve was derived from tem-

peratures recorded over a dense canopy and the upper curve was recorded over a sparse canopy. A hyperbolic fit was applied to each dataset.

A simple hyperbolic fit was used to parameterise the relationship between canopy and understory temperatures. Two degrees of freedom were available for the curve fitting and the component temperatures were regressed to obtain each relationship. The hyperbola was constrained by forcing both temperatures to be equal at the low temperature asymptote. The high temperature asymptote and radius of curvature of the hyperbola were the free regression parameters.

The apparent density of the canopy was estimated using understory and foliage temperatures and a linear mixture model (see Chapter 4). Foliage temperature was approximated to air temperature on all occasions. Measurements over completely closed tree canopies indicate that this is not always a valid assumption. Differences of up to 2°C were recorded between dense foliage and air temperatures at the time of satellite overpass. The mean canopy density was estimated using diurnal radiative temperatures for partially closed canopies recorded on 4 separate occasions (Table 5-6).

| Date | Canopy density | s |
|----------|----------------|------|
| 279/1995 | 0.23 | 0.01 |
| 280/1995 | 0.00 | 0.02 |
| 283/1995 | 0.06 | 0.01 |
| 284/1995 | 0.17 | 0.03 |
| 150/1996 | 0.84 | 0.42 |

Table 5-6 Mean tree canopy densities estimated at Tambuti using component temperatures.

The density of the tree canopy was not related to the actual density of the woodland itself. It was apparent that the tree canopy itself does not always present an opaque surface to the infrared radiometer.

Chizengeni

The short grass canopy at Chizengeni was uniformly low (roughly 0.01 - 0.05 m in height) and evenly exposed to solar radiation. No shading was present within the radiometric field of view. It was not possible to determine any vertical temperature gradients within the grass. The radiative temperature in general decreased with view zenith angle, and temperatures measured at oblique viewing angles were moderately correlated with the nadir radiative surface temperature. The relative difference between nadir and oblique radiative surface temperatures (Figure 5-15) illustrates the magnitude of this effect. The sparse grass did not behave as a uniform isotropically radiating body, and there was some angular dependence to the ensemble emission from the surface.

The sparse grass was assumed to be a heterogeneous mixture of vegetation and soil. Using a linear mixture model, the ensemble emission from the surface was related to the component temperatures and fractional cover (see Chapter 2). Using radiative temperatures measured at two or more observation angles, coupled with an appropriate canopy architecture parameterisation, the vegetation and soil temperatures and the fractional cover were determined. Multi-angle (more than 3 independent looks) data were recorded during the second field experiment on 5 separate occasions over a period of approximately 40 hours. The mean fractional vegetation cover was estimated to be 0.60 ± 0.27 from radiative temperatures recorded at 0, 55 and 70 degree zenith angles. The fractional vegetation cover was estimated manually to be approximately 0.66 ± 0.1 . The two independent estimates are in excellent agreement. Assuming the measured estimates for the fractional cover, vegetation and soil temperatures were determined using dual angle radiative surface temperatures (Figure 5-17). Data were combined from both field experiments, between which the fractional vegetation cover differed.

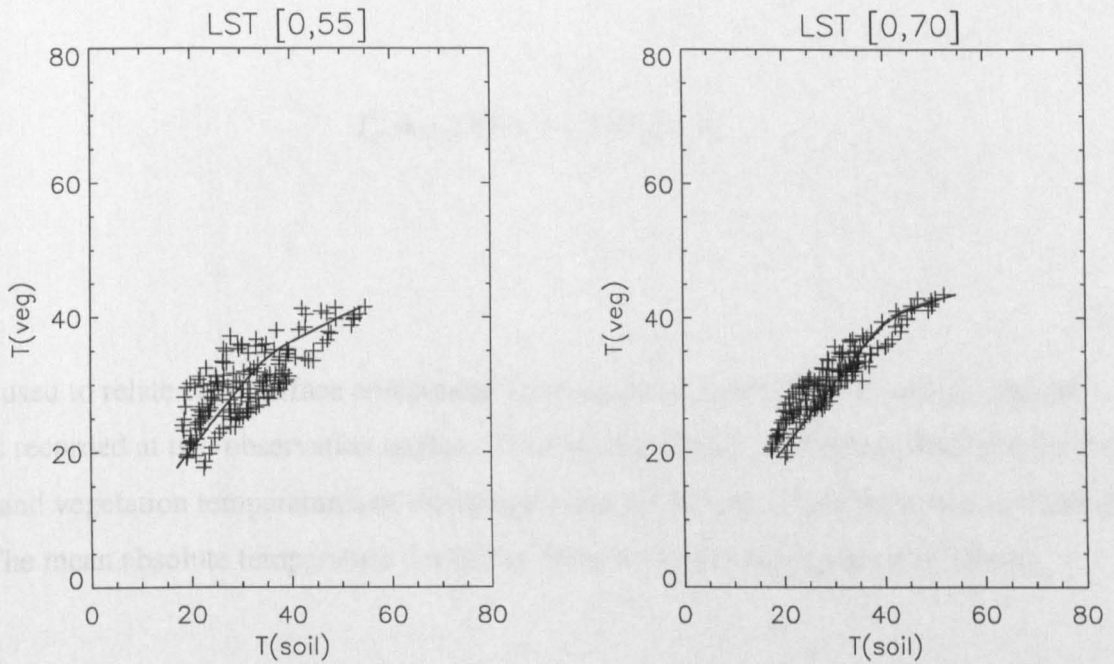


Figure 5-17 Scatter plot of vegetation and soil component temperatures at Chizengeni derived from dual angle radiative temperatures recorded at a) 0 and 55 degree and b) 0 and 70 degree zenith angles.

The broad scatter between vegetation and soil temperatures indicates that there was no truly unique relationship between the two within the short sparse canopy. Reasons for departure from the idealised trend could include inaccurate estimation of the fractional vegetation cover, incorrect parameterisation of the canopy architecture and could also result from errors in temperature measurements propagated through the component temperature separation model. A hyperbolic fit was used to parameterise the relationship between vegetation and soil temperatures. The standard deviations of vegetation and soil temperature estimates from the mean hyperbolic trends was 0.26°C . The relatively low variation in fractional vegetation cover did not seem to affect the relationship between component temperatures significantly, and there was no significant difference in the relationship determined from temperatures recorded during each field campaign.

A linear parameterisation of the form

$$T_c = a_0T(\theta_1) + a_1T(\theta_2) + a_2$$

(5.5)

was used to relate each surface component temperature, T_c , to radiative surface temperatures recorded at two observation angles. Multiple regression coefficients obtained for the soil and vegetation temperatures of the sparse grass at Chizengeni are presented in Table 5-7. The mean absolute temperature deviations from each relationship are also shown.

| θ_1 | θ_2 | a0 | a1 | a2 | mad |
|------------|------------|---------|---------|---------|-------|
| Vegetation | | | | | |
| 0 | 55 | -1.0245 | 2.0224 | 0.0394 | 0.047 |
| 0 | 70 | 4.0830 | -3.0876 | -0.0391 | 0.133 |
| Soil | | | | | |
| 0 | 55 | -0.2100 | 1.2113 | -0.0702 | 0.033 |
| 0 | 70 | 2.8538 | -1.8570 | -0.0211 | 0.089 |

Table 5-7 Coefficients for separation of vegetation and soil component temperatures from dual angle radiative temperatures over short grass at Chizengeni.

The residual prediction errors associated with the surface component temperature retrieval algorithms are illustrated in Figure 5-18. There was no significant bias associated with each algorithm. The correlations were in all instances higher than were obtained through linear regression.

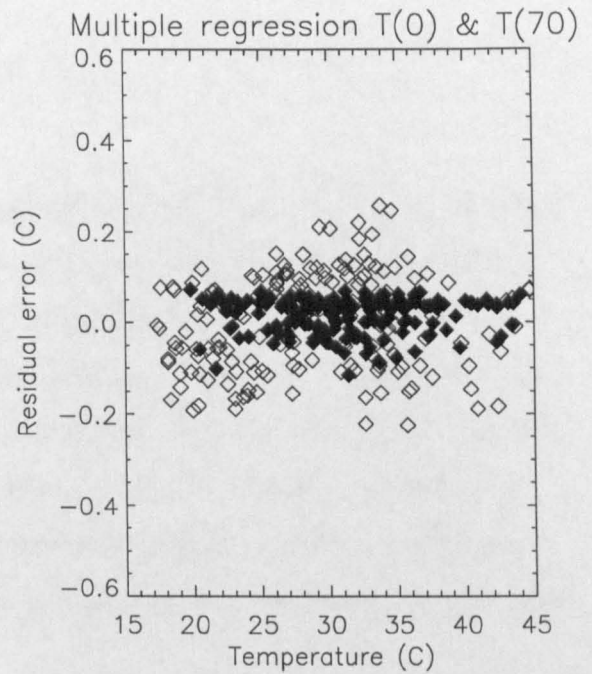
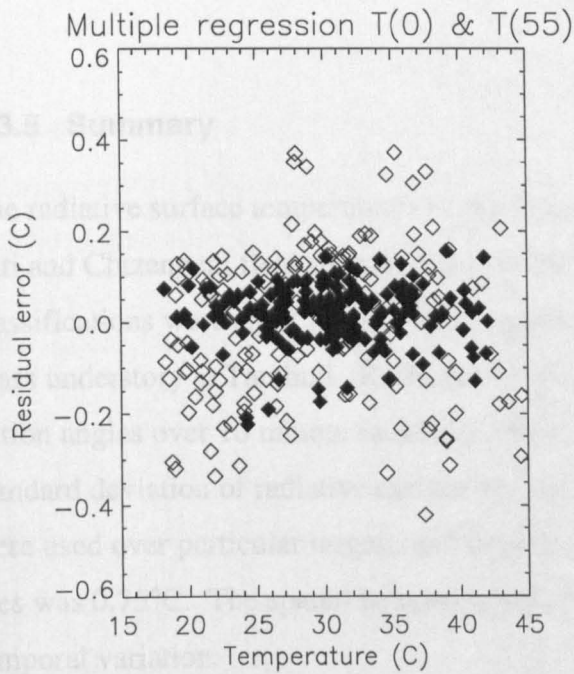


Figure 5-18 Scatter plots of residual error associated with vegetation (solid) and soil temperature algorithms for a) 0 and 55 degree and b) 0 and 70 degree zenith angles.

The multiple regression component temperature retrieval coefficients were used to estimate vegetation and soil temperatures on occasions where dual-angle radiometric measurements were made. The mean vegetation and soil temperatures estimated over the sparse grass at Chizengeni at the time of satellite overpass are listed in Table 5-8.

| Date | T _{VEGETATION} | S _{VEGETATION} | T _{SOIL} | S _{SOIL} |
|----------|-------------------------|-------------------------|-------------------|-------------------|
| 136/1996 | 25.19 | 1.32 | 27.05 | 1.93 |
| 137/1996 | 30.44 | 0.66 | 22.46 | 1.14 |
| 138/1996 | 35.27 | 1.36 | 42.22 | 1.88 |
| 139/1996 | 33.16 | 0.19 | 33.72 | 0.26 |

Table 5-8 Chizengeni sparse grass canopy vegetation and soil temperatures estimated at the time of overpass of the ERS satellite.

5.3.5 Summary

The radiative surface temperatures of principal surface elements were estimated at the Tambuti and Chizengeni field sites during two field campaigns (Table 5-5). The gross canopy classifications were short grass at Chizengeni and medium density woodland with a tall grass understory at Tambuti. Radiometric measurements were made at a variety of observation angles over 10 minute sampling intervals throughout each day. The mean temporal standard deviation of radiative surface temperatures was 1.23°C. Duplicate instruments were used over particular targets, and the mean standard deviation between adjacent samples was 0.75°C. The spatial heterogeneity of most targets was significantly lower than the temporal variation.

The radiative temperatures of certain elements exhibited pronounced angular variability. This was attributed to the effects of viewing heterogeneous targets composed of distinct surface components. The effects of shadowing were also observed. Using end member temperatures, and assuming the foliage temperature was approximately equal to air temperature, the mean tree canopy density at Tambuti was estimated to vary between 6 % and 84 %. Understory temperatures were then calculated using the approximate canopy density. Comparisons between simultaneous nadir and oblique radiative temperatures recorded above partially closed tree canopies illustrated the difference between shaded and unshaded understory temperatures (see Table 5-7).

A linear mixture model was coupled with radiative temperatures and a simple canopy architecture to separate the soil and vegetation temperatures of the sparse grass at Chizengeni. Using radiative temperatures recorded at three view zenith angles the fractional vegetation cover was estimated to be 0.65 ± 0.27 , in excellent agreement with *in situ* measurements. Retrieval coefficients relating the vegetation and soil component temperatures to dual-angle radiative temperatures were calculated using multiple regression. Table 5-8 contains estimates of the surface component temperatures at Chizengeni at the time of overpass of the ATSR satellite radiometer. The temperatures recorded on day 137 in 1996 indicate that the vegetation was hotter than the soil, which is at odds with expectations. Here, the temperatures were recorded within the seepage zone of the Chizengeni dambo, which represents only a small fraction of the total area (less than 5%). The high soil moisture within the seep-

age zone (see Figure 4-10) may account for the apparent breakdown of the model and the anomalous temperatures determined. These data can be compared with land surface temperatures derived from ATSR data.

5.4 Land Surface Temperatures derived from the ATSR

Radiative land surface temperatures were calculated over the Chizengeni and Tambuti field sites using ATSR infrared brightness temperatures (BT's) with both the RAL radiative transfer model and the dual-angle LST retrieval algorithm of Prata (1993).

The ATSR data were recorded during the 35 day repeat phase of ERS1 and ERS2, and the satellite dataset exhibited good temporal resolution. Cloud clearing algorithms were used to identify contaminated pixels and data are presented for clear sky conditions only.

The Prata dual-angle retrieval algorithm relates the mean nadir LST to the ATSR nadir and forward BT's. No radiative transfer model was required for this technique, although *in situ* estimates of the atmospheric transmittance were necessary. The ATSR radiometric brightness temperatures and the *in-situ* radiosonde data were sufficient to generate LST retrieval coefficients using LST's derived from both the Prata dual-angle algorithm and the full radiative transfer solution.

The nadir and forward ATSR LST obtained using the radiative transfer model were used to investigate the surface heterogeneity at sub-pixel resolution using a linear mixture model coupled with *in situ* data.

5.4.1 Temperature Heterogeneity

The spatial resolution of ATSR BT's is approximately 1 km². The geolocation accuracy of the BT product was observed to vary through time and according to surface elevation (see Chapter 5). Using a temporally coregistered sequence of clear satellite imagery the Chizengeni and Tambuti field sites were identified. The area required to confidently encompass each site throughout the sequence was typically greater than single pixel accuracy. Figure 4-8 and Figure 4-13 show ATSR 1.6 μm reflectance images of the Chizengeni and Tambuti field sites. The confident locations of each site are highlighted.

Figure 5-20 and Figure 5-22 are the cloud-free ATSR 12 μm BT image sequences isolated at Chizengeni and Tambuti respectively. The sequences are ordered by day of year and a crude annual temperature cycle can be readily identified. Strong distinctions between vegetated and non-vegetated areas were also apparent at both sites (see Figure 4-8 and Figure 4-13).

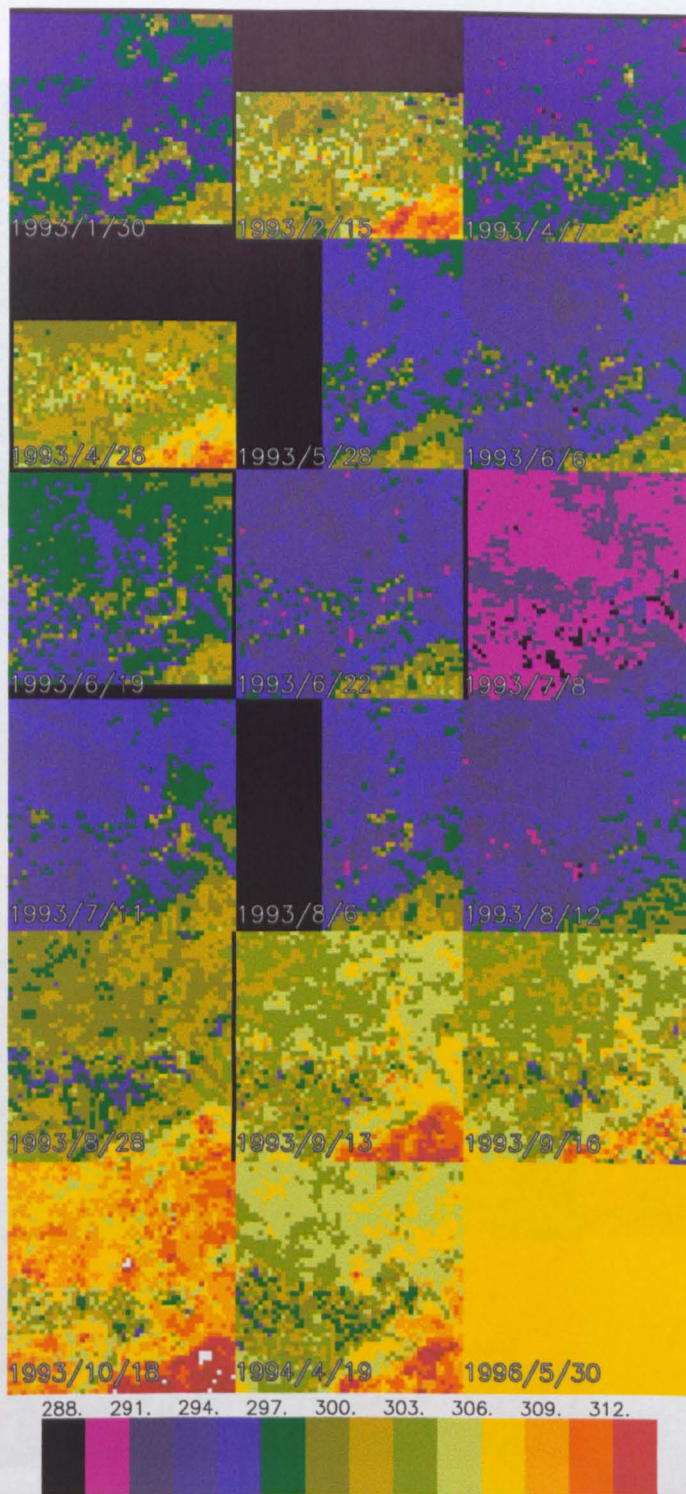


Figure 5-19 ATSR 12 μm brightness temperature image sequence surrounding the Chizengeni field site. The confident location of the field site is highlighted within the imagery.

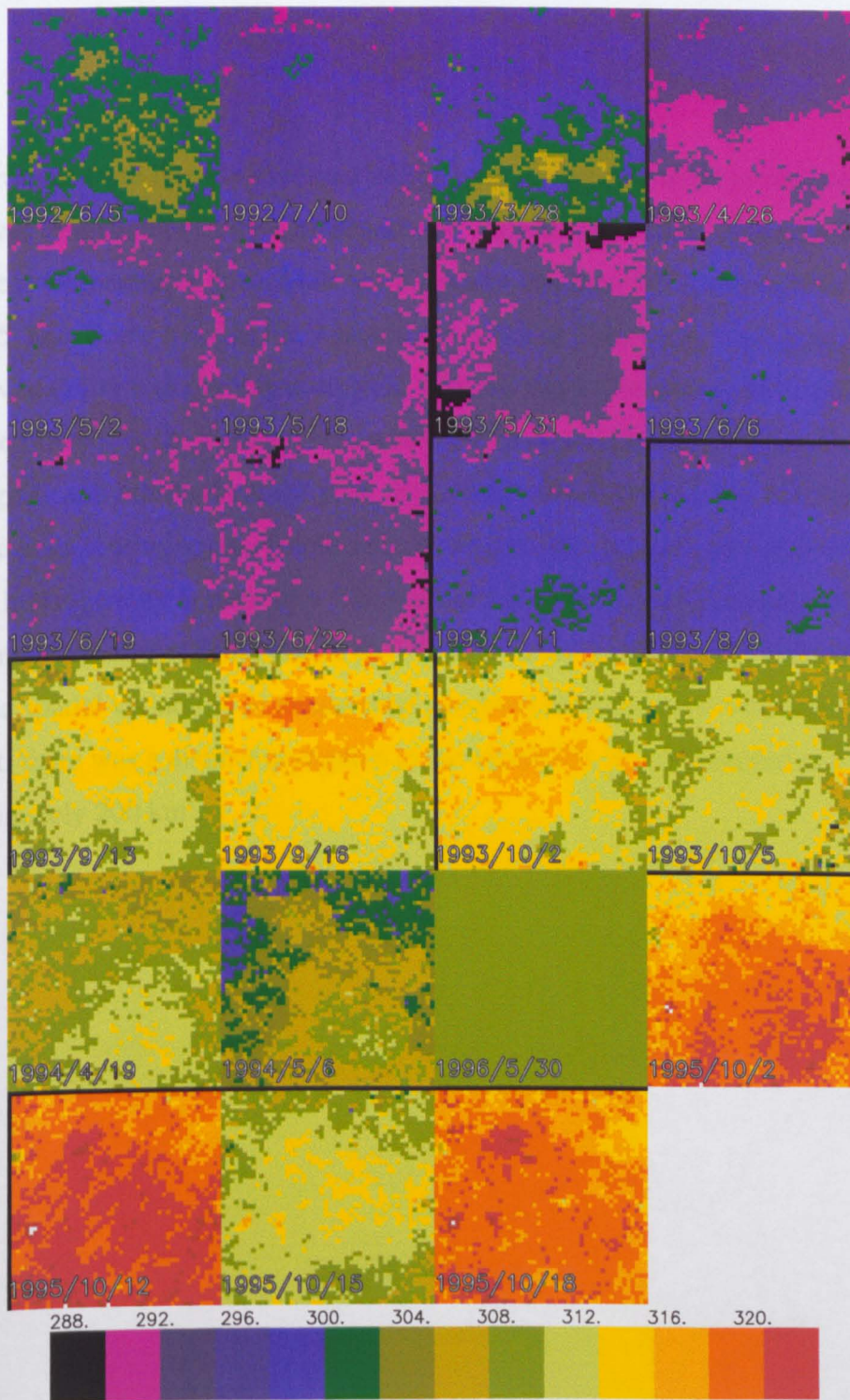


Figure 5-20 ATSR 12 μ m brightness temperature image sequence surrounding the Tambuti field site. The confident location of the field site is highlighted within the imagery.

Temperatures were linearly averaged within each region of interest to represent the mean brightness temperature of the Chizengeni and Tambuti field sites. The standard deviation of brightness temperatures at each site was typically less than 1.5°C throughout the year (see Figure 5-21). Some trend in the standard deviation at Chizengeni was apparent, and the spatial variability was roughly correlated with the vegetation cover. No similar relationship could be inferred at the Tambuti site, where the roughness length of vegetation cover did not vary significantly throughout the year. By considering the variability in brightness temperature at increasing spatial resolutions, it was possible to qualitatively determine the degree of heterogeneity at each site. The standard deviation of temperatures at different spatial resolutions was compared to the baseline variance within each field site. At Chizengeni, the spatial variability in temperature progressively increased with scale, whereas at Tambuti there was a distinct asymptote to the variability which occurred at a resolution of approximately 200 km².

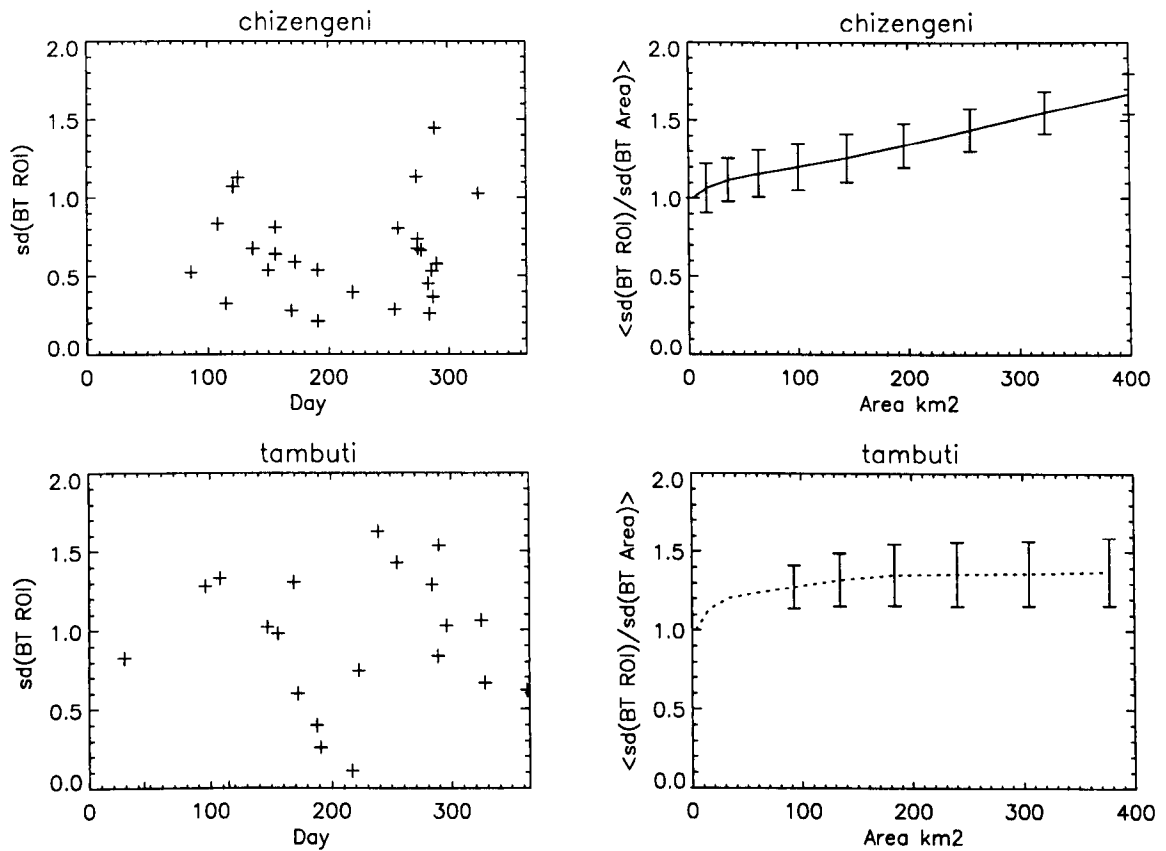


Figure 5-21 ATSR Brightness temperature heterogeneity within the study areas, showing a) the annual variation in the standard deviation of the 12 μm channel at Chizengeni, b) the mean ratio throughout the year of the 12 μm standard deviation at Chizengeni to that of increasingly larger areas centred on the Chizengeni site and c) and d) similar plots for the Tambuti region.

5.4.2 LST estimation

The nadir LST was estimated using both the RAL radiative transfer model and the dual-angle algorithm of Prata. Each method required some ancillary meteorological data to determine the magnitude of the atmospheric correction. Tropospheric temperature and humidity profiles recorded at a nearby meteorological station were used to estimate the atmospheric transmittance and emittance within the ATSR infrared channels.

The surface emissivity of each site was estimated using tabulated data. Compound emissivities were constructed to represent the mean surface emissivity for a heterogeneous surface using linear mixtures of the appropriate vegetation and soil emissivities. For this purpose the fractional vegetation cover was crudely estimated using ATSR 1.6 μm channel data to construct a surface reflectance index. The temporal change of the compound surface emissivity was observed to vary between 0.925 and 0.945 at the Chizengeni site and 0.971 and 0.976 at the Tambuti site. The standard deviation of the compound emissivities was 0.01.

Figure 5-22 shows the temporal variation in LST at Chizengeni calculated using the ATSR 12 μm brightness temperatures with the RADGEN radiative transfer model and the dual-angle algorithm of Prata.

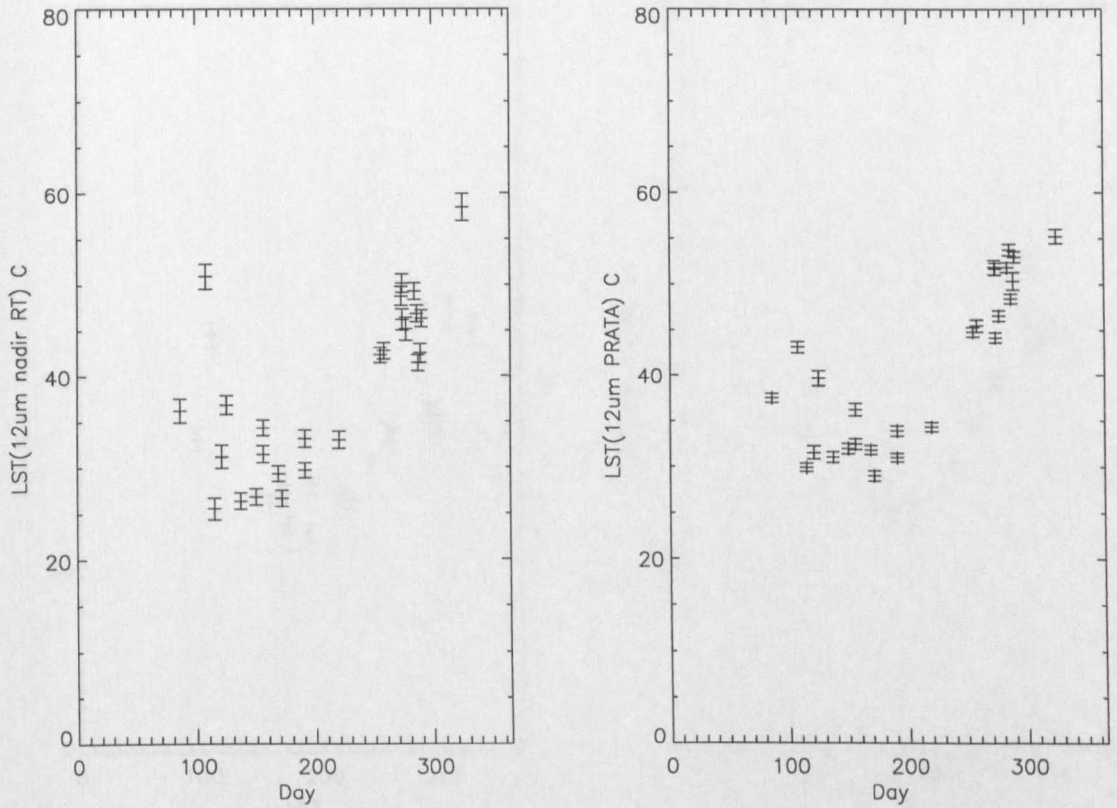


Figure 5-22 Land surface temperature estimated at Chizengeni from ATSR 12 μm data using (a) the RAL radiative transfer model and (b) the dual-angle algorithm of Prata.

The distinct annual trend was apparent in both estimates of LST. The data were recorded between 1991 and 1996, with the majority collected in 1993. Figure 5-23 shows similar plots of LST's derived at the Tambuti site using both techniques.

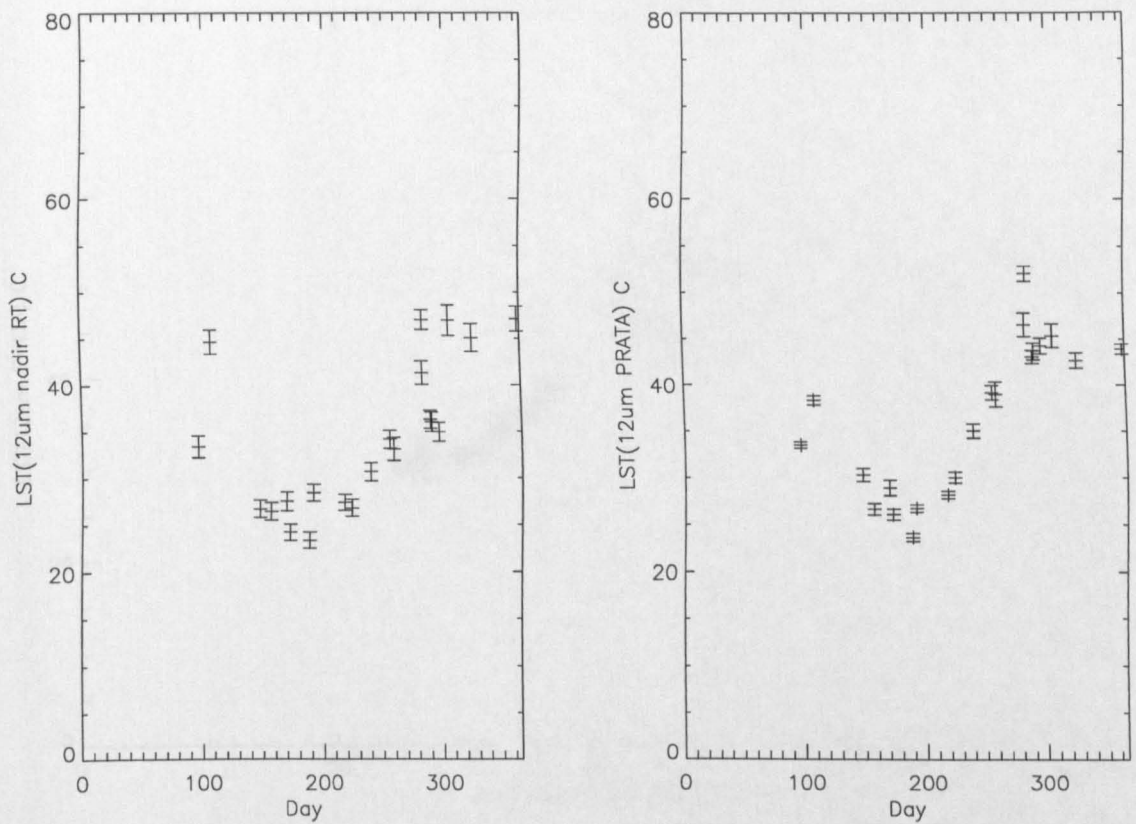
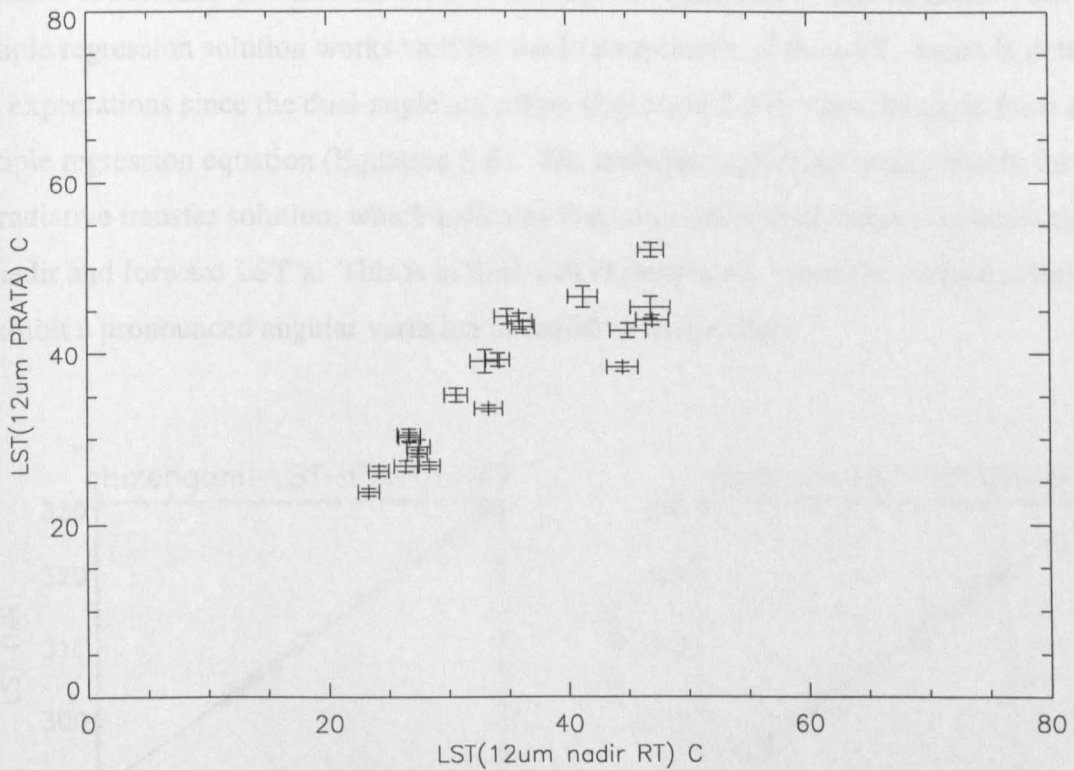


Figure 5-23 Land surface temperature estimated at Tambuti from ATSR 12 μm data using (a) the RAL radiative transfer model and (b) the dual-angle algorithm of Prata.

Scatter plots of the LST estimates (Figure 5-24 and Figure 5-25) highlight the magnitude of the closure between the two methods at the Chizengeni and Tambuti sites. The RAL radiative transfer model and the dual-angle algorithm of Prata agreed more closely over the Chizengeni field area.



Fig

Figure 5-25 Scatter plot of land surface temperatures estimated at Tambuti using the RAL radiative transfer model against the dual-angle algorithm of Prata.

Coefficients relating the LST derived from both the Prata dual-angle algorithm and the RAL radiative transfer model to the ATSR nadir and forward brightness temperatures were derived using multiple linear regression, so that a retrieval algorithm of the form

$$T_S = a_0 T_{nadir} + a_1 T_{forward} + a_2 \quad (5.6)$$

could be used to estimate the LST in the absence of atmospheric data.

Figure 5-26 shows scatter plots of the nadir LST's derived from both the radiative transfer solution and the Prata dual-angle algorithm against the multiple regression solution relating

each LST to the nadir and forward BT's of the ATSR 11 μm and 12 μm channels. The multiple regression solution works well for the Prata estimate of the LST, which is in line with expectations since the dual-angle algorithm (Equation 2-37) takes the same form as the multiple regression equation (Equation 5-6). The multiple regression works poorly for the full radiative transfer solution, which indicates that some additional effect is contributing to the nadir and forward LST's. This is in line with expectations, since the surface is thought to exhibit a pronounced angular variation in radiative temperature.

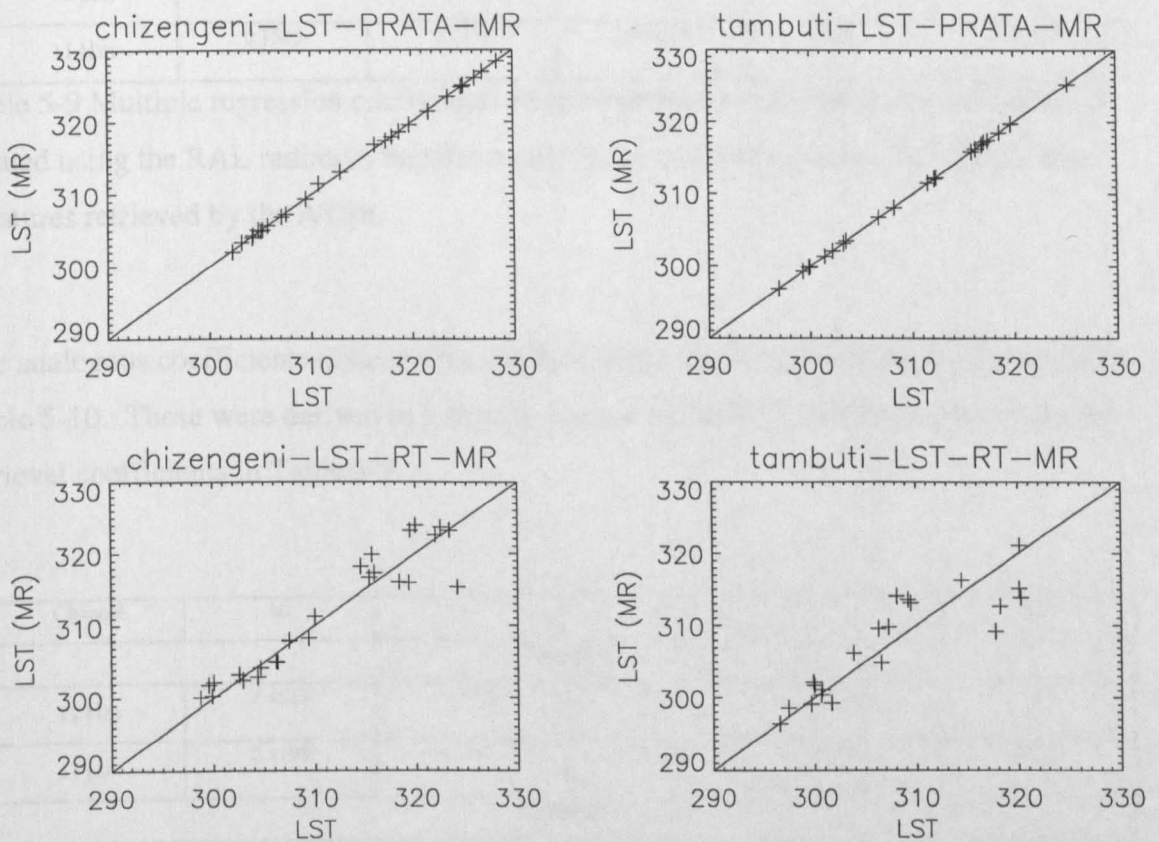


Figure 5-26 Scatter plots of the nadir LST's derived from the full radiative transfer solution (RT) and the Prata dual-angle algorithm (PRATA) against the multiple regression solution relating each LST to the nadir and forward BT's of the ATSR 11 μm and 12 μm channels.

Table 5-9 shows the regression coefficients obtained for the ATSR 11 μm and 12 μm channels using the RAL radiative transfer model LST calculated at Chizengeni and Tambuti.

The Prata and radiative transfer LST retrieval coefficients are empirical and are appropriate for the Chizengeni and Tambuti sites only.

| Channel | a0 | a1 | a2 | r | mad |
|------------------|--------|---------|----------|------|------|
| Chizengeni | | | | | |
| 12 μm | 1.8369 | -0.6452 | -51.6985 | 0.94 | 2.24 |
| 11 μm | 1.0588 | 0.1911 | -68.7642 | 0.98 | 1.49 |
| Tambuti | | | | | |
| 12 μm | 2.0233 | -1.1134 | 28.3427 | 0.88 | 2.83 |
| 11 μm | 0.7585 | 0.7351 | -143.905 | 0.91 | 1.78 |

Table 5-9 Multiple regression coefficients relating the nadir land surface temperature calculated using the RAL radiative transfer model to the nadir and forward brightness temperatures retrieved by the ATSR.

The analogous coefficients obtained for the dual-angle algorithm of Prata are presented in Table 5-10. These were derived in a similar manner to the RAL radiative transfer model retrieval coefficients in Table 5-9.

| Channel | a0 | a1 | a2 | r | Mad |
|------------------|--------|---------|---------|------|------|
| Chizengeni | | | | | |
| 12 μm | 2.4513 | -1.3834 | -14.069 | 0.99 | 0.17 |
| 11 μm | 2.4199 | -1.3577 | -12.867 | 0.99 | 0.16 |
| Tambuti | | | | | |
| 12 μm | 2.4089 | -1.3930 | -2.5975 | 0.99 | 0.03 |
| 11 μm | 2.4166 | -1.4061 | -1.1627 | 0.99 | 0.02 |

Table 5-10 Multiple regression coefficients relating the nadir land surface temperature calculated using the dual-angle algorithm of Prata to the nadir and forward brightness temperatures retrieved by the ATSR.

5.4.3 Angular Variation in LST

Characteristic angular variations of radiative surface temperature were observed over different surface elements at Chizengeni and Tambuti with ground based instrumentation. Using the RAL radiative transfer model to correct ATSR brightness temperatures for atmospheric effects, the apparent LST was estimated at both the nadir and forward viewing angles. The difference between the nadir and forward LST was observed to vary throughout the year at the Chizengeni and Tambuti field sites (Figure 5-27 and Figure 5-28). The angular difference was greater over the Tambuti site than at Chizengeni.

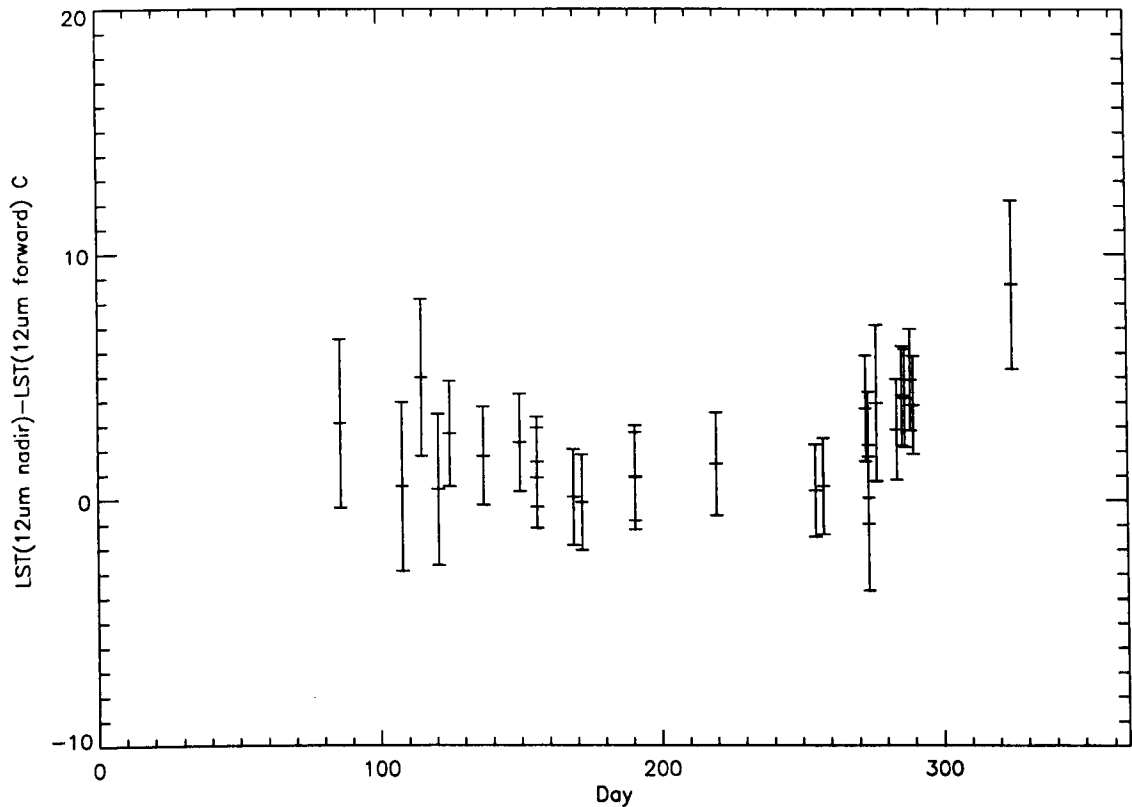


Figure 5-27 Temporal variation in the difference between land surface temperature derived from the ATSR nadir and forward 12 μm channels at Chizengeni.

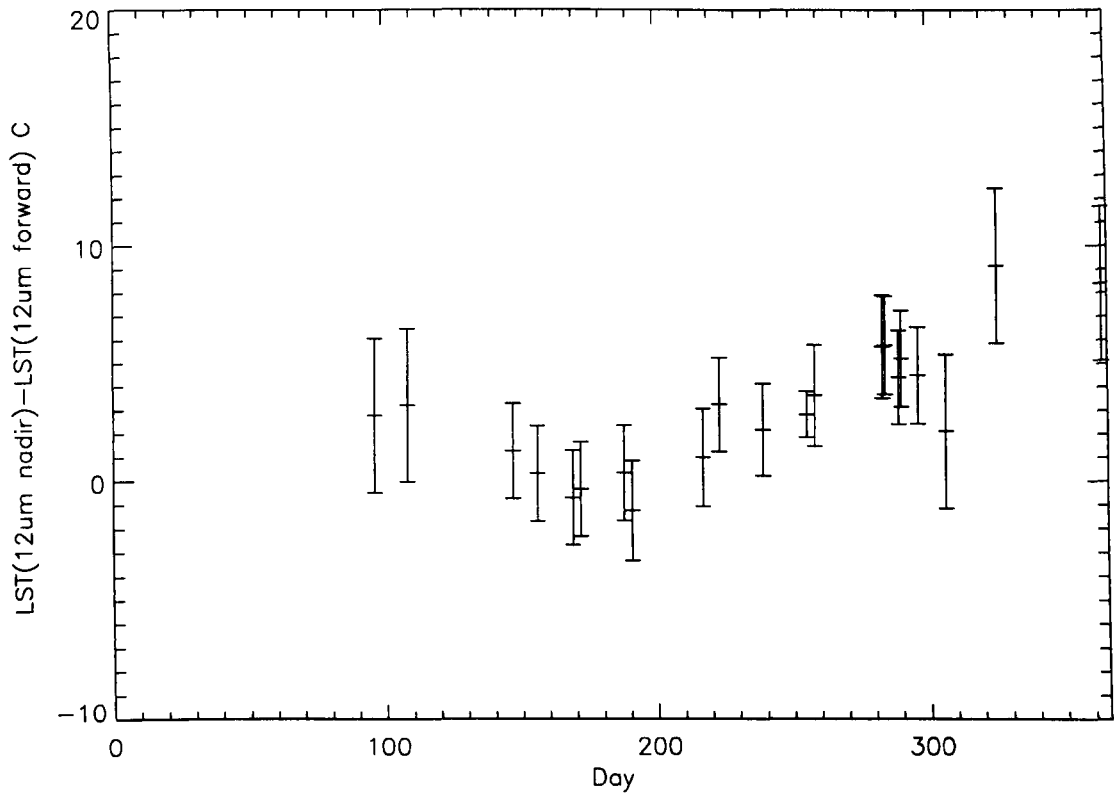


Figure 5-28 Temporal variation in the difference between land surface temperature derived from the ATSR nadir and forward 12 μm channels at Tambuti.

A nadir-forward temperature difference is commonly observed when comparing ATSR BT's, and is a result of the differential atmospheric correction. To establish whether the similar result in LST was valid, and not an artifact of the RAL radiative transfer code, the relationship between BT and LST was investigated. The nadir-forward temperature difference was strongly correlated with temperature for both BT and LST estimates, and on all but 2 occasions the BT nadir-forward difference was greater than the corresponding LST difference. However, the magnitude of the brightness temperature was in all instances smaller than the LST. This is qualitatively in line with expectations, since the radiative transfer code should account for the differential atmospheric attenuation that occurs between the nadir and forward views. If the surface exhibited no angular variation in radiative temperature then the LST nadir-forward difference should reduce to zero after atmospheric correction. However, the LST still exhibits significant nadir-forward differences at both the

Chizengeni and Tambuti field sites (see Figure 5-29 and Figure 5-30), which suggests that the surfaces exhibit some angular variation in radiative temperature detectable at the ATSR satellite resolution.

The angular difference in LST's derived from ATSR dual-angle data at Chizengeni and Tambuti were positively correlated with the nadir surface temperature. Hotter surfaces exhibited greater angular variations in temperature. A scatter plot of the nadir-forward temperature difference against the absolute nadir LST illustrates this relationship (see Figure 5-29 and Figure 5-30). The magnitude of the effect was smaller at Chizengeni than at Tambuti.

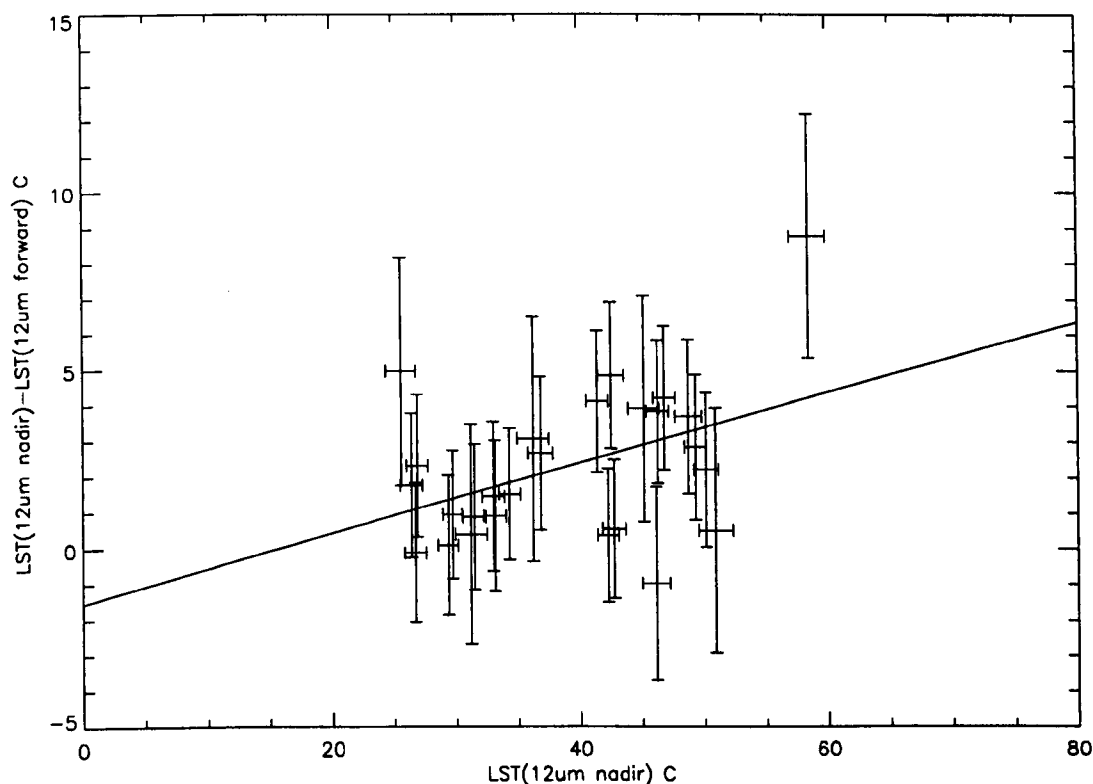


Figure 5-29 Scatter plot of nadir-forward land surface temperature difference against the nadir land surface temperature derived from the ATSR 12 μm channel at Chizengeni.

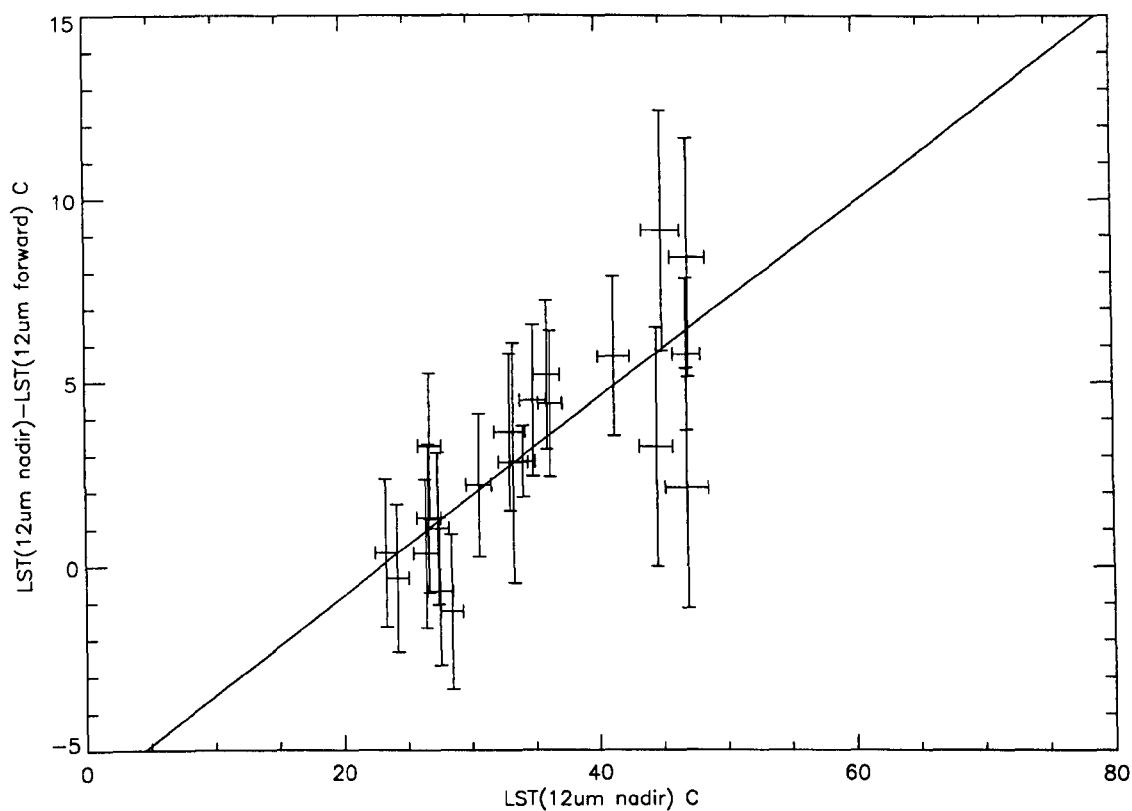


Figure 5-30 Scatter plot of nadir-forward land surface temperature difference against the nadir land surface temperature derived from the ATSR 12 μm channel at Tambuti.

$$T_{forward} = a_0 T_{nadir} + a_1$$

Using a linear parameterisation of the form

(5.7)

the forward (55 degree) LST was related to the nadir LST at each location. Table 5-11 provides a summary of linear regression coefficients relating the nadir and forward LST's at Chizengeni and Tambuti.

| Channel | a0 | a1 | mad | r |
|------------------|--------|--------|------|------|
| Chizengeni | | | | |
| 12 μm | 0.9011 | 28.567 | 1.48 | 0.97 |
| 11 μm | 0.9186 | 23.661 | 0.96 | 0.99 |
| Tambuti | | | | |
| 12 μm | 0.7313 | 79.593 | 1.31 | 0.96 |
| 11 μm | 0.7360 | 78.853 | 1.15 | 0.97 |

Table 5-11 Linear regression coefficients relating the nadir and forward land surface temperatures derived from dual-angle ATSR brightness temperatures.

5.4.4 Mixed Surface LST separation

The radiative temperature of a mixed surface can be described as a linear mixture of distinct component temperatures. In the simplest of cases we can consider only the vegetation and soil components. A surface with heterogeneous vegetation cover can exhibit significant angular variation in radiative temperature when differentials occur between the canopy and soil temperatures. Traditional dual-angle LST algorithms fail to predict the true surface temperature under these circumstances.

Using a canopy architecture model to describe the vegetation fraction presented to an imaging radiometer the angular variation in LST can be estimated. To completely delineate the vegetation and soil temperatures requires radiative temperatures measured at three independent observation angles, since the actual (nadir) vegetation fraction is also unknown.

ATSR dual-angle LST's can be used to infer significant information about a heterogeneous surface. The annual variation in fractional vegetation cover at Chizengeni and Tambuti was poorly documented, and was largely related to the episodic rainfall. Parameterising the annual trend in the vegetation cover could easily bias estimates of component temperatures. The least significant variable is the vegetation temperature, which can only assume a discrete range of values whilst the foliage is photosynthetically active. The soil temperature is restricted principally through the process of evaporation alone.

Using the *in situ* radiometric temperatures recorded at Chizengeni and Tambuti, empirical relationships were established between the soil and vegetation temperature (see Figure 5-16 and Figure 5-17). A hyperbolic relationship was fitted between the soil/understory and vegetation temperatures each instance. At Tambuti, the relationship between canopy and understory (a mixture of soil and grass) temperatures was variable throughout the year (see Figure 5-16). For dense canopies the foliage temperature was close to air temperature, whilst sparse canopy temperatures were similar to the understory temperature. At Chizengeni, the relationship between vegetation and soil temperature did not vary significantly between the two periods of measurement.

To reduce the number of free parameters in the component temperature retrieval model the vegetation temperature was constrained to lie at upper and lower limits (e.g. Figure 5-16). The empirical vegetation and soil temperature relationships derived for each site were used to provide an upper limit for the vegetation temperature. Air temperature was used as a lower estimate for vegetation temperature, which is a reasonable approximation for photosynthetically active vegetation (e.g. Prata, 1994). At these limits the vegetation temperature was related to the soil temperature through hyperbolic relationships empirically determined at each location.

By constraining the vegetation temperature between these fixed boundaries the number of free parameters in the component temperature separation model was reduced to two.

ATSR dual-angle LST's were used in conjunction with high and low temperature constraints to estimate boundaries for the vegetation and soil temperatures and the vegetation fraction. Vegetation temperature estimates derived from the component temperature separation model were not fixed to fall precisely upon the solutions for the upper and lower vegetation temperature constraints. The model derives temperatures such that the mean deviation of soil and vegetation was minimised to produce the least error solution.

The empirically derived relationships between vegetation and soil temperatures at Chizengeni and Tambuti generally provided upper estimates for the vegetation temperature (see Figure 5-31 and Figure 5-32). The absolute temperature deviation was minimised to obtain the vegetation and soil temperature estimates and fractional vegetation cover. The air temperature parameterisation generally produced lower estimates of vegetation temperature

with higher soil temperatures (see Figure 5-33 and Figure 5-34). The fractional vegetation cover calculated under the *in situ* parameterisation exhibits significantly lower temporal variability than the analogous estimate under the air temperature parameterisation.

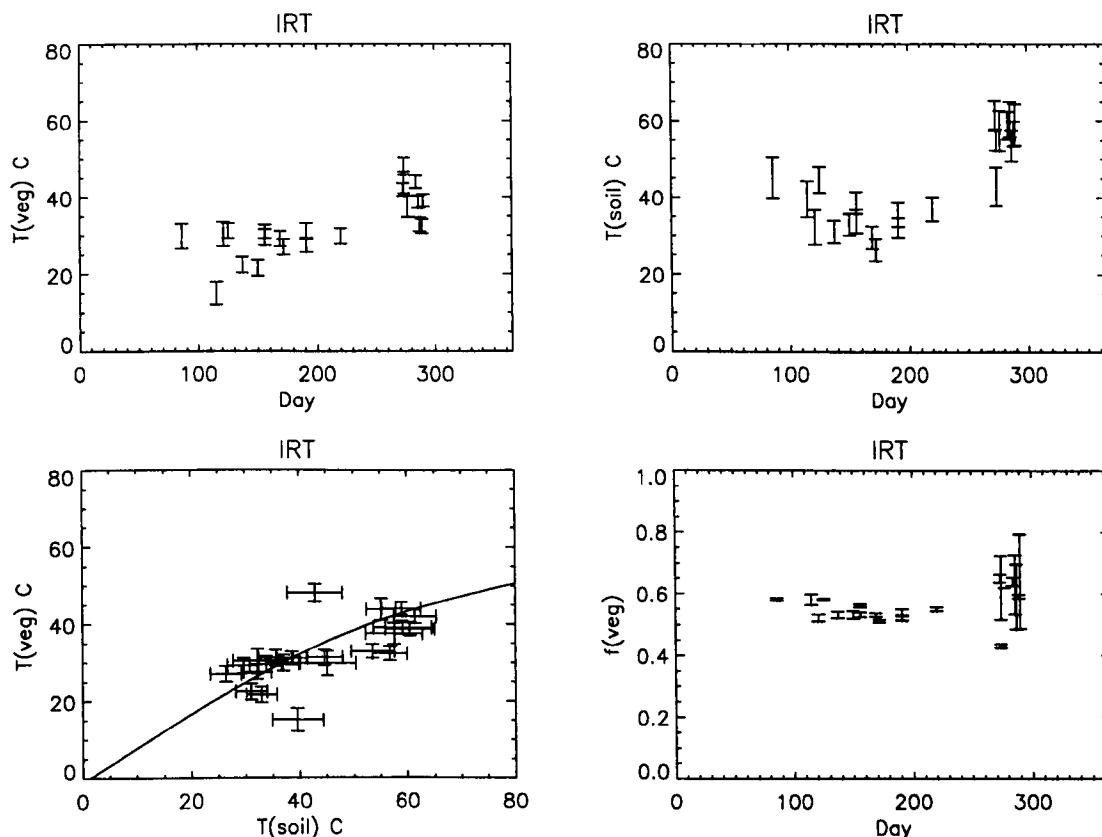


Figure 5-31 Soil and vegetation temperatures and fractional vegetation cover estimated from dual-angle ATSR 12 μm land surface temperatures at Chizengeni. An empirical relationship derived from *in situ* infrared radiometric temperatures was used to constrain the vegetation and soil temperatures.

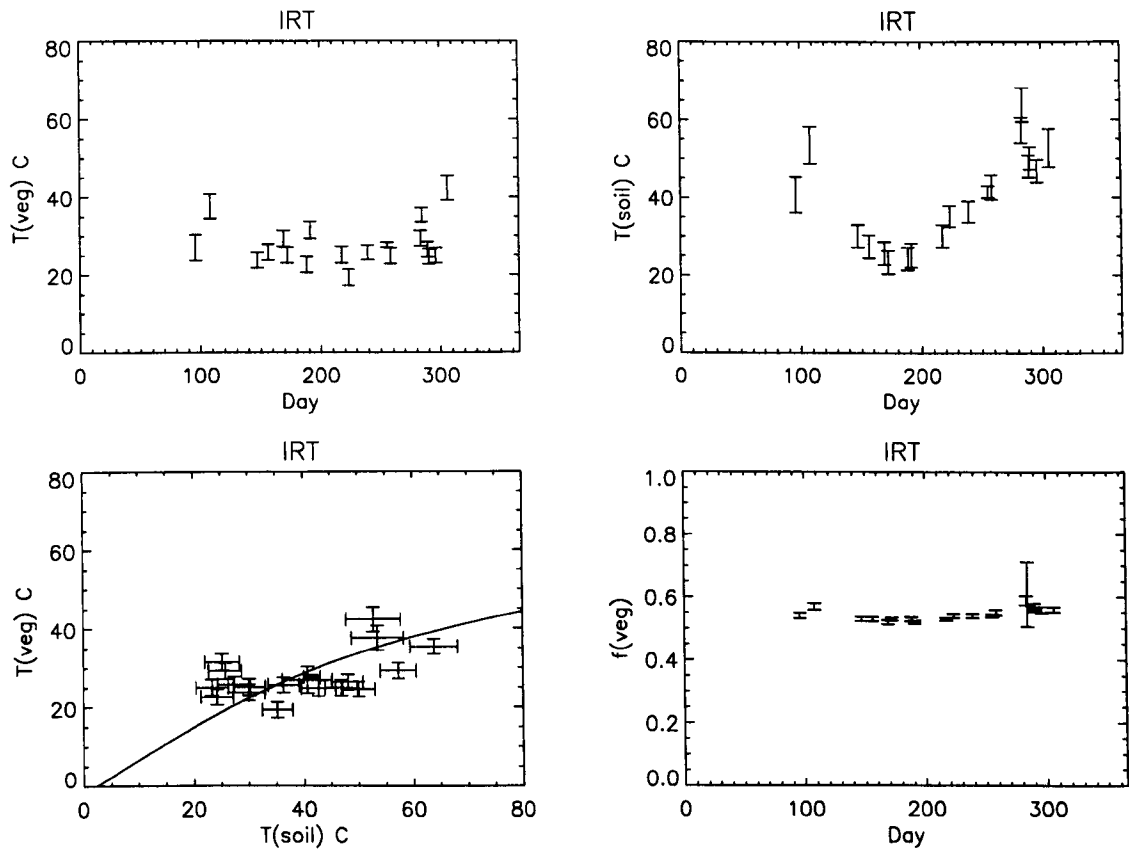


Figure 5-32 Soil and vegetation temperatures and fractional vegetation cover estimated from dual-angle ATSR 12 μm land surface temperatures at Tambuti. An empirical relationship derived from *in situ* infrared radiometric temperatures was used to constrain the vegetation and soil temperatures.

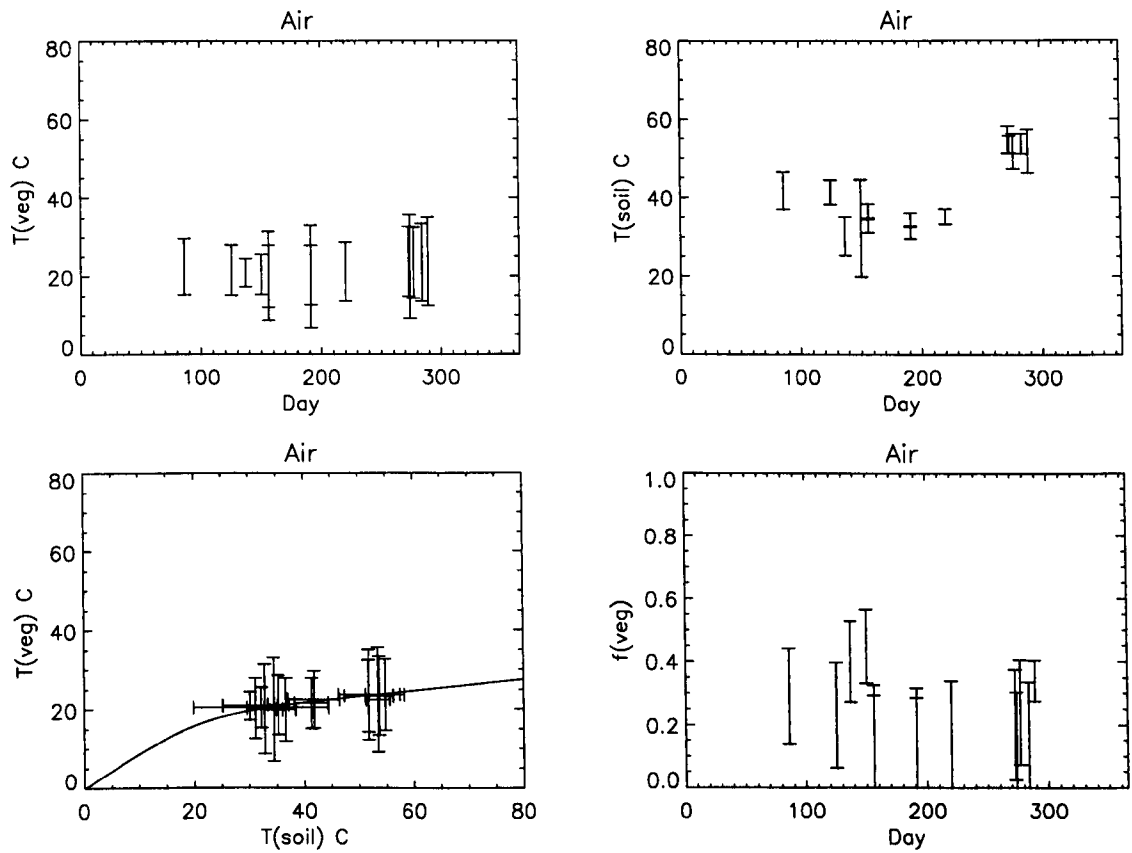


Figure 5-33 Soil and vegetation temperatures and fractional vegetation cover estimated from dual-angle ATSR 12 μm land surface temperatures at Chizengeni. Air temperature was used to constrain the vegetation temperature.

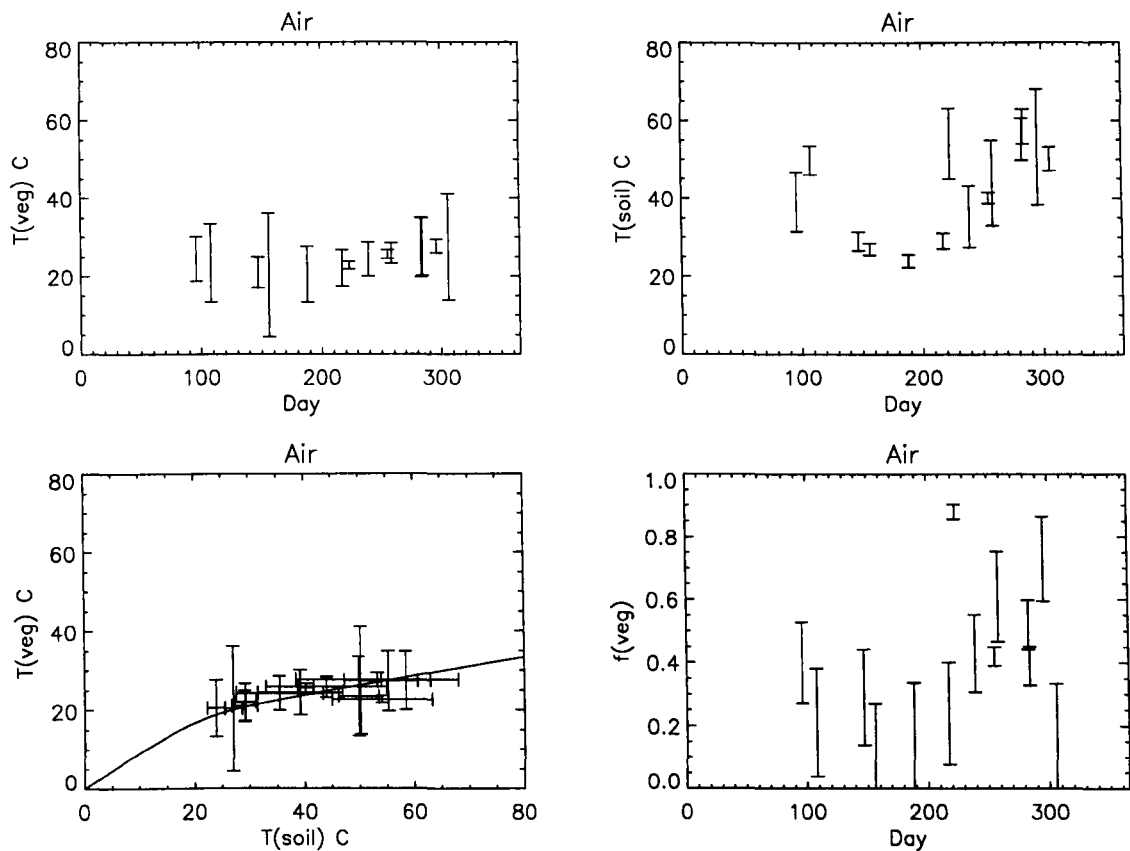


Figure 5-34 Soil and vegetation temperatures and fractional vegetation cover estimated from dual-angle ATSR 12 μm land surface temperatures at Tambuti. Air temperature was used to constrain the vegetation temperature.

Coefficients relating the two estimates of vegetation and soil temperature and fractional vegetation cover to nadir and forward ATSR brightness temperatures were derived using multiple regression. A linear retrieval algorithm of the form

$$P = a_0 T_{nadir} + a_1 T_{forward} + a_2$$

(5.8)

was used to relate each parameter to the ATSR 11 μm and 12 μm brightness temperatures. The coefficients and regression statistics for Chizengeni and Tambuti are presented in Table

5-12 for each method of equation reduction (i.e. using either the empirical IR relationship or the air temperature parameterisation).

| Reduction Method | Channel | Parameter | a0 | a1 | a2 | r | mad |
|-------------------|---------|-------------------|-------|-------|---------|------|------|
| Chizengeni | | | | | | | |
| IR | 12um | T _{VEG} | -1.19 | 2.78 | -167.45 | 0.93 | 2.38 |
| | | T _{SOIL} | 5.18 | -4.53 | 109.52 | 0.93 | 2.99 |
| | | F _{VEG} | 0.01 | -0.01 | 0.01 | 0.59 | 0.02 |
| | 11um | T _{VEG} | -1.05 | 2.49 | -127.91 | 0.93 | 2.19 |
| | | T _{SOIL} | 5.07 | -4.41 | 105.57 | 0.94 | 2.34 |
| | | F _{VEG} | 0.04 | -0.05 | 2.63 | 0.70 | 0.03 |
| AIR | 12um | T _{VEG} | 0.50 | -0.41 | 266.61 | 0.64 | 0.77 |
| | | T _{SOIL} | 4.95 | -4.43 | 142.48 | 0.90 | 3.67 |
| | | F _{VEG} | 0.07 | -0.09 | 7.13 | 0.81 | 0.06 |
| | 11um | T _{VEG} | 0.49 | -0.39 | 262.87 | 0.87 | 0.48 |
| | | T _{SOIL} | 4.38 | -3.65 | 83.32 | 0.91 | 2.96 |
| | | F _{VEG} | 0.09 | -0.12 | 8.10 | 0.73 | 0.08 |
| Tambuti | | | | | | | |
| IR | 12um | T _{VEG} | -1.11 | 2.70 | -168.40 | 0.93 | 2.46 |
| | | T _{SOIL} | 4.63 | -4.10 | 141.10 | 0.89 | 4.04 |
| | | F _{VEG} | 0.01 | -0.01 | 1.25 | 0.74 | 0.02 |
| | 11um | T _{VEG} | -1.17 | 2.66 | -142.74 | 0.93 | 2.30 |
| | | T _{SOIL} | 4.58 | -3.87 | 84.85 | 0.90 | 3.87 |
| | | F _{VEG} | 0.01 | -0.01 | 0.82 | 0.86 | 0.02 |
| AIR | 12um | T _{VEG} | 1.28 | -1.24 | 278.47 | 0.98 | 0.47 |
| | | T _{SOIL} | 6.92 | -7.42 | 438.14 | 0.88 | 4.77 |
| | | F _{VEG} | 0.12 | -0.16 | 12.82 | 0.71 | 0.09 |
| | 11um | T _{VEG} | 0.81 | -0.60 | 233.69 | 0.78 | 0.76 |
| | | T _{SOIL} | 5.52 | -5.29 | 229.87 | 0.78 | 4.76 |
| | | F _{VEG} | 0.10 | -0.13 | 8.97 | 0.77 | 0.07 |

Table 5-12 Multiple regression coefficients relating the vegetation and soil temperature and vegetation fraction to ATSR nadir and forward brightness temperatures at Chizengeni and Tambuti. The dual-angle equations were reduced using the empirical temperature relationships (IR) and the air temperature parameterisation (AIR).

The mean fractional vegetation cover was estimated at Chizengeni and Tambuti as an average of the empirical and air temperature solutions. Regression coefficients were determined for the mean fractional vegetation cover and the retrieval algorithm with the best performance (11 μm or 12 μm) was chosen. The spatial variation in fractional vegetation cover was estimated for each ATSR image by extrapolating the optimal algorithm. Temporal sequences of mean fractional vegetation cover images were produced for the area surrounding the Chizengeni and Tambuti field sites (Figure 5-35 and Figure 5-36). The retrieval algorithms incorporate empirically determined parameters particular to each field site.

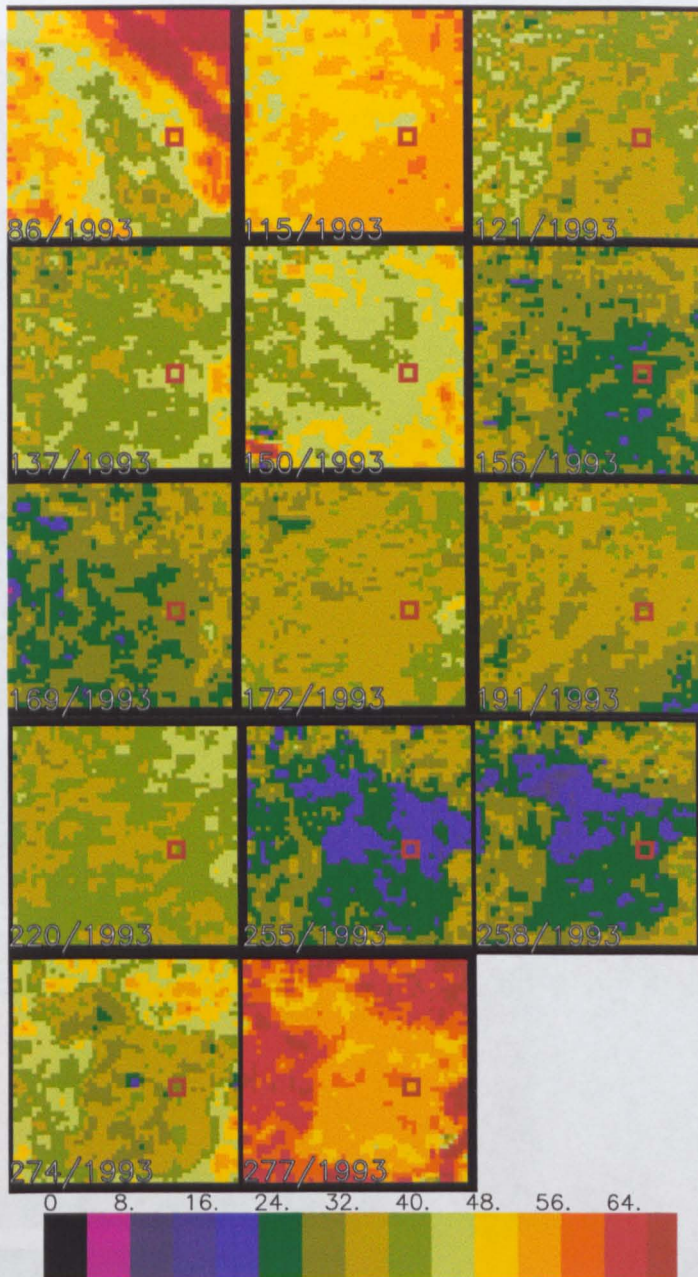


Figure 5-35 Temporal sequence of mean fractional vegetation cover derived from dual-angle ATSR brightness temperatures around the Chizengeni field site.

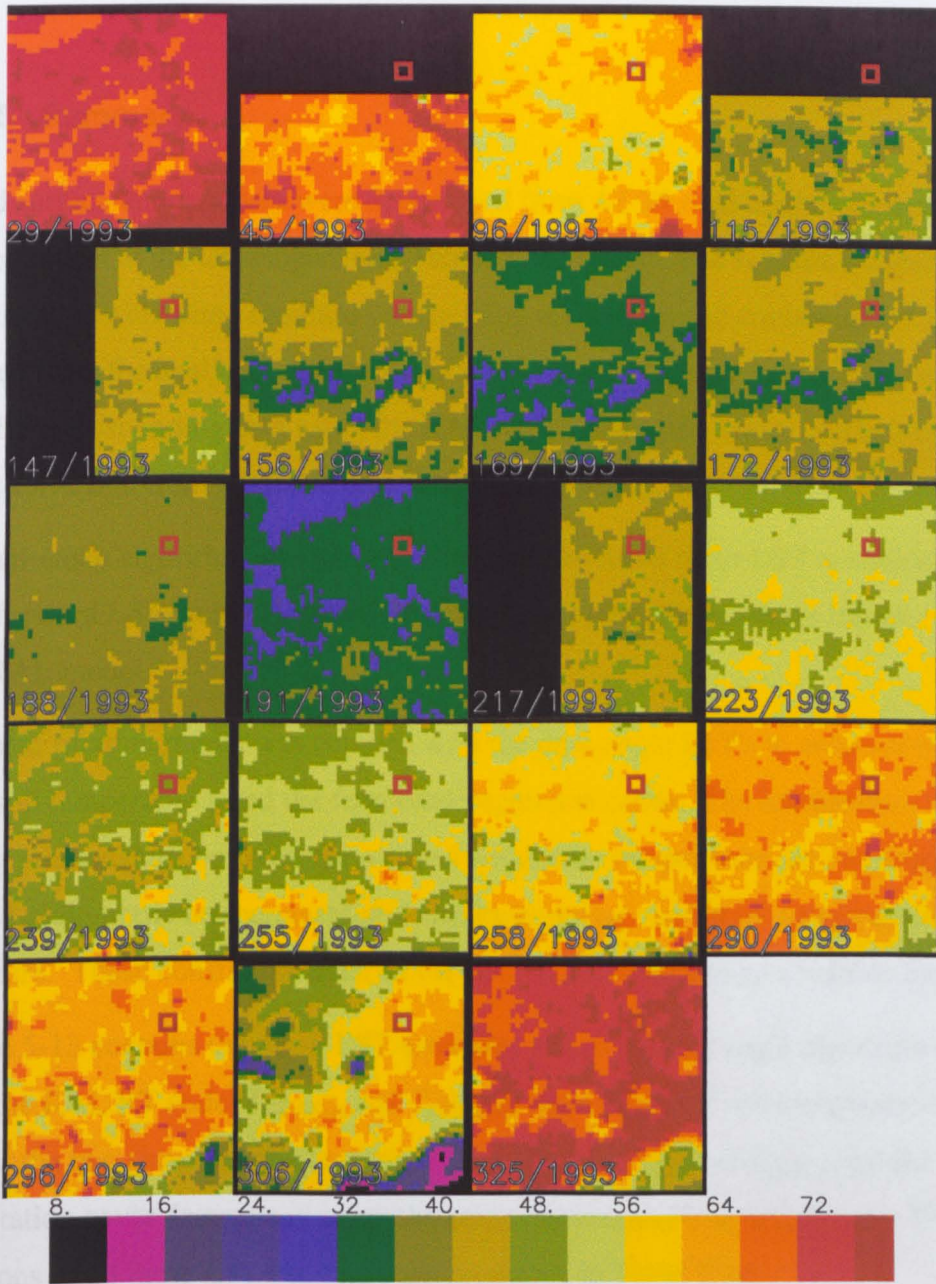


Figure 5-36 Temporal sequence of mean fractional vegetation cover derived from dual-angle ATSR brightness temperatures around the Tambuti field site.

5.4.5 Summary

Land surface temperatures were determined from ATSR dual-angle radiometric brightness temperatures at the Chizengeni and Tambuti field sites. The satellite imagery were filtered for cloudy pixels using standard thresholding techniques and contaminated data were excluded from the analysis. Atmospheric transmittance and emittance were calculated from nearby radiosounding data using the RAL radiative transfer code. Surface emissivity data were estimated from tabulated data within the literature.

A dual-angle algorithm was used to determine the mean nadir LST at each site. The nadir and forward LST were calculated explicitly by solving the radiative transfer equation using the RAL model.

A linear mixture model was coupled with the dual-angle LST's to estimate the vegetation and soil temperatures and the fractional vegetation cover. The temperature were constrained using relationships between the soil and vegetation temperature derived empirically from infrared radiometric temperatures and also by equating vegetation temperature to the air temperature. These constraints reduced the dual-angle equations to a soluble format.

Table 5-13 contains the mean LST estimates using the dual-angle algorithm of Prata T_{PRATA} and the RAL RT code, $T_{RT(NAD)}$ and $T_{RT(FOR)}$, vegetation and soil component LST estimates under the two temperature constraints $T_{V(IR)}$, $T_{V(AIR)}$, $T_{S(IR)}$ and $T_{S(AIR)}$, and the fractional vegetation cover determined using the same constraints $F_{V(IR)}$ and $F_{V(AIR)}$. The standard deviations of all these LST estimates are presented in Table 5-14.

| Date | T _{PRATA} | T _{RT(NAD)} | T _{RT(FOR)} | T _{V(IR)} | T _{V(AIR)} | T _{S(IR)} | T _{S(AIR)} | F _{V(IR)} | F _{V(AIR)} |
|------------------|--------------------|----------------------|----------------------|--------------------|---------------------|--------------------|---------------------|--------------------|---------------------|
| Chizengeni 11 um | | | | | | | | | |
| 1993/86 | 37.53 | 36.23 | 33.16 | 29.77 | 22.46 | 45.17 | 41.78 | 0.58 | 0.29 |
| 1994/108 | 43.13 | 50.95 | 50.44 | - | 15.27 | - | 51.62 | - | 0.02 |
| 1993/115 | 29.97 | 25.58 | 20.62 | 15.04 | - | 39.61 | - | 0.58 | - |
| 1993/121 | 31.61 | 31.22 | 30.83 | 30.30 | 20.92 | 32.26 | 31.77 | 0.52 | 0.05 |
| 1994/125 | 39.71 | 36.83 | 34.16 | 31.22 | 21.55 | 44.64 | 41.33 | 0.58 | 0.23 |
| 1993/137 | 31.10 | 26.41 | 24.65 | 22.34 | 20.88 | 31.10 | 30.17 | 0.53 | 0.40 |
| 1993/150 | 32.04 | 26.88 | 24.57 | 21.52 | 20.46 | 33.00 | 32.18 | 0.53 | 0.45 |
| 1993/156 | 32.53 | 31.50 | 30.63 | 29.49 | 20.02 | 33.85 | 32.79 | 0.53 | 0.10 |
| 1992/156 | 36.29 | 34.34 | 32.82 | 31.03 | 19.94 | 38.66 | 36.67 | 0.56 | 0.14 |
| 1993/169 | 31.89 | 29.37 | 29.28 | 29.16 | - | 29.62 | - | 0.53 | - |
| 1993/172 | 29.06 | 26.72 | 26.84 | 27.01 | - | 26.40 | - | 0.51 | - |
| 1992/191 | 31.03 | 29.73 | 28.79 | 27.52 | 20.27 | 32.22 | 31.16 | 0.52 | 0.13 |
| 1993/191 | 33.93 | 33.15 | 32.25 | 31.12 | 19.87 | 35.63 | 34.47 | 0.54 | 0.09 |
| 1993/220 | 34.38 | 33.01 | 31.56 | 29.79 | 21.10 | 37.05 | 35.29 | 0.55 | 0.16 |
| 1993/255 | 44.84 | 42.28 | 41.91 | - | 25.70 | - | 42.79 | - | 0.03 |
| 1993/258 | 45.52 | 42.76 | 42.21 | - | 24.16 | - | 43.53 | - | 0.04 |
| 1995/273 | 51.92 | 48.75 | 45.04 | 41.89 | 23.67 | 61.42 | 54.75 | 0.65 | 0.20 |
| 1993/274 | 44.21 | 46.16 | 47.14 | 48.03 | - | 42.89 | - | 0.62 | - |
| 1995/274 | 51.73 | 50.18 | 47.96 | 43.73 | 22.43 | 55.15 | 53.47 | 0.43 | 0.11 |
| 1993/277 | 46.59 | 45.17 | 41.24 | 37.50 | 23.36 | 57.55 | 51.79 | 0.62 | 0.24 |
| 1995/284 | 51.88 | 49.31 | 46.46 | 43.96 | 23.44 | 58.91 | 53.69 | 0.64 | 0.15 |
| 1995/286 | 53.84 | 46.82 | 42.59 | 38.70 | 23.19 | 60.47 | 53.96 | 0.63 | 0.24 |
| 1995/287 | 48.46 | 41.42 | 37.29 | 32.88 | 23.40 | 53.55 | 48.91 | 0.59 | 0.30 |
| 1995/289 | 50.41 | 42.51 | 37.64 | 32.38 | 23.76 | 56.75 | 51.81 | 0.59 | 0.34 |
| 1995/290 | 53.05 | 46.29 | 42.44 | 39.04 | 23.92 | 59.09 | 52.73 | 0.64 | 0.23 |
| 1992/325 | 55.28 | 58.47 | 49.70 | - | 23.58 | - | 74.81 | - | 0.34 |
| Chizengeni 12 um | | | | | | | | | |
| 1993/86 | 36.91 | 34.59 | 31.88 | 28.89 | 22.42 | 42.47 | 39.49 | 0.58 | 0.29 |
| 1994/108 | 42.46 | 47.84 | 46.37 | - | 22.29 | - | 49.96 | - | 0.08 |
| 1993/115 | 29.77 | 27.18 | 24.90 | 21.99 | 21.53 | 33.31 | 32.87 | 0.54 | 0.50 |
| 1993/121 | 30.62 | 30.14 | 29.97 | 29.75 | 19.47 | 30.56 | 30.35 | 0.52 | 0.02 |
| 1994/125 | 39.86 | 37.31 | 35.28 | 33.05 | 21.34 | 43.28 | 40.51 | 0.58 | 0.17 |
| 1993/137 | 30.65 | 25.75 | 23.87 | 21.39 | 20.88 | 30.74 | 30.30 | 0.53 | 0.48 |
| 1993/150 | 32.23 | 27.50 | 25.61 | 23.09 | 20.37 | 32.54 | 31.20 | 0.53 | 0.34 |
| 1993/156 | 31.34 | 30.89 | 30.67 | 30.36 | 21.17 | 31.47 | 31.18 | 0.52 | 0.03 |
| 1992/156 | 35.12 | 33.90 | 33.05 | 31.98 | 19.64 | 36.24 | 35.13 | 0.54 | 0.08 |
| 1993/169 | 31.39 | 28.86 | 28.81 | 28.75 | - | 28.95 | - | 0.51 | - |
| 1993/172 | 28.30 | 25.50 | 25.27 | 24.95 | 19.49 | 26.10 | 25.82 | 0.51 | 0.05 |
| 1992/191 | 30.70 | 29.62 | 28.90 | 27.93 | 20.13 | 31.53 | 30.68 | 0.52 | 0.10 |
| 1993/191 | 33.12 | 32.51 | 32.06 | 31.47 | 20.49 | 33.73 | 33.14 | 0.53 | 0.05 |
| 1993/220 | 34.57 | 33.19 | 32.06 | 30.63 | 20.67 | 36.29 | 34.89 | 0.54 | 0.12 |
| 1993/255 | 44.82 | 41.94 | 41.29 | - | 24.27 | - | 42.85 | - | 0.05 |
| 1993/258 | 45.30 | 42.11 | 41.18 | 39.44 | 21.01 | 44.18 | 43.40 | 0.43 | 0.06 |
| 1995/273 | 49.19 | 47.19 | 45.40 | 42.24 | 22.42 | 51.33 | 49.81 | 0.45 | 0.10 |
| 1993/274 | 44.15 | 44.32 | 44.27 | - | - | - | - | - | - |
| 1995/274 | 52.78 | 50.50 | 48.39 | 43.64 | 23.73 | 54.95 | 53.63 | 0.39 | 0.11 |
| 1993/277 | 47.28 | 44.53 | 41.10 | 37.95 | 23.52 | 55.62 | 50.19 | 0.63 | 0.22 |
| 1995/284 | 52.75 | 50.14 | 47.87 | 43.70 | 24.06 | 55.25 | 53.50 | 0.44 | 0.12 |
| 1995/286 | 49.29 | 45.08 | 43.43 | 41.49 | 22.39 | 49.76 | 47.50 | 0.56 | 0.10 |
| 1995/287 | 49.79 | 43.75 | 40.40 | 37.20 | 23.26 | 54.34 | 49.28 | 0.62 | 0.22 |
| 1995/289 | 50.53 | 43.52 | 39.46 | 35.26 | 23.45 | 55.66 | 50.59 | 0.60 | 0.27 |
| 1995/290 | 54.23 | 48.45 | 45.40 | 42.82 | 23.96 | 58.85 | 53.20 | 0.65 | 0.17 |
| 1992/325 | 51.45 | 55.49 | 50.38 | - | 23.23 | - | 63.82 | - | 0.22 |

Table 5-13 Mean and component land surface temperatures derived from dual-angle ATSR brightness temperatures at Chizengeni and Tambuti using the algorithm of Prata, the RAL radiative transfer code and a semi-empirical linear mixture model to delineate vegetation and soil components.

| Date | T _{PRATA} | T _{RT(NAD)} | T _{RT(FOR)} | T _{V(IR)} | T _{V(AIR)} | T _{S(IR)} | T _{S(AIR)} | F _{V(IR)} | F _{V(AIR)} |
|------------------|--------------------|----------------------|----------------------|--------------------|---------------------|--------------------|---------------------|--------------------|---------------------|
| Tambuti 11.11.11 | | | | | | | | | |
| 1993/96 | 33.53 | 33.41 | 30.62 | 26.98 | 24.42 | 40.68 | 39.16 | 0.54 | 0.40 |
| 1994/108 | 38.37 | 44.61 | 41.39 | 37.62 | 23.50 | 53.49 | 49.81 | 0.57 | 0.21 |
| 1993/147 | 30.34 | 26.75 | 25.48 | 23.78 | 21.04 | 30.05 | 29.04 | 0.53 | 0.29 |
| 1993/156 | 26.69 | 26.51 | 26.20 | 25.77 | 20.34 | 27.35 | 26.97 | 0.53 | 0.07 |
| 1993/169 | 28.98 | 27.58 | 28.29 | 29.26 | - | 25.72 | - | 0.52 | - |
| 1993/172 | 26.11 | 24.26 | 24.61 | 25.05 | - | 23.36 | - | 0.53 | - |
| 1993/188 | 23.70 | 23.40 | 23.07 | 22.63 | 20.50 | 24.27 | 23.91 | 0.53 | 0.15 |
| 1993/191 | 26.76 | 28.49 | 29.75 | 31.46 | - | 25.17 | - | 0.52 | - |
| 1993/217 | 28.22 | 27.47 | 26.48 | 25.16 | 22.05 | 30.06 | 29.15 | 0.53 | 0.24 |
| 1993/223 | 30.05 | 26.84 | 23.60 | 19.36 | 22.74 | 35.22 | 54.09 | 0.54 | 0.88 |
| 1993/239 | 35.06 | 30.70 | 28.53 | 25.73 | 24.29 | 36.36 | 35.38 | 0.54 | 0.43 |
| 1993/255 | 39.19 | 34.17 | 31.35 | 27.69 | 25.58 | 41.49 | 40.13 | 0.54 | 0.42 |
| 1993/258 | 39.02 | 33.13 | 29.51 | 24.93 | 25.86 | 42.66 | 43.93 | 0.55 | 0.61 |
| 1995/283 | 46.58 | 41.30 | 35.61 | 29.32 | 27.41 | 57.25 | 55.21 | 0.59 | 0.52 |
| 1995/284 | 52.11 | 46.98 | 41.23 | 35.37 | 27.54 | 63.84 | 58.41 | 0.61 | 0.39 |
| 1995/289 | 43.08 | 36.31 | 31.92 | 26.52 | 27.62 | 48.03 | 49.63 | 0.56 | 0.62 |
| 1993/290 | 43.69 | 36.05 | 30.86 | 24.68 | 27.61 | 50.05 | 57.01 | 0.57 | 0.73 |
| 1993/296 | 44.26 | 34.96 | 30.48 | 24.99 | 27.70 | 46.87 | 53.20 | 0.56 | 0.73 |
| 1993/306 | 45.38 | 46.96 | 44.85 | 42.32 | 27.51 | 52.75 | 50.19 | 0.56 | 0.15 |
| 1993/325 | 42.69 | 45.07 | 35.93 | - | 28.71 | - | 75.57 | - | 0.68 |
| 1992/363 | 43.87 | 47.10 | 38.69 | - | 27.25 | - | 67.90 | - | 0.54 |
| Tambuti 12.11.11 | | | | | | | | | |
| 1993/96 | 34.79 | 33.79 | 31.76 | 29.12 | 24.54 | 39.11 | 37.41 | 0.54 | 0.29 |
| 1994/108 | 39.51 | 44.11 | 40.41 | 36.23 | 22.86 | 54.38 | 50.22 | 0.58 | 0.24 |
| 1993/147 | 31.08 | 27.77 | 26.80 | 25.50 | 20.96 | 30.30 | 29.33 | 0.53 | 0.19 |
| 1993/156 | 27.50 | 27.25 | 26.98 | 26.62 | 21.15 | 27.96 | 27.63 | 0.53 | 0.06 |
| 1993/169 | 29.52 | 27.52 | 27.73 | 28.01 | - | 26.96 | - | 0.53 | - |
| 1993/172 | 25.22 | 23.50 | 24.10 | 24.92 | - | 21.93 | - | 0.52 | - |
| 1993/188 | 22.84 | 23.53 | 24.13 | 24.95 | - | 21.96 | - | 0.52 | - |
| 1993/191 | 27.15 | 28.24 | 29.08 | 30.22 | - | 26.03 | - | 0.52 | - |
| 1993/217 | 27.77 | 28.16 | 28.46 | 28.87 | - | 27.38 | - | 0.52 | - |
| 1993/223 | 30.08 | 27.77 | 25.72 | 23.06 | 22.74 | 33.13 | 32.84 | 0.54 | 0.51 |
| 1993/239 | 36.04 | 31.55 | 29.27 | 26.30 | 24.21 | 37.50 | 36.26 | 0.54 | 0.40 |
| 1993/255 | 40.96 | 35.26 | 31.78 | 27.37 | 25.59 | 44.38 | 43.04 | 0.55 | 0.46 |
| 1993/258 | 40.95 | 34.68 | 30.69 | 25.79 | 25.79 | 45.27 | 45.27 | 0.56 | 0.56 |
| 1995/283 | 43.84 | 41.23 | 38.78 | 35.71 | 27.45 | 47.75 | 45.34 | 0.55 | 0.24 |
| 1995/284 | 54.19 | 49.14 | 44.46 | 39.53 | 27.12 | 62.58 | 57.29 | 0.60 | 0.29 |
| 1995/289 | 44.65 | 38.71 | 35.07 | 30.62 | 27.50 | 48.43 | 46.35 | 0.56 | 0.42 |
| 1993/290 | 43.64 | 37.23 | 33.19 | 28.23 | 27.64 | 47.96 | 47.36 | 0.56 | 0.53 |
| 1993/296 | 44.54 | 36.85 | 33.84 | 30.04 | 27.62 | 44.80 | 43.21 | 0.55 | 0.42 |
| 1993/306 | 45.09 | 45.03 | 43.67 | 41.96 | 27.65 | 48.73 | 47.05 | 0.55 | 0.11 |
| 1993/325 | 43.36 | 45.20 | 37.04 | 29.76 | 28.83 | 70.31 | 68.62 | 0.65 | 0.62 |
| 1992/363 | 45.88 | 47.65 | 38.77 | - | 27.42 | - | 70.06 | - | 0.56 |

Table 5-13 (continued) Mean and component land surface temperatures derived from dual-angle ATSR

brightness temperatures at Chizengeni and Tambuti using the algorithm of Prata, the RAL radiative transfer code and a semi-empirical linear mixture model to delineate vegetation and soil components.

| Date | SPRATA | SRT(NAD) | SRT(FOR) | SV(IR) | SV(AIR) | SS(IR) | SS(AIR) | SFV(IR) | SFV(AIR) |
|------------------|--------|----------|----------|--------|---------|--------|---------|---------|----------|
| Chizengeni 11 um | | | | | | | | | |
| 1993/86 | 0.98 | 2.56 | 6.39 | 6.38 | 14.32 | 10.60 | 9.39 | 0.01 | 0.30 |
| 1994/108 | 1.33 | 2.77 | 6.28 | - | 130.65 | - | 4.92 | - | 0.42 |
| 1993/115 | 0.89 | 2.37 | 5.94 | 6.01 | - | 9.39 | - | 0.03 | - |
| 1993/121 | 1.46 | 2.55 | 5.62 | 6.33 | 62.30 | 9.09 | 4.55 | 0.02 | 0.41 |
| 1994/125 | 1.69 | 2.01 | 3.81 | 3.94 | 12.81 | 6.76 | 6.11 | 0.00 | 0.33 |
| 1993/137 | 1.18 | 1.79 | 3.61 | 4.10 | 7.07 | 5.83 | 9.94 | 0.02 | 0.26 |
| 1993/150 | 1.08 | 1.75 | 3.57 | 4.07 | 10.20 | 5.66 | 24.67 | 0.03 | 0.23 |
| 1993/156 | 1.14 | 1.84 | 3.65 | 4.11 | 22.70 | 6.04 | 3.31 | 0.02 | 0.39 |
| 1992/156 | 1.37 | 1.75 | 3.24 | 3.47 | 15.96 | 5.68 | 3.58 | 0.01 | 0.37 |
| 1993/169 | 0.94 | 1.66 | 3.55 | 3.94 | - | 5.83 | - | 0.01 | - |
| 1993/172 | 1.08 | 1.75 | 3.49 | 4.08 | - | 5.69 | - | 0.01 | - |
| 1992/191 | 0.95 | 1.57 | 3.23 | 3.72 | 15.30 | 5.17 | 3.05 | 0.01 | 0.38 |
| 1993/191 | 1.07 | 1.85 | 3.80 | 4.17 | 26.14 | 6.32 | 3.35 | 0.02 | 0.39 |
| 1993/220 | 0.98 | 1.84 | 3.76 | 4.07 | 15.02 | 6.32 | 3.92 | 0.01 | 0.36 |
| 1993/255 | 1.02 | 1.66 | 3.39 | - | 130.15 | - | 2.77 | - | 0.42 |
| 1993/258 | 1.33 | 1.85 | 3.43 | - | 54.64 | - | 2.97 | - | 0.41 |
| 1995/273 | 1.60 | 2.11 | 3.78 | 3.41 | 17.78 | 7.81 | 7.07 | 0.03 | 0.35 |
| 1993/274 | 1.16 | 2.26 | 4.95 | 4.58 | - | 10.13 | - | 0.21 | - |
| 1995/274 | 1.31 | 1.99 | 3.84 | 5.63 | 26.55 | 5.33 | 4.30 | 0.01 | 0.39 |
| 1993/277 | 1.13 | 2.51 | 5.85 | 5.46 | 18.06 | 10.49 | 8.96 | - | 0.33 |
| 1995/284 | 1.07 | 1.79 | 3.68 | 3.31 | 19.82 | 7.22 | 5.03 | 0.03 | 0.37 |
| 1995/286 | 1.22 | 1.79 | 3.62 | 3.36 | 41.32 | 9.14 | 10.14 | 0.20 | 0.10 |
| 1995/287 | 1.11 | 1.73 | 3.58 | 3.63 | 45.70 | 8.05 | 12.20 | 0.21 | 0.13 |
| 1995/289 | 1.86 | 2.10 | 3.56 | 3.71 | 22.79 | 6.41 | 11.22 | 0.01 | 0.13 |
| 1995/290 | 1.23 | 1.82 | 3.58 | 3.32 | 123.46 | 10.73 | 10.58 | 0.31 | 0.11 |
| 1992/325 | 1.50 | 2.91 | 6.20 | - | 42.88 | - | 5.25 | - | 0.12 |
| Chizengeni 12 um | | | | | | | | | |
| 1993/86 | 0.90 | 1.44 | 3.62 | 3.63 | 9.77 | 5.86 | 7.18 | 0.01 | 0.31 |
| 1994/108 | 1.12 | 1.90 | 4.74 | - | 32.70 | - | 3.96 | - | 0.40 |
| 1993/115 | 0.78 | 1.31 | 3.38 | 3.67 | 21.25 | 5.07 | 124.44 | 0.02 | 0.21 |
| 1993/121 | 1.34 | 1.53 | 3.43 | 3.88 | 127.60 | 5.49 | 2.69 | 0.01 | 0.43 |
| 1994/125 | 1.32 | 1.20 | 2.75 | 2.78 | 12.22 | 4.60 | 3.74 | 0.00 | 0.36 |
| 1993/137 | 1.22 | 1.30 | 2.79 | 3.16 | 12.07 | 4.35 | 123.54 | 0.02 | 0.22 |
| 1993/150 | 1.13 | 1.25 | 2.72 | 3.09 | 6.66 | 4.24 | 6.82 | 0.02 | 0.28 |
| 1993/156 | 1.12 | 1.21 | 2.55 | 2.92 | 45.91 | 4.11 | 2.05 | 0.01 | 0.42 |
| 1992/156 | 1.18 | 1.13 | 2.34 | 2.58 | 19.17 | 3.85 | 2.16 | 0.01 | 0.40 |
| 1993/169 | 0.82 | 1.04 | 2.70 | 3.08 | - | 4.05 | - | 0.01 | - |
| 1993/172 | 1.04 | 1.22 | 2.64 | 3.07 | 30.17 | 4.13 | 2.13 | 0.01 | 0.41 |
| 1992/191 | 1.07 | 1.14 | 2.25 | 2.61 | 14.31 | 3.63 | 2.11 | 0.01 | 0.39 |
| 1993/191 | 0.98 | 1.16 | 2.55 | 2.84 | 30.13 | 4.10 | 2.08 | 0.01 | 0.42 |
| 1993/220 | 0.84 | 1.24 | 2.62 | 2.88 | 14.29 | 4.25 | 2.62 | 0.01 | 0.38 |
| 1993/255 | 0.97 | 1.18 | 2.62 | - | 30.25 | - | 2.17 | - | 0.42 |
| 1993/258 | 1.18 | 1.30 | 2.64 | 3.80 | 30.42 | 3.66 | 2.39 | 0.01 | 0.41 |
| 1995/273 | 0.90 | 1.03 | 2.60 | 3.50 | 19.44 | 3.40 | 2.87 | 0.01 | 0.39 |
| 1993/274 | 1.28 | 1.47 | 3.09 | - | - | - | - | - | - |
| 1995/274 | 1.27 | 1.28 | 2.68 | 4.34 | 20.34 | 3.42 | 3.42 | 0.07 | 0.39 |
| 1993/277 | 1.06 | 1.46 | 3.48 | 3.19 | 14.18 | 6.23 | 6.62 | 0.01 | 0.34 |
| 1995/284 | 1.04 | 1.13 | 2.56 | 3.61 | 18.29 | 3.40 | 3.51 | 0.00 | 0.38 |
| 1995/286 | 0.94 | 1.05 | 2.86 | 2.94 | 19.57 | 4.45 | 2.84 | 0.01 | 0.39 |
| 1995/287 | 1.01 | 1.13 | 2.80 | 2.59 | 25.01 | 6.87 | 8.18 | 0.20 | 0.09 |
| 1995/289 | 1.67 | 1.52 | 2.72 | 2.75 | 15.82 | 4.90 | 7.48 | 0.01 | 0.09 |
| 1995/290 | 1.12 | 1.22 | 2.81 | 2.50 | 123.75 | 9.86 | 10.03 | 0.31 | 0.08 |
| 1992/325 | 0.84 | 1.62 | 4.87 | - | 124.73 | - | 6.99 | - | 0.10 |

Table 5-14 Standard deviations of the mean and component land surface temperatures derived from dual-angle ATSR brightness temperatures at Chizengeni and Tambuti using the algorithm of Prata, the RAL radiative transfer code and a semi-empirical linear mixture model to delineate vegetation and soil components.

| Date | SPRATA | SRT(NAD) | SRT(FOR) | SV(IR) | SV(AIR) | SS(IR) | SS(AIR) | SFV(IR) | SFV(AIR) |
|---------------|--------|----------|----------|--------|---------|--------|---------|---------|----------|
| Tambuti 12.11 | | | | | | | | | |
| 1993/96 | 0.70 | 2.30 | 6.13 | 6.69 | 11.33 | 9.05 | 15.36 | 0.02 | 0.26 |
| 1994/108 | 0.98 | 2.59 | 5.98 | 6.22 | 20.01 | 9.59 | 7.34 | 0.02 | 0.34 |
| 1993/147 | 1.38 | 1.88 | 3.55 | 4.11 | 7.88 | 5.75 | 4.71 | 0.01 | 0.31 |
| 1993/156 | 1.29 | 1.93 | 3.54 | 4.08 | 31.63 | 5.92 | 3.13 | 0.01 | 0.40 |
| 1993/169 | 1.61 | 1.97 | 3.47 | 4.07 | - | 5.93 | - | 0.01 | - |
| 1993/172 | 1.14 | 1.71 | 3.60 | 4.05 | - | 5.86 | - | 0.01 | - |
| 1993/188 | 0.90 | 1.73 | 3.61 | 4.08 | 14.24 | 5.78 | 3.23 | 0.01 | 0.37 |
| 1993/191 | 0.82 | 1.75 | 3.81 | 4.32 | - | 6.16 | - | 0.01 | - |
| 1993/217 | 0.79 | 1.67 | 3.79 | 4.26 | 9.37 | 5.84 | 3.92 | 0.01 | 0.32 |
| 1993/223 | 1.16 | 1.83 | 3.54 | 4.06 | 1.94 | 5.53 | 18.19 | 0.01 | 0.05 |
| 1993/239 | 1.55 | 1.95 | 3.37 | 3.90 | 8.65 | 5.64 | 15.73 | 0.01 | 0.24 |
| 1993/255 | 1.54 | 1.94 | - | 1.19 | 2.27 | 3.01 | 2.84 | 0.01 | 0.06 |
| 1993/258 | 2.66 | 2.45 | 3.53 | 4.16 | 5.18 | 6.26 | 21.97 | 0.02 | 0.29 |
| 1995/283 | 2.52 | 2.48 | 3.59 | 3.90 | 15.26 | 6.62 | 10.80 | 0.03 | 0.16 |
| 1995/284 | 1.64 | 2.11 | 3.58 | 3.74 | 14.88 | 8.68 | 8.94 | 0.21 | 0.12 |
| 1995/289 | 1.41 | 1.90 | 3.52 | 3.92 | 9.57 | 5.69 | 131.13 | 0.02 | 0.23 |
| 1993/290 | 1.83 | 2.09 | 3.50 | 3.89 | 5.53 | 5.88 | 134.08 | 0.02 | 0.22 |
| 1993/296 | 1.77 | 2.04 | 3.60 | 4.02 | 3.50 | 5.89 | 29.68 | 0.02 | 0.27 |
| 1993/306 | 2.60 | 3.29 | 5.63 | 6.18 | 27.24 | 9.95 | 6.09 | 0.02 | 0.37 |
| 1993/325 | 1.62 | 2.98 | 5.88 | - | 18.86 | - | 140.11 | - | 0.19 |
| 1992/363 | 1.15 | 2.69 | 5.96 | - | 124.45 | - | 9.27 | - | 0.18 |
| Tambuti 12.11 | | | | | | | | | |
| 1993/96 | 0.65 | 1.24 | 3.52 | 3.83 | 8.42 | 5.07 | 5.59 | 0.01 | 0.30 |
| 1994/108 | 1.05 | 1.86 | 4.65 | 4.73 | 15.91 | 7.26 | 7.82 | 0.02 | 0.33 |
| 1993/147 | 1.39 | 1.38 | 2.77 | 3.18 | 9.34 | 4.39 | 2.94 | 0.01 | 0.35 |
| 1993/156 | 1.62 | 1.48 | 2.39 | 2.80 | 27.42 | 4.17 | 2.23 | 0.01 | 0.41 |
| 1993/169 | 1.57 | 1.50 | 2.63 | 3.03 | - | 4.51 | - | 0.01 | - |
| 1993/172 | 1.36 | 1.30 | 2.89 | 3.28 | - | 4.57 | - | 0.01 | - |
| 1993/188 | 0.88 | 1.11 | 2.47 | 2.80 | - | 3.87 | - | 0.01 | - |
| 1993/191 | 0.79 | 1.09 | 2.54 | 2.87 | - | 3.96 | - | 0.01 | - |
| 1993/217 | 0.75 | 1.05 | 2.51 | 2.85 | - | 3.84 | - | 0.01 | - |
| 1993/223 | 1.43 | 1.38 | 2.35 | 2.73 | 21.54 | 3.90 | 124.67 | 0.01 | 0.20 |
| 1993/239 | 2.25 | 1.83 | 2.69 | 3.21 | 8.35 | 4.74 | 12.93 | 0.01 | 0.25 |
| 1993/255 | 1.66 | 1.55 | - | 0.94 | 1.64 | 2.36 | 2.32 | 0.01 | 0.04 |
| 1993/258 | 2.84 | 2.09 | 2.81 | 3.31 | 122.74 | 5.13 | 14.02 | 0.02 | 0.19 |
| 1995/283 | 2.25 | 1.73 | 2.64 | 3.05 | 10.59 | 4.65 | 5.51 | 0.01 | 0.32 |
| 1995/284 | 1.57 | 1.43 | 2.58 | 2.63 | 12.04 | 4.46 | 6.11 | 0.02 | 0.08 |
| 1995/289 | 1.71 | 1.54 | 2.77 | 3.08 | 17.84 | 4.52 | 13.08 | 0.02 | 0.16 |
| 1993/290 | 2.74 | 2.02 | 2.90 | 3.36 | 52.66 | 5.14 | 13.14 | 0.02 | 0.19 |
| 1993/296 | 2.65 | 2.02 | 2.79 | 3.32 | 19.67 | 5.07 | 128.97 | 0.02 | 0.20 |
| 1993/306 | 2.84 | 2.40 | 3.51 | 4.04 | 25.59 | 6.49 | 3.93 | 0.01 | 0.38 |
| 1993/325 | 1.92 | 2.37 | 4.82 | 4.60 | 33.00 | 8.25 | 8.84 | 0.20 | 0.17 |
| 1992/363 | 1.29 | 1.98 | 4.77 | - | 13.80 | - | 7.41 | - | 0.14 |

Table 5-14 (continued) Standard deviations of the mean and component land surface temperatures derived from dual-angle ATSR brightness temperatures at Chizengeni and Tambuti using the algorithm of Prata, the RAL radiative transfer code and a semi-empirical linear mixture model to delineate vegetation and soil components.

5.5 A comparison between Satellite and terrestrial radiative temperatures

Radiometric surface temperatures were recorded at the Chizengeni and Tambuti field site with both satellite and terrestrial radiometers. The satellite data were collected by the ATSR1 and ATSR2 instruments at approximately 1 km² pixel resolution. The *in situ* data was recorded with Everest infrared radiometers during two field campaigns with typical radiometric surface footprints of less than 1 m². The data were corrected for atmospheric effects using the RAL radiative transfer code and the empirical equations of Idso.

The ATSR has a unique dual-angle viewing geometry which records surface emission at nadir and approximately 55 degree zenithal (forward) observation angles. In-situ radiometric temperatures were also recorded at these nadir and forward viewing angles. At both the Chizengeni and Tambuti field sites significant angular variation in radiative land surface temperature (LST) was recorded over the dominant vegetation classes. This effect was also apparent in the ATSR satellite LST's. Figure 5-37 and Figure 5-38 indicate the magnitude of the angular LST variation recorded at each site with the *in situ* infrared radiometers and the ATSR satellite sensors. The forward LST is significantly correlated with the nadir LST at both spatial resolutions. The scatter plots of the nadir-forward LST difference against the nadir LST (Figure 5-37 and Figure 5-38) indicate little departure between the satellite and terrestrial relationships. The magnitude of the angular decrease in LST was smaller over the open grassland savannah site at Chizengeni than over the medium density woodland at Tambuti.

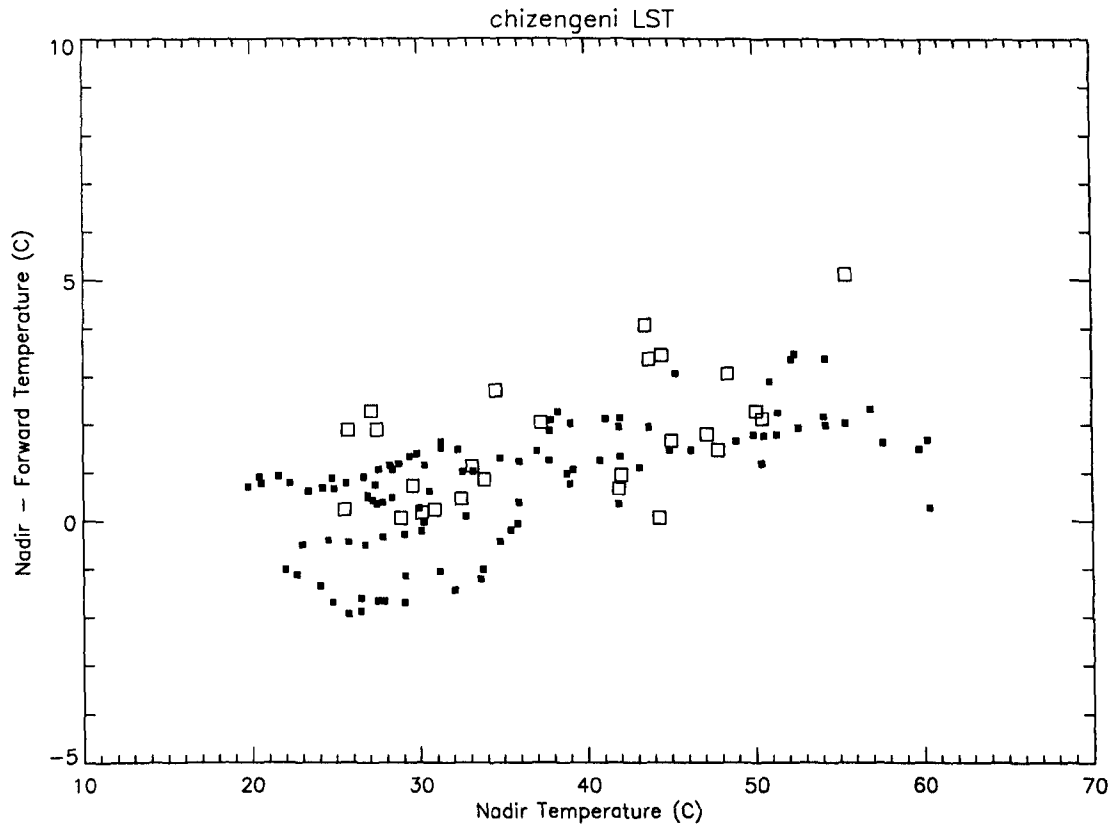


Figure 5-37 Scatter plot of nadir-forward temperature differences against the nadir temperature at Chizengeni derived from infrared radiometric temperatures (solid squares) and the ATSR 11 μm channel.

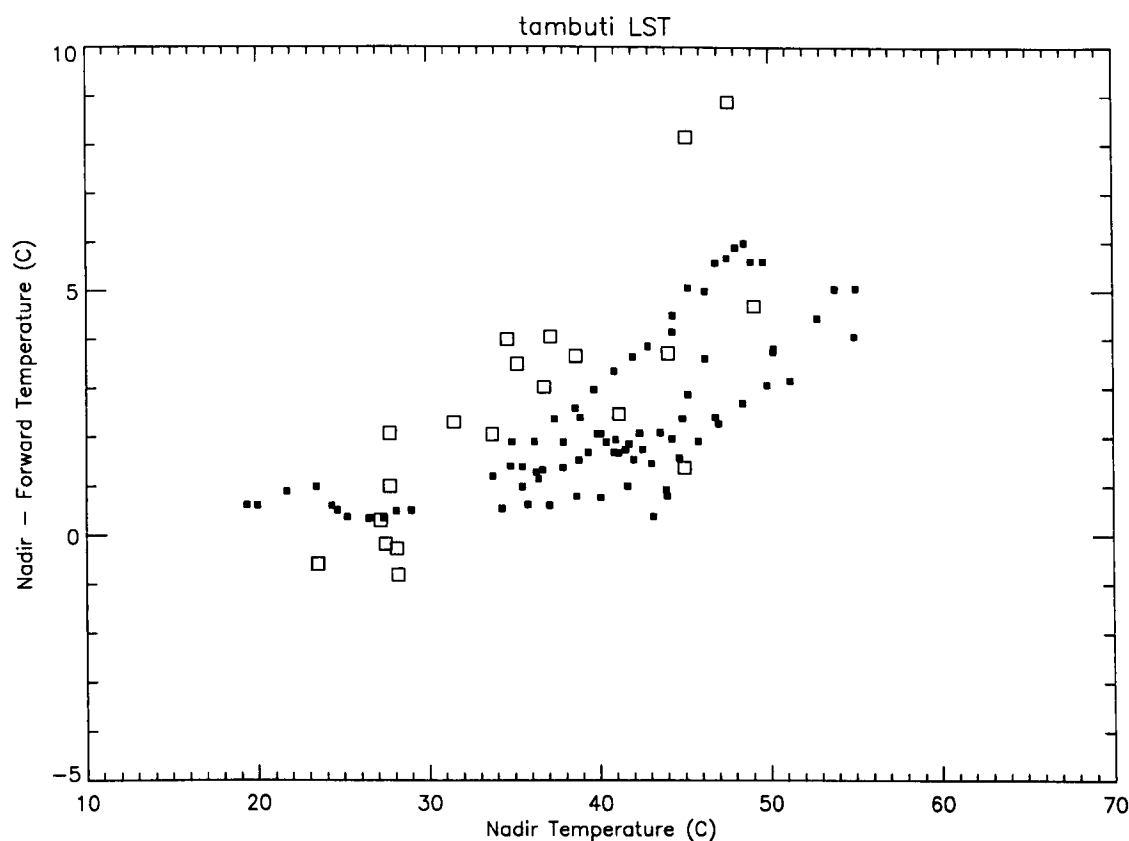


Figure 5-38 Scatter plot of nadir-forward temperature differences against the nadir temperature at Tambuti derived from infrared radiometric temperatures (solid squares) and the ATSR 11 μm channel.

Assuming that each surface can be approximated as a two component surface, the dual-angle ATSR LST's were used to form simultaneous equations which related the vegetation and soil temperatures to the fractional vegetation cover. By specifying reasonable boundary conditions for the vegetation temperature (the least variable parameter), the equations were reduced to a soluble format. Air temperature was used as a convenient (and typically lower) limit for the vegetation temperature. The second limit was obtained from relationships between the vegetation and soil temperatures that were empirically derived at each location. The range of fractional vegetation cover estimates obtained by constraining the vegetation temperature at Chizengeni and Tambuti are shown in Figure 5-39 and Figure 5-40. The fractional vegetation cover was recorded at Chizengeni during each field campaign. In Oc-

tober 1995 the fractional cover was estimated to be approximately 50 %, and in May 1996 the vegetation cover was 66 %.

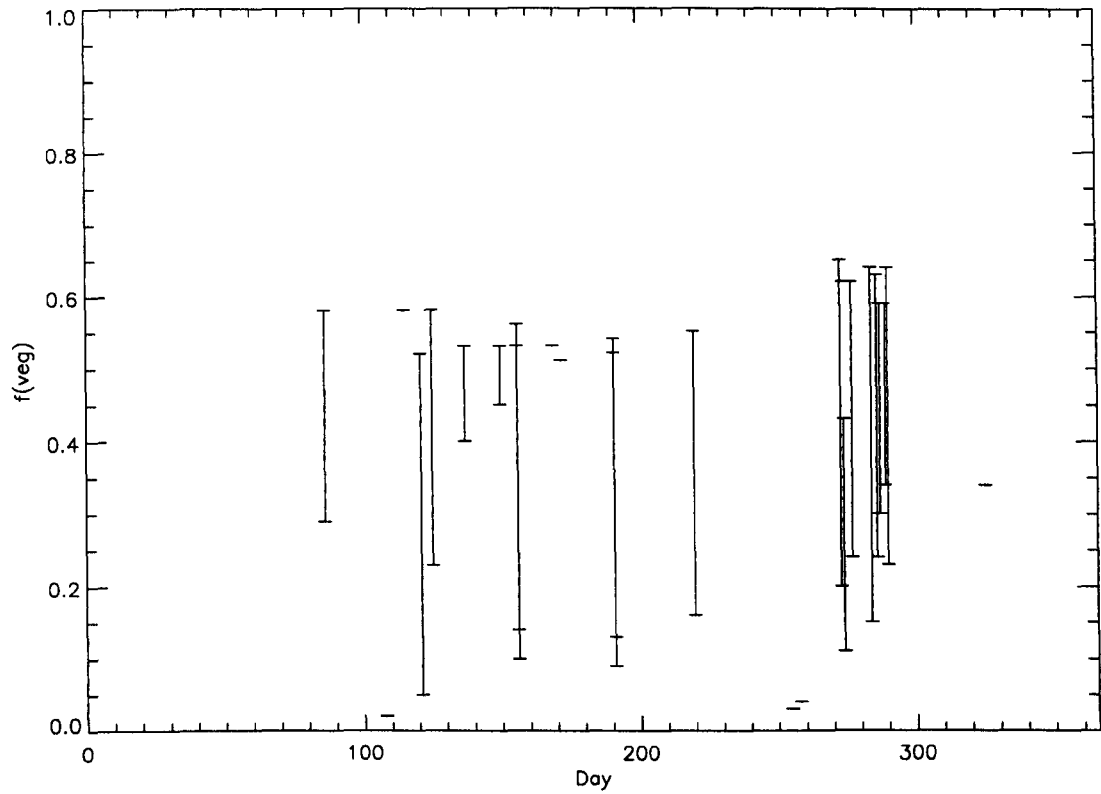


Figure 5-39 Range of fractional vegetation cover estimates obtained by constraining the dual-angle ATSR LST equations at Chizengeni.

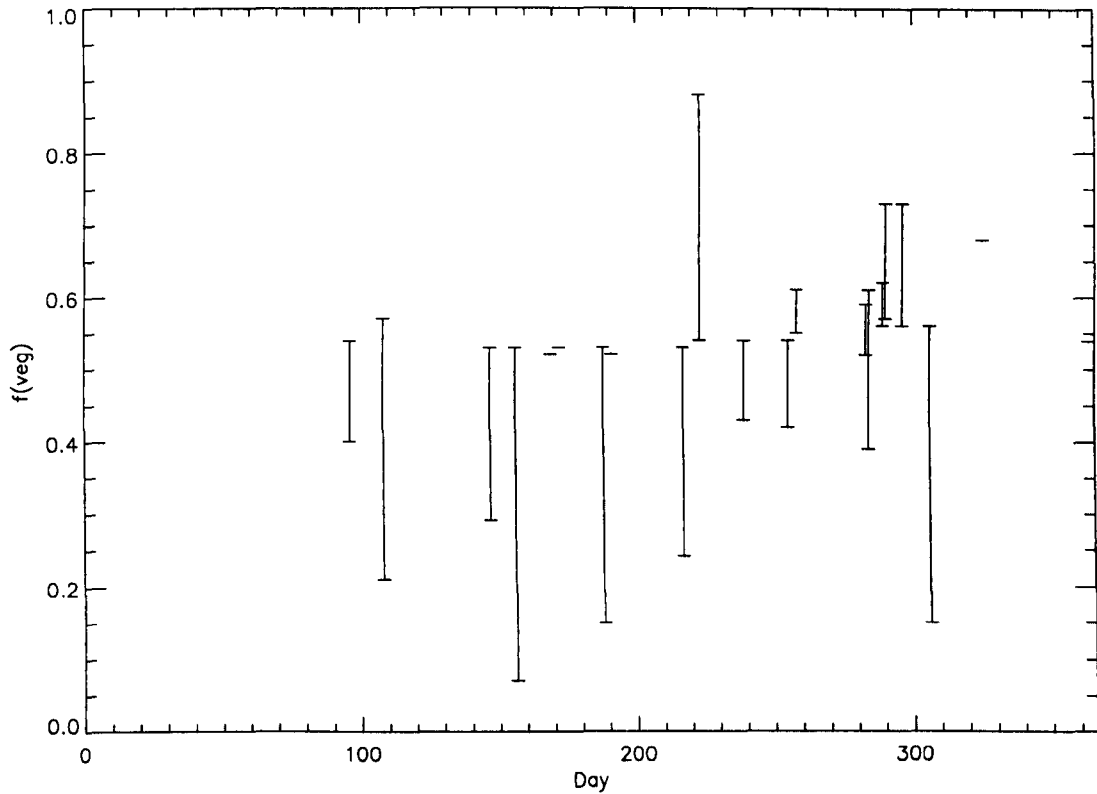


Figure 5-40 Range of fractional vegetation cover estimates obtained by constraining the dual-angle ATSR LST equations at Tambuti.

Empirical relationships were derived from *in situ* data which related the vegetation and soil or understory temperatures at Chizengeni and Tambuti through a hyperbolic parameterisation. These functions were integrated into a linear mixture model which related component temperatures to dual-angle radiative surface temperatures assuming an appropriate canopy architecture. The hyperbolic parameterisations were used to constrain temperature relationships within the model and reduce the number of unknown quantities. Scatter plots of the vegetation and soil or understory component temperatures derived from both *in situ* and ATSR dual-angle radiative temperatures (Figure 5-41 and Figure 5-42) indicates the magnitude of the departure between each estimate. The empirical relationships were determined during two periods of field measurements, and at the Tambuti site there was a significant difference in temperature relationships within the surface between each experiment. The range of vegetation temperatures possible between the upper and lower temperature con-

straints was large at both locations, and this is reflected in the scatter in derived soil temperatures and fractional cover.

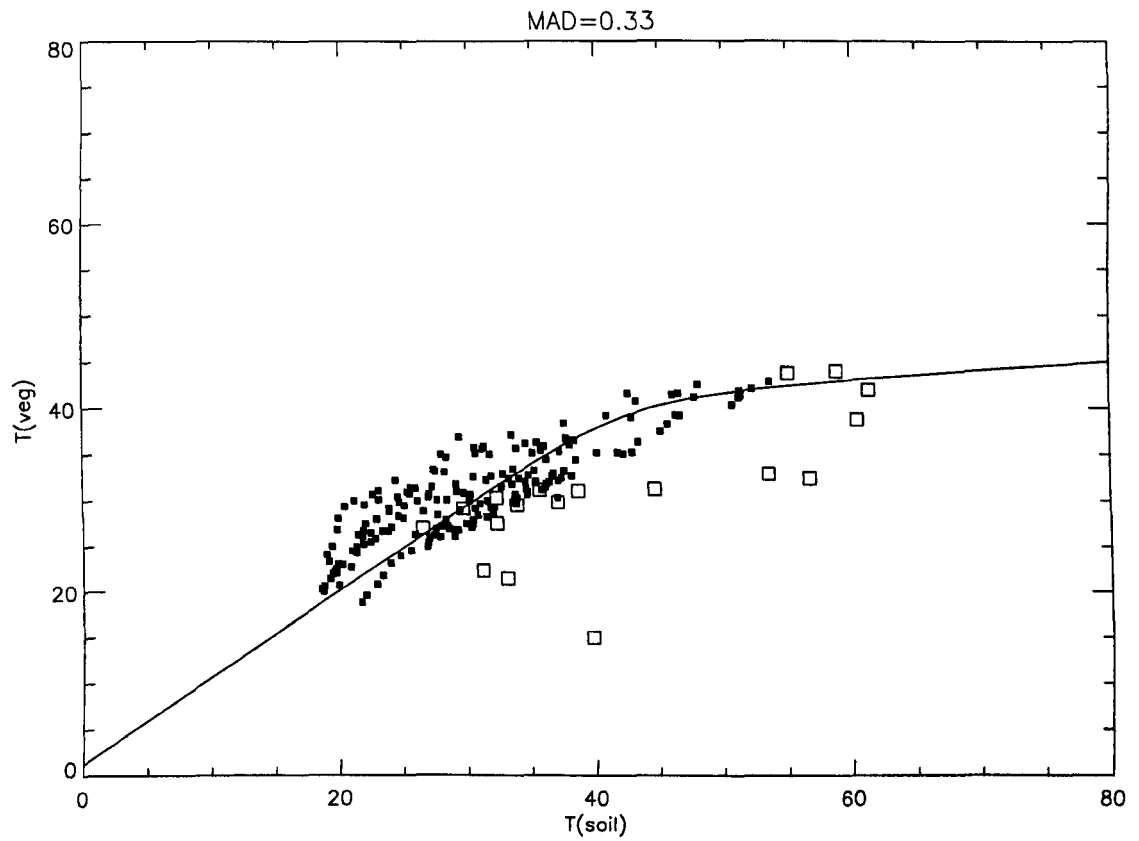


Figure 5-41 Scatter plot of vegetation and soil temperatures derived from *in situ* (solid) and ATSR dual-angle radiative temperatures at Chizengeni.

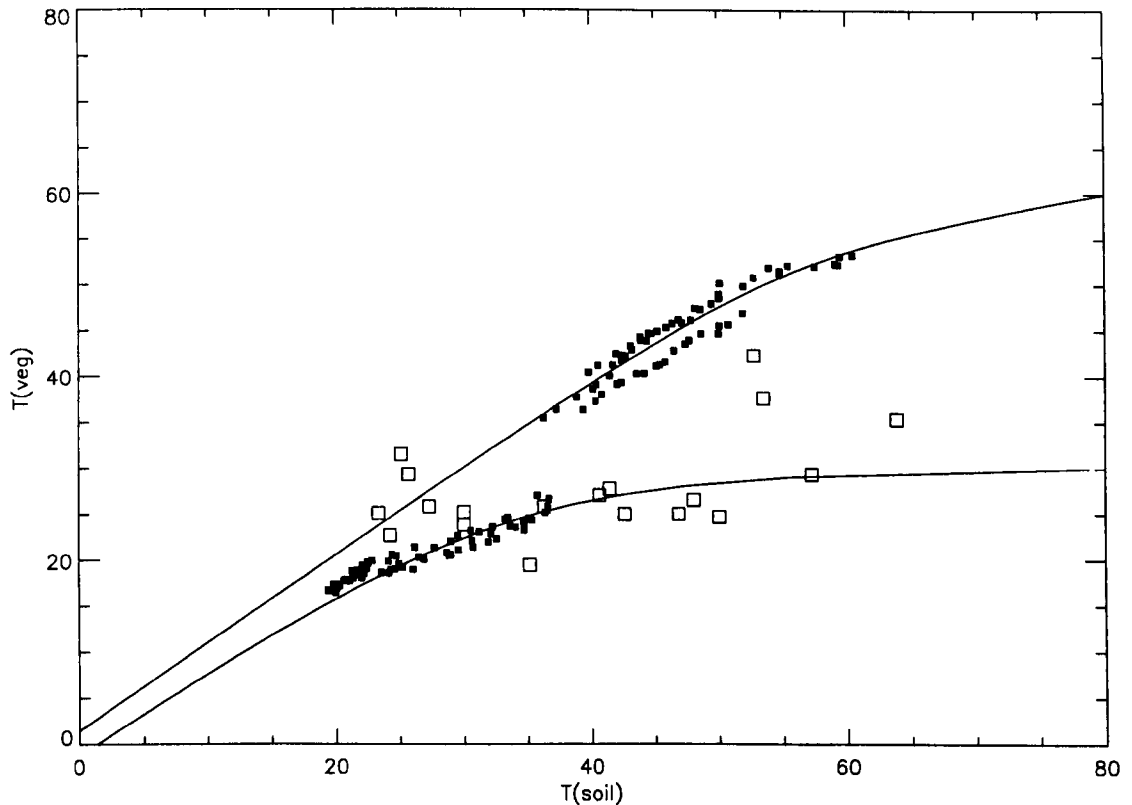


Figure 5-42 Scatter plot of vegetation and understory temperatures derived from *in situ* (solid) and ATSR dual-angle radiative temperatures at Tambuti.

Very few conjunctions occurred between satellite overpasses and *in situ* measurements due to cloud intervention. At the Chizengeni site there were only 2 days where simultaneous satellite and ground data were recorded. Both of these occurred during the first period of field experiments. At the Tambuti site there were also only 2 conjunctions, and again these both occurred during the first field campaign. For direct intercomparisons, the dataset is extremely poor and the results cannot be readily used to verify any particular method of LST modeling. Table 5-15 presents the temperature estimates obtained during these conjunctions. Mean LST's were derived using the dual-angle algorithm of Prata (T_{PRATA}), the nadir and forward LST derived from the RAL Radiative Transfer model ($T_{RT(NAD)}$ and $T_{RT(FOR)}$). The vegetation and soil/understory temperatures were derived from the linear mixture model using *in situ* IR data and air temperature as constraints ($T_{V(IR)}$, $T_{V(AIR)}$, $T_{S(IR)}$ and $T_{S(AIR)}$). Individual component temperatures were estimated from *in situ* radiative tem-

peratures over grass, shrubs, trees and soil (T_{GRASS} , T_{SHRUB} , T_{TREE} and T_{SOIL}). Table 5-16 contains the standard deviations for each of these estimates.

| Date | ATSR | | | | | | | IR | | | | T _{AIR} |
|------------------|--------------------|----------------------|----------------------|--------------------|---------------------|--------------------|---------------------|--------------------|--------------------|-------------------|-------------------|------------------|
| | T _{PRATA} | T _{RT(NAD)} | T _{RT(FOR)} | T _{V(IR)} | T _{V(AIR)} | T _{S(IR)} | T _{S(AIR)} | T _{GRASS} | T _{SHRUB} | T _{TREE} | T _{SOIL} | |
| Chizengeni | | | | | | | | | | | | |
| 11 μm | | | | | | | | | | | | |
| 1995/27 3 | 47.2 | 45.4 | 49.2 | 22.4 | 42.2 | 49.8 | 51.3 | 48.7 | 28.4 | - | 55.9 | - |
| 1995/27 4 | 50.5 | 48.4 | 52.8 | 23.7 | 43.6 | 53.6 | 54.9 | 52.5 | 28.5 | - | 49.9 | - |
| 12 μm | | | | | | | | | | | | |
| 1995/27 3 | 48.8 | 45.0 | 51.9 | 23.7 | 41.9 | 54.8 | 61.4 | 48.7 | 28.4 | - | 55.9 | - |
| 1995/27 4 | 50.2 | 48.0 | 51.7 | 22.4 | 43.7 | 53.5 | 55.1 | 52.5 | 28.5 | - | 49.9 | - |
| Tambuti | | | | | | | | | | | | |
| 11 μm | | | | | | | | | | | | |
| 1995/28 3 | 41.2 | 38.8 | 43.8 | 27.4 | 35.7 | 45.3 | 47.8 | 44.5 | - | 43.4 | - | 25.7 |
| 1995/28 4 | 49.1 | 44.5 | 54.2 | 27.1 | 39.5 | 57.3 | 62.6 | 53.5 | - | 50.7 | - | 26.8 |
| 12 μm | | | | | | | | | | | | |
| 1995/28 3 | 41.3 | 35.6 | 46.6 | 27.4 | 29.3 | 55.2 | 57.3 | 44.5 | - | 43.4 | - | 25.7 |
| 1995/28 4 | 47.0 | 41.2 | 52.1 | 27.5 | 35.4 | 58.4 | 63.8 | 53.5 | - | 50.7 | - | 26.8 |

Table 5-15 Summary of estimates of Land Surface Temperatures obtained during conjunctions between satellite (ATSR) and *in situ* (Infrared Radiometer).

| Date | ATSR | | | | | | | IR | | | | |
|--------------|--------------------|----------------------|----------------------|--------------------|---------------------|--------------------|---------------------|--------------------|--------------------|-------------------|-------------------|------------------|
| | T _{PRATA} | T _{RT(NAD)} | T _{RT(FOR)} | T _{V(IR)} | T _{V(AIR)} | T _{S(IR)} | T _{S(AIR)} | T _{GRASS} | T _{SHRUB} | T _{TREE} | T _{SOIL} | T _{AIR} |
| Chizengeni | | | | | | | | | | | | |
| 11 μ m | | | | | | | | | | | | |
| 1995/27 3 | 1.0 | 2.6 | 0.9 | 19.4 | 3.5 | 2.9 | 3.4 | 1.3 | 1.0 | - | 1.4 | - |
| 1995/27 | 1.3 | 2.7 | 1.3 | 20.3 | 4.3 | 3.4 | 3.4 | 1.7 | 0.7 | - | 1.2 | - |
| 12 μ m | | | | | | | | | | | | |
| 1995/27 3 | 2.1 | 3.8 | 1.6 | 17.8 | 3.4 | 7.1 | 7.8 | 1.3 | 1.0 | - | 1.4 | - |
| 1995/27 4 | 2.0 | 3.8 | 1.3 | 26.6 | 5.6 | 4.3 | 5.3 | 1.7 | 0.7 | - | 1.2 | - |
| Tambuti | | | | | | | | | | | | |
| 11 μ m | | | | | | | | | | | | |
| 1995/28 3 | 1.7 | 2.6 | 2.2 | 10.6 | 3.1 | 5.5 | 4.7 | 2.0 | - | 1.0 | - | 1.0 |
| 1995/28 4 | 1.4 | 2.6 | 1.6 | 12.0 | 2.6 | 6.1 | 4.5 | 1.5 | - | 1.0 | - | 0.8 |
| 12 μ m | | | | | | | | | | | | |
| 1995/28 3 | 2.5 | 3.6 | 2.5 | 15.3 | 3.9 | 10.8 | 6.6 | 2.0 | - | 1.0 | - | 1.0 |
| 1995/28 4 | 2.1 | 3.6 | 1.6 | 14.9 | 3.7 | 8.9 | 8.7 | 1.5 | - | 1.0 | - | 0.8 |

Table 5-16 Summary of standard deviations for Land Surface Temperatures obtained during conjunctions between satellite (ATSR) and *in situ* (Infrared Radiometer).

Chapter 6

Conclusions and suggestions for future work

6.1 Main Conclusions

As outlined in Chapter 1, the objective of this thesis was to investigate the spatial and temporal variation of the land surface temperature (LST) over a sparsely vegetated region. Two spatially extensive and florally distinct locations, an open grassland (Chizengeni) and a medium density woodland (Tambuti), were identified in Zimbabwe within which to perform the study. The LST was remotely sensed at different resolutions using both spaceborne and ground-based instrumentation. In-situ radiative surface temperatures were recorded over individual surface elements during field experiments conducted in October 1995 and May 1996. The ATSR satellite radiometers periodically recorded radiative temperatures over the same area with an earth footprint of approximately 1 km² before, during and after each experiment.

As well as deriving the spatial and temporal variation in the LST over each region, the work has demonstrated the use of dual-angle ATSR radiometric temperatures to interrogate the surface at sub-pixel resolution. Estimates of the canopy and understory temperatures and the fractional vegetation cover were obtained over heterogeneous terrain using the satellite data.

Five principal questions were asked of this work in the introduction, and these will now be answered in detail.

i) How is the land surface temperature related to the Infrared emission from the Earths' surface ?

Infrared radiation from the Earth's surface is affected by the presence of the intervening atmosphere. A set of clear sky radiosoundings was used to investigate the temporal variation in atmospheric emittance and transmittance at infrared wavelengths over the study area.

Both empirical and numerical methods were used to estimate the atmospheric emittance, and there was excellent agreement between the independent techniques (see Figure 5-9). The empirical equations, which were derived from a set of globally representative atmospheric radiosoundings, perform satisfactorily over the region of interest and the mean absolute deviation between empirical and numerical estimates was 1.1 W m^{-2} . The empirical equations were required to correct broadband infrared radiometric temperatures which were recorded beyond the spectral domain of the radiative transfer code. The diurnal variation in the atmospheric correction was shown to vary between 0 and 10°C on a typical day. The magnitude of the diurnal variation was significant and should be adequately considered when using synoptic datasets.

After correcting for the effects of the atmosphere, radiative temperatures were derived from surface infrared emission recorded by the ATSR satellite radiometer. The surface emissivity was in all instances derived from tabulated data presented within the literature. It was beyond the scope of this work to determine *in situ* emissivity data, although the impact of estimation errors and the effects of angular variations were considered. The differential atmospheric absorption between the ATSR nadir and forward views was used to parameterise the atmospheric correction. Location specific LST retrieval algorithms were derived which related the nadir LST at each site to the nadir and forward infrared brightness temperatures recorded by the ATSR (see Table 5-9). The algorithms were compared to the semi-empirical dual-angle LST retrieval algorithm of Prata (1993), which required an estimate of atmospheric transmittance to define the retrieval coefficients (see Figure 5-24 and Figure 5-25). It was observed that the LST's calculated using Prata's equations was typically greater than the LST's determined via a complete solution of the radiative transfer equation. The LST retrieval algorithm of Prata was derived for homogeneous, single component surface cover, and did not accommodate any mechanism to deal with angular differences in radiometric surface temperature that could be present over mixed surfaces. If Prata's model were to attribute an enhanced angular decrease in radiometric temperature entirely to increased atmospheric attenuation then one would expect the algorithm to underestimate the real LST. However, this was at odds with observations and the reason for this remains unclear. The vegetation structure at Chizengeni (open grassland) exhibited far less spatial heterogeneity than at Tambuti (medium density woodland), and Prata's algorithm yielded closer results to

the location specific radiative transfer retrieval at the Chizengeni site. This was in line with expectations, since the angular variation in LST was less pronounced over the open grassland.

ii) How does the land surface temperature vary spatially and temporally over different canopy architectures ?

In-situ estimates of the LST indicated that the spatial variation in temperature within discrete surface elements, such as soils and vegetation classes, was generally lower than the standard deviation over the sampling interval (see Table 5-4). The mean standard deviation over the sampling interval for all surface categories studied was 1.15°C. The only surface component to exhibit substantially larger spatial than temporal variability was the long grass at Tambuti. The mean difference recorded between instruments measuring the long grass temperature was 1.6°C. The grass was approximately 0.5 m in height and the nadir fractional cover was not complete, but too difficult to measure *in situ*. Vertical temperature gradients of comparable magnitude have been previously observed throughout columnar vegetation (Lagouarde *et al.*, 1995; Kimes *et al.*, 1980). It is thought that the particularly large variability is an artifact of the vertical structure. The spatial variability in surface component temperatures was not the dominant source of uncertainty within the field experiments. Temporal variations were typically larger in magnitude. The mean calibration accuracy of the infrared radiometers was 0.33°C (see Chapter 4).

The temperature differentials that existed between individual surface components were typically much larger than the temporal variability across the sampling interval (see Figure 5-10). At Tambuti, differences of greater than 25°C were observed between canopy and soil temperatures. At the time of overpass of the ATSR satellite, temperature differentials of around 10°C were common between vegetation and soils (see Table 5-5). At low temperatures all surfaces were approximately in thermodynamic equilibrium, whilst at high temperatures significant departure between component temperatures was apparent. Empirical equations were proposed which related the vegetation, soil and understory temperatures at each field site. At Chizengeni the soil and grass temperatures were isolated using a linear mixture model coupled with dual angle radiometric temperatures. The vegetation was ex-

tremely sparse on both occasions due to heavy grazing (see Figure 4-10) and the measured seasonal change in canopy architecture was not dramatic. There was no significant difference in the relationship between soil and grass temperatures recorded during separate field campaigns and a single formula was used to parameterise the trend. The grass temperature did not exceed a threshold of approximately 45°C, and the mean deviation of soil and vegetation temperatures from the hyperbolic relationship was 0.27°C. The woodland canopy at Tambuti ranged from dense to sparse throughout the year. Shrub and tree green leaf temperatures were close to air temperature when measured in isolation, and the relationship between canopy and understory temperatures was quite different during each field campaign (see Figure 5-16). For dense canopies an upper temperature threshold of around 30°C was apparent, whilst sparse canopy temperatures exceeded 55°C. Two separate temperature relationships were derived for the sparse and dense canopies and the mean deviation was 0.22°C and 0.18°C respectively. When the tree canopy was sparse a similar relationship was observed between vegetation and soil temperatures as at Chizengeni.

At the coarse resolution of the ATSR satellite (approximately 1 km²) the spatial variation in temperature within the field study areas varied between approximately 0.25 and 1.75°C throughout the year (see Figure 5-21). The minimum spatial variability occurred towards the end of the dry season, when the fraction of photosynthetically active vegetation was close to zero. This was in line with expectations, as the temperature of senescent vegetation is relatively unconstrained within the near surface atmosphere. At Chizengeni, the spatial temperature heterogeneity was qualitatively correlated with fractional vegetation cover. The relationship was less pronounced at Tambuti, and the annual variation in temperature heterogeneity was more erratic, but in general larger in magnitude. The temporal variation in fractional vegetation cover was complicated at Tambuti because of the woodland canopy, which was present throughout the dry season. In-situ measurements over bare trees indicated that small temperature differentials existed within sparsely foliated canopies. The temporal variation in LST derived from the ATSR data was much larger than the spatial variability within each field study area (see Figure 5-22 and Figure 5-23). The spatial variability of the satellite and terrestrial component radiative temperatures were similar in magnitude. Both the Chizengeni savannah and the Tambuti woodland are spatially

homogeneous canopies at the coarse satellite resolution, although temperature heterogeneity was present across each area (see Figure 5-19 and Figure 5-20).

iii) Is there evidence of angular variations in land surface temperature estimates ?

The ensemble radiative temperature of a heterogeneous surface is weighted by the temperature and fractional cover of each distinct element. The fractional vegetation cover of natural canopies typically increases with observation angle, so that a forest of trees viewed obliquely presents 100 % vegetation cover irrespective of the nadir value. If temperature differentials exist within the canopy then the radiative temperature may exhibit pronounced angular variability. Vegetation, for a variety of reasons, is typically cooler than the surrounding soil. The nadir fractional vegetation cover of the sparse open grassland at Chizengeni varied from 50 to 66 % throughout the year, and the radiative temperature was observed to decrease significantly with instrument viewing angle on each occasion (see Figure 5-15). The magnitude of the decrease was correlated with the absolute surface temperature, and the largest decreases were recorded when the surface was hottest. At low temperatures the surface elements were in thermodynamic equilibrium. Lagouarde *et al.* (1995) observed similar variations over various plant canopies and concluded that this was a standard feature over vegetation due to its vertical structure. The vegetation was unstressed and angular decreases of up to 3.5°C were observed at relatively low temperatures. Much larger differences have been recorded over a wheat canopy (Kimes *et al.*, 1980), but the angular measurements were not recorded simultaneously. The comparatively small angular decreases in radiative temperature recorded over the short grass at Chizengeni indicate that the temperature differences between the vegetation and the soil were not extreme. The regional water stress and the localised heavy grazing are both factors which would enhance the thermodynamic coupling between the canopy and soil. The angular variation in radiative temperature within the woodland at Tambuti proved difficult to determine. Dual-angle radiometric measurements above the tree canopy were severely contaminated by shade, so that the canopy and understory temperatures frequently could not be uniquely isolated (see Figure 5-13). The angular variation in tree canopy temperature was derived from data col-

lected in the absence of shade, and differences of up to 6.5°C were observed. The angular radiative temperature of the tall grass understory was monitored on a number of occasions, and at temperatures below 50°C no significant variation was observed. The grass was dense enough to obscure the soil surface from view on most occasions, and the irregular nature of the canopy confused any vertical temperature gradients that could be inferred from the structure. The spatial heterogeneity of the grass temperature exceeded any angular variations that were recorded. Whilst no particular angular temperature variations were recorded over the understory or the treetops, the woodland canopy was expected to exhibit a pronounced angular temperature decrease because of the larger scale heterogeneity of the canopy as a whole.

Similar angular variations in the radiative LST were also observed in the dual-angle ATSR coarse resolution satellite data. The angular decrease was shown to be independent of the differential atmospheric attenuation which occurs between the two viewing geometries. A pronounced annual trend in the nadir-forward temperature difference was apparent and this was qualitatively correlated with the fractional vegetation cover, so that the largest differences occurred over dense canopies. The difference between ATSR nadir and forward LST's indicated that the angular decrease was greater over the Tambuti woodland than the Chizengeni savannah (see Figure 5-29 and Figure 5-30). In-situ measurements suggested that the difference between vegetation and soil temperature was greater within the woodland at Tambuti. A direct comparison was made between ground-based and satellite retrieved estimates of the angular decrease in radiative temperature (see Figure 5-37 and Figure 5-38), and there was good closure between the two sensing techniques. The fraction of shade present within the tree canopy at Tambuti at the time of satellite overpass was not significant. The angular decrease in radiative temperature aggregated with scale, so that heterogeneities in the canopy architecture that are far beyond the resolution of the radiometer contributed to the ensemble surface emission. The effect was apparent over both an open grassland and a medium density woodland which had markedly different canopy architectures. Blackbody cavity effects, which are frequently supposed to occur within heterogeneous canopies, were not significant at either location.

iv) How can dual angle satellite data be used to investigate heterogeneous canopies ?

In-situ radiative surface temperatures were recorded over an open grassland simultaneously at 3 different observation angles. The component temperatures and fractional cover were estimated using a linear mixture model to aggregate the ensemble surface emission and an appropriate canopy architecture to describe the angular variation in vegetation cover. The nadir fractional vegetation cover was estimated to be 0.60 ± 0.27 using the multi-angle radiative temperatures, which was in excellent agreement with the value of 0.66 ± 0.1 determined manually at the same location. A similar investigation was conducted over a woodland canopy to estimate the mean density of the foliage. Radiative temperatures were recorded simultaneously above and below the tree canopy and the foliage density was estimated to vary between 6 and 84 % on different occasions throughout the year. Empirical equations were derived to relate the grass and soil temperatures over the grassland site and the canopy and understory temperatures at the woodland site.

ATSR radiative temperatures were shown to exhibit significant angular variation, which was qualitatively correlated with the fractional vegetation cover at each location. The angular variation in LST was largely independent of spatial scale, and the dual-angle radiative temperatures were used to investigate the canopy architecture over an extended time period. To uniquely delineate the temperatures and fractional cover within a two component surface using a linear mixture model requires radiative temperatures recorded at three observation angles. The empirical component temperature relationships were used to provide an upper constraint upon the surface temperature regime, and air temperature was used as the lower temperature constraint. The inclusion of these reasonable boundary conditions for the component temperatures reduced the number of angular radiative temperatures required to two. ATSR dual-angle radiative surface temperatures were used to derive vegetation and soil or understory temperatures and the fractional vegetation cover at each location (see Figures 5-32 to 5-35). The mean difference between estimates of vegetation and soil/understory temperatures using the lower and upper temperature constraints was 10.7 and 2.9°C over the grassland site and 4.7 and 3.3°C over the woodland canopy. In general the soil temperature estimates exhibited the lowest variability. The largest difference between temperature esti-

mates occurred for the vegetation temperature at the grassland site. This indicates that air temperature was a poor low temperature parameterisation for the short grass canopy, where the thermodynamic interaction between the vegetation and soil was particularly enhanced. The mean standard deviations of vegetation and soil/understory temperatures were 10.9 and 7.1°C at the grassland site and 8.4 and 8.8°C at the woodland site. These errors are excessively high, and are biased by particularly erroneous data with errors greater than 15°C. The modal standard deviation for all component temperature estimates was 3.2°C. The difference between vegetation and soil temperatures separated using the dual-angle data was greater than 31°C at certain times of the year. Temporal variations in component temperature differences were significantly larger than the typical estimation accuracy. The range of fractional vegetation cover estimates was particularly large. This was a direct result of the inability to accurately parameterise the component temperature relationship at sub-synoptic times throughout the year. The excessively large fractional cover errors yielded by this technique, which were on occasion greater than 50 %, did not significantly affect the estimates of component temperatures.

Retrieval algorithms were derived which related the vegetation and soil or understory temperatures and the component fractional cover to the nadir and forward ATSR brightness temperatures at each location (see Table 5-12). The accuracy of the algorithms was dominated by the errors within the component temperature parameterisations. The algorithms were applied across the wider catchment areas of each study location to determine the spatial and temporal variation in fractional vegetation cover (see Figure 5-35 and Figure 5-36).

v) What does this work tell us about the reliability of land surface temperatures derived from satellite data, and is the technique applicable on a global scale ?

Land surface temperatures can be derived from satellite measured radiances using differential retrieval algorithms to parameterise the effects of the intervening atmosphere and the emissive characteristics of the surface. Over uniform surfaces the LST has been estimated using both split-window and dual-angle differential radiometry. The use of ATSR dual-angle satellite radiances has been shown to significantly improve the estimation of surface

temperatures when compared to traditional split-window methods. Over heterogeneous terrain however, complications arise because of the potential for asymmetry in the surface emittance at sub-pixel resolution. In-situ measurements have indicated that the angular variation in radiative surface temperature over both sparse grassland and medium density woodland can result in differences of up to 6.5°C between nadir and forward views. Atmospherically corrected satellite radiative temperatures have shown this effect to be spatially invariant over the same surface. Such asymmetric emittance would invalidate any LST estimate derived using a traditional dual angle retrieval algorithm. The angular variation in radiative surface temperature is however a potentially useful feature of sparse, heterogeneous canopies. Using confident boundary conditions for the temperature relationships between the canopy and understorey derived from *in situ* data, component temperatures were calculated from ATSR dual-angle data with a modal accuracy of 3.2°C. Retrieval algorithms were then derived to relate the component temperatures to the nadir and forward ATSR brightness temperatures. The mean absolute deviation of the retrieval algorithms from the component temperatures was between 2.2 and 4.8°C.

The technique relies heavily upon *in situ* parameterisations for the temperature boundary conditions. Without these constraints, radiative temperatures from at least 3 independently observation angles are required to delineate temperatures over a two component surface. If the relative fractional cover of each component is well known then only dual-angle data are required. In many instances the fractional vegetation cover can be accurately determined, using *in situ* knowledge or remotely sensed vegetation indices. However, significant angular variations in radiative temperatures are only observed when the spatial heterogeneity is pronounced and marked temperature differentials exist within the surface. The relatively large errors associated with the temperature separation are only acceptable when temperature differentials are extreme. Semi-arid climates provide ideal conditions for these experiments, but the crucial factor is then the vegetation cover, which is typically ill defined. Moreover, the temporal variation in vegetation cover is a key factor in the analysis, and parameterising the trend could significantly affect the temperature separation.

6.2 Future work

This thesis combined three major areas of work, namely the collection of *in situ* field measurements, the processing of satellite data and modeling the radiative transfer from heterogeneous canopies. Whilst significant results were achieved during the work, there are a number of areas where future work would be instrumental in the validation of the technique and the successful application of the results. These topics are now discussed.

6.2.1 (i) Fieldwork

The study involved extensive *in situ* fieldwork to determine both empirical surface component temperature relationships and to obtain coincident ground-based and ATSR satellite estimates of the surface temperature for intercomparison. Field experiments were conducted on two occasions, which were timed to be approximately at the end of the dry and wet seasons, when surface vegetation cover was anticipated to be at opposite extremes. The analysis of locally obtained atmospheric radiosoundings revealed these dates to lie almost exclusively within the two annual periods of intensive atmospheric instability. For successful satellite conjunctions, which are still required to validate the technique, field campaigns should not be attempted during changeable conditions. Only two cloud-free coincidences were achieved with the ATSR1 and ATSR2 satellites from a potential list of 30 overpasses. The second goal, to parameterise the thermodynamic relationships within the surface, should be performed at regular intervals throughout the year. Whilst no particular annual variation was observed over the short grass at Chizengeni, the woodland canopy at Tambuti exhibited significantly different temperature relationships between field campaigns. The nature of the vegetation and understory temperature relationships suggested a strong dependence upon foliage density, again an ephemeral quantity. Component temperature measurements at synoptic time-scales would lead to an improved understanding of the thermodynamic interactions within the canopy. Understory shading was also apparent within the woodland temperature dataset, and much of the dual angle *in situ* data were contaminated differentially. Shaded surfaces were not considered during the simple two component temperature separation, but the model could be extended to determine the influence upon the satellite data. Finally, *in situ* measurements of the surface emissivity were not

made, and estimates were obtained from the literature. Moderately accurate emissivity data can be collected using relatively simple apparatus (e.g. Buettner and Kern, 1965), if only for corroborative purposes.

6.2.2 (ii) Satellite data

The satellite data were corrected for atmospheric effects using an atmospheric radiosounding dataset recorded at the nearby meteorological station. These profiles were collected at one time of day only, and a simple adiabatic heating model was used to obtain estimates at sub-synoptic time-scales. It was not possible to validate the atmospheric heating model (see Appendix A), and no similar experiments were present within the literature. The effects of the diurnal variation upon the atmospheric transmittance and emittance were investigated using diurnal surface level data, but again these could not be independently verified. A simple study of the diurnal variation in atmospheric transmittance and emittance could be conducted during each field campaign with little effort.

The satellite LST's were derived using both the ATSR 11 μm and 12 μm data. No particular significance was attached to the two estimates, and no preferential estimate was identified. The surface emissivity data was too coarse to permit high resolution spectral analysis of the satellite radiances. Without extensive laboratory effort to determine the spectral variation of the surface emissivity, the only way to resolve the differences between the ATSR 11 μm and 12 μm LST's would be to obtain sufficient satellite and ground-based coincidences to infer emissivity values.

The fractional vegetation cover was found to be a key unknown parameter in the subsequent canopy modeling. Numerous vegetation indices exist within the literature and these could be used to estimate the fractional cover. A substantial dataset of visible and near infrared satellite imagery of the same area would be required for this study, as there was insufficient ATSR2 data to permit this exercise. This would not be a difficult investigation and could prove extremely valuable if the estimates were shown to be adequate for component temperature modeling purposes.

6.2.3 (iii) Canopy Modeling

The angular variation in fractional vegetation cover was parameterised using a standard canopy architecture model for a random distribution of spherically orientated leaf elements. Other canopy architecture model should be tested over each area, in particular over the short grass at Chizengeni. A simple photographic study of each canopy would produce an empirical estimate of the actual variation for comparison.

The component temperature separation is an extremely useful tool for surface energy balance studies. The magnitude of the heat flux from a surface is related to the temperature potential difference and the resistance to heat transfer from the surface itself. The combined heat flux from a heterogeneous surface can be modeled by adding fluxes in series or parallel according to their contribution within a canopy. Soil, vegetation and atmosphere interaction models require implicit knowledge of the component temperatures and the relative resistances. In-situ measurements of the heat flux, using for instance the Bowen-Ratio technique, could be used in conjunction with component radiative temperatures to determine the resistance to heat transfer over each surface. The heat flux could then be calculated on an areal basis and combined with ancillary data to determine the energy partition at the surface, which would provide estimates of the evaporation rate.

Appendix A

Atmospheric heating model

Introduction

Sixty clear sky atmospheric radiosoundings were recorded at Harare meteorological station between 1992 and 1996. The tropospheric temperature and vapour pressure profiles were used to estimate atmospheric emittance and transmittance in the infrared wavelength region using a radiative transfer model. These parameters were used to correct satellite and terrestrial radiometric surface temperatures for atmospheric effects.

The meteorological data were collected at 0200 am local time. The Along Track Scanning Radiometer records infrared brightness temperatures close to the meteorological station at approximately 1030 am. An atmospheric heating model was used to extrapolate the one time of day radiosounding data to sub-synoptic time-scales. The details of the model are discussed.

Model description

Water vapour is the dominant absorber and emitter of infrared radiation within the atmosphere. The atmospheric heating model was based upon the assumption that the total water vapour content within the atmosphere remains constant throughout any 24 hour period. The equation of state for water vapour, which behaves as an ideal gas, can be written as

$$e_a = \frac{\chi RT}{M_v}$$

(A.1)

where X is the absolute humidity, R is the universal gas constant (8.134 KJ mol⁻¹ K⁻¹), T is the temperature in Kelvin and M_V is the molecular weight of water vapour (18.016 g mol⁻¹).

Radiosonde ascents recorded the atmospheric temperature and

relative humidity. The relative humidity is the ratio of the vapour pressure (e_a) to the saturation vapour pressure (e_s). A numerical expression for the saturation vapour pressure (Pa) is given by Rosenberg et al. (1983) as

$$e_s = (10 \times 0.61078) e^{\left(\frac{17.269(T+273.16)}{(T+273.16)+237.3} \right)}$$

(A.2)

The absolute humidity can then be written in terms of the atmospheric temperature and relative humidity (RH), so that

$$\chi = R_H (10 \times 0.61078) e^{\left(\frac{17.269(T+273.16)}{(T+273.16)+237.3} \right)} \left(\frac{18.016}{8.134T} \right)$$

(A.3)

Adiabatic processes occur with no net loss or gain of energy. Within the atmosphere, a parcel of air can be heated adiabatically and its temperature and pressure will change without affecting the external environment. In the heating model thermodynamic processes were assumed to occur adiabatically within a finite column of air. The model was one dimensional and no interactions were permitted with the surrounding atmosphere.

For an adiabatic process, the temperature and pressure are polytropically related so that

$$T = P^{\left(\frac{c_p - c_v}{c_p}\right)} \quad (\text{A.4})$$

where c_p and c_v are the specific heat capacity of the air at constant pressure and volume respectively. For dry air, $(c_p - c_v)/c_v$ is approximately 0.29.

The vertical temperature gradient within the troposphere is known as the environmental lapse rate. Assuming hydrostatic equilibrium holds within the column, the rate of change of temperature with height can be written as

$$\frac{dT}{dz} = -\frac{g}{c_p} \quad (\text{A.5})$$

where $dT/dz > 0$ conventionally represents temperature decreasing with height.

This quantity is known as the dry adiabatic lapse rate (DALR), and is approximately equal to -10°C per km. The environmental lapse rate averages around -6 to -7°C per km in the troposphere, but can assume a wide range of values at individual locations. The difference between the actual lapse rate and the DALR is a measure of the vertical stability within the atmosphere. Figure A-1 indicates the magnitude of the annual variation of the environmental lapse rate calculated from the radiosonde ascents at Harare.

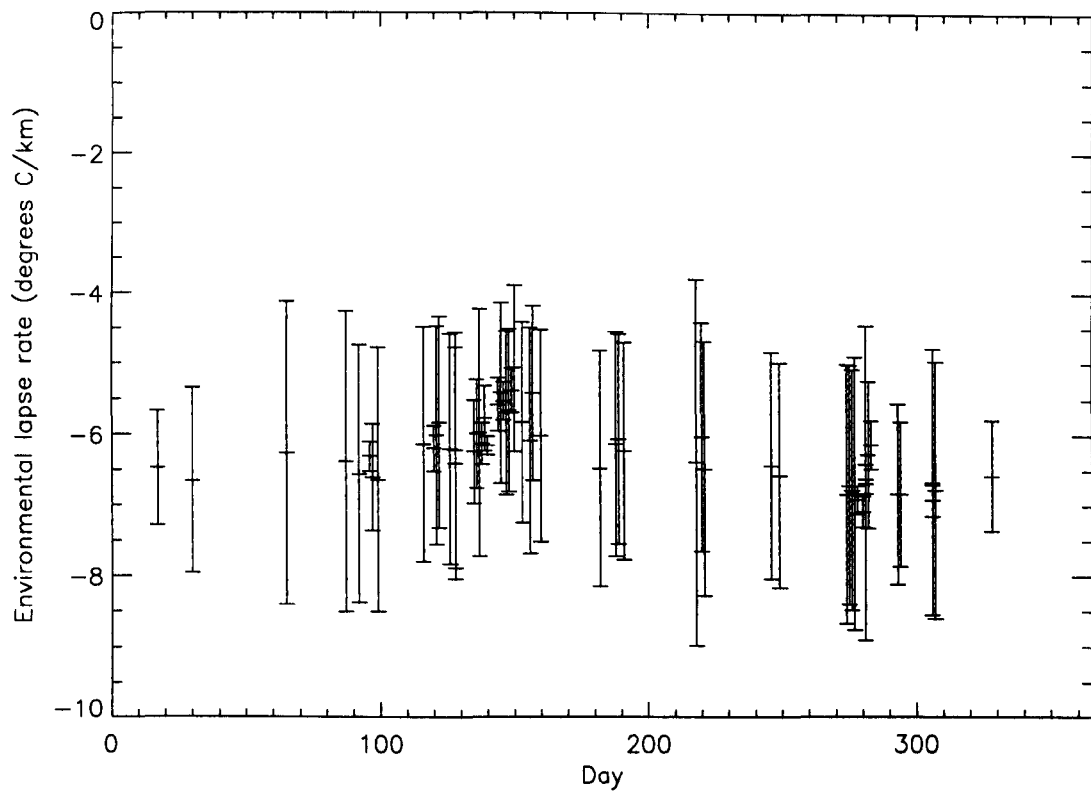


Figure A-1 Annual variation in the mean environmental lapse rate at Harare between 1992 and 1996.

The environmental lapse rate at Harare was temporally stable and there was moderate departure from the DALR. For wet atmospheres, thermodynamic processes are not necessarily adiabatic, and either condensation or evaporation of water vapour can occur.

To roughly conserve the diurnal atmospheric water content the mixing ratio of water vapour derived from each radiosonde ascent was constrained at the surface, so that

$$w = \frac{\left(\frac{e_0}{P_0} \right)}{\left(1 - \left(\frac{e_0}{P_0} \right) \right)}$$

(A.6)

The specific heat capacity of moist air can be expressed in terms of the water vapour mixing

$$c_{P_{WET}} - c_{V_{WET}} = \frac{(c_P - c_V)}{(1 + w(1 + e))}$$

ratio, so that

(A.7)

and

$$c_p = (1 + 0.87w(1 + w))c_p$$

(A.8)

The atmospheric pressures were free to oscillate in line with the diurnal heating regime. Given an estimate of the surface-level air temperature at a later time during the day, the atmospheric temperature profile was recalculated assuming a constant environmental lapse rate.

Hourly automatic weather station records were used to derive empirical relationships between the daily maximum and minimum surface level air temperature and the air temperature at sub-synoptic time-scales. The air temperature at the time of radiosonde ascents was correlated with the daily minimum air temperature, and the daily maximum temperature was correlated with the temperature at the time of satellite overpass (approximately 1030 am). The mean temperature deviation from these relationships was 1.3 and 1.2°C respectively. Thirty six consecutive months of weather station data were used.

Pressure levels throughout the atmosphere were recalculated according to the new atmospheric temperature profile, so that

$$P_{new} = P_{old} \left(\frac{T_{new}}{T_{old}} \right)^{\left(\frac{1}{k} \right)}$$

(A.9)

where $k=(C_{PWET}-C_{PWET})/C_{PWET}$ describes the polytropic relationship for a wet atmosphere.

The heated water vapour density can then be calculated from the ideal gas law so that

$$r_{new} = \frac{P_{new}}{R_{gas} T_{new}}$$

(A.10)

and

$$e_{new} = \frac{P_{new} w}{1 + w}$$

(A.11)

The absolute humidity can then be expressed in terms of the atmospheric temperature and vapour pressure using Equation A.1

References

- Barnes, S. L., and Lilly, D. K., 1975. Covariance analysis of severe storm environments. *Ninth Conference on Severe Local Storms*, Norman, American Meteorological Society, 301-306.
- Barton, I. J., Zavody, M. A., O'Brien, D. M., Cutten, D. R., Saunders, R. W., and Llewellyn-Jones, D. T., 1989. Theoretical approaches for satellite-derived sea surface temperatures. *Journal of Geophysical Research*, **94**, No. D3, 3365-3375.
- Becker, F., 1987. The impact of spectral emissivity on the measurement of land surface temperature from a satellite. *International Journal of Remote Sensing*, **8**, No. 10, 1509-1522.
- Becker, F., Ramanantsizehena, P., and Stoll, M. P., 1985. Angular variation of the bidirectional reflectance of base soils in the thermal infrared band. *Applied Optics*, **24**, No. 3, 365-375.
- Becker, F., and Li, Z. L., 1990. Temperature-independent spectral indices in thermal infrared bands. *Remote Sensing of the Environment*, **32**, 17-33.
- Bell, M., Faulkner, R., Hotchkiss, P., Lambert, R., Roberts, N., and Windram, A., 1987. The use of dambos in rural development, with reference to Zimbabwe. *Final Report of ODA Project R3869*, ENG 505/512/10.

Berry, K. H., 1981. Emissivity of a cylindrical black-body cavity with a re-entrant cone end face. *Journal of Physics E: Scientific Instrumentation*, **14**, 629-632.

Brunt, D., 1932. Notes on radiation in the atmosphere. *Quarterly Journal of the Royal Meteorological Society*, **58**, 389-418.

Brutsaert, W. B., 1982. *Evaporation into the atmosphere*. Reidel, Dordrecht.

Buettner, K. J. K., and Kern, C. D., 1965. The determination of infrared emissivities of terrestrial surfaces. *Journal of Geophysical Research*, **70**, 1329-1337.

Chandos, R. J., and Chandos, R. E., 1974. Radiometric properties of isothermal, diffuse wall cavity sources. *Applied Optics*, **13**, No. 9, 2142-2152.

Chehbouni, A., Njoku, E. G., Lhomme, J.-P., and Kerr, Y. H., 1995. Approaches for average surface flux parameters and fluxes over heterogeneous terrain. *Journal of Climate*, **8**, 1386-1393.

Choudhury, B. J., 1996. Comparison of two models relating precipitable water to surface humidity using globally distributed radiosonde data over land surfaces. *International Journal of Remote Sensing*, **16**, 663-675.

Choudhury, B. J., Idso, S. B., and Reginato, R. J., 1986. Analysis of a resistance-energy balance method for estimating daily evaporation from wheat plots using one-time-of-day infrared temperature observations. *Remote sensing of Environment*, **19**, 253-268.

Choudhury, B. J., Reginato, R. J., and Idso, S. B., 1986. An analysis of infrared temperature observations over wheat and calculation of latent heat flux. *Agricultural and Forest Meteorology*, **37**, 75-88.

Crago, R. D., 1996. Conservation and variability of the evaporative fraction during the daytime, *Journal of Hydrology*, 1996.

Deschamps, P. Y., and Phulpin, T., 1980. Atmospheric correction of infrared measurements of Sea Surface Temperature using channels at 3.7, 11 and 12 μm . *Boundary-Layer Meteorology*, **18**, 131-143.

Domen, S. R., 1991. Emissivity of aluminized mylar. *Radiation Physics and Chemistry*, **37**, No. 2, 199-201.

Dundas, R. M., 1997. The Use of ATSR to Measure the Radiative Properties of Aerosol Particles. Ph.D Thesis, University of Leicester.

Fels, S. B., 1986. Analytic representations of standard atmosphere temperature profiles. *Journal of Atmospheric Science*, **43**, No. 2, 219-221.

Friedl, M. A., 1995. Modelling land surface fluxes using a sparse canopy model and radiometric surface temperature measurements. *Journal of Geophysical research*, **100**, No. D12, 25435-25446.

Fuchs, M., and Tanner, C. B., 1967. Surface temperature measurements of bare soils. *Journal of Applied Meteorology*, **7**, 303-305.

- Garratt, J. R., and Hicks, B. B., 1973. Momentum, heat and water vapour transfer to and from natural and artificial surfaces. *Quarterly Journal of the Royal Meteorological Society*, **99**, 680-687.
- Gross, E. P., 1955. Shape of collision-broadened spectral lines., *Physics Review*, **97**, 395-403.
- Goody, R., and Yung, Y., 1989. *Atmospheric Radiation*. Oxford University Press, New York, 2nd edition, 528 pp.
- Guillory, A. R., and Jedlovic, G. J., 1993. A technique for deriving column-integrated water content using VAS split-window data. *Journal of Applied Meteorology*, **3**, 1226-1241.
- Hatfield, J. L., Reginato, R. J., and Idso, S. B., 1983. Comparison of long-wave radiation calculation methods over the United States. *Water Resources Research*, **19**, No. 1, 285-288.
- Hipps, L. E., 1989. The infrared emissivities of soil and *Artemisia tridentata* and subsequent temperature corrections in a shrub-steppe ecosystem. *Remote Sensing of Environment*, **27**, 337-342.
- Huband, N. D. S., and Monteith, J. L., 1986. Radiative surface temperature and energy balance of a wheat canopy. *Boundary-Layer Meteorology*, **36**, 1-17.
- Humes, K. S., Kustas, W. P., Moran, M. S., Nichols, W. D., and Wertz, M. A., 1994. Variability of emissivity and surface temperature over a sparsely vegetated surface, *Water Resources Research*, **30**, No. 5, 1299-1310.

Hutchinson, K. D., and Hardy, K. R., 1995. Threshold functions for automated cloud analyses of global meteorological satellite imagery. *International Journal of Remote Sensing*, **16**, No. 18, 3665-3680.

Idso, S. B., 1981. A set of equations for full-spectrum and 8-14 μm and 10.5-12.5 μm thermal radiation from cloudless skies. *Water Resources Research*, **17**, No. 2, 295-304.

Idso, S. B., 1981. An experimental determination of the radiative properties and climatic consequences of atmospheric dust under non-duststorm conditions., *Atmosphere and Environment*, **15**, 1251-1259.

Idso, S. B., and Jackson, R. D., 1969. Thermal radiation from the atmosphere., *Journal of Geophysical Research*, **74**, 3397-5403.

Jackson, R. D., Hatfield, J. L., Reginato, R. J., Idso, S. B., and Pinter, Jr. P. J., 1983. Estimation of daily evapotranspiration from one time-of-day measurements. *Agricultural Water Management*, **7**, 35-362.

Kalma, J. D., Alksnis, H., and Laughlin, G. P., 1988. Calibration of small infra-red surface temperature transducers. *Agricultural and Forest Meteorology*, **43**, 83-98.

Kalma, J. D and Jupp, D. L. B., 1991. Estimating evaporation from pasture using infrared thermometry: evaluation of a one-layer resistance model. *Agricultural and Forest Meteorology*, **51**, 223-246.

Kimball, B. A., Idso, S. B., and Aase, J. K., 1982. A model of thermal radiation from partly cloudy and overcast skies. *Water Resources Research*, **18**, No. 4, 931-936.

Kimes, D. S., Idso, S. B., Pinter Jr., Reginato, R. J., and Jackson, R. D., 1980. View angle effects in the radiometric measurement of plant canopy temperatures. *Remote sensing of environment*, **10**, 273-284.

Kimes, D. S., Sellers, P. J., and Diner, D. J., 1987. Extraction of spectral hemispherical reflectance (albedo) of surfaces from nadir and directional reflectance data. *International Journal of Remote Sensing*, **8**, No. 12, 1727-1746.

Kohsiek, W., De Bruin, H. A. R., The, H., and Van Den Hurk, B., 1993. Estimation of the sensible heat flux of a semi-arid area using surface and radiative temperature measurements. *Boundary-Layer Meteorology*, **63**, 213-230.

Kustas, W. P., 1990. Estimates of evapotranspiration with a one- and two-layer model of heat transfer over partial canopy cover. *Journal of Applied Meteorology*, **29**, 704-715.

Kustas, W. P., Choudhury, B. J., Moran, M. S., Reginato, R. J., Jackson, R. D., Gay, L. W., and Weaver, H. L., 1989. Determination of sensible heat flux over sparse canopy using thermal infrared data. *Agricultural and Forest Meteorology*, **44**, 197-216.

Labeled, J., and Stoll, M. P., 1991. Angular variation of land surface spectral emissivity in the thermal infrared: laboratory investigation on bare soils. *International Journal of Remote Sensing*, **12**, No. 11, 2299-2310.

Labeled, J., and Stoll, M. P., 1991. Spatial variability of land surface emissivity in the thermal infrared band: spectral signature and effective surface temperature. *Remote Sensing of Environment*, **38**, 1-17.

Labeled, J., Li, Z. L., and Stoll, M. P., 1993. Land surface temperature retrieval from ATSR over the Niamey (Niger) area. *Proceedings of the Second ERS-1 Symposium, 'space at the service of our environment'*. Hamburg, Germany, 389-392.

Lagouarde, J. P., Kerr, Y. H., and Brunet, Y., 1995. An experimental study of angular effects on surface temperature for various plant canopies and bare soils. *Agricultural and Forest Meteorology*, **77**, 167-190.

Lhomme, J.-P., Chehbouni, A., and Monteny, B., 1994. Effective parameters of surface energy balance in heterogeneous landscape. *Boundary-Layer Meteorology*, **71**, 297-309.

Maul, G. A., and Sidran, M., 1973. Atmospheric effects on ocean surface temperature sensing from the NOAA satellite scanning radiometer. *Journal of Geophysical Research*, **78**, 1909-1916.

Mason, I. M., Sheather, P. H., Bowles, J. A., and Davies, G., 1996. Blackbody calibration sources of high accuracy for a spaceborne infrared instrument: the Along Track Scanning Radiometer. *Applied Optics*, **35**, No. 4, 629-639.

Mutlow, C. T., Llewellyn-Jones, D. T., Zavody, A. M., Barton, I. J., 1994. Sea surface temperature measurements by the along track scanning radiometer (ATSR) on ESA's ERS-1 satellite – Early results., *Journal of Geophysical Research*, **99**, C11, 22575-22588.

Nerry, F., Labeled, J., and Stoll, M. P., 1988. Emissivity signatures in the thermal IR band for remote sensing: calibration procedure and method of measurement. *Applied Optics*, **27**, No. 4, 758-764.

Norman, J. M., and Becker, F., 1995. Terminology in thermal infrared remote sensing of natural surfaces. *Agricultural and Forest Meteorology*, **77**, 153-166.

Norman, J. M., Kustas, W. P., and Humes, K. S., 1995. Source approach for estimating soil and vegetation energy fluxes in observations of directional radiometric surface temperature. *Agricultural and Forest Meteorology*, **77**, 263-293.

Ohwada, Y., 1984. Evaluation of the integrated emissivity of a black body. *Japanese Journal of Applied Physics*, **23**, No. 3, 167-68.

Prata, A. J., 1993. Land surface temperatures derived from the advanced very high resolution radiometer and the along-track scanning radiometer 1. Theory. *Journal of Geophysical Research*, **98**, No. D9, 16689-16702.

Prata, A. J., 1994. Land surface temperatures derived from the advanced very high resolution radiometer and the along-track scanning radiometer 2. Experimental results and validation of AVHRR algorithms. *Journal of Geophysical Research*, **99**, No. D6, 13025-13058.

Remillard, J. T., Everson, M. P., and Weber, W. H., 1992. Loss mechanisms in optical light pipes. *Applied Optics*, **31**, No. 34, 7232-7241.

Rosenberg, N. J., Blad, B. L., and Verma, S. B., 1983. *Microclimate: The biological environment* (second edition). Wiley-Interscience.

Rothman, L. S., *et al.*, 1987, The HITRAN database: 1986 edition., *Applied Optics*, **26**, 4058-4097.

Salby, M. L., 1996. *Fundamentals of atmospheric physics*. Academic press.

Salisbury, J. W., and D'Aria, D. M., 1992. Emissivity of terrestrial materials in the 8-14 μm atmospheric window. *Remote Sensing of Environment*, **42**, 83-106.

Salisbury, J. W., Wald, A., and D'Aria, D. M., 1994. Thermal-infrared remote-sensing and Kirchhoff law .1. Laboratory measurements. *Journal of Geophysical Research-Solid Earth*, **99**, No. B6, 11897-11911.

Saunders, R. W., and Kriebel, K. T., 1988. An improved method for detecting clear sky and cloudy radiances from AVHRR data. *International Journal of Remote Sensing*, **9**, 123-150.

Settle, J. J., and Drake, N. A., 1993. Linear mixing and the estimation of ground cover proportions. *International Journal of Remote Sensing*, **14**, No. 6, 1159-1177.

Smith, A. H., Saunders, R. W., and Zavody, A. M., 1994. The validation of ATSR using aircraft radiometer data over the tropical Atlantic., *Journal of Atmospheric and Oceanic Technology*, **11**, 789-800.

Sobrino, J. A., Li, Z-L., Stoll, M. P., and Becker, F., 1996. Multi-channel and multi-angle algorithms for estimating sea and land surface temperature with ATSR data. *International Journal of Remote Sensing*, **17**, No. 11, 2089-2114.

Stewart, J. B., 1995. Turbulent surface fluxes derived from radiometric surface temperature of sparse prairie grass. *Journal of Geophysical Research*, **100**, No. D12, 25429-25433.

Stewart, J. B., and Verma, S. B., 1992. Comparison of surface fluxes and conductances at two contrasting sites within the FIFE area. *Journal of Geophysical Research*, **97**, No. D17, 18623-18628.

Stewart, J. B., Kustas, W. P., Humes, K. S., Nichols, W. D., Moran, M. S., and De Bruin, H. A. R., 1994. Sensible heat flux- radiometric surface temperature relationship for eight semi-arid areas. *Journal of Applied Meteorology*, **33**, No. 9, 1110-1117.

Stewart, J. B., Engman, E. T., Feddes, R. A., and Kerr, Y., *Editors* 1996. *Scaling up in Hydrology using Remote Sensing*Wiley, Chichester.

Stierwalt, D. L, Bernstein, J. B., and Kirk, D. D., 1963. Measurement of infrared spectral absorptance of optical materials. *Applied Optics*, **2**, No. 11, 1169-1173.

Swinbank, W. C., 1963. Long-wave radiation from clear skies., *Quarterly Journal of the Royal Meteorological Society*, **89**, 339-348.

Van de Griend, A. A., Owe, M., Groen, M., and Stoll, M. P., 1991. Measurement and spatial variation of thermal infrared surface emissivity in a savanna environment. *Water Resources Research*, **27**, No. 3, 371-379.

Verma, S. B., Rosenberg, N. J., and Blad, B. L., 1978. Turbulent exchange coefficients for sensible heat and water vapour under advective conditions. *Journal of Applied Meteorology*, **17**, 330-338.

Vining, R. C., and Blad, B. L., 1992. Estimation of sensible heat flux from remotely sensed canopy temperatures. *Journal of Geophysical Research*, **97**, No. D17, 18951-18954.

Whitten, D. G. A., and Brooks, J. R. V., 1972. *Dictionary of geology*. Penguin.

Wright, I. R., 1990. A laboratory calibration of infrared thermometers. *International Journal of Remote Sensing*, **11**, No. 1, 181-186.

Zavody, A. M., Gorman, M. R., Lee, D. J., Eccles, D., Mutlow, C. W., and Llewellyn-Jones, D. T., 1994. The ATSR data processing scheme developed for the EODC. *International Journal of Remote Sensing*, **15**, No. 4, 827-843.

Zavody, A. M., Mutlow, C. T., and Llewellyn-Jones, D. T., 1995. A radiative transfer model for Sea Surface Temperature retrieval for the along-track-scanning-radiometer. *Journal of Geophysical Research*, **100**, No. C1, 937-952.